

Molecular dynamics simulations of martensitic transformation in iron

Ou, Xiaoqin

DOI

[10.4233/uuid:00852372-e240-48c8-a621-c07b45836189](https://doi.org/10.4233/uuid:00852372-e240-48c8-a621-c07b45836189)

Publication date

2017

Document Version

Final published version

Citation (APA)

Ou, X. (2017). *Molecular dynamics simulations of martensitic transformation in iron*. [Dissertation (TU Delft), Delft University of Technology]. <https://doi.org/10.4233/uuid:00852372-e240-48c8-a621-c07b45836189>

Important note

To cite this publication, please use the final published version (if applicable).
Please check the document version above.

Copyright

Other than for strictly personal use, it is not permitted to download, forward or distribute the text or part of it, without the consent of the author(s) and/or copyright holder(s), unless the work is under an open content license such as Creative Commons.

Takedown policy

Please contact us and provide details if you believe this document breaches copyrights.
We will remove access to the work immediately and investigate your claim.

Molecular dynamics simulations of martensitic transformation in iron

Proefschrift

ter verkrijging van de graad van doctor
aan de Technische Universiteit Delft,
op gezag van de Rector Magnificus prof.ir. K.C.A.M. Luyben,
voorzitter van het College voor Promoties,
in het openbaar te verdedigen op
dinsdag 19 december 2017 om 12:30 uur

door

Xiaoqin OU

Master of Engineering in Material Engineering, Central South University, China
geboren te Chongqing, China

This dissertation has been approved by

Promotor: Prof. dr. ir. J. Sietsma

Copromotor: Dr. M.J. Santofimia Navarro

Composition of the doctoral committee:

Rector Magnificus	chairman
Prof. dr. ir. J. Sietsma	Delft University of Technology, promotor
Dr. M.J. Santofimia Navarro	Delft University of Technology, copromotor

Independent members:

Prof. dr. ir. L.A.I. Kestens	Delft University of Technology
Prof. dr. ir. L.J. Sluys	Delft University of Technology
Prof. dr. J.T.M. de Hosson	University of Groningen
Prof. dr. H. Urbassek	Technischen Universität Kaiserslautern, Germany
Dr. ir. C. Bos	Tata Steel Europe, the Netherlands

The research leading to these results has received funding from the European Research Council under the European Union's Seventh Framework Programme FP7/2007 – 2013/ERC grant agreement no. [306292].



This thesis is dedicated to my parents.

谨将此论文献给我的父母！

Contents

1. Introduction	1
1.1 Aim of the thesis	2
1.2 Contents of the thesis	2
1.3 References	5
2. Molecular dynamics simulations of fcc-to-bcc transformation in iron - A review	7
2.1 Introduction	8
2.1.1 Background	8
2.1.2 Martensitic transformation paths	8
2.1.3 Interatomic potentials	9
2.2 Martensitic transformation in pure iron with fcc crystal structure	10
2.3 Martensitic transformation in pure iron containing fcc/bcc interfaces	14
2.3.1 Effects of crystallographic orientations on the fcc-to-bcc transformation	14
2.3.2 Effect of temperature on the fcc-to-bcc transformation	18
2.3.3 Other factors affecting the fcc-to-bcc transformation	20
2.4 Conclusions	22
2.5 References	24
3. Atomistic aspects of martensitic transformation in iron containing bcc/fcc interfaces in the Nishiyama-Wassermann orientation relationship by molecular dynamics simulation	27
3.1 Introduction	28
3.2 Simulation methods	28
3.3 Results and discussion	30
3.4 Conclusions	33
3.5 References	35
4. Mechanisms controlling the propagation of bcc/fcc semi-coherent interfaces in iron by molecular dynamics simulations	38
4.1 Introduction	39
4.2 Simulation methods	39
4.3 Results and discussion	41
4.3.1 Growth of the bcc phase at the bcc/fcc interfaces	41
4.3.1.1 System NW	44
4.3.1.2 System KS	46
4.3.1.3 System Nagano	47
4.3.2 Model for growth of bcc phase at the bcc/fcc interfaces	49
4.3.3 Displacement of the atoms involved in the growth of the bcc phase at the bcc/fcc interfaces	52
4.4 Conclusions	54
4.5 References	55
5. Homogeneous nucleation of bcc phase in fcc iron by molecular dynamics simulation	58

5.1 Introduction	59
5.2 Methods	61
5.2.1 Simulation methods	61
5.2.2 Thermodynamic analysis	61
5.2.3 Calculation of shape parameter	64
5.3 Results and discussion	64
5.3.1 Molecular dynamics simulation of the bcc nucleation	64
5.3.2 Classical nucleation of bcc phase from fcc bulk	65
5.3.3 Nonclassical nucleation of bcc phase from fcc bulk	68
5.3.3.1 Aggregation of nuclei	68
5.3.3.2 Stepwise nucleation	72
5.3.4 Temperature of the bcc nuclei	74
5.4 Conclusions	75
5.5 References	77
6. Heterogeneous nucleation of bcc phase at dislocations in fcc/fcc grain boundaries in iron by molecular dynamics simulations	80
6.1 Introduction	81
6.2 Methods	82
6.2.1 Simulation methods	82
6.2.2 Thermodynamic analysis	84
6.3 Results and discussion	86
6.3.1 Nucleation of bcc phase at dislocations	86
6.3.2 Applicability of Cahn's nucleation theory	89
6.3.3 Deviations from Cahn's nucleation theory	91
6.3.3.1 Stepwise nucleation	91
6.3.3.2 Aggregation of bcc nuclei	93
6.3.3.3 Temperature of bcc nuclei	95
6.4 Conclusions	96
6.5 References	98
7. Effects of elastic strain on the nucleation and growth of bcc phase in fcc iron by molecular dynamics simulations	102
7.1 Introduction	103
7.2 Simulation methods	104
7.3 Results and discussion	105
7.3.1 System with a single fcc crystal in Simulation cell 1	105
7.3.2 System with fcc/fcc grain boundaries	112
7.3.2.1 The fcc-to-bcc transformation in Simulation cell 2	112
7.3.2.2 Coarsening of bcc grains	115
7.4 Conclusions	119
7.5 References	121

8. Conclusions and outlook	124
8.1 Conclusions	125
8.2 Outlook for future research.....	126
Summary	129
Samenvatting	132
Acknowledgements	135
List of publications	138
About the author	140

Chapter 1

Introduction

Martensitic transformation, which has been studied intensively for about half a century, takes place during the quenching process of steels in the austenitic state and involves motion of atoms moving over less than an interatomic distance at a velocity possibly as high as that of sound [1]. There are still significant uncertainties with regard to the mechanisms controlling the nucleation and growth of martensite inside the austenite in steels. These mechanisms affect the overall kinetics of the martensitic phase transformation and determine the final microstructures, and correspondingly the properties of the bulk materials. The martensitic phase in iron has a body-centered cubic (bcc) structure and the austenitic phase has a face-centered cubic (fcc) structure. A better understanding of the nucleation and growth of bcc phase in the fcc lattice will significantly contribute to the development of steels with enhanced mechanical properties.

There are two types of nucleation, namely homogeneous nucleation and heterogeneous nucleation. Homogeneous nucleation takes place when one phase forms inside the crystals without defects. Heterogeneous nucleation refers to the product phase initiating from defects, such as grain boundaries and dislocations, during the phase transformation in polycrystalline materials [2]. According to the classical nucleation theory [3], which is known to describe the nucleation processes during phase transformations and recrystallisation in materials, the nucleus needs to overcome an energy barrier in order to become stable. In the field of colloids, nonclassical nucleation mechanisms [4] proposed that the high energy barrier envisioned by the classical nucleation theory can be avoided through processes, such as the aggregation of nuclei and the formation of metastable intermediate structures. It remains an interesting scientific question to which degree the classical or the nonclassical nucleation mechanisms apply to the nucleation process during the martensitic transformation in steels. From observations on the growth stage of the bcc phase forming in steels, Offerman *et al.* predicted according to the classical nucleation theory that the critical nucleus consists of 10-100 atoms [5]. However, other researchers reported a larger critical size, including about 320 atoms [6]. Such discrepancy is attributed to the experimental difficulty in observing the nucleation process in bulk materials.

After nucleation, the bcc phase grows in the fcc matrix by the propagation of bcc/fcc interfaces. The bcc grains were found to prefer to grow in a specific orientation relationship, mainly the Nishiyama-Wassermann [7] and the Kurdjumov-Sachs [8] orientation relationships, with the parent fcc phase in steels [9]. The mechanisms controlling the bcc growth at such bcc/fcc interfaces are not entirely

understood. Besides, internal strain is induced by the fcc-to-bcc transformation, while in turn an external strain leads to the fcc-to-bcc transformation in TRIP steels as well [10,11]. The internal and external strain affect the homogeneity of the final microstructure, and thus the mechanical properties of materials. Therefore, it is interesting to investigate the effects of external strain on the microstructural development during the fcc-to-bcc transformation in iron.

In summary, nucleation and growth of bcc phase during the fcc-to-bcc transformation plays an important role in controlling the microstructures and mechanical properties of steels in industry. However, the dominant mechanisms are not yet clear and require further studies. Molecular dynamics simulation is among the very few techniques to investigate the nucleation and growth of ferrite during the phase transformations in steels at the atomic scale [12].

1.1 Aim of the thesis

The thesis includes the following two objectives:

(1) To study the atomistic mechanisms controlling the growth of bcc phase during the fcc-to-bcc transformation in iron by molecular dynamics simulations. The growth of bcc phase from existing semicoherent bcc/fcc interfaces will be studied at isothermal conditions. The nature of the bcc growth in the original fcc bulk will be determined. Besides, effects of external strain on the microstructural evolution of bcc phase during the fcc-to-bcc transformation will be studied as well.

(2) To study homogeneous and heterogeneous nucleation of bcc phase in the fcc phase in iron at the atomic scale by molecular dynamics simulations. The corresponding thermodynamics is studied in the format of the classical nucleation theory and considering nonclassical aspects. Besides, the microstructures, such as the orientation relations and morphologies of the newly formed bcc nuclei will be investigated.

1.2 Contents of the thesis

Based on the aim of the thesis, it contains the following six chapters:

Chapter 2 is a review of literature on the nucleation and growth of bcc phase in iron by molecular dynamics simulations in recent years. Published investigations on the fcc-to-bcc transformation in iron by molecular dynamics simulations are discussed. It reviews structural factors, simulation conditions and interatomic interaction potentials, which affect the fcc-to-bcc transformation in iron.

Chapter 3 shows atomistic aspects of the fcc-to-bcc transformation in iron with semi-coherent bcc/fcc interfaces in the Nishiyama-Wassermann orientation relationship. The following results are observed in this simulation: 1) The original bcc phase propagates into the original fcc phase in a faceted style; 2)

Homogeneous nucleation of the bcc phase takes place inside the fcc bulk; 3) Heterogeneous nucleation of bcc phase takes place nearby the progressing bcc/fcc interfaces, impeding their further propagation; 4) Two bcc platelets in identical crystallographic orientation relation coalesce to form a coarser bcc grain. Based on the observed phenomena in this chapter, the following Chapters 4-7 will investigate the mechanisms related to the bcc growth and the thermodynamics of the bcc nucleation in fcc iron by molecular dynamics simulations.

Chapter 4 studies the mechanisms controlling the growth of bcc from bcc/fcc semi-coherent interfaces in iron at 300 K by molecular dynamics simulations. Besides the bcc/fcc interfaces in the Nishiyama-Wassermann orientation relationship studied in Chapter 3, other two semi-coherent bcc/fcc interfaces have been investigated, which are in the Kurdjumov-Sachs orientation relationship and another randomly selected orientation relationship. The direction and magnitude of the atomistic displacements during the fcc-to-bcc transformation determine whether the existing bcc grain grows from the bcc/fcc interfaces in a diffusional or diffusionless (martensitic) nature. The mechanisms describing the growth of the existing bcc phase into the fcc bulk are investigated in the present chapter.

Chapter 5 investigates the homogeneous nucleation of bcc in a fcc grain in iron at 160 K by molecular dynamics simulation. A universal method is proposed to analyse the thermodynamics of nucleation based on the output of the molecular dynamics simulation. This method can be applied to a variety of materials during liquid-solid solidification process or solid-solid phase transformations. The nucleation thermodynamics is studied in the framework of the classical nucleation theory as well as including nonclassical mechanisms. The agreement between the present molecular dynamics data and the prediction of classical nucleation theory indicates to what extent the classical nucleation theory can describe the nucleation process during the fcc-to bcc transformation. Results indicate that the classical nucleation theory describes reasonably the postcritical stage of a bcc nucleus, but overestimates the energy barrier for forming a stable nucleus. The homogeneous nucleation process involves nonclassical nucleation pathways studied in the field of nanomaterials [4], applying to the current case during the fcc-to-bcc transformation in iron.

Chapter 6 describes the heterogeneous nucleation of bcc at the fcc/fcc grain boundaries in iron at 100 K by molecular dynamics simulations. The thermodynamics of the nucleation is studied in the frame of Cahn's model [13], which describes the nucleation of one phase at dislocations. The thermodynamic analysis method in the present chapter is derived from the one proposed in Chapter 5. The estimated elastic constants and interface energies are compared with the results from previous experiments and simulations. Besides, phenomena that are not considered in Cahn's model but are observed in the simulations are described in this chapter as well. Results show that the bcc nucleation at dislocations on fcc/fcc boundaries is more complex than that generally accepted, involving for example the existence of intermediate state, aggregation of discrete subnuclei and high-temperature nuclei relative to their surroundings.

Chapter 7 presents a preliminary study on the effects of strain on the nucleation and coarsening of bcc phase in fcc iron by molecular dynamics simulations. Previous experimental results in literature [12,13] indicate both enhanced hardness and ductility of steels due to the strain induced by the martensitic transformation. Those enhanced properties can be related to the microstructure, especially the grain size, of the product steels. Thus the present chapter includes several cases on the development of the microstructure during the fcc-to-bcc transformation in iron under external strain. The crystallographic orientations between the product bcc phase and the parent fcc phase are analysed, which correlate to the coalescence of neighbouring bcc grains and the formation of twinning bcc structures in iron under external strain.

Chapter 8 summarises the conclusions of the thesis. The outlook of the present research is also included.

1.3 References

- [1] M. J. Santofimia, L. Zhao, R. Petrov, C. Kwakernaak, W. G. Sloof and J. Sietsma, 'Microstructural development during the quenching and partitioning process in a newly designed low-carbon Steel', *Acta Mater.*, 2011, 59, 6059-6068.
- [2] H. Sharma, J. Sietsma and S. E. Offerman, 'Preferential nucleation during polymorphic transformations', *Sci. Rep.*, 2016, 6, 30860.
- [3] J. W. Christian, 'The theory of transformations in metals and alloys', first ed., Pergamon, Oxford, 1981.
- [4] J. Lee, J. Yang, S. G. Kwon and T. Hyeon, 'Nonclassical nucleation and growth of inorganic nanoparticles', *Nat. Rev. Mater.*, 2016, 1, 16034.
- [5] S. E. Offerman, N. H. van Dijk, J. Sietsma, S. Grigull, E. M. Lauridsen, L. Margulies, H. F. Poulsen, M. Th. Rekvelde and S. van der Zwaag, 'Grain nucleation and growth during phase transformations', *Science*, 2002, 298, 1003-1005.
- [6] H. I. Aaronson, W. F. Lange III and G. R. Purdy, 'Discussion to "Grain nucleation and growth during phase transformations" by S.E. Offerman et al.', *Science*, 298, 1003 (November 1, 2002)', *Scripta Mater.*, 2004, 51, 931-935.
- [7] Z. Nishiyama, 'X-ray investigation of the mechanism of the transformation from face-centred to body-centred cubic lattice', *Sci. Rep. Tohoku Imp. Univ.*, 1934, 23, 637-664. Cited by M. G. Hall, H. I. Aaronson and K. R. Kinsman, 'The structure of nearly coherent fcc: bcc boundaries in a Cu-Cr alloy', *Surf. Sci.*, 1972, 31, 257-274.
- [8] G. V. Kurdjumov and G. Sachs, 'Über den mechanismus der stahlhärtung', *Z. Phys.*, 1930, 64, 325-343. Cited by M. G. Hall, H. I. Aaronson and K. R. Kinsman, 'The structure of nearly coherent fcc: bcc boundaries in a Cu-Cr alloy', *Surf. Sci.*, 1972, 31, 257-274.
- [9] H. Landheer, S. E. Offerman, R. H. Petrov and L. A. I. Kestens, 'The role of crystal misorientations during solid-state nucleation of ferrite in austenite', *Acta Mater.*, 2009, 57, 1486-1496.
- [10] T. -H Ahn, C. -S Oh, D. H. Kim, K. H. Oh, H. Bei, E. P. George and H. N. Han, 'Investigation of strain-induced martensitic transformation in metastable austenite using nanoindentation', *Scripta Mater.*, 2010, 63, 540-543.
- [11] S. Zaeferrer, J. Ohlert and W. Bleck, 'A study of microstructure, transformation mechanisms and correlation between microstructure and mechanical properties of a low alloyed TRIP steel', *Acta Mater.*, 2004, 52, 2765-2778.
- [12] X. S. Yang, S. Sun, X. L. Wu, E. Ma and T. Y. Zhang, 'Dissecting the mechanism of martensitic transformation via atomic scale observations', *Sci. Rep.*, 2014, 4, 6141.
- [13] J. W. Cahn, 'Nucleation on dislocations', *Acta Metall.*, 1957, 5, 169-172.

Chapter 2

Molecular dynamics simulations of fcc-to-bcc transformation in iron - A review

Abstract:

Molecular dynamics simulation has been used in the literature to study the martensitic fcc-to-bcc transformation in iron at the atomic scale. The chapter presents the available interatomic interaction potentials for iron, which describe the properties of different phases present in that system. Studies on the fcc-to-bcc transformation in iron by molecular dynamics simulations are discussed in the present chapter. Factors affecting the fcc-to-bcc transformation in iron are analysed: a) structural factors, such as grain/phase boundaries, grain sizes and stacking faults; b) simulation conditions, such as the presence of free surfaces, external stress/strain and temperature; c) the interatomic interaction potential. The main emphasis of the present chapter is on results giving insight into the mechanisms governing the processes of nucleation and growth of bcc phase in iron.

* This chapter is based on a scientific paper:

X. Ou, Molecular dynamics simulations of fcc-to-bcc transformation in pure iron: a review, *Materials Science and Technology*, 2016, 33(7): 822-835.

2.1 Introduction

2.1.1 Background

As one of the most important construction materials, steel is widely used in a variety of industrial fields, such as the automotive, gas transport and power generation [1]. The thermodynamic phase diagram for pure iron indicates three different crystal structures as well as the liquid phase. Under the standard atmospheric pressure, iron exhibits the body centred cubic (bcc) crystal structure from room temperature to 1184 K (α -Fe, ferrite) and from 1665 to 1809 K (δ -Fe, δ -ferrite), the close-packed face centred cubic (fcc) structure (γ -Fe, austenite) between 1184 K and 1665 K. Under a pressure above about 13 GPa, the ϵ -Fe with a hexagonal close-packed (hcp) structure is stable at 0 K [2].

Martensite forms from austenite during the quenching process of steels [3,4]. In carbon steels, martensite is supersaturated with carbon and has a highly strained body-centered tetragonal (bct) crystal structure (α' -Fe). In pure iron, however, martensite has a bcc structure due to the absence of carbon (α -Fe). The formation of martensite involves a collective movement of atoms over less than an interatomic distance at a velocity possibly as high as that of sound [5]. Due to the difficulty in observing these atomic processes, experimental studies on the nature of martensitic transformation are limited.

Molecular dynamics (MD) simulation proves to be one of the methods that can contribute to a better understanding of the experimental results and the mechanisms of the martensitic transformation [6-8]. The present chapter critically reviews recently-published investigations on the fcc-to-bcc transformation in pure iron by MD simulations. Factors that affect the mechanisms of fcc-to-bcc transformation are summarised, such as the grain size of fcc crystals, the orientation relationships (ORs) at the bcc/fcc interfaces and the simulation temperatures.

2.1.2 Martensitic transformation paths

During the martensitic transformation, the coordinated movement of atoms leads to a specific OR between the parent fcc (γ) and the newly formed bcc (α) lattices, in which a pair of close-packed planes in the α and γ phases are parallel or nearly parallel. In 1924, Bain proposed the fcc to bcc crystal structure transformation path by defining a bct unit cell in the fcc crystal [9]. The Bain path involves in an expansion of z -axis by about 21% and a contraction of x , y -axes by about 12%. However, the mainly observed ORs between the fcc parent phase and bcc martensite differ from the one predicted by the Bain transformation [10]. Several alternative ORs were proposed between the parent fcc phase and the product bcc phase, including the Kurdjumov-Sachs orientation relationship (KS OR) [11], the Nishiyama-Wassermann orientation relationship (NW OR) [12], the Pitsch orientation relationship (Pitsch OR) [13,14], the Greninger-Troiano orientation relationship (GT OR) and the inverse Greninger-Troiano orientation relationship (GT' OR) [15]. The ORs for these transformation paths are

as follows:

Bain OR [9]:

$$\{001\}_\gamma \parallel \{001\}_\alpha, \langle 100 \rangle_\gamma \parallel \langle 110 \rangle_\alpha$$

KS OR [11]:

$$\{111\}_\gamma \parallel \{011\}_\alpha, \langle 101 \rangle_\gamma \parallel \langle 111 \rangle_\alpha$$

NW OR [12]:

$$\{111\}_\gamma \parallel \{011\}_\alpha, \langle 112 \rangle_\gamma \parallel \langle 011 \rangle_\alpha$$

Pitsch OR [13,14]:

$$\{010\}_\gamma \parallel \{101\}_\alpha, \langle 101 \rangle_\gamma \parallel \langle 111 \rangle_\alpha$$

GT OR [15]:

$$\{111\}_\gamma \parallel \{011\}_\alpha, \langle 51217 \rangle_\gamma \parallel \langle 71717 \rangle_\alpha$$

GT' OR [15]:

$$\{51217\}_\gamma \parallel \{71717\}_\alpha, \langle 111 \rangle_\gamma \parallel \langle 011 \rangle_\alpha$$

The two models with the NW and KS ORs introduce a main shear in the $\langle 112 \rangle$ direction of the $\{111\}$ plane, which explains the existence of the conjugate habit planes in the martensitic transformation. The NW and KS ORs are about 5.16° apart from each other, the GT OR is an intermediate between them. The GT' OR is an intermediate between the Pitsch OR and the KS OR. About 90% of the observations on the α - γ phase transformation indicate either the NW or KS OR or an OR that is close to these two [16].

2.1.3 Interatomic potentials

There are three varieties of interatomic potentials for MD simulations for iron, namely the embedded-atom method (EAM) potential [17-24], bond-order potential [25] and the modified embedded-atom method (MEAM) potential [2]. The EAM potentials mainly rely on a central force description, while the bond-order and MEAM potentials are angular-dependent potentials.

Engin *et al.* [26] calculated the free energies of several existing interatomic potentials for iron using the metric scaling and thermodynamic integration methods. Thus, relative stabilities of the fcc and bcc phases were characterised. It was found that, among all available EAM potentials, the 'Finnis-Sinclair' potential [17], 'Johnson-Oh' potential [18] and 'Ackland' potential [19] indicate the lowest free energy for the bcc phase at all temperatures. Thus, bcc phase is more stable than the fcc phase for these three potentials. The 'Meyer-Entel' potential [20] is the only EAM potential that allows the bi-directional fcc-bcc phase transformation in iron as studied by Engin *et al.* [26]. The 'Meyer-Entel' potential [20] shows equilibrium between fcc and bcc at a temperature of around 550 ± 50 K. The fcc phase is stable above this temperature and the bcc phase is stable below this temperature. Engin *et al.* [26] also studied the 'Chamati' potential [21], which describes both the low-temperature bcc phase and high-temperature fcc phase. Besides, there are also some other EAM potentials for iron, such as the 'Farkas' potential [22], 'Mendelev' potential [23] and 'Simonelli' potential [24].

Recently, a bond-order potential was established by Müller *et al.* [25] for iron. Besides the γ/α transition, this potential is also able to describe the γ/δ transition at 2210 K, just below the melting temperature of 2270 K. Bi-directional phase transitions between the bcc and fcc iron were also studied by Tateyama *et al.* [27] using the modified ‘Finnis-Sinclair’ potential with a cut-off function in the atomic charge density. The cut-off distance of the atomic charge density has an effect on the relative stability between the bcc and fcc phases at high temperature. The bcc phase is stable when applying a long cut-off distance and the fcc is stable when applying a short cut-off distance. Therefore, the bi-directional phase transformation between fcc and bcc phase across the transition temperature of iron from bcc-to-fcc phase (A_3 temperature of the potential) was incorporated by changing the cut-off distance at the A_3 temperature ($T_{A_3}=1516$ K for the ‘Finnis-Sinclair’ potential). Moreover, two MEAM potentials for iron were proposed by Lee *et al.* [2]. Compared with the EAM potential, the MEAM potential includes the effects of the angular distribution of the background electron density of adjacent atoms.

2.2 Martensitic transformation in pure iron with fcc crystal structure

In MD simulation, the simplest way to start the solid-solid phase transformation is with a metastable crystal structure. For simulations of martensitic transformation in iron, the fcc structure is the metastable phase for most potentials as indicated by Engin *et al.* [26]. The Gibbs free energy difference between the two phases will lead to spontaneous fcc-to-bcc transformation at sufficiently high temperature for atomic mobility, on account that no volume or other constraints hinders the phase transformation.

Engin and Urbassek [28] studied the fcc-to-bcc transformation using the ‘Finnis-Sinclair’ potential, which describes a stable bcc phase. The fcc-to-bcc transformation was characterised by the evolution of the free energy while a unit cell of fcc structure is distorted along the Bain path to the bcc structure. Simulations were done at 1200 K and 1400 K, respectively. An initial configuration of perfect fcc was constructed and the temperature was fixed at zero pressure. The martensitic transformation occurred spontaneously at 1400 K with non-periodic boundary conditions in all directions, while no transformation took place at 1200 K. The thermal fluctuations within the simulation volume induced the phase transformation. The fcc phase, as shown in figure 2-1(a), transformed to the bcc phase with an intermediate twin structure at 200 ps (figure 2-1(b)), which vanished finally at 400 ps (figure 2-1(c)). In experiments, the typical twin structure also forms during the martensitic transition in steel. However, it remains stable because the volume of the martensite phase is constrained by the surrounding austenitic matrix. Besides, an incubation time during the simulation was needed for the martensitic transformation because an activation energy must be overcome to bring the system into a favourable condition for the cooperative movement of atoms.

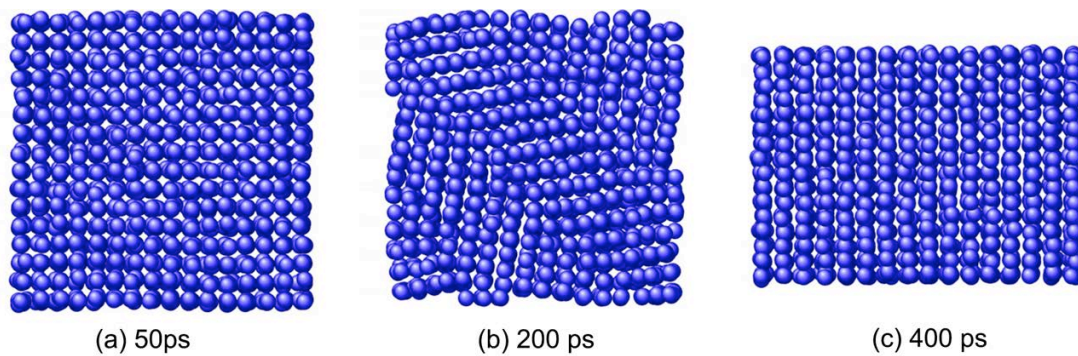


Figure 2-1 Cross-sectional view through the transforming crystallite ($T=1400$ K) at various stages of the transformation process: (a) the initial fcc crystal at 50 ps; (b) the transformed bcc phase with twin structure; (c) the twin structure diminished in the final bcc grain [28].

It should be noted that ‘homogeneous nucleation’ of bcc phase was reported to take place without nucleation sites such as extended defects, dislocations or grain boundaries. However, non-periodic boundary conditions were employed in all directions during the simulations, which means that free surfaces may provide the nucleation sites for the fcc-to-bcc transformation. Considering that different crystal structures were in the same colour in the configurations shown in figure 2-1, the adaptive common neighbour analysis (a-CNA) should be a good choice in distinguishing the crystallographic structures of different phases and locating phase interfaces or grain boundaries. This may help determine whether the bcc phase nucleated homogeneously inside the fcc phase or heterogeneously at the surfaces. Furthermore, it is difficult to distinguish neighbouring nucleation sites in a system with a small volume, which includes only several thousands of atoms. A simulation system containing a number of atoms on the order of 10^6 should be suitable for the observation of nucleation sites. External constraints, i.e. fixed volume of the simulated system, will also have an effect on the fcc-to-bcc transformation. With the volume of the system fixed, for instance in the NVT ensemble with periodic boundary conditions, no phase transformation happened even at high temperatures while the transformation occurred spontaneously without an incubation period for an entirely free system [28].

By introducing internal means of pressure relaxation, the fcc-to-bcc phase transformation did occur in simulations with fixed volume [28,29]. Previous studies [30] indicated that martensitic transformation also took place in a simulation with a high density of vacancies in the bulk of Fe-Ni alloys. Isolated non-spherical particles [31] or an array of fcc nanoparticles can also contribute to martensitic nucleation in simulations with decreasing temperature, for which the fcc phase transformed to bcc locally near triple junctions of grains [32]. Two fcc grains in a twin geometry were embedded in an fcc matrix, as shown in figure 2-2. The fcc-to-bcc transformation started at the boundary between the two grains and propagated horizontally, which resulted in heterogeneous structures. It was proposed that the combination of the interface energy and the free volume at the grain boundaries induced the spontaneous transformation [28].

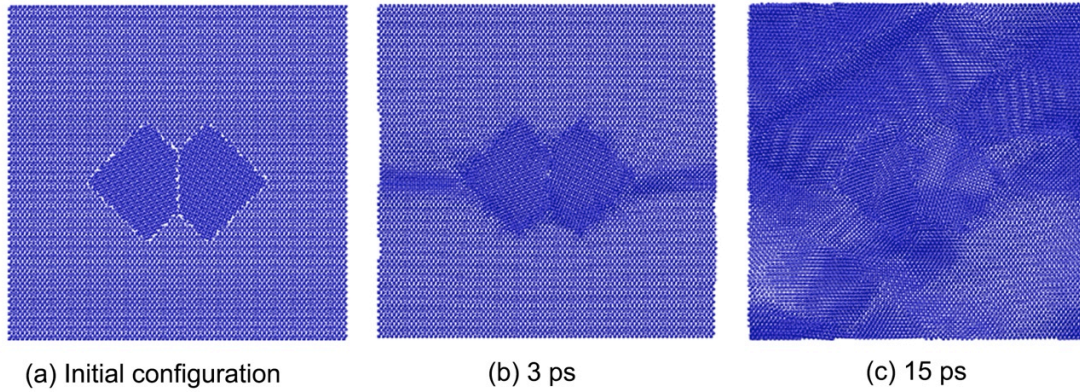


Figure 2-2 Cross-sectional view through the simulation crystallite containing a grain boundary at the beginning of the simulation, and at two times during the transformation at 0 K: (a) initial fully fcc configuration, (b) the fcc-to-bcc transformation initiating from the grain boundaries at 3 ps, (c) the final heterogeneous structure resulting from the fcc-to-bcc transformation at 15 ps [28].

The role of fault band intersections on the nucleation of martensite from austenite was investigated by Sinclair and Hoagland [33] by MD simulations. Two types of dislocations, $\gamma D = \frac{a_{fcc}}{6} [\bar{1} \bar{1} \bar{2}] (\bar{1} \bar{1} 1)$ and $\alpha B = \frac{a_{fcc}}{6} [\bar{1} 1 2] (1 \bar{1} 1)$ were placed in the simulation cell, introducing faults passing through the simulation cell. The type γD dislocation created a band of stacking faults on every second atomic plane, generating a T/2 faults. The type αB dislocation created a band of stacking faults on every third atomic plane, generating a T/3 faults. Thus the fault band intersection proposed by Olson and Cohen [34] was obtained at the intersection area of those two fault bands, as shown in figure 2-3. The EAM potential by Ackland *et al.* [20] indicates a higher cohesive energy of the fcc and hcp lattices at the stacking faults than that of the bcc lattice at all temperatures. After relaxation of the simulation cell, nucleation and growth of bcc phase took place and this transformation started first within the intersection volume. The crystallography of the product bcc phase indicated the Pitsch OR. That was different from experimental results, which mostly indicate orientations close to the KS and NW OR. Recently, Song and Hoyt [35] studied the crystallographic orientations of the bcc nuclei formed at the grain boundaries of a polycrystalline fcc matrix in iron by MD simulations using the ‘Ackland’ potential as well [19]. The bcc grains nucleated heterogeneously at the fcc grain boundaries with at least one interface boundary oriented with the fcc crystal in the NW or KS OR. The KS OR was the dominant orientation between the product bcc phase and the parent fcc phase. The forming bcc/fcc interface propagated by a terrace-ledge-kink growth mechanism. Besides, the bcc nucleation at the fcc grain-boundary triple junctions took place in the absence of an activation energy barrier according to Song and Hoyt [36].

For simulations in nanoscale systems, the surface may exert strong influences on the fcc-to-bcc transformation due to the finite size. Sandoval and Urbassek [37] studied the solid-solid phase transitions in cylindrical iron nanowires and the dependence of transition temperature on the tensile stress applied in the axial direction based on the EAM potential proposed by Meyer and Entel [20]. It was observed that the fcc-to-bcc transformation temperature was inversely proportional to the applied axis stress at relatively small values (lower than 3 GPa). The plastic deformation of the nanowire took

place with a critical tensile stress higher than 3 GPa, above which the fcc-to-bcc phase transition was inhibited. For the nanowires, the specific surface area facilitated the phase transition. The transformation starting from the surface was heterogeneous while that in the bulk was homogeneous.

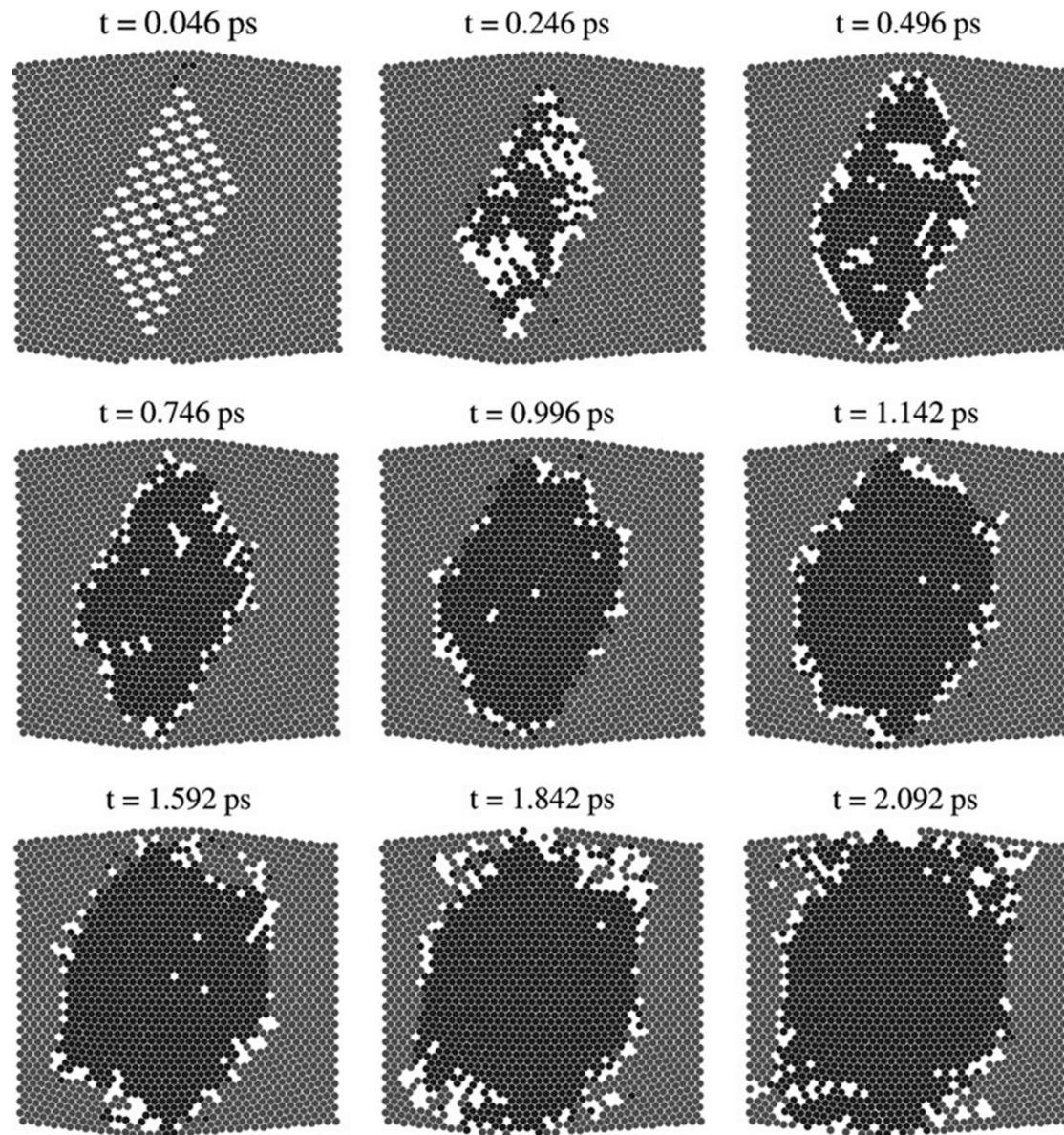


Figure 2-3 Graphical illustration of simulation cell (viewed along the $[0\ 1\ 1]_{fcc}$ direction) as a function of relaxation time (given above each image) showing the gradual formation of a structure with 8-coordinated atoms (dark gray) first within the intersection volume followed by growth into the fault bands and unfaulted fcc matrix.

Colours of atoms represent different structures: white-hcp, light grey-fcc, dark grey-bcc. [33]

From the analysis above, external stresses or strain, defects (i.e. stacking faults), free surface and grain boundaries contribute to the fcc-to-bcc transformation in iron by MD simulation. A simulation cell with fixed volume may exhibit no transformation at any temperature. The martensitic transformation will preferentially start at regions where strain or stress exist. If homogeneous nucleation occurs, an incubation time is needed for forming the critical nucleus, indicating that an activation energy is involved. Additionally, introducing grain boundaries will also facilitate the fcc-to-bcc transformation, due to the high potential energy stored in the grain boundaries. The investigations mentioned above

mainly focus on the conditions that contribute to the nucleation and growth of bcc phase in fcc iron. However, none of them focuses on the nucleation mechanisms of bcc phase. It is interesting to study how homogeneous or heterogeneous bcc nuclei initiate and become stabled inside fcc iron, which plays an important role in the microstructural evolution of materials.

2.3 Martensitic transformation in pure iron containing fcc/bcc interfaces

By MD simulation, the structural and dynamic properties of the bcc/fcc interface during the martensitic transformation in Fe can be studied. Since the fcc is metastable at low temperatures, the bcc phase will grow.

2.3.1 Effects of crystallographic orientations on the fcc-to-bcc transformation

The martensitic transformation is characterised by the specific crystallographic orientations between the fcc and bcc phases, which correspond to different transformation paths. The most common orientation relations between the product bcc phase and fcc phase are the KS OR and NW OR, which are therefore the most frequently studied orientations at the bcc/fcc interfaces in the initial configurations of MD simulations.

Bos *et al.* [6] constructed two interfaces, close to the Bain and KS orientations, to study the fcc-to-bcc transformation at constant temperature using MD simulation based on the 'Johnson-Oh' potential [18]. The initial configuration included two bcc/fcc interfaces, as shown in figure 2-4. Systems with different sizes and with periodic boundaries in either two or three directions were examined, as shown in Table 2-1. In System A without free surfaces, there was no significant interface movement at different temperatures analysed. For systems B, C and D with at least one free boundary, the fcc/bcc interface moved after an incubation time. Longer incubation time was involved for systems with larger volume to surface area ratio, because larger absolute misfit had to be accommodated at the free surface. During the incubation time, a specific interface structure, apparently containing dislocations, formed for all systems, which appeared to be essential for the martensitic transformation afterwards. The movement of the atoms during the transformation was highly coordinated over a small distance and slip occurred along closely packed crystallographic planes. The fcc-to-bcc transformation was of a martensitic nature.

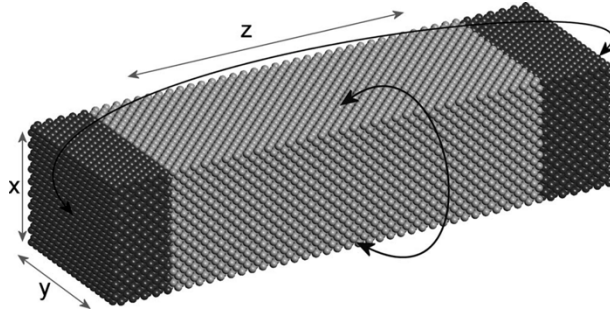


Figure 2-4 A typical starting configuration for interface type C, a system with only one nonperiodic direction (the y direction). Bcc atoms are dark; fcc atoms are light. The x direction in the figure coincides with the $[1\ 0\ 0]_{fcc}$ direction, y with $[0\ 1\ 0]_{fcc}$, and z with $[0\ 0\ 1]_{fcc}$. [6]

Table 2-1 This table provides an overview of the simulations performed by Bos *et al.* [6].

Interface type	fcc atoms	bcc atoms	fcc xy planes	bcc xy planes	fcc x rows	fcc y columns	bcc x rows	bcc y columns
A, fcc{100}/bcc{110}, fcc(100)/bcc(011), x -, y - and z -directions periodic, $T=1520$ K								
	6600	5544	30	22	20	11	18	14
B, fcc{100}/bcc{110}, fcc(100)/bcc(011), x -, and z -direction, periodic, $T=810$ K								
$\eta=11.5$ Å	9240	7920	30	22	22	14	20	18
$\eta=15.8$ Å	30800	15840	50	22	44	14	40	18
$\eta=19.9$ Å	46200	23760	50	22	44	21	40	27
C, fcc{100}/bcc{110}, fcc(100)/bcc(011), x - and z directions periodic, $T=304, 506, 810,$ and 1316 K								
$\eta=25.0$ Å	21560	7920	70	22	22	14	20	18
D, fcc{111}/bcc{110}, fcc(112)/bcc(011), z -direction periodic, $T=304, 810, 1012,$ and 1316 K								
$\eta=17.0$ Å	33264	16000	42	20	36	22	40	20
$\eta=17.0$ Å	76032	16000	96	20	36	22	40	20

η represents the volume to surface area ratio.

Tateyama *et al.* [38,39] investigated the kinetics of $(1\ 1\ 0)_{bcc}|| (1\ 1\ 1)_{fcc}$ interfaces following various orientation relationships in iron during the fcc-to-bcc transformation by MD simulation. The ‘Finnis-Sinclair’ potential [17] was used. Four initial configurations were investigated, two of which had the NW and KS OR. The others were two intermediate ORs between the NW and KS OR, which were prepared by rotating the OR 2° and 4° from the NW OR with respect to the $[1\ 1\ 1]_{fcc}$ axis, respectively. Two propagation modes were found: planar and needle-like propagation. For all orientations between NW and near NW ORs, a planar propagation of the fcc-bcc interface was observed at the initial stage of the phase transformation. For KS and near KS ORs, however, a needle-like propagation was found after an initial planar propagation, as shown in figure 2-5. The fcc-to-bcc transformation started preferentially at the areas with small atomic stress that corresponded to the areas with good lattice matching between the fcc and bcc lattices. The ratio of matching area in the NW relation was found to be higher than that of the KS relation, which was the reason for the planar and needle-like propagation modes of the bcc/fcc interface in the NW and KS OR, respectively [38,39]. Besides, the velocity of the needle-like growth was calculated to be ten times higher than that of the planar propagation at the initial propagation stage. In this study, the driving force for the phase transformation during the interface propagation was not discussed, because the energy difference

between the bcc and fcc phase was independent of temperature according to the ‘Finnis-Sinclair’ potential [17].

The MD simulations by Maresca and Curtin [40] indicated the structure and motion of bcc/fcc interfaces that matched the experimental observations on dislocated lath martensite. The $(1\ 1\ 1)_{fcc} \parallel (0\ 1\ 1)_{bcc}$ planes were parallel for the bcc/fcc interfaces, the habit planes of which were misoriented for 10° to 20° about the $[\bar{1}\ 0\ 1]_{fcc}$ direction. When the $[\bar{1}\ 0\ 1]_{fcc}$ and $[\bar{1}\ \bar{1}\ 0]_{bcc}$ close-packed directions were misoriented by an angle of $3.11^\circ \leq \varphi \leq 5.7^\circ$ around the $[1\ 1\ 1]_{fcc}$ directions, similar to that performed by Tateyama *et al.* [38], the bcc/fcc interfaces were glissile and athermal at finite temperature up to 600 K. However, the bcc/fcc interfaces with the misorientation $\varphi = 0$ (KS OR), 10° were neither glissile nor athermal. The motion of those interfaces required an external stress above 400 MPa at 0 K.

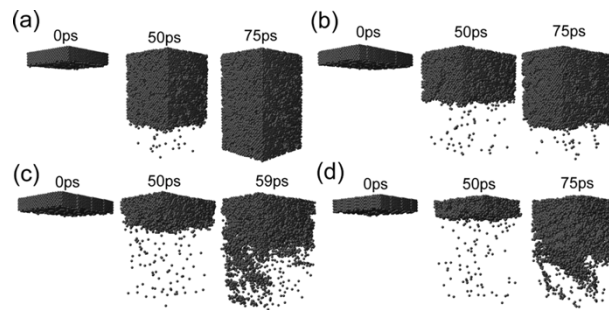


Figure 2-5 Snapshots of the calculation cell with the interface of (a) NW OR, (b) the intermediate OR with a rotation angle of 2.00° from NW, (c) the intermediate OR with a rotation angle of 4.00° from NW OR and (d) KS OR during relaxation. Only atoms with bcc configuration are shown in (a)-(d) for clarity. [38]

Wang and Urbassek [41,42] also studied the influence of the bcc/fcc interfaces in NW or KS OR on the fcc-to-bcc transformation in iron at 100 K. The ‘Meyer-Entel’ potential [20] was used in the MD simulation in order to describe the bidirectional transformations between the bcc and fcc phases. Different characteristics of the nucleation and interface motion were observed during the simulation process. For systems with NW OR, both homogeneous and heterogeneous nucleation of the bcc phase was observed during the martensitic transformation, as shown in figure 2-6. ‘Heterogeneous growth’ (as described by the authors) occurred at the phase boundaries and involved the interface motion with a velocity of 24 m/s, which was much slower than the interface velocity reported by Tateyama *et al.* [38,39]. The homogeneous nucleation of new bcc phase was oriented towards the parent fcc phase in the KS relationship. The bcc phase growing from the phase boundary had a different OR from the bcc phase nucleating homogeneously inside the bulk fcc phase, which led to grain boundaries separating the initial bcc phase and the homogeneously nucleated bcc phase. For systems with the KS OR, however, the fcc-to-bcc phase transformation was dominated by homogeneous nucleation and no heterogeneous nucleation was observed. Stacking faults, rather than grain boundaries, were found in the product bcc phase. Besides, the newly formed and initial bcc phase had exactly the same crystallographic orientation. Thus the parent fcc crystal transformed to the product bcc phase following the KS relationship.

It should be noted that the studies by Wang and Urbassek [41,42] named the growth of the bcc phase at the original interfaces as ‘heterogeneous growth’ referring to the growth of the original bcc phase whereas they named ‘homogeneous growth’ of bcc phase referring to the growth of the bcc nuclei nucleating homogeneously inside the fcc bulk. In reality, those terminologies for the homogeneous or heterogeneous nucleation of bcc phase are confusing. For the homogeneous nucleation, an examination work has been performed by the present author in iron with one single fcc crystal including 108,000 atoms by MD simulations using the ‘Meyer-Entel’ potential. The simulation is performed at the constant temperature of 100 K and under the atmosphere pressure with periodic boundary conditions. No homogeneous nucleation is observed in 500 ps. Therefore, the bcc nuclei may not form homogeneously but heterogeneously inside the fcc bulk in investigations [41,42], where the stacking faults resulting from the relaxation of the original bcc/fcc interface may act as the heterogeneous nucleation site for the bcc phase, as shown by the atoms coloured in light blue in figure 2-6.

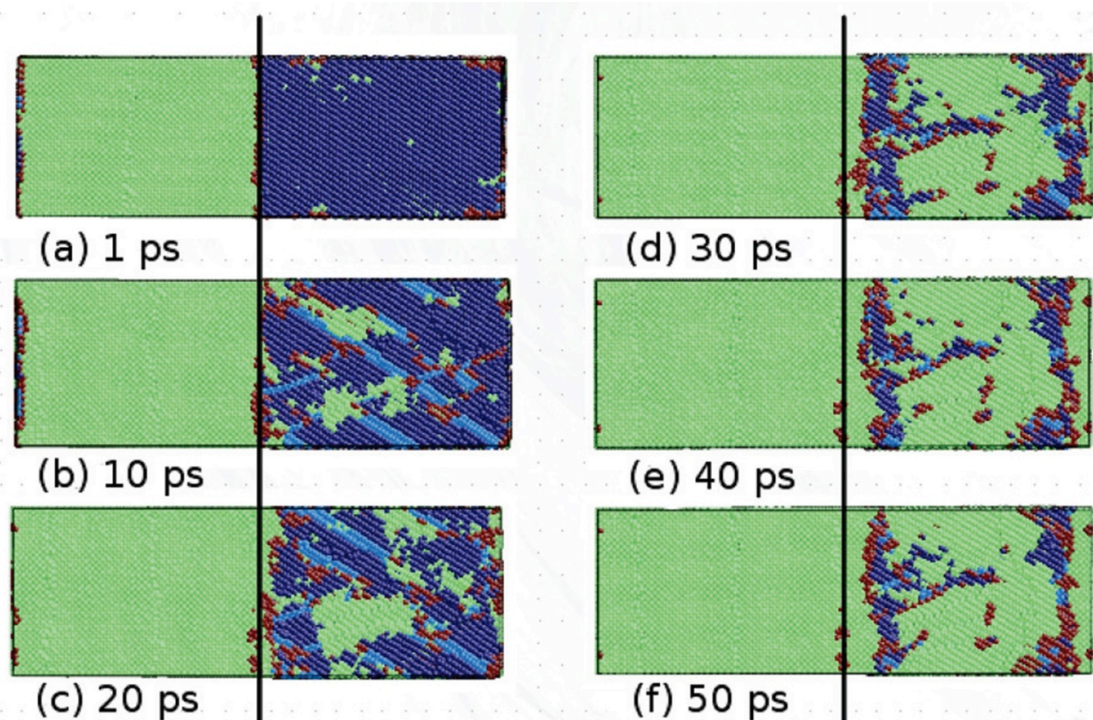


Figure 2-6 Snapshots showing the time evolution of the fcc-to-bcc transition (NW interface) at 100 K. The original position of the interface has been marked by a black line. Colours represent different crystallographic structures: green-bcc, dark blue-fcc, light blue-hcp, red-unknown. [42]

From the analysis described above, it can be seen that the orientation relations between the fcc and bcc phase at the interfaces may affect the mechanisms of interface migration, as well as the nucleation and growth of the newly formed bcc phase. The NW or near NW ORs seem to be more favorable to the planar growth of the interfaces. Due to its poorer lattice matching between the fcc and bcc phase, the interface of the KS OR moves much faster than that of an NW OR, in a needle-like way. Moreover, the crystallographic orientations of the initial bcc/fcc interfaces have effects on the resulting orientation of the bcc nuclei forming inside the fcc bulk. Additionally, the heterogeneously nucleated bcc phase at the bcc/fcc interfaces tends to have a different orientation with the homogeneously nucleated bcc phase inside the fcc bulk. The reason may be related to the internal strain or stress induced from the fcc-to-

bcc transformation occurring at the bcc/fcc interfaces, which nonetheless needs further investigation. Therefore, it is necessary to take into account the effects of different crystallographic orientations of bcc/fcc interfaces when performing MD simulation in pure iron.

2.3.2 Effect of temperature on the fcc-to-bcc transformation

Wang and Urbassek [43] studied the effects of temperature on the deformation induced fcc-to-bcc transformation in a simulation cell containing a bcc/fcc interface in the NW OR. Five temperatures were analysed ranging from 300 to 700 K. A strong temperature dependence of the bcc nucleation was observed. With shear applied, the fcc phase transformed to the bcc phase at temperatures below 500 K while the reverse bcc-to-fcc transformation took place for temperatures above 500 K. Both homogeneous and heterogeneous nucleation of the bcc phase were observed with shear at 300 K, while only heterogeneous nucleation of the bcc phase took place at the phase boundary sheared at 400 K. Because the driving force for the nucleation is smaller at a temperature closer to the transition temperature (550 ± 50 K).

By introducing a parallel array of steps (or disconnections) into the original fcc/bcc interfaces, Song and Hoyt [44,45] studied the velocities, mobility and activation energy for motion of the fcc/bcc interface in pure Fe at temperatures in the range of 600-1400 K. The 'Ackland' potential [19] was used, which describes a stable bcc phase. The fcc crystal is tilted by 4.04° from the NW relationship, thus a series of equally spaced parallel steps were introduced at the interface boundary, which are known as structural disconnections, as shown in figure 2-7. The interface boundary fluctuated during growth, indicating that some steps grew faster than the others. The interface velocities were calculated to be in the range of 0.7-3.4 m/s, which were considerably lower than the interface velocity (on the order of 400 m/s) reported by Bos *et al.* [6]. The temperature dependence of the interface mobility in the form of Arrhenius plot showed a linear relationship, indicating a thermally activated atomic mechanism for interface migration. The study by Bos *et al.* [6] also indicated the thermally-activated interface motion as the interface velocity decreased linearly with increasing temperature. The free energy difference between the bcc and fcc phases acted as the driving force for the interface motion. The activation energy was found to be 16 ± 5 kJ/mol, which was considerably lower than experiments on the massive transformation in Fe alloys. The study by Bos *et al.* [6] reported a lower activation energy of 5.8 kJ/mol. It was reported that the interface motion proceeded by the lateral translation of the glissile secondary disconnections, as seen in figure 2-8. The primary disconnections acted as heterogeneous nucleation sites for the continuous formation of new secondary disconnections, thus the nucleation was the operative mechanism of the interface migration.

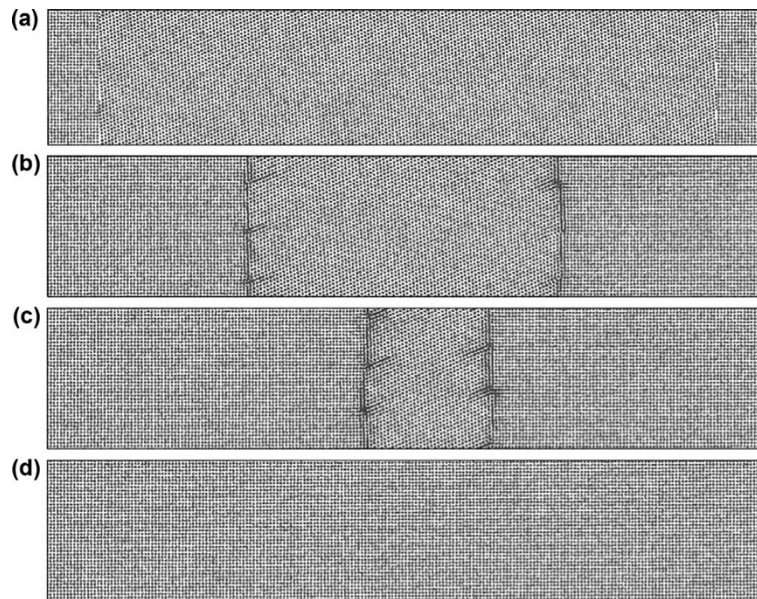


Figure 2-7 An example of the fcc-to-bcc transformation process for a temperature of 800 K. (a) The initial state of the simulation box shows a sandwich structure, with two bcc phases connecting the two sides of a fcc phase. (b and c) The positions of the interfaces at 5 and 10 ns. (d) The equilibrium bcc phase after the transformation. [44]

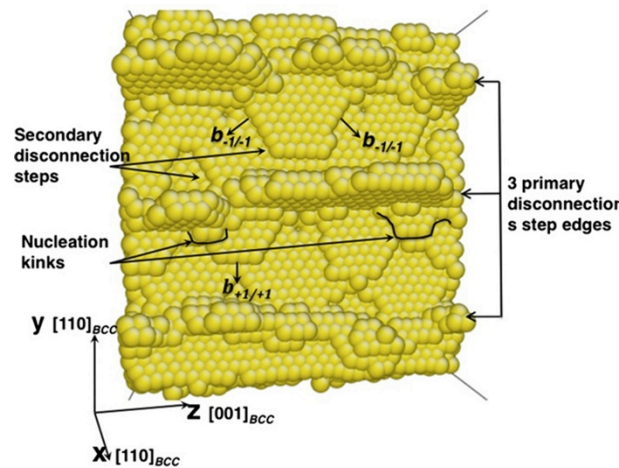


Figure 2-8 Cross-sectional view normal to the interface $(1\ 1\ 0)_{bcc}$ during the transformation with only the bcc atoms indicated. Islands of the bcc nucleate on the edge of the primary disconnection steps and several secondary disconnections grow along their Burgers vectors direction in each terrace plane. Only bcc atoms are shown. [45]

Different temperatures have an effect on the nucleation of the bcc phase and migration of bcc/fcc interfaces in fcc iron, as mentioned above. Meanwhile, different relaxation temperature will also affect the relative stabilities between the bcc and fcc phase. Tateyama *et al.* [27] modified the ‘Finnis-Sinclair’ potential [17] by introducing the cut-off distance of the atomic charge densities. The cut-off distance of the atomic charge density, which generates the attractive force, affects the relative stability between the bcc and fcc phases as a function of temperature. At high temperature, the bcc was stable at a long cut-off distance and the fcc was stable at a short cut-off distance. After relaxation of the system at 1516 K (T_{A3} for ‘Finnis-Sinclair’ potential), the bcc-to-fcc phase transformation was observed for the cut-off distance of 3.17 Å or less while the fcc-to-bcc transformation was observed for the cut-off

distance of 3.21 Å or more. For the cut-off distance between 3.17 and 3.21 Å, no phase transformation was found. Then the fcc/bcc interface was relaxed at three temperatures, which were 1511 K, 1516 K and 1521 K, respectively. The cut-off distances $R_c = 3.3$ Å at 1511 K and $R_c = 3.1$ Å at 1521 K. The motion of the fcc/bcc interface is shown in figure 2-9. At 1511 K, the fcc to bcc phase transformation was found and no interface motion was found at 1516 K. Relaxation at 1521 K induced the bcc-to-fcc phase transformation. It should be noted that the propagation of the interface with an NW OR followed a planar-like growth, which coincides with the previous results published by Tateyama *et al.* [38,39].

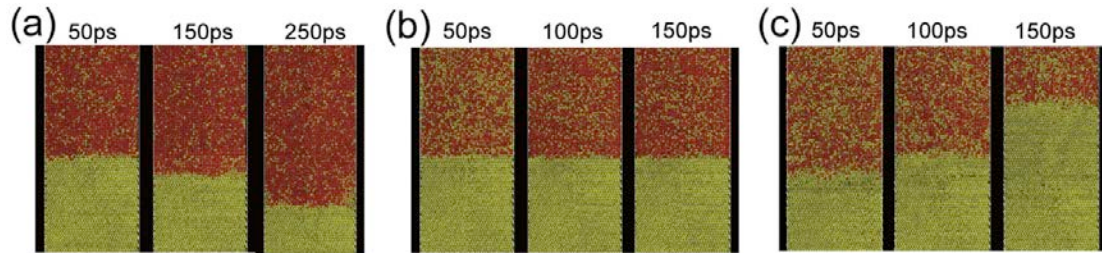


Figure 2-9 Snapshots of the fcc-bcc configuration with the NW orientation relationship during relaxation at various temperatures: (a) 1511 K (below A3 temperature of the ‘Finnis-Sinclair’ potential), (b) 1516 K (the A3 temperature) and (c) 1521 K (above the A3 temperature). Brown and yellow spheres represent atoms with the bcc and fcc configurations, respectively. [27]

As can be seen from the discussion above, temperature has an important effect on the nucleation and growth process of the bcc phase in the fcc-to-bcc transformation. Heterogeneous nucleation may occur at both low and high temperatures while homogeneous nucleation may happen at low temperature due to the requirement of forming a critical nucleus, requiring a substantial driving force. As for the interface mobility, temperature seems to have a different influence for the different EAM potentials. For the EAM potential that exhibits an fcc-to-bcc transition temperature, the interface velocity was smaller when the temperature was closer to the transition temperature. For the EAM potentials that have a stable bcc phase at all temperatures, the interface mobility tended to increase with temperature, because the interface migration is thermally activated. However, it is not clear whether the different EAM potential will affect the nucleation of bcc phase. Further, it is significant to choose the proper cutoff distance for the EAM potential because it may affect the stability of the fcc and bcc phases at high temperatures. The cut-off distance can be also used to influence the relative stability of the fcc and bcc phases.

2.3.3 Other factors affecting the fcc-to-bcc transformation

Recently, the dependence of martensitic transformation on external stresses became a major issue. Such stresses develop invariably in realistic situations, either by external influences or by the developing microstructure itself. The martensitic transformation itself leads to stresses due to the change in lattice structure and volume of the new phase [7]. Wang and Urbassek [43] studied the effects of shear deformation on the fcc-to-bcc transformation in iron by MD simulations. The shear deformation was applied to the bcc-fcc system with bcc/fcc interfaces in the NW OR, as shown in figure 2-10. The shear deformation ϵ_{xz} was connected to the shear angle ϑ via $\epsilon_{xz} = \tan\vartheta$. Without

shear deformation, the system was stable with no fcc-to-bcc transformation taking place at 300 K. Both homogeneous and heterogeneous nucleation was observed when shear angles were up to 20° , as shown in figure 2-11. The homogeneously formed bcc phase occupied 70% of the space in the original fcc phase, which inhibited the interface movement. The homogeneously nucleated bcc phase had a different crystallographic orientation relation from the heterogeneously nucleated bcc phase at the original bcc/fcc interface, leading to the survival of grain boundaries in the final configuration. Besides, the relief structure evolved on the surface during shearing due to the applied shear deformation, which resulted from a considerable lattice distortion and a high residual stress during the martensitic phase transition.

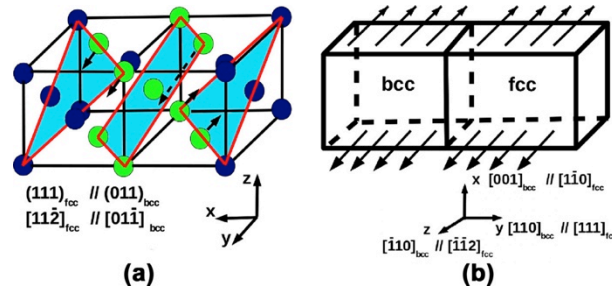


Figure 2-10 (a) NW relationship during the martensitic transition. The blue atoms are fcc and the green are bcc. The blue planes indicate the $\{111\}_{fcc}$ planes. The arrows indicate the first motion of the atoms (shear deformation of the $\{111\}_{fcc}$ planes in the $[11\bar{2}]_{fcc}$ direction), which initiates the phase transition; the dashed arrow indicates the invariant direction, which is shared by the bcc and fcc phases. (b) The shear deformation that is applied to the bcc-fcc system. Orientations are indicated. [43]

Recently, Yang *et al.* [46,47] investigated the plastic deformation induced $\gamma(fcc) \rightarrow \epsilon(hcp) \rightarrow \alpha'(bcc)$ martensitic transformation in iron by MD simulations using the 'Mendelev' potential [23]. The martensitic transformation at the bcc/fcc interfaces either with KS OR or Pitsch OR was found to obey the Borgers-Burgers-Olson-Cohen model [48,49]. A hard sphere model from fcc to bcc phase transformation was proposed by Bogers and Burgers for the martensitic transformation in steels [49]. Based on the Bogers and Burgers model, Olson and Cohen [48] indicated that the fcc phase transformed to an hcp structure and then to the bcc structure during the martensitic transformation. Two shears were involved in the fcc-to-bcc transformation. The first shear was $\frac{a_f}{18}[1\bar{2}\bar{1}]$ on every $(11\bar{1})_{fcc}$ plane and the second shear was $\frac{a_f}{16}[\bar{1}2\bar{1}]$ on every $(111)_{fcc}$ plane, which corresponded to the T/3 and 3T/8 transformation dislocation, respectively (T represents a Shockley partial dislocation for fcc twin shear and a_f represents the lattice parameter of fcc phase). The results coincided well with their experimental observations by high-resolution transmission electron microscopy.

The above investigations indicate that the external shear stress induces the fcc-to-bcc transformation in iron. The fcc-to-bcc transformation in turn leads to internal stress inside the bulk. The fcc-to-bcc transformation following a specific orientation relationship in iron involves contraction and expansion in specific crystallographic directions [9-15]. Therefore, it is expected that external stress or strain in different directions have varying influences on the orientations of the deformation-induced bcc phase inside the fcc phase. The fcc-to-bcc transformation prefers to follow a specific martensitic variant,

which minimizes the total energy required for the mechanically induced phase transformation of metastable fcc phase [50]. Besides, it is interesting to investigate the effects of external stress or strain on the growth of the product bcc grains. Since bcc grains with identical orientations tend to coalesce to form a coarser grain [51], the selection of specific crystallographic orientation relation during the fcc-to-bcc transformation under external stress or strain may intensify the coalescence process, affecting the mechanical properties of materials. Therefore, it is meaningful to study the effects of stress and strain on the nucleation and growth of bcc phase in fcc iron, which affects the final microstructure and mechanical properties of materials.

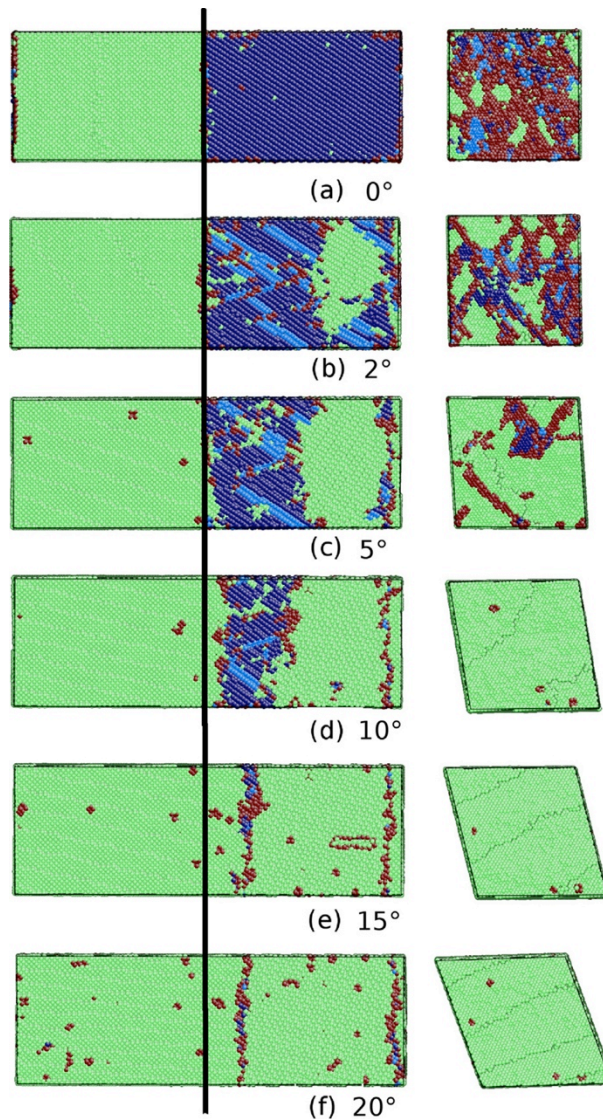


Figure 2-11 Snapshots showing the local structure of the fcc-bcc biphasic system at a temperature of 300 K for shear angles of up to 20°. The pictures on the left show the phase evolution in the y - z plane; those on the right show the original interface plane (x - z plane) in the middle of the system. The colors denote the local crystal structure. Green: bcc; dark blue: fcc; light blue: hcp; red: unknown. The original interface position is marked by a black line. [43]

2.4 Conclusions

In summary, MD simulation establishes a bridge between theory and experimental observations, which extends the understanding and knowledge of the mechanisms of nucleation and growth of martensitic forming in fcc iron at an atomistic scale. The fcc-to-bcc transformation is found to take place in the MD simulations by introducing structural defects, such as fcc/fcc grain boundaries, dislocations, phase interfaces and stacking faults. External conditions, such as temperature, stress/strain and free surfaces, will also affect the evolution of the fcc-to-bcc transformation. Regardless of the investigations, understanding of the mechanisms controlling the nucleation and growth of martensite is still far from complete. The key questions that demand further studies are as follows:

1) The homogeneous or heterogeneous nucleation mechanisms of bcc phase in fcc iron. Most of the MD simulations were focused on studies of the mechanisms of martensitic transformation from a structural point of view. Few studies aim at analysing the nucleation process. It is still unclear how the bcc nucleus initiates and stabilises inside the solid bulk of fcc iron. The thermodynamics of the martensitic nucleation, either homogeneously or heterogeneously, is a challenging and interesting field for future investigation on iron.

2) The growth mechanisms of bcc phase during the fcc-to-bcc transformation. The fcc-to-bcc transformation in iron prefers to follow a specific crystallographic orientation. Depending on the crystallographic orientation relation between the bcc and fcc phase, the bcc/fcc interfaces may or may not be glissile. For the glissile interfaces, it depends whether its motion is thermally activated. It will be useful to understand the growth of bcc phase at the bcc/fcc interfaces, especially those in the NW and KS ORs, which are the most frequently observed orientations, because the growth of bcc grains determines the microstructural evolution, and thus the mechanical properties of the materials.

Therefore, the present thesis will concentrate on these problems, aiming to promote the understanding of martensitic transformation in iron and steels.

2.5 References

- [1] N. Gunkelmann, E. M. Bringa, K. Kang, G. J. Ackland, C. J. Ruestes and H. M. Urbassek, 'Polycrystalline iron under compression: plasticity and phase transitions', *Phys. Rev. B*, 2012, 86, 144111.
- [2] T. Lee, M. I. Baskes, S. M. Valone and J. D. Doll, 'Atomistic modeling of thermodynamic equilibrium and polymorphism of iron', *J. Phys.: Condens. Matter*, 2012, 24, 225404.
- [3] A. L. Roitburd and G. V. Kurdjumov, 'The nature of martensitic transformations', *Mater. Sci. Eng.*, 1979, 39, 141-167.
- [4] M. J. Santofimia, L. Zhao, R. Petrov, C. Kwakernaak, W. G. Sloof and J. Sietsma, 'Microstructural development during the quenching and partitioning process in a newly designed low-carbon steel', *Acta Mater.*, 2011, 59, 6059-6068.
- [5] R. F. Bunshah and R. F. Mehl, 'The rate of propagation of martensite', *Trans. AIME*, 1953, 197, 1251-1258.
- [6] C. Bos, J. Sietsma and B. J. Thijsse, 'Molecular dynamics simulation of interface dynamics during the fcc-bcc transformation of a martensitic nature', *Phys. Rev. B*, 2006, 73, 104117.
- [7] B. J. Wang, E. Sak-Saracino, N. Gunkelmann and H. M. Urbassek, 'Molecular-dynamics study of the α - γ phase transition in Fe-C', *Comput. Mater. Sci.*, 2014, 82, 399-404.
- [8] Z. Yang and R. A. Johnson, 'An EAM simulation of the alpha-gamma iron interface', *Modell. Simul. Mater. Sci. Eng.*, 1993, 1, 707-716.
- [9] L. Sandoval, H. M. Urbassek and P. Entel, 'The Bain versus Nishiyama-Wassermann path in the martensitic transformation of Fe', *New J. of Phys.*, 2009, 11, 103027.
- [10] G. Miyamoto, N. Takayama and T. Furuhashi, 'Accurate measurement of the orientation relationship of lath martensite and bainite by electron backscatter diffraction analysis', *Scripta Mater.*, 2009, 60, 1113-1116.
- [11] G. V. Kurdjumov and G. Sachs, 'Über den mechanismus der stahlhärtung', *Z. Phys.*, 1930, 64, 325-343. Cited by M. G. Hall, H. I. Aaronson and K. R. Kinsman, 'The structure of nearly coherent fcc: bcc boundaries in a Cu-Cr alloy', *Surf. Sci.*, 1972, 31, 257-274.
- [12] Z. Nishiyama, 'X-ray investigation on the mechanism of transformation from face-centred to body-centred cubic lattice', *Sci. Rep. Tohoku Imp. Univ.*, 23, 1934, 637-664. Cited by M. G. Hall, H. I. Aaronson and K. R. Kinsman, 'The structure of nearly coherent fcc: bcc boundaries in a Cu-Cr alloy', *Surf. Sci.*, 1972, 31, 257-274.
- [13] W. Pitsch, 'Der Orientierungszusammenhang zwischen zementit und austenit', *Acta Metall.*, 1962, 10, 897-900.
- [14] W. Pitsch, 'The martensite transformation in thin foils of iron- nitrogen alloys', *Philos. Mag.*, 1959, 4, 577-584.
- [15] A. B. Greninger and A. R. Troiano, 'The mechanism of martensite formation', *Trans. AIME.*, 1949, 185, 590-598.
- [16] T. Fukino and S. Tsurekawa, 'In-situ SEM/EBSD observation of alpha/gamma phase transformation in Fe-Ni alloy', *Mater. Trans.*, 2008, 49, 2770-2775.

- [17] M. W. Finnis and J. E. Sinclair, 'A simple empirical n-body potential for transition', *Philos. Mag. A*, 1984, 50, 45-55.
- [18] R. A. Johnson and D. J. Oh, 'Analytic embedded atom method model for bcc metals', *J. Mater. Res.*, 1989, 4, 1195-1201.
- [19] G. J. Ackland, D. J. Bacon, A. F. Calder and T. Harry, 'Computer simulation of point defect properties in dilute Fe-Cu alloy using a many-body interatomic potential', *Philos. Mag. A*, 1997, 75, 713-732.
- [20] R. Meyer and P. Entel, 'Martensite-austenite transition and phonon dispersion curves of Fe_{1-x}Ni_x studied by molecular-dynamics simulations', *Phys. Rev. B*, 1998, 57, 5140-5147.
- [21] H. Chamati, N. Papanicolaou, Y. Mishin and D. Papaconstantopoulos, 'Embedded-atom potential for Fe and its application to self-diffusion on Fe (100)', *Surf. Sci.*, 2006, 600, 1793-1803.
- [22] R. Pasianot, D. Farkas and E. J. Savino, 'Empirical many-body interatomic potential for bcc transition metals', *Phys. Rev. B*, 1991, 43, 6952-6961.
- [23] M. I. Mendeleev, S. Han, D. J. Srolovitz, G. J. Ackland, D. Y. Sun and M. Asta, 'Development of new interatomic potentials appropriate for crystalline and liquid iron', *Phil. Mag.*, 2003, 83, 3977-3994.
- [24] G. Simonelli, R. Pasianot and E. J. Savino, 'Embedded-atom-method interatomic potentials for bcc-iron', *Mater. Res. Soc. Symp. Proc.*, 1993, 291, 567-572.
- [25] M. Müller, P. Erhart and K. Albe, 'Analytic bond-order potential for bcc and fcc iron-comparison with established embedded-atom method potentials', *J. Phys.: Condens. Matter*, 2007, 19, 326220.
- [26] C. Engin, L. Sandoval and H. M. Urbassek, 'Characterization of Fe potentials with respect to the stability of the bcc and fcc phase', *Modell. Simul. Mater. Sci. Eng.*, 2008, 16, 035005.
- [27] S. Tateyama, Y. Shibuta, T. Kumagai and T. Suzuki, 'A molecular dynamics study of bidirectional phase transformation between bcc and fcc iron', *ISIJ Int.*, 2011, 51, 1710-1716.
- [28] C. Engin and H. M. Urbassek, 'Molecular-dynamics investigation of the fcc → bcc phase transformation in Fe', *Comput. Mater. Sci.*, 2008, 41, 297-304.
- [29] Yu. N. Gornostyrev, V. N. Urtsev, M. K. Zhalutdinov, P. Entel, A.V. Kaptan and A. R. Kuznetsov, 'Reconstruction of grain boundaries during austenite-ferrite transformation', *Scripta Mater.*, 2005, 53, 153-158.
- [30] K. Kadau, M. Gruner, P. Entel and M. Kretz, 'Modeling structural and magnetic phase transitions in iron-nickel nanoparticles', *Phase Transit.*, 2003, 76, 355-365.
- [31] K. Kadau and P. Entel, 'Atomistic investigations of the thermodynamical stability and martensitic nucleation of Fe₈₀Ni₂₀ nanoparticles', *Phase Transit.*, 2002, 75, 59-65.
- [32] K. Kadau, P. Entel and P. S. Lomdahl, 'Molecular dynamics study of martensitic transformations in sintered Fe-Ni nanoparticles', *Comp. Phys. Commun.*, 2002, 147, 126-129.
- [33] C. W. Sinclair and R. G. Hoagland, 'A molecular dynamics study of the fcc → bcc transformation at fault intersections', *Acta Mater.*, 56, 2008, 4160-4171.
- [34] G. B. Olson and M. Cohen, 'A mechanism for the strain-induced nucleation of martensitic transformations', *J. Less-Common Met.*, 1972, 28, 107-118.
- [35] H. Song and J. J. Hoyt, 'An atomistic simulation study of the crystallographic orientation relationships during the austenite to ferrite transformation in pure Fe', *Modell. Simul. Mater. Sci. Eng.*,

2015, 23, 085012.

[36] H. Song and J. J. Hoyt, 'Barrier-free nucleation at grain-boundary triple junctions during solid-state phase transformations', *Phys. Rev. Lett.*, 2016, 117, 238001.

[37] L. Sandoval and H. M. Urbassek, 'Finite-size effects in Fe-nanowire solid-solid phase transitions: a molecular dynamics approach', *Nano letters*, 2009, 9, 2290-2294.

[38] S. Tateyama, Y. Shibuta and T. Suzuki, 'Orientation relationship in fcc-bcc phase transformation kinetics of iron: a molecular dynamics study', *ISIJ Int.*, 2010, 50, 1211-1216.

[39] S. Tateyama, Y. Shibuta and T. Suzuki, 'A molecular dynamics study of the fcc-bcc phase transformation kinetics of iron', *ISIJ Int.*, 2008, 59, 971-974.

[40] F. Maresca and W. A. Curtin, 'The austenite/lath martensite interface in steels: structure, athermal motion, and in-situ transformation strain revealed by simulation and theory', *Acta Mater.* 2017, 134, 302-323.

[41] B. J. Wang and H. M. Urbassek, 'Atomistic dynamics of the bcc \leftrightarrow fcc phase transition in iron: Competition of homo- and heterogeneous phase growth', *Comput. Mater. Sci.*, 2014, 81,170-177.

[42] B. J. Wang and H. M. Urbassek, 'Phase transitions in an Fe system containing a bcc/fcc phase boundary: An atomistic study', *Phys. Rev. B*, 2013, 87, 104108.

[43] B. J. Wang and H. M. Urbassek, 'Molecular dynamics study of the α - γ phase transition in Fe induced by shear deformation', *Acta Mater.*, 2013, 61, 5979-5987.

[44] H. Song and J. J. Hoyt, 'A molecular dynamics simulation study of the velocities, mobility and activation energy of an austenite-ferrite interface in pure Fe', *Acta Mater.*, 2012, 60, 4328-4335.

[45] H. Song and J. J. Hoyt, 'An atomistic simulation study of the migration of an austenite-ferrite interface in pure Fe', *Acta Mater.*, 2013, 61, 1189-1196.

[46] X. S. Yang, S. Sun, X. L. Wu, E. Ma and T. Y. Zhang, 'Dissecting the Mechanism of Martensitic Transformation via Atomic Scale Observations', *Sci. Rep.*, 2014, 4, 6141.

[47] X. S. Yang, S. Sun and T. Y. Zhang, 'The mechanism of bcc α' nucleation in single hcp ϵ laths in the fcc $\gamma \rightarrow$ hcp $\epsilon \rightarrow$ bcc α' martensitic phase transformation', *Acta Mater.*, 2015, 95, 264-73.

[48] G. B. Olson. and M. Cohen, 'A general mechanism of martensitic nucleation-Part II. FCC \rightarrow BCC and other martensitic transformations', *Metall. Trans. A*, 1976, 7, 1905-1914.

[49] A. J. Bogers and W. G. Burgers, 'Partial dislocations on the {110} planes in the b.c.c. lattice and the transition of the f.c.c. into the b.c.c. lattice', *Acta Met.*, 1964, 12, 255-261.

[50] H. N. Han, C. G. Lee, C. -S. Oh, T. -H. Lee and S. -J. Kim, 'A model for deformation behavior and mechanically induced martensitic transformation of metastable austenitic steel', *Acta Mater.*, 2004, 52, 5203-5214.

[51] J. H. Pak, D. W. Suh and H. K. D. H. Bhadeshia, 'Promoting the coalescence of bainite platelets', *Scripta Mater.*, 2012, 66, 951-953.

Chapter 3

Atomistic aspects of martensitic transformation in iron containing bcc/fcc interfaces in the Nishiyama-Wassermann orientation relationship by molecular dynamics simulation

Abstract:

Molecular dynamics simulations have been employed to study the effect of fcc/bcc interfaces in the Nishiyama-Wassermann orientation relationship on the fcc-to-bcc transformation at 300 K in pure iron. Simulations show the growth of the original bcc phase present in the initial configuration as well as the nucleation and growth of new bcc grains in the original fcc phase. During growth, both heterogeneous and homogenous bcc nuclei impede the propagation of the original bcc/fcc interface. In some locations, neighboring newly-nucleated bcc plates merge into a single bcc grain. The fcc phase transforms to bcc by a predominantly martensitic mechanism.

* This chapter is based on a scientific paper:

X. Ou, J. Sietsma, M.J. Santofimia, Molecular dynamics simulation of the effects of fcc/bcc interfaces on the nucleation and growth of martensite in iron, *Proceedings of the International Conference on Solid-Solid Phase Transformations in Inorganic Materials (PTM)*, Whistler, Canada. 2015, pp 817-823.

3.1 Introduction

In the majority of steels, the structure, energy and kinetics of ferrite (bcc)/austenite (fcc) phase boundaries play a key role in phase transformations and microstructure formation [1]. In general, it is proposed that the fcc-to-bcc transformation paths mainly follow the Nishiyama-Wassermann (NW) [2] or the Kurdjumov-Sachs (KS) [3] orientation relationship (OR) [4]. Previous studies [5,6,7-10] have investigated the fcc-to-bcc transformation in iron with fcc/bcc interfaces in either the NW or KS OR by molecular dynamics (MD) simulations. However, reported MD simulations of the fcc-to-bcc transformations in iron varied, considering the differences of fcc/bcc interface orientations and the embedded atom method (EAM) potential used.

The fcc/bcc interfaces with different ORs affect the nucleation and growth of bcc phase, either at the interfaces or inside the original fcc phase. Song and Hoyt [9,10] observed heterogeneous nucleation of bcc phase at the primary facets at the interface, which led to the interface migration towards the fcc bulk. In studies by Wang and Urbassek [7,8,11], homogenous nucleation of new bcc phase inside the original fcc phase was observed both in the configurations with interfaces in the NW and KS ORs, while heterogeneous nucleation of bcc phase only took place at the interfaces in the NW OR. The heterogeneous nucleation resulted in the thermally activated interface migration, which was impeded by the homogeneous nucleation of bcc phase inside the fcc bulk. Furthermore, Maresca and Curtin [12] reported glissile and athermal bcc/fcc interfaces without bcc nucleation in fcc iron by MD simulations. Considering those discrepancies, more studies are necessary to reveal the mechanisms regarding to the migration of bcc/fcc interfaces, homogeneous and heterogeneous nucleation of bcc phase and the subsequent coarsening mechanism in fcc iron. The present chapter studies the effects of semi-coherent fcc/bcc interfaces in the NW OR on the fcc-bcc transformation with MD simulations in a pure iron system containing both fcc and bcc phases.

3.2 Simulation methods

In the present work, the embedded-atom method (EAM) potential by Mendeleev *et al.* [13,14] was used. This potential describes the bcc phase to be stable in the temperature range of 0 to 1820 K. It has been successfully employed in describing the martensitic transformation in iron with bcc/fcc interfaces by MD simulations [15,16], for which two systems with bcc/fcc interfaces in the Pitsch OR and KS OR were studied. The deformation induced $\gamma(\text{fcc}) \rightarrow \epsilon(\text{hcp}) \rightarrow \alpha'(\text{bcc})$ martensitic transformation was observed at the bcc/fcc interfaces in the MD simulations based on the Mendeleev potential [13,14], which coincides with experimental observations using the high resolution transmission electron microscopy (HRTEM). Besides, the potential is in better agreement with the experimental lattice parameter, elastic constants, point-defect energies, bcc-fcc transformation energy, liquid density, liquid structure factor, melting temperature and other properties than other existing EAM iron potentials

[13,14]. It provides a better coincidence of the cohesive energy difference (or the driving force) $\Delta E_{fcc-bcc}$ between the bcc and fcc phase with the density functional theory (DFT) results as well [17].

The interface was constructed according to the NW OR. The matching of closest packed planes $(111)_{fcc} \parallel (110)_{bcc}$ is established at the interface and the $[001]_{bcc}$ direction is aligned parallel to the $[1\bar{1}0]_{fcc}$ direction in the y axis. The simulation has been performed considering periodic boundaries in all three directions, so the system has no free surfaces. The dimensions in the x and y directions have been chosen to ensure that the elastic strain due to volume mismatch is kept to a minimum. The mismatches in x and y directions are 0.08% and 0.03%, respectively, which implies elastic stresses lower than 150 MPa, leading to negligible additional strain energy. The dimensions of each phase, as well as other detailed information of the system, are listed in Table 3.1. Lattice parameters (fcc: 3.658 Å, bcc: 2.855 Å) for fcc and bcc have been obtained at 0 K. The potential energy difference between the fcc and bcc phase at 0 K is 0.122 eV. In experiments, lattice parameters at 0 K for fcc and bcc are 3.562 and 2.860 Å, respectively [17].

Table 3-1 Parameters for the system studied in this work. x_L , y_L and z_L denote the lengths of the systems in the three cartesian directions. Lengths are indicated both in Å and unit cells (UC). The crystal orientations are for fcc:

x : $[\bar{1}\bar{1}2]$; y : $[1\bar{1}0]$; z : $[111]$; for bcc in NW orientation: x : $[\bar{1}10]$; y : $[001]$; z : $[110]$.

x_L (Å)	y_L (Å)	z_L (Å)	x_L (UC) _{bcc}	y_L (UC) _{bcc}	z_L (UC) _{bcc}	x_L (UC) _{fcc}	y_L (UC) _{fcc}	z_L (UC) _{fcc}	fcc atoms	bcc atoms
205.92	82.77	91.06	51	29	10	23	16	8	70656	59160

The snapshot shown in figure 3-1 represents the initial, unrelaxed configuration. The adaptive common neighbor analysis (a-CNA) [18] was chosen as the discriminator to determine the local structure around atoms. The lattice mismatching and possible overlapping of fcc/bcc atoms at the boundaries resulted in hcp or unknown structures for some atoms. The system contains two bcc/fcc interfaces perpendicular to the z direction considering the periodicity conditions.

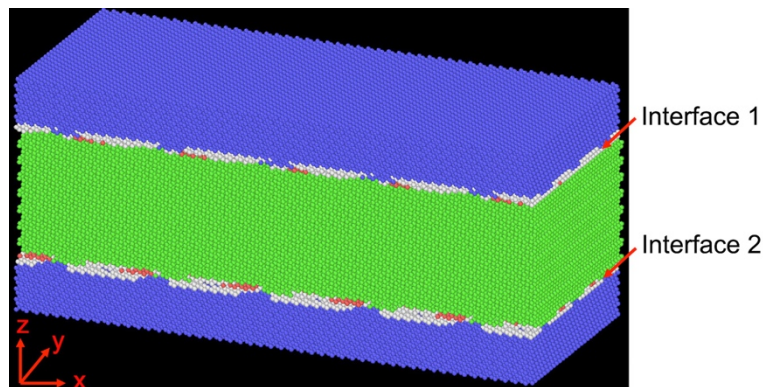


Figure 3-1 The initial, unrelaxed configuration, with periodic conditions in all three directions. Colours represent different crystallographic structures: bcc-blue; fcc-green; unidentified-white, hcp-red. The x direction in the figure coincides with the fcc $[\bar{1}\bar{1}2]$ direction, y with fcc $[1\bar{1}0]$, and z with fcc $[111]$.

The method of energy minimization was used to relax the system as follows: all atoms in fcc bulk were fixed while the atoms in the bcc bulk phase were allowed to move in the z direction. Thus the

simulation box can expand/contract perpendicular to the phase boundaries, in order to minimise the high stress caused by the phase misfit at the phase boundary. The dimensions of the box in the x and y direction were not changed during relaxation. The pressure perpendicular to the interface relaxed to less than 20 MPa. The simulation was performed at zero pressure and at constant temperature, using a barostat and a thermostat of the Nosé-Hoover type at 300 K (NPT ensemble). The simulations last for a total time of 1000 ps. The simulations were performed with the open-source LAMMPS code [19].

3.3 Results and discussion

Figure 3-2 shows snapshots of the fcc-bcc phase transformation process. The black line and the yellow line represent the original fcc/bcc interfaces. It can be seen that the fcc to bcc phase transformation starts from the fcc/bcc interfaces and the original bcc phase grows into the original fcc crystal in a locally faceted style, as arrow A shows. Homogeneous nucleation of bcc phase, as arrow B shows, is found to occur inside the original fcc phase. Heterogeneous nucleation of bcc phase, as shown by arrow C, takes place near the fcc/bcc interface. In some locations at 10 ps in figure 3-2(d), neighboring newly-nucleated bcc plates merge into a single bcc grain. However, grain boundaries exist in the final configuration and separate the neighboring bcc plates with different orientations at 1000 ps.

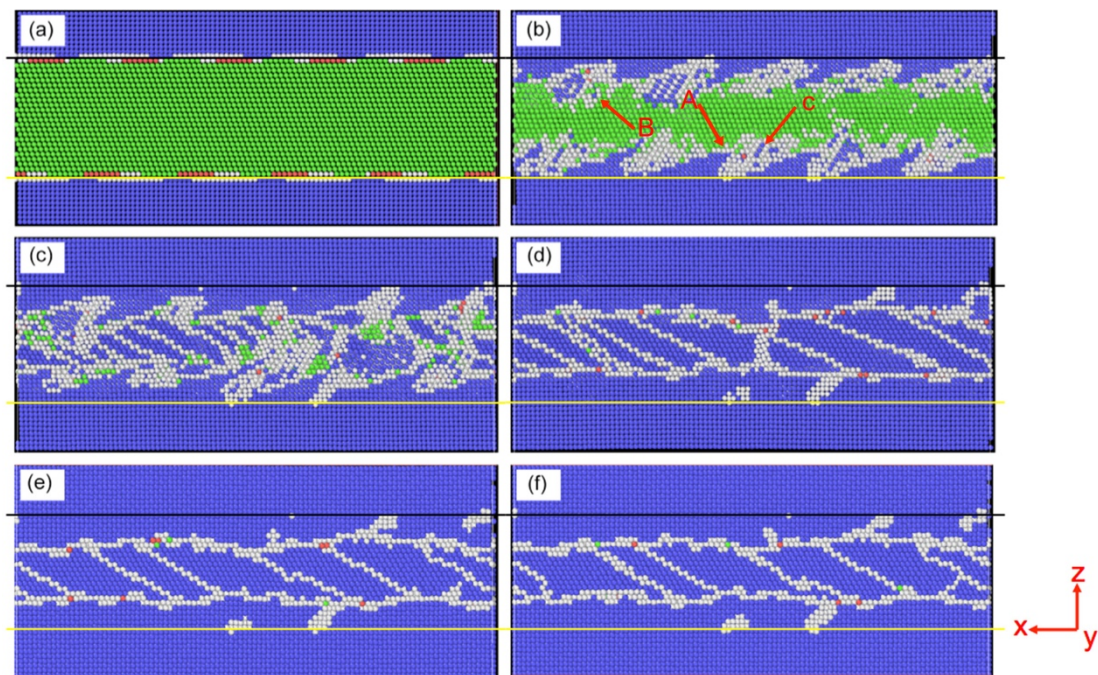


Figure 3-2 Snapshots showing the time evolution of the fcc-bcc transition: (a) 0 ps, (b) 1 ps, (c) 2.5 ps, (d) 10 ps, (e) 100 ps, (f) 1000 ps. The original positions of the interface 1 and 2 are marked by a black line and a yellow line, respectively. The colours denote the local crystal structure as in figure 3-1.

Figures 3-3 (a), (b) show the time evolution of the potential energy and the a-CNA structure analysis of the system during 1000 ps. In order to see the initial stage of phase transformation more clearly, figures 3-3 (c) and (d) show the time evolution of the potential energy and the a-CNA calculation of the system during the first 10 ps. From figure 3-3(c), it is seen that the potential energy of the system decreases

quickly during the initial 10 ps, and then decreases slowly to the equilibrium value after ~ 50 ps. Table 3-2 shows the fractions of different phases at 0, 10 and 1000 ps. Almost all fcc transforms to bcc phase, leaving 14.5% atoms with unknown structure. They act as the grain boundaries separating bcc grains with different orientations, as shown in figures 3-2 (d)-(f). At 1000 ps, part of the thin neighboring bcc plates has merged into a single bcc grain, leading to the decrease of the density of grain boundaries.

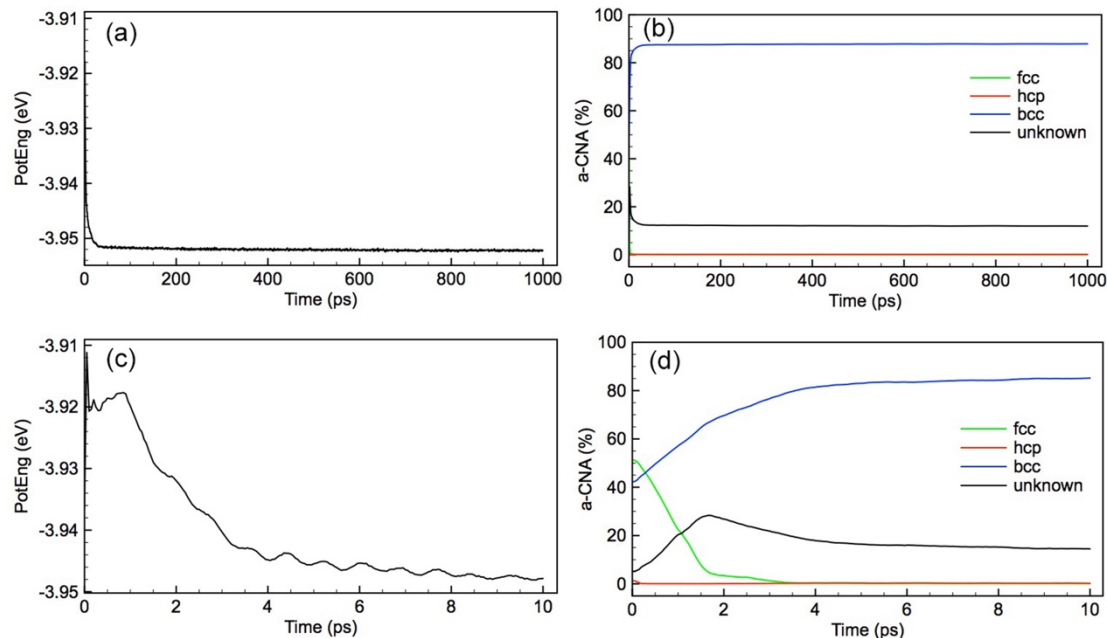


Figure 3-3 Time evolution of the potential energy (a) and the a-CNA calculation (b) of the system during 1000 ps.

In order to see the initial stage of phase transformation more clearly, (c) and (d) are used to show the time evolution of the potential energy (a) and the a-CNA calculation (b) of the system during the first 10 ps.

Table 3-2 Phase fractions of the system at 0, 10 and 1000 ps

Simulation time (ps)	Phase fractions (%)			
	fcc	bcc	hcp	unknown
0	51.3	42.2	1.4	5.2
10	0.1	85.2	0.2	14.5
1000	0	87.9	0.1	12.0

Figure 3-4 shows the phase transformation in local regions inside the original fcc phase. Both homogeneous nucleation and heterogeneous nucleation are found to occur at different sites inside the original fcc phase. After an incubation time of 0.25 ps, homogeneous nucleation inside the original fcc bulk phase is observed. Figure 3-5 shows the three-dimensional snapshot of the homogeneous nuclei formed inside the original fcc bulk. Once the critical size is reached, the new bcc nucleus starts to grow in the original fcc phase.

Heterogeneous nucleation, which starts from pre-existing defects such as surfaces, grain boundaries and phase boundaries [9], is also observed to take place near the propagating fcc/bcc interface. From figure 3-2, it is seen that the original fcc/bcc interface propagates into the original fcc phase in a faceted way. At the root of the faceted interface, a triple junction forms and the locally high interface

energy provides the driving force for the heterogeneous nucleation of new bcc phase. The heterogeneous bcc nuclei are in the KS OR with the parent fcc phase, as is shown by the blue rectangle in Figure 3-4(b). However, it seems that the heterogeneously nucleated bcc phase prefers to grow along the close packed direction $[1\ 1\ 0]_{fcc}$ of fcc phase, as the red arrow shows in Figure 3-4(b). The propagation of the original fcc/bcc interface is impeded where homogeneous and heterogeneous nucleation of bcc phase is found.

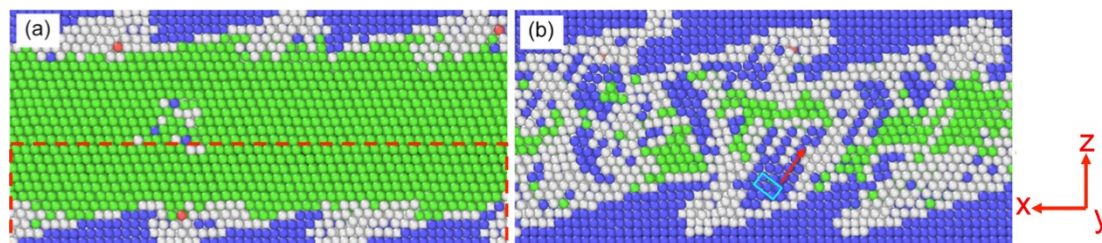


Figure 3-4 Time evolution of phase transformation in the original fcc part, which lies between the black and yellow lines in figure 3-3, (a) 0.5 ps, (b) 1.5 ps. The colours denote the local crystal structure as in figure 3-1.

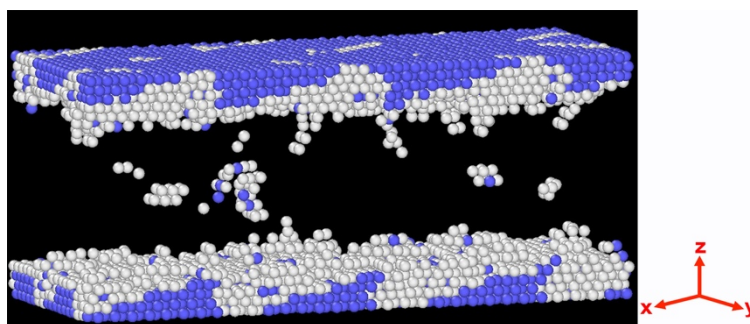


Figure 3-5 Three-dimensional snapshot of the volume shown in figure 3-4 at 0.50 ps. All the fcc and hcp phases were deleted leaving only the bcc phase and unknown phase. The colours denote the local crystal structure as in figure 3-1.

Figure 3.6 shows the distribution of displacements of atoms in the final configuration at 1000 ps with respect to their original positions. The displacements in figure 3-6(b) refer to atoms that transformed from fcc to bcc phase and located between the black and yellow lines in figure 3-2. The displacements are in the range between 0.007 and 5.947 Å. At 300 K, the interatomic distance is 2.477 Å for bcc lattice. From figure 3-6(a), it can be seen that the atoms with small atomic displacements correspond to the new bcc grains forming inside the original fcc phase and the bcc phase growing from the original bcc phase. The atoms with displacements on the order of an interatomic distance are mainly located at the grain boundaries, which correspond to the unidentified atoms in figure 3-2(f). The transformation with displacement less than an interatomic distance is regarded as non-diffusive, or rather a martensitic transformation. It is determined that the displacements of 92.3% of the atoms are less than one interatomic distance of 2.477 Å, which indicates a predominant mechanism of martensitic transformation.

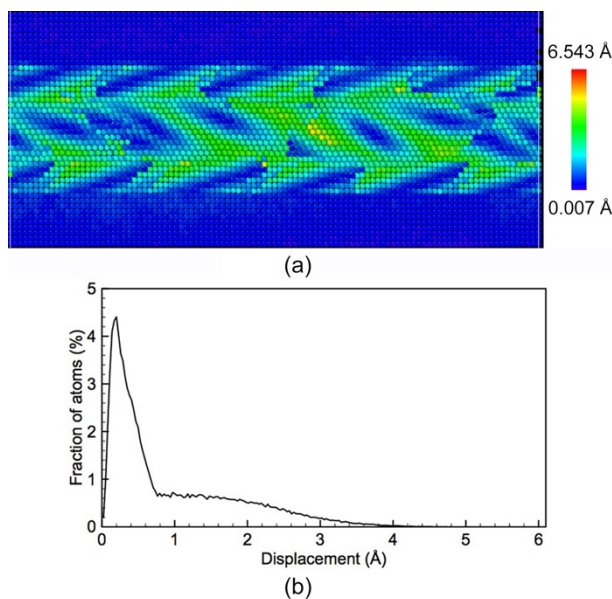


Figure 3-6 (a) View of the xz plane of the simulation system at 1000 ps with atoms coloured according to their displacements, (b) displacement distribution for atoms in the region between the black and yellow lines in figure 3-6(a).

3.4 Conclusions

By means of molecular dynamics simulations, a mobile fcc/bcc interface in the NW orientation relationship has been shown in a pure iron system with an EAM potential. The original bcc/fcc interfaces migrate into the parent fcc phase in a faceted way, which indicates that the original bcc phase grows faster in some regions than the others at the original bcc/fcc interfaces. The underlying reasons leading to this faceted growth of interfaces need further exploration. The following Chapter 4 will focus on the mechanisms controlling the propagation of bcc/fcc interfaces in different crystallographic orientations.

Besides, heterogeneous nucleation takes place nearby the propagating bcc/fcc interfaces, while homogeneous of bcc phase occurs inside the original fcc phase. Chapter 5 studies the mechanisms of homogeneous nucleation of bcc phase inside a single fcc crystal, based on which Chapter 6 analyses the heterogeneous nucleation of bcc phase at dislocations on fcc/fcc grain boundaries.

Additionally, it is found that the formation of bcc nuclei in the KS OR impedes the further propagation of the original fcc/bcc interfaces in the NW OR. Locally, neighboring bcc grains merge into a single coarser bcc grain. The fcc phase transforms to bcc by a predominantly martensitic mechanism. Martensitic transformation following a specific transformation path induces internal strain and stress in specific crystallographic directions, which may lead to the formation of bcc nuclei with selected orientations and the coalescence of bcc grains during growth. Chapter 7 investigates the strain induced fcc-to-bcc transformation in fcc iron by introducing external strain or stress to simulation cells.

3.5 References

- [1] T. Nagano and M. Enomoto, 'Calculation of the interfacial energies between α and γ iron and equilibrium particle shape', *Metall. Mater. s Trans. A*, 2006, 37, 929-937.
- [5] S. Tateyama, Y. Shibuta and T. Suzuki, 'Orientation relationship in fcc-bcc phase transformation kinetics of iron: a molecular dynamics study', *ISIJ Int.*, 2010, 50, 1211-1216.
- [6] S. Tateyama, Y. Shibuta and T. Suzuki, 'A molecular dynamics study of the fcc-bcc phase transformation kinetics of iron', *Scripta Mater.*, 2008, 59, 971-974.
- [2] Z. Nishiyama, 'Mechanism of transformation from face-centred to body-centred cubic lattice', *Sci. Rep. Tohoku Imp. Univ.*, 1934, 23, 637-664. Cited by M. G. Hall, H. I. Aaronson and K. R. Kinsman, 'The structure of nearly coherent fcc: bcc boundaries in a Cu-Cr alloy', *Surf. Sci.*, 1972, 31, 257-274.
- [3] G. V. Kurdjumov and G. Sachs, 'Über den mechanismus der stahlhärtung', *Z. Phys.*, 1930, 64, 325-343. Cited by M. G. Hall, H. I. Aaronson, and K. R. Kinsman, 'The structure of nearly coherent fcc: bcc boundaries in a Cu-Cr alloy', *Surf. Sci.*, 1972, 31, 257-274.
- [4] T. Fukino and S. Tsurekawa, 'In-Situ SEM/EBSD Observation of α/γ Phase Transformation in Fe-Ni Alloy', *Mater. Trans.*, 2008, 49, 2770-2775.
- [7] B. J. Wang and H. M. Urbassek, 'Atomistic dynamics of the bcc - fcc phase transition in iron: Competition of homo- and heterogeneous phase growth', *Comput. Mater. Sci.*, 2014, 81, 170-177.
- [8] B. J. Wang and H. M. Urbassek, 'Molecular dynamics study of the α - γ phase transition in Fe induced by shear deformation', *Acta Mater.*, 2013, 61, 5979-5987.
- [9] H. Song and J. J. Hoyt, 'An atomistic simulation study of the migration of an austenite-ferrite interface in pure Fe,' *Acta Mater.*, 2013, 61, 1189-1196.
- [10] H. Song and J. J. Hoyt, 'A molecular dynamics simulation study of the velocities, mobility and activation energy of an austenite-ferrite interface in pure Fe', *Acta Mater.*, 2012, 60, 4328-4335
- [11] B. J. Wang and H. M. Urbassek, 'Phase transitions in an Fe system containing a bcc/fcc phase boundary: An atomistic study', *Phys. Rev. B*, 2013, 87, 104108.
- [12] F. Maresca and W. A. Curtin, 'The austenite/lath martensite interface in steels: structure, athermal motion, and in-situ transformation strain revealed by simulation and theory', *Acta Mater.* 2017, 134, 302-323.
- [13] <http://www.ctcms.nist.gov/potentials/Fe.html>. Accessed on September 4th, 2017.
- [14] M. I. Mendeleev, S. Han, D. J. Srolovitz, G. J. Ackland, D. Y. Sun and M. Asta, 'Development of new interatomic potentials appropriate for crystalline and liquid iron', *Phil. Mag.*, 2003, 83, 3977-3994.
- [15] X. S. Yang, S. Sun, X. L. Wu, E. Ma and T. Y. Zhang, 'Dissecting the mechanism of martensitic transformation via atomic scale observations', *Sci. Rep.*, 2014, 4, 6141.
- [16] X. S. Yang, S. Sun and T. Y. Zhang, 'The mechanism of bcc α' nucleation in single hcp ϵ laths in the fcc $\gamma \rightarrow$ hcp $\epsilon \rightarrow$ bcc α' martensitic phase transformation', *Acta Mater.*, 2015, 95, 264-273.
- [17] M. Müller, P. Erhart and K. Albe, 'Analytic bond-order potential for bcc and fcc iron comparison with established embedded-atom method potentials', *J. Phys.: Condens. Matter*, 2007, 19, 326220.

Atomistic aspects of martensitic transformation in iron containing bcc/fcc interfaces in the Nishiyama-Wassermann orientation relationship by molecular dynamics simulation

[18] A. Stukowski, 'Structure identification methods for atomistic simulations of crystalline materials', *Modell. Simul. Mater. Sci. Eng.*, 2012, 20, 045021.

[19] S. Plimpton, 'Fast parallel algorithms for short-range molecular dynamics', *J. Comp. Phys.*, 1995, 117, 1-19. <http://lammps.sandia.gov/>. Accessed on September 4th, 2017.

Chapter 4

Mechanisms controlling the propagation of bcc/fcc semi-coherent interfaces in iron by molecular dynamics simulations

Abstract:

Molecular dynamics simulations have been used to study the effects of different orientation relationships between fcc and bcc phases on the bcc/fcc interfacial propagation in pure iron systems at 300 K. Three semi-coherent bcc/fcc interfaces have been investigated. In all the cases, results show that growth of the bcc phase starts in the areas of low potential energy and progresses into the areas of high potential energy at the original bcc/fcc interfaces. The phase transformation in areas of low potential energy is of a martensitic nature while that in the high potential energy areas involves occasional diffusional jumps of atoms.

* This chapter is based on a scientific paper:

X Ou, J Sietsma and M J Santofimia, Molecular dynamics simulations of the mechanisms controlling the propagation of bcc/fcc semi-coherent interfaces in iron, *Modell. Simul. Mater. Sci. Eng.* 24 (2016) 055019.

4.1 Introduction

Martensitic transformation has been studied extensively by experiments and simulations [1-7]. The martensite phase tends to have specific crystallographic orientation relations with the austenite phase [8-11], mainly the Nishiyama-Wassermann (NW) [10] or Kurdjumov-Sachs (KS) [11] orientation relationships (ORs). Previous studies by molecular dynamics (MD) simulations [12-19] show that bcc/fcc interfaces in iron grew into the fcc bulk to some degree depending on the crystallographic orientations. Bos *et al.* [4] studied two bcc/fcc interfaces close to the Bain OR and KS OR using the Johnson and Oh potential [20]. The bcc/fcc interfaces were mobile and a single bcc grain was obtained in the final structure. Besides, dislocation glide occurred along closely packed planes in both the fcc and bcc crystalline structures during the martensitic transformation. Wang and Urbassek [14,18] studied a bcc/fcc interface with either the NW or the KS OR using the Meyer-Entel [21] potential. The fcc/bcc interfaces slightly roughened during proceeding into the original fcc phase. The bcc/fcc interface studied by Song and Hoyt [16,17] was tilted by 4.04° about the NW OR using the Ackland potential [22], thus a series of parallel steps (or primary structural disconnections) was introduced into the interfaces. The mobile interface migrated by the rapid advance of the mobile defects forming on the primary disconnections and a single bcc grain was obtained.

In the previous Chapter 3, the results indicate that the bcc/fcc interfaces in the NW OR propagate into the fcc iron in a faceted way, as observed by MD simulation. Therefore, it is expected that some regions at the bcc/fcc interfaces are more favourable to preferable growth than the others. In the present chapter, three systems with different semi-coherent bcc/fcc interfaces are introduced to investigate the mechanisms controlling the growth of the original bcc phase in iron by MD simulations. Main aspects are based on the atomic configuration during the transformation and the energy distribution of the atoms.

4.2 Simulation methods

The present work uses the Mendeleev potential [23,24], which has been applied in describing the martensitic transformation in iron with bcc/fcc interfaces by MD simulations [25,26]. The Mendeleev potential has been described in Section 3.2 of Chapter 3 in this thesis. The two well-known crystallographic orientation relationships between the austenite and ferrite phases in steel are the NW and the KS ORs [27], which are described as:

$$\text{N-W: } (1\ 1\ 0)_{bcc} \parallel (1\ 1\ 1)_{fcc}, [0\ 0\ 1]_{bcc} \parallel [1\ \bar{1}\ 0]_{fcc}$$

$$\text{K-S: } (1\ 1\ 0)_{bcc} \parallel (1\ 1\ 1)_{fcc}, [1\ \bar{1}\ 1]_{bcc} \parallel [1\ \bar{1}\ 0]_{fcc}$$

Both relationships have the closest packed planes in the two phases parallel: $\{1\ 1\ 1\}_{fcc} \parallel \{1\ 1\ 0\}_{bcc}$. In this work, the studied systems with the above two interfaces are called System NW and System KS, respectively. Besides, a third semi-coherent bcc/fcc interface with higher interfacial energy is also studied. In this work, the orientation of this third interface will be identified with the name ‘Nagano

Mechanisms controlling the propagation of bcc/fcc semi-coherent interfaces in iron by molecular dynamics simulations

OR' and the corresponding system as 'System Nagano'. The interface with the Nagano OR originates from the previous studies by Nagano and Enomoto [7], in which a high energy interface was obtained by rotating the fcc bulk of the NW system over 90° around the $[0\ 0\ 1]_{bcc} \parallel [\bar{1}\ 0\ 1]_{fcc}$ axis.

The detailed information of the three systems is listed in Table 4-1. The simulation was performed assuming periodic boundaries in all three directions and in absence of free surfaces. The dimensions in the x and y directions were carefully chosen to ensure that the elastic strain due to volume mismatch is kept to a minimum. The mismatches in x and y directions are 0.08% and 0.03% for System NW, 0.10% and 0.07% for System KS, 0.07% and 0.03% for System Nagano, respectively. These small strains imply stresses less than 150 MPa, leading to negligible additional strain energy. Lattice parameters for fcc (3.658 Å) and bcc (2.855 Å) are obtained at 0 K and the potential-energy difference between the fcc and bcc phase at 0 K is 0.122 eV per atom. From experimental studies lattice parameters at 0 K are concluded for fcc and bcc to be 3.562 Å and 2.860 Å, respectively [22].

Table 4-1 Systems studied in this work. x , y , and z denote the lengths of the systems in the three Cartesian directions. Lengths are indicated both in Å and unit cells (UC).

System	x (Å)	y (Å)	z (Å)	x_{bcc} UC	y_{bcc} UC	z_{bcc} UC	x_{fcc} UC	y_{fcc} UC	z_{fcc} UC	fcc atoms	bcc atoms
NW, $(1\ 1\ 0)_{bcc} \parallel (1\ 1\ 1)_{fcc}$, $[\bar{1}\ 1\ 0]_{bcc} \parallel [\bar{1}\ \bar{1}\ 2]_{fcc}$	205.91	82.76	91.06	51	29	10	23	16	8	70656	59160
KS, $(1\ 1\ 0)_{bcc} \parallel (1\ 1\ 1)_{fcc}$, $[\bar{1}\ 1\ 2]_{bcc} \parallel [\bar{1}\ \bar{1}\ 2]_{fcc}$	223.79	113.74	91.06	32	23	10	25	22	8	105600	88320
Nagano, $(1\ 1\ \bar{2})_{fcc} \parallel (1\ 1\ 0)_{bcc}$, $[\bar{1}\ 1\ 0]_{bcc} \parallel [1\ 1\ 1]_{fcc}$	278.59	82.77	112.06	69	29	10	44	16	8	135168	80040

The method of energy minimization was used to relax the system. Relaxation was performed as follows: all atoms in fcc bulk were fixed while the atoms in the bcc bulk phase were allowed to move in the z direction. Thus the simulation box can expand/contract perpendicular to the phase boundary, so that the high stress caused by the phase misfit at the phase boundary is reduced. The dimensions of the box in the x and y directions were not changed during relaxation. The pressure perpendicular to the interface relaxed to less than 20 MPa.

After energy minimization, the relaxed configuration was used as the initial configuration in the following simulations. The simulations were performed at constant pressure and temperature, using a barostat and a thermostat of the Nosé-Hoover type at 300 K under the pressure of 10^5 Pa (NPT ensemble). The MD time step was fixed at 0.00050 ps per step and the simulations for System NW, KS and Nagano last for a total time of 1000, 1000 and 1500 ps, respectively. Calculations were performed with the open-source LAMMPS code [28].

To reveal the atomistic mechanisms related to the fcc-to-bcc transformation, a discriminator needs to be used to determine atoms as belonging to either the fcc or bcc phase. Stukowski [29] proposed a

simple extension to the common neighbour analysis (CNA) method as the adaptive common neighbour analysis (a-CNA) method that made it suitable for multi-phase systems. Therefore, the a-CNA was chosen as the discriminator in the present study. The configurations are displayed using the software OVITO [30].

The snapshot shown in figure 4-1 represents the initial, relaxed configurations for the three systems. The lattice mismatch of fcc/bcc atoms at the boundaries resulted in the hcp or unidentified structures of some atoms. The system always contained two bcc/fcc interfaces perpendicular to the z direction considering the periodicity conditions. Each bcc/fcc interface includes two monolayers: one belongs to fcc bulk and the other belongs to bcc bulk, as shown by figure 4-1(d), which shows the enlarged region inside the red rectangle in figure 4-1(a).

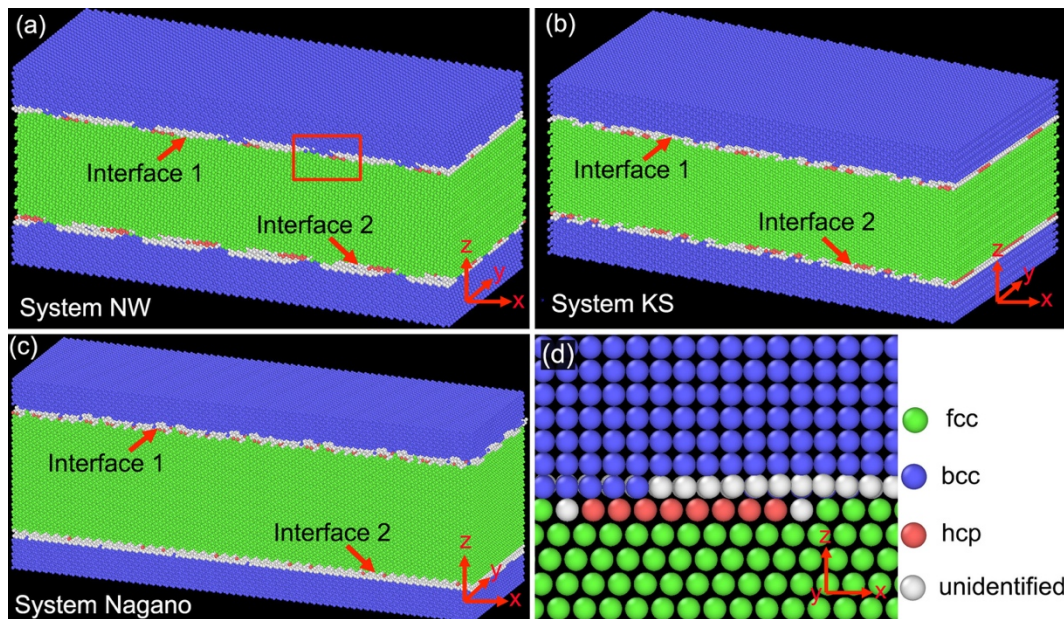


Figure 4-1 The initial, relaxed configurations of (a) System NW, (b) System KS and (c) System Nagano. (d) represents the enlarged region as inside the red rectangle in figure (a). Colours represent different phase structures: blue-bcc; green-fcc; red-hcp; white-unidentified.

4.3 Results and discussion

4.3.1 Growth of the bcc phase at the bcc/fcc interfaces

Figure 4-2 shows the propagation of the bcc/fcc interfaces at 0, 0.15 0.5 and 10 ps in System NW (a), System KS (b) and System Nagano (c), respectively. In each configuration, only 2 bcc planes plus 12 fcc planes perpendicular to the bcc/fcc interface are included. It is found that the original bcc phase starts propagating into the fcc phase at 0.05 ps. The faceted growth of the original bcc phase is then observed for the three systems, as shown by the configurations at 0.15 and 0.5 ps in figures 4-2 (a)-(c). The bcc/fcc interface propagation involves up to 7 atomic layers into the original fcc phase in the three

Mechanisms controlling the propagation of bcc/fcc semi-coherent interfaces in iron by molecular dynamics simulations

systems between 0 ps and 1.0 ps. Nucleation of bcc phase takes place nearby the bcc/fcc interfaces and inside the fcc bulk at around 1.0 ps, which impedes the further propagation of the interfaces.

Homogeneous nucleation of bcc phase inside the fcc bulk was also observed in the MD simulations [14,18] based on the Meyer-Entel Potential [21], in which the fcc-to-bcc transformation in iron with bcc/fcc interfaces in an NW or KS OR was studied. The growth of these bcc nuclei hindered the propagation of the original bcc/fcc interfaces. Similar to the results in the present studies, the bcc/fcc interfaces in the NW OR based on the Meyer-Entel potential [21] propagated into the original fcc bulk for some distance perpendicular to the interface plane, while the interfaces in the KS OR did not move into the fcc bulk significantly. However, only propagation of the bcc/fcc interface, but not the bcc nucleation inside the fcc bulk, was observed by Song and Hoyt [16,17]. They found that the bcc/fcc interfaces propagated into the original fcc bulk until the whole system transformed to a single bcc grain.

Considering that the bcc/fcc interface by Song and Hoyt [16,17] was several degrees away from the perfect NW OR, the introduced defects at the interfaces might contribute to the propagation of the bcc/fcc interfaces into the whole fcc bulk. Figure 4-3 shows an examination performed in the present study in iron with bcc/fcc interfaces in the regular NW OR, based on the Ackland Potential [22]. The results are compared with those based on the Mendelev potential [23]. As expected, the faceted propagation of the bcc/fcc interface in the NW OR is also observed in iron in the initial 0.5 ps with the Ackland potential [22]. The only difference is that earlier nucleation of bcc phase occurs in the fcc bulk with the Mendelev potential [23], as was reported by Wang and Urbassek [14,18], due to its small energy barrier (less than 1 meV/atom) for a transition from fcc to bcc along the Bain path [26]. Nevertheless, the present study focuses on the transformation mechanisms at the bcc/fcc interfaces, excluding any effect resulting from the nucleation of bcc phase inside the fcc bulk. Similar observations related to the propagation of the bcc/fcc interfaces by the Mendelev potential [23] and the Ackland potential [22] indicate the same mechanism of the fcc-to-bcc transformation at the interfaces from both potentials. Besides, this study focuses on the results during the initial 0.5 ps, when the nucleation of bcc phase has not taken place yet. Thus the propagation of bcc/fcc interfaces in present study is not affected by the bcc nucleation inside the fcc bulk. It should be noted that the faceted growth in System KS/Nagano is less obvious than that in System NW. Some parts of the interface in System KS do not move at all, as shown in the configuration at 10 ps of figure 4-2(b). The position of the original bcc/fcc interface is marked by a red triangle in each configuration.

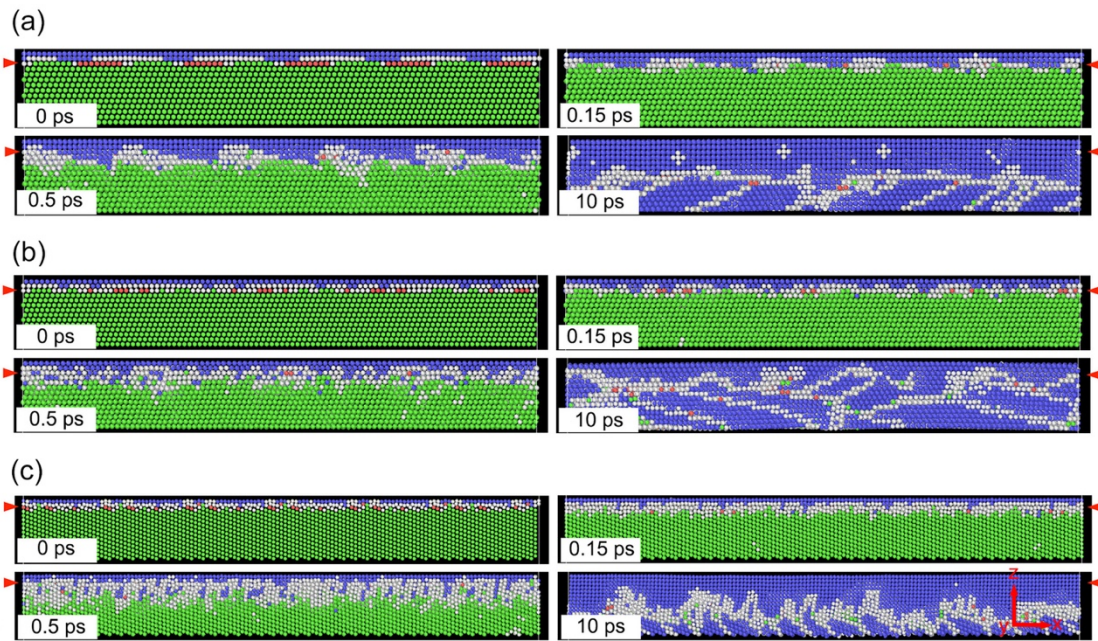


Figure 4-2 Propagation of one of the bcc/fcc interfaces of (a) System NW, (b) System KS and (c) System Nagano, respectively. The position of the original bcc/fcc interface is marked by a red triangle in each configuration.

Colours represent different phase structures: blue-bcc; green-fcc; red-hcp; white-unidentified.

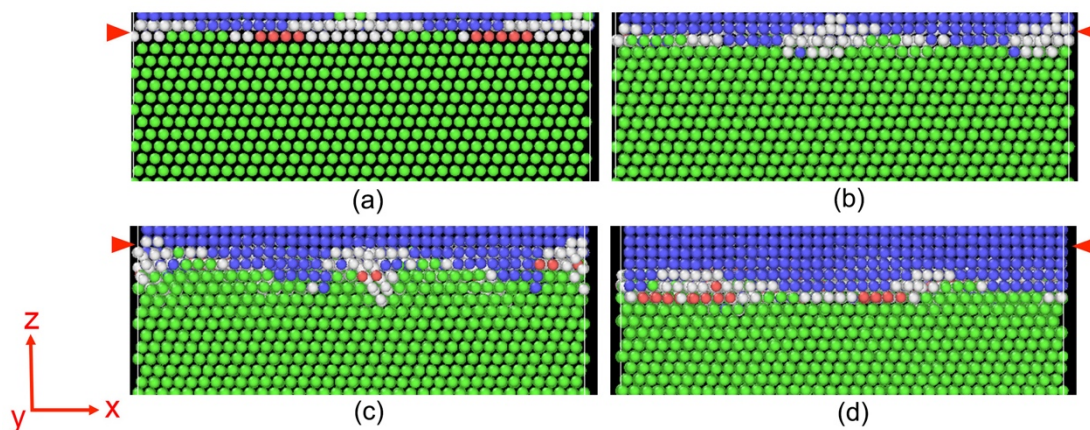


Figure 4-3 Propagation of one of the bcc/fcc interfaces in the NW OR in iron using the Ackland Potential [22] at different simulation times: (a) 0 ps; (b) 0.15 ps; (c) 0.5 ps and (d) 10 ps. The position of the original bcc/fcc interface is marked by a red triangle in each configuration. Colours represent different phase structures: blue-bcc; green-fcc; red-hcp; white-unidentified.

The present study will focus on the fcc-to-bcc transformation through the bcc/fcc interface propagation during the first 0.5 ps. This phenomenon is studied focusing on the energy distribution of the atoms and the atomic configurations between the fcc and bcc planes at the interfaces. The analysis focuses on the phase transformation on the interfacial plane belonging to the fcc bulk. The bcc layer at the interface is presented for a better view of the stacking of atoms between the original bcc and fcc planes. The potential energies of the bcc/fcc interfaces are studied. In present studies, for clarity in the comparisons between different configurations, the low-energy areas and high-energy areas are considered as the areas with potential energies corresponding to the lowest 20% and highest 60% of the corresponding

colour bars in each individual configuration for System NW, System KS and System Nagano, respectively.

4.3.1.1 System NW

Figure 4-4(a) shows the superposed view of the $(1\ 1\ 1)_{fcc}$ and $(1\ 1\ 0)_{bcc}$ planes at the matching area of the interface with NW OR at 0 ps. The atoms are coloured according to their potential energy, which is found in the range of -3.960 eV to -3.470 eV. Wang and Urbassek [18] also studied the potential energy of atoms on the interface plane with the NW OR and found that the original periodic structure of the interface was strongly disturbed after the relaxation process. In the present study, however, the bcc/fcc interfaces is less affected as the low-energy areas, in red dashed circles, appear periodically to some degree. The low-energy areas are located where atoms on the fcc mono layer have potential energies in the range between -3.960 eV and -3.862 eV, as 20% of the range of the colour bar in figure 4-4(a). It is calculated that 30.5% of atoms on the fcc layer belongs to the low-energy areas. Correspondingly, the high-energy areas are those with potential energies ranged between -3.764 eV and -3.470 eV, which takes 60% of the height of the whole colour bar in figure 4-4(a). 10.6% of atoms belong to the high-energy areas.

Figure 4-4(b) shows the time evolution of the phase transformation at the fcc/bcc interface with NW OR during 10 ps and the colours indicate the local atomic structure as those in figure 4-1. The areas in the black circles at 0 ps in figure 4-4(b) correspond to those in the red circles in figure 4-4(a), that is, low potential energy areas. It is found that some atoms in the fcc-plane at the bcc/fcc interfaces are unidentified or identified with an hcp structure. This is because atoms at the bcc/fcc interfaces can have a mixture of fcc- and bcc-surroundings and therefore are either unidentified or recognized with an hcp structure. Similarly, atoms near grain boundaries or vacancies may also be unidentified. From snapshots at 0.15 and 0.5 ps in figure 4-4(b), it is found that the fcc-to-bcc transformation involving the growth of the original bcc phase starts from the low-energy areas and finalizes at the high-energy areas at the interface. This finding will be analysed in detail in the next paragraph. Defects, i.e. vacancies, are found to remain at the sites where the final phase transformation takes place, as shown in the configuration at 10 ps in figure 4-4(b). This may be caused by density differences between the fcc and bcc crystals. It was reported by Tateyama *et al.* [13] that atoms in the fcc region were rearranged into the bcc structure at the bcc/fcc interface to compensate for lattice mismatch during the sequential fcc-to-bcc transformation. The residual lattice mismatch may remain in the bcc structure since time for thermal relaxation was insufficient in the simulation time.

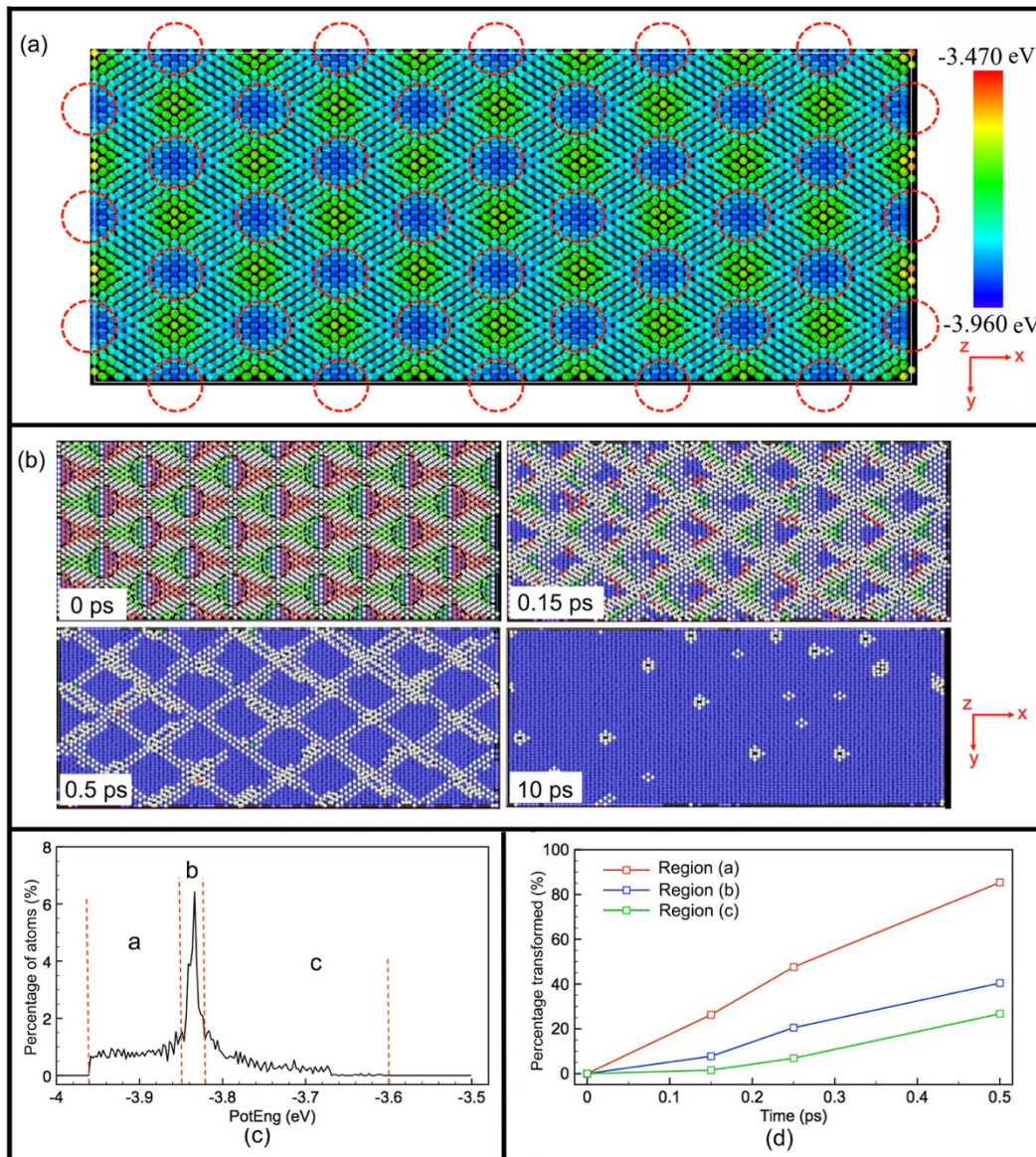


Figure 4-4 (a) Superposed view of $(1\ 1\ 1)_{fcc}$ and $(1\ 1\ 0)_{bcc}$ planes at the matching area of the interface with NW OR at 0 ps. Atoms have been coloured according to their potential energy, as the colour bar shows; (b) Phase transformation in the original fcc/bcc interfacial planes in System NW, the top plane belongs to the fcc bulk and the bottom plane belongs to the bcc bulk. The colours denote the local crystal structures as in Figure 4-1; (c) Energy distribution of atoms in the fcc monolayer at the original fcc/bcc interface in System NW at 0 ps; (d) Time evolution of the fraction of atoms transformed to bcc in individual regions in the fcc monolayer at the original fcc/bcc interface in the NW OR.

Table 4-2 shows the total number of atoms in the fcc mono layer at the interface with NW OR as well as the number of atoms in the same fcc mono layer having initial potential energies falling within three different ranges. The distribution of their initial potential energy is illustrated in figure 4-4(c). The number of fcc-atoms transforming to bcc is clearly related to their initial potential energy. This is explicitly shown in figure 4-4(d), where it is found that atoms tend to transform linearly with time in the three regions. It is estimated that the slopes are 190%, 82% and 27% for Region (a), (b) and (c), respectively. The slopes are calculated from data between 0 ps and 0.25 ps, which correspond to times

Mechanisms controlling the propagation of bcc/fcc semi-coherent interfaces in iron by molecular dynamics simulations

well before a decrease of the transformation rate is observed. Transformation in Region (a), is faster than that in Region (b), which is followed by that in Region (c). The results indicate statistically that the growth of original bcc phase develops from low-energy areas to high-energy areas at the original bcc/fcc interfaces with NW OR.

Table 4-2 Number of atoms in the monolayer of fcc plane at the original fcc/bcc interface at 0 ps. N_{total} represents the total number of atoms in the monolayer of fcc plane; N_a , N_b and N_c are the number of atoms distributed in potential energy ranges (a)-(c).

System	N_{total}	N_a/N_{total}	N_b/N_{total}	N_c/N_{total}
NW		(-3.96, -3.85) eV	(-3.85, -3.82) eV	(-3.82, -3.60) eV
	2944	1064	1034	846
KS		(-4.0, -3.85) eV	(-3.85, -3.80) eV	(-3.80, -3.5) eV
	4400	1410	1921	1069
Nagano		(-4.0, -3.65) eV	(-3.65, -3.0) eV	-
	4224	2816	1408	-

4.3.1.2 System KS

Figure 4-5(a) is the superposed view of the $(1\ 1\ 1)_{fcc}$ and $(1\ 1\ 0)_{bcc}$ planes at the matching areas of the interface with KS OR at 0 ps. The potential energy is distributed between -4.016 eV and -3.464 eV. The low-energy areas are marked in red dashed ellipses corresponding to areas in the black dashed ellipses in figure 4-5(b), which shows the development of the local crystallographic structure. The low-energy areas include atoms on the fcc mono layer with potential energies in the range between -4.016 eV and -3.906 eV. 13.9% of atoms on the fcc layer belongs to the low-energy areas. The high-energy areas are located where atoms have potential energies ranged between -3.795 eV and -3.464 eV. 22.7% atoms belong to the high-energy areas. Similar to System NW, the growth of bcc phase at the original fcc/bcc interfaces in System KS starts from the low-energy areas, as seen from snapshots at 0.15 and 0.5 ps in figure 4-5(b). Then it develops into areas with high potential energies where eventually a number of defects, i.e. vacancies, are observed, as shown by the unidentified atoms at 10 ps.

Figure 4-5(c) shows the distribution of the potential energy of atoms in the mono fcc plane at the original bcc/fcc interfaces with KS OR. The potential energy is divided into Regions (a)-(c). The number of atoms distributed in the three regions at the initial configuration is included in Table 4-2. Similar to System NW, atoms transforming to bcc during the initial 0.5 ps are mostly located in low-energy areas corresponding to Region (a) and (b). The fraction of atoms transformed also follows a nearly linear relationship with time for each energy region (see figure 4-5(d)). It is estimated that the slopes are 138%, 53% and 10% for Region (a), (b) and (c), respectively. The slopes are also calculated before 0.25 ps as for System NW. However, the transformation at the interface with KS OR is slower than that with NW OR, as indicated by the lower gradient for each region in figure 4-5(d).

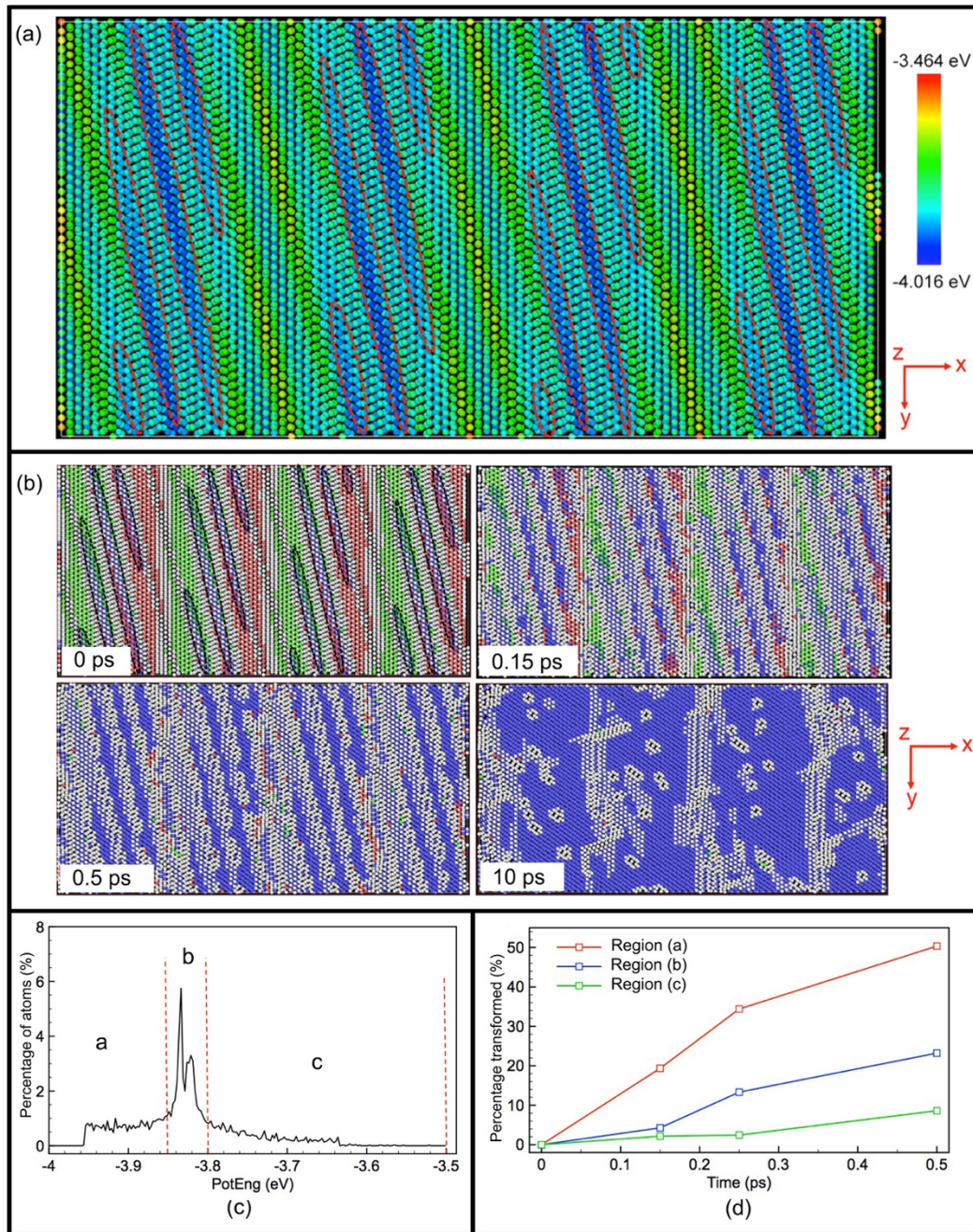


Figure 4-5 (a) Superposed view of $(1\ 1\ 1)_{fcc}$ and $(1\ 1\ 0)_{bcc}$ planes at the matching area of the interface with KS OR at 0 ps. Atoms have been coloured according to their potential energy, as the colour bar shows; (b) Phase transformation in the original fcc/bcc interfacial planes, the top plane belongs to the fcc bulk and the bottom plane belongs to the bcc bulk in System KS at different simulation times. The colours denote the local crystal structure as in figure 4-1; (c) Energy distribution of atoms in the fcc monolayer at the original fcc/bcc interface in System KS at 0 ps; (d) Time evolution of the fraction of atoms transformed to bcc in individual regions in the fcc monolayer at the original fcc/bcc interface in the KS OR.

4.3.1.3 System Nagano

Figure 4-6(a) is the superposed view of $(1\ 1\ \bar{2})_{fcc}$ and $(1\ 1\ 0)_{bcc}$ planes at the matching areas of the interface in Nagano OR at 0 ps. The atoms are coloured according to their potential energy, which

Mechanisms controlling the propagation of bcc/fcc semi-coherent interfaces in iron by molecular dynamics simulations

ranges from -4.118 eV to -3.009 eV. The areas with low potential energy ranged between -4.118 eV and -3.896 eV are included in the red dashed ellipses. 11.8% of atoms on the mono fcc layer are included in the low-energy areas. Areas with potential energies between -3.674 and -3.009 eV are defined as high-energy areas. 33.3% atoms are included in these areas. The bcc phase grows from the low-energy areas to the high-energy areas in System Nagano, which can be seen from the snapshots at 0.15-10 ps in figure 4-6(b), similarly to System NW and System KS. Besides, vacancies are found at the end of the phase transformation, as labeled by the red arrow in figure 4-6(b).

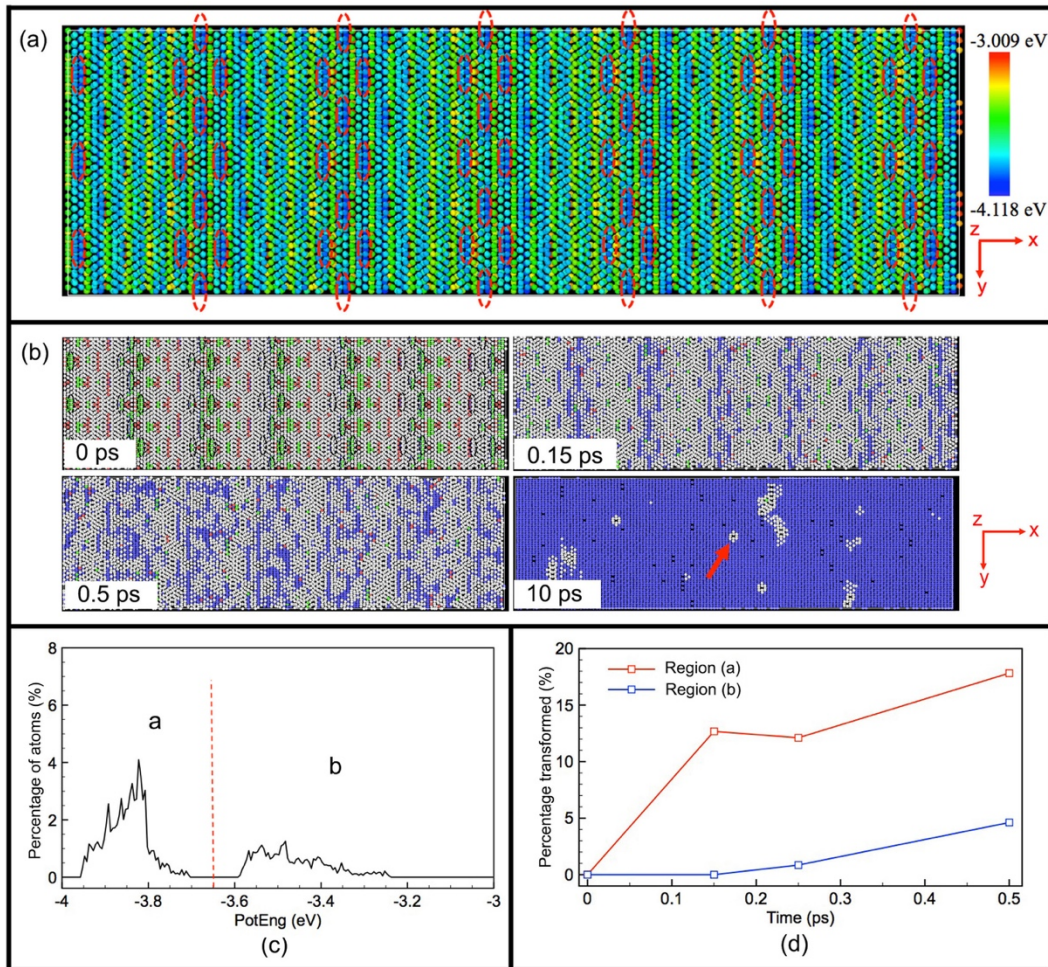


Figure 4-6 (a) Superposed view of $(1\ 1\ \bar{2})_{fcc}$ and $(1\ 1\ 0)_{bcc}$ planes at the matching area of the interface in the Nagano OR at 0 ps. Atoms have been coloured according to their potential energy, as the colour bar shows; (b) Phase transformation in the original fcc/bcc interfacial planes, the top plane belongs to the fcc bulk and the bottom plane belongs to the bcc bulk in System Nagano at different simulation times. The colours denote the local crystal structure as in figure 4-1; (c) Energy distribution of atoms in the fcc monolayer at the original fcc /bcc interface in the Nagano OR at 0 ps; (d) Time evolution of the fraction of atoms transformed to bcc in individual regions in the fcc monolayer at the original fcc/bcc interface in the Nagano OR.

The atoms in the mono fcc-plane at the interface are grouped into low-energy region (a) and high-energy region (b). The number of atoms falling in these two regions is included in Table 4-2. Figure 4-6(c) shows the distribution of atoms in Region (a) and (b) at 0 ps. It should be noted that, compared to System NW and System KS, a group of atoms on the fcc plane at the bcc/fcc interfaces have rather

high potential energies, above -3.7 eV, and no atoms on the fcc plane at the original bcc/fcc interface have a potential energy in the range of -3.7 eV and -3.6 eV. This originates from the construction process of System Nagano, when an array of terraces is created by rotating the fcc bulk for 90° from the NW system around the $[0\ 0\ 1]_{bcc} \parallel [\bar{1}\ 0\ 1]_{fcc}$ axis. Defects at the terraces lead to the involved atoms having high potential energies. The large proportion of atoms transformed to bcc in Region (a) indicates the preferable growth of bcc phase in low-energy areas, as observed for System NW and System KS.

It is worthwhile to note that the transformation at the interfaces with Nagano OR is much slower than at interfaces with NW OR and KS OR in the initial 0.5 ps, which can be seen from the smaller fraction of atoms transformed at each time point in figure 4-6(d). It is roughly calculated that 53% of atoms on the fcc plane at the original bcc/fcc interfaces transformed to bcc during the first 0.5 ps for System NW, 28% for System KS, followed by 13% for System Nagano. The higher transformation rate for System NW and KS than for System Nagano indicates that the bcc phase more readily grows at the original bcc/fcc interfaces with NW and KS ORs in comparison to the artificial Nagano OR. This may be related to the higher fraction of low-energy interface areas for System NW and System KS than System Nagano. The interface energy contains chemical and mechanical contributions, the latter of which originates from the elastic energy stored in the vicinity of the interface between the fcc and bcc phases [31]. Therefore, a lower fraction of high-energy areas at the interface implies a lower elastic energy and transformation barrier [32]. The higher fraction of high-energy areas at the bcc/fcc interface of System Nagano results in higher internal stress, thus higher elastic energy and higher energy barrier for the martensite transformation during the interface propagation.

It is concluded that growth of original bcc phase in the three semi-coherent bcc/fcc interfaces starts from the areas of low potential energy and develops into high potential energy areas, leaving vacancies in the bcc lattice at the end of the phase transformation. The mechanisms related to this phenomenon will be discussed in detail in the following section.

4.3.2 Model for growth of bcc phase at the bcc/fcc interfaces

Figure 4-7(a) shows the initial growth of original bcc phase in the low-energy areas at the bcc/fcc interface for System NW at 0 and 0.15 ps. The colours of atoms in upper figures show the phase structures and those in the lower figures represent the potential energy of atoms. The areas in which the phase transformation starts are indicated by the yellow dashed triangles and the early transformed atoms are labeled with yellow asterisks. During the fcc-to-bcc transformation, atoms labeled by asterisks tend to move in the direction indicated by the light blue arrows. The configuration of atoms in the two layers after phase transformation is labeled by the light blue parallelogram. Figures 4-7 (b)-(c) show the corresponding configurations in low energy locations for System KS and System Nagano, respectively. The early transformed atoms and the atomic configurations of two $\{1\ 1\ 0\}_{bcc}$ planes are marked by asterisks and parallelograms, respectively. Also these details of the atomic configurations

Mechanisms controlling the propagation of bcc/fcc semi-coherent interfaces in iron by molecular dynamics simulations

show that the growth of the original bcc phase starts from the low-energy areas at the original bcc/fcc interfaces for System NW, System KS and System Nagano.

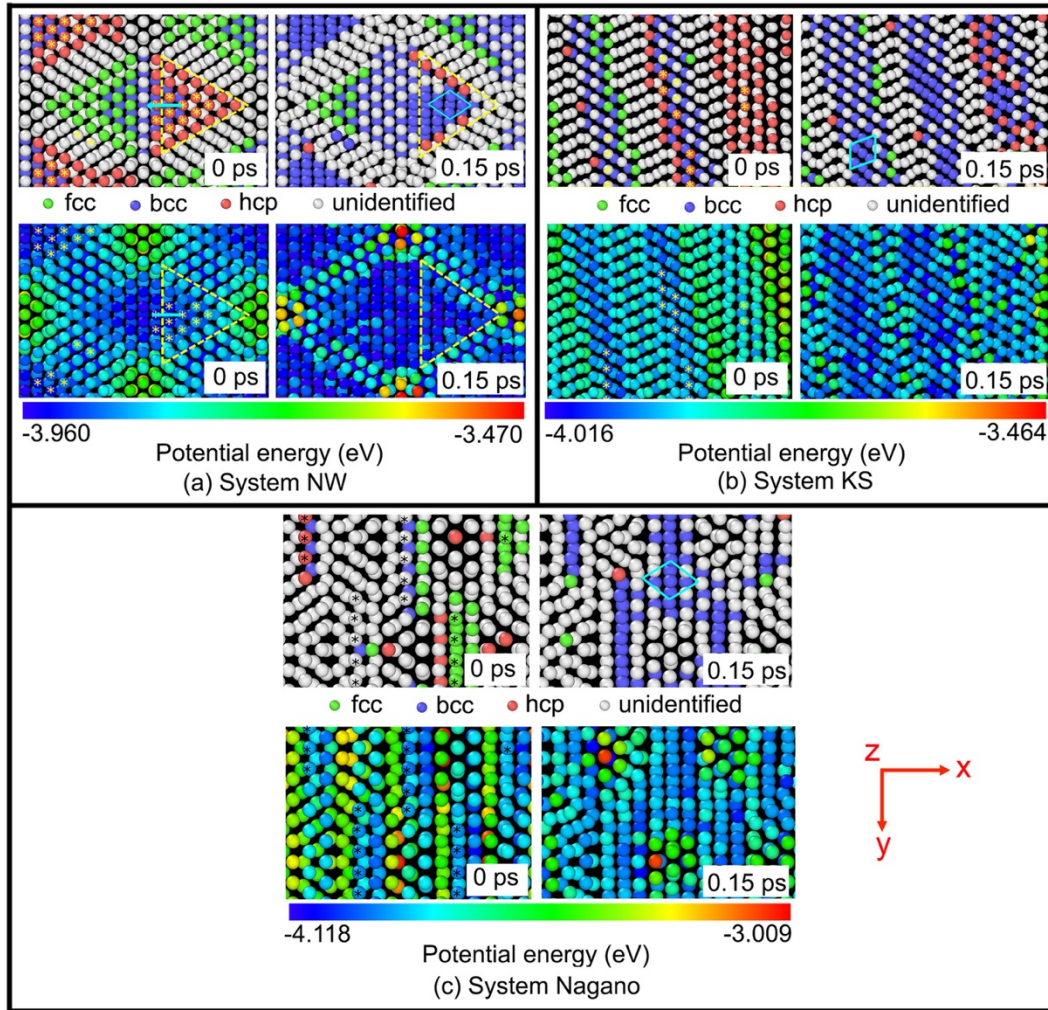


Figure 4-7 (a) Enlarged superposed view of $(1\ 1\ 1)_{fcc}$ and $(1\ 1\ 0)_{bcc}$ planes at the interface with NW OR at different simulation times; (b) Enlarged superposed view of $(1\ 1\ 1)_{fcc}$ and $(1\ 1\ 0)_{bcc}$ planes at the interface with KS OR at different simulation times; (c) Enlarged superposed view of $(1\ 1\ \bar{2})_{fcc}$ and $(1\ 1\ 0)_{bcc}$ planes at the interface in System Nagano at different simulation times.

The configuration of atoms in the fcc and bcc planes at the initial configuration in this low-energy area was previously reported by Olson and Cohen [33], as shown in figure 4-8(a). They developed a faulting mechanism for the complete fcc-to-bcc lattice deformation based on the ‘hard sphere’ lattice deformation model suggested by Bogers and Burgers [34]. They illustrated the fcc-to-bcc transformation through two shears: the first shear takes place over one-third of the Burgers vector of a Shockley partial dislocation for fcc twin shear ($a_{fcc}/18 < 1\ 1\ 2 >_{fcc}$ on $\{1\ 1\ 1\}_{fcc}$ plane); the second shear corresponds to three-eighths of a Shockley partial dislocation for fcc twin shear ($a_{fcc}/16 < 1\ 1\ 2 >_{fcc}$ on the $\{1\ 1\ 1\}_{fcc}$ plane or $a_{bcc}/8 < 1\ 1\ 0 >_{bcc}$ on the $\{1\ 1\ 0\}_{bcc}$ plane). After the first shearing in the $\{1\ 1\ 1\}_{fcc}$ plane, each atom advances to a saddle-point position, which is energetically achievable under the given thermal and thermodynamic conditions. Figure 4-8(a) shows the configuration of planes obtained at the saddle-point position. In order to obtain the actual configuration

of $\{110\}_{bcc}$ planes, which is shown by the blue parallelogram, a second shear is taking place, with a displacement of $a_{fcc}/16 \langle 112 \rangle_{fcc}$, as shown by the blue arrow in figure 4-8(a).

A similar configuration of atoms to figure 4-8(a), which are chosen inside the yellow triangles in figure 4-7(a), is observed at the original bcc/fcc interfaces for System NW, especially those marked by asterisks and the successive layer of atoms. The corresponding snapshots before and after phase transformation are shown in figure 4-8(b). Compared with the model by Bogers and Burgers [34], these atoms are already at the positions of the saddle-point and thus no first shear is involved. The transformation to the bcc structure involved a displacement of $a_{fcc}/16 \langle 112 \rangle_{fcc}$ referred to the fcc structure [34]. This corresponds to a shearing displacement of $a_{fcc}/16 [11\bar{2}]_{fcc}$ in the negative x direction, as the light blue arrow shows. Similarly, the successive fcc-to-bcc transformation for the atoms identified with an fcc structure in snapshot at 0 ps in figure 4-7(a) involves a shearing displacement of $a_{fcc}/16 [\bar{1}\bar{1}2]_{fcc} \parallel [\bar{1}10]_{bcc}$ in the positive x direction.

The configuration of atoms in the low potential energy area at the original bcc/fcc interface before and after the fcc-to-bcc phase transformation is shown in figure 4-8(c) for System KS and in figure 4-8(d) for System Nagano, respectively. The light blue parallelograms indicate the regular configuration of $(110)_{bcc}$ planes and the light blue arrows illustrate the displacement in the direction $(\bar{1}10)_{bcc}$. It is found that System KS and System Nagano share the same shearing model [33,34] with System NW regarding the growth of original bcc phase at the bcc/fcc interfaces in low potential energy locations.

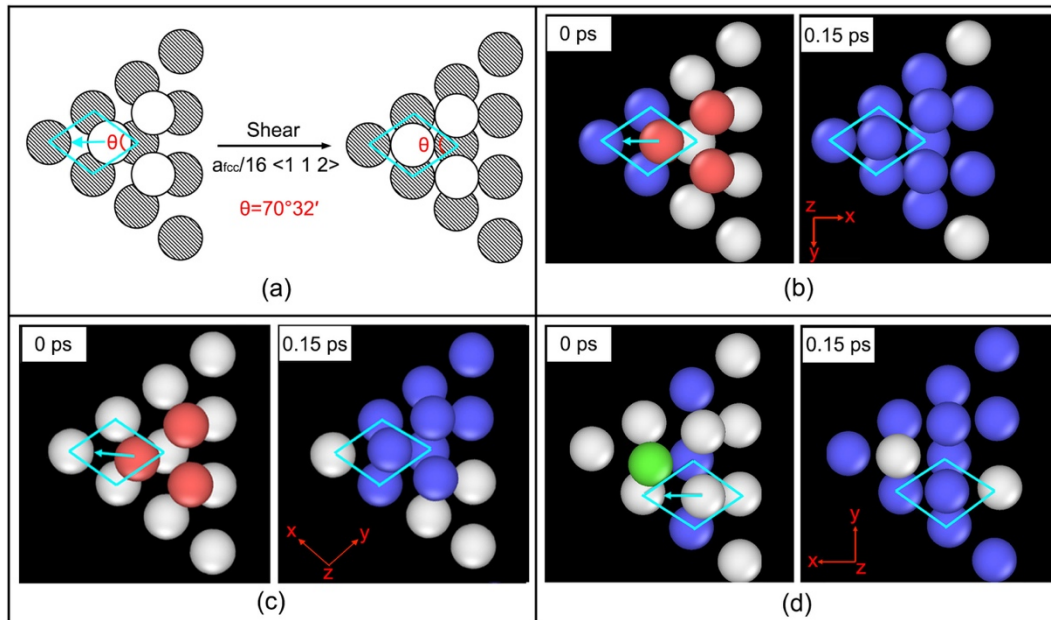


Figure 4-8 (a) Configuration of $\{110\}_{bcc}$ type planes after the $a_{fcc}/16 \langle 112 \rangle_{fcc}$ in the $\{111\}_{fcc}$ plane and the proper configuration in a regular bcc structure after the successive shearing of these $\{110\}_{bcc}$ type planes. The mechanism was previously reported in [33,34]; (b-d) Corresponded configurations of atoms at the interface for System NW (b), System KS (c) and System Nagano (d) at 0 ps and 0.15 ps. The colours of atoms in (b-d) denote the local crystal structure as in figure 4-1.

From the above, the growth of original bcc phase in low potential energy areas in the three systems share the same faulting mechanism proposed by Olson and Cohen [33] based on Bogers and Burgers' initial concept [31]. Yang *et al.* [25,26] verified the 'two-shear' Bogers-Burgers-Olson-Cohen (BBOC) model experimentally after examining the deformation-induced martensitic transformation in an austenitic stainless steel with high-resolution transmission electron microscopy (HRTEM). The two shears of 'T/3-3/8T' (T represents a Shockley partial dislocation for fcc twin shear) during the deformation-induced $\gamma(\text{fcc}) \rightarrow \epsilon(\text{hcp}) \rightarrow \alpha'(\text{bcc})$ phase transformation was confirmed with the HRTEM observations, as well as with their MD simulation results of the interfaces between the fcc and bcc phases with Pitsch OR and two KS orientation relations. In the present simulations, however, the detailed study into the atomic displacements during the phase transformation at the bcc/fcc interfaces indicates that the model does not apply entirely, but only locally, i.e. in the low potential energy areas at the bcc/fcc interfaces. Furthermore, only the second shear but not the first one is involved during the growth of original bcc phase. The absence of the first shear may explain the relatively rapid fcc-to-bcc transformation at the low-energy areas at the bcc/fcc interfaces. For the high-energy areas at the interfaces, however, diffusion might be needed for atoms to reach their equilibrium positions so as to obtain the true bcc lattices.

4.3.3 Displacement of the atoms involved in the growth of the bcc phase at the bcc/fcc interfaces

Figure 4-9(a) shows the local snapshot of one mono bcc plane with atoms marked by 3D vectors showing their displacements in the first 10 ps. The plane corresponds to the fcc-plane at the original bcc/fcc interface with NW OR. Atoms with low potential energies inside the red triangle are found to move in a collective manner for a small displacement and the neighbouring atoms of each atom remain unchanged. For atoms with higher initial potential energies, the displacements tend to be larger. A small portion of atoms with high potential energies involves a displacement on the order of an interatomic distance or larger. Those atoms at the high-energy areas move randomly, with characteristics of diffusional jumps of atoms. Vacancies appear where the diffusional jump is observed, as is labeled by the small red circle. The high-energy areas also display the change of neighboring atoms and the creation of new atomic arrangement.

Similar to that of System NW, the growth of bcc phase at the low energy areas at the interfaces also involves a locally collective motion of atoms with small displacements for System KS and System Nagano, as shown by the red ellipses in figure 4-9 (b) and (c), respectively. By comparing the displacement vectors of atoms on both sides of the red lines at high energy areas in figure 4-9 (b) and (c), the collective motion of atoms on one side of the red lines is neighbored on the other side by another group of atoms moving collectively in a different direction. Despite the collective motion, the atomic displacements for either group of atoms are on the order of or even higher than one interatomic distance. For the two layers of atoms alongside the red lines, they lose their original neighbours due to their large displacements in different directions. Thus the atomic neighbours change and defects such as vacancies, as labeled by the small red circles, are found in these areas.

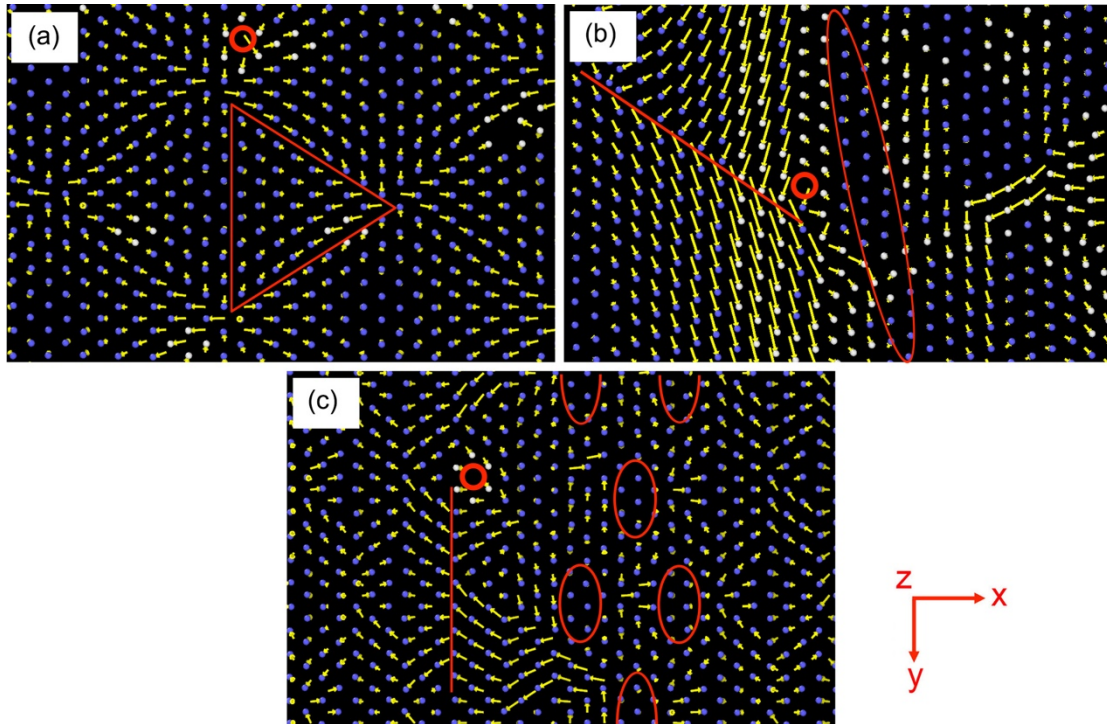


Figure 4-9 Snapshots of atoms with 3-dimensional displacement vectors for System NW (a), System KS (b) and System Nagano (c). The local regions involved in (a)-(c) belong to the mono fcc-plane at the interfaces and the corresponding displacements are calculated at 10 ps.

Figure 4-10(a) indicates the corresponding displacement distribution of atoms in figure 4-9(a) for System NW. It is found that 99.9% of atoms undergo a displacement less than 2.4 \AA for System NW. Combined with the above results, the growth of original bcc phase at the original bcc/fcc interfaces with the NW OR involves a mixed mechanism, which is of a predominantly martensitic nature in the low potential energy areas and a possibly diffusional nature for some of the atoms in high potential energy areas. For System KS, 90.3% of the atoms undergo a displacement smaller than 2.4 \AA , as shown in figure 4-10(b). Similar to System NW, the growth of bcc phase in low potential energy areas is of a martensitic nature. The growth of bcc phase in the high energy areas in System KS may involve in a diffusional mechanism. The result in figure 4-10(c) indicates that approximately 99.2% of atoms have a displacement less than 2.4 \AA for System Nagano. The final 0.8% atoms belong to the ones located at high potential energy positions and may involve diffusional displacement.

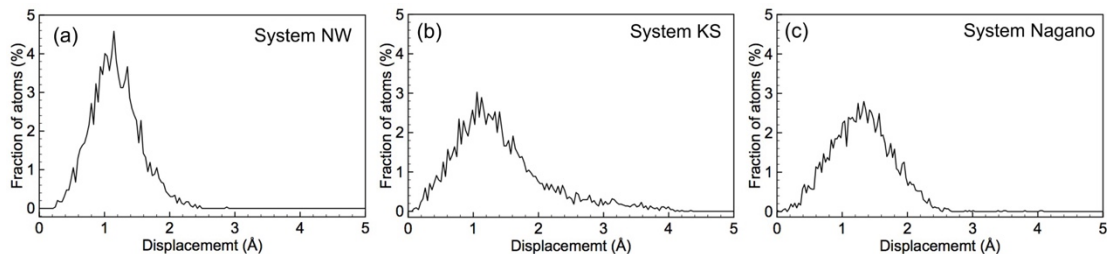


Figure 4-10 Displacement distribution of atoms on the mono fcc-plane at the interfaces for System NW (a), System KS (b) and System Nagano (c) at 10 ps.

From the present analysis, a predominantly martensitic mechanism is confirmed for the growth of original bcc phase in the low potential energy areas at the bcc/fcc interfaces for System NW, System KS and System Nagano. However, diffusional jumps of atoms may be involved during the growth of bcc phase in the high potential energy areas. A higher fraction of atoms with a displacement on the order of one interatomic distance is found in System KS than in System NW and System Nagano. This indicates that more atoms are involved in the diffusional transformation during the growth of bcc/fcc interfaces in System KS. This is shown to be leading to more defects, i.e. vacancies, in the high-energy areas at the final configuration. Besides, the displacements of atoms in the low potential energy areas are much smaller than those in the high potential energy areas. The absence of the first shear during the fcc-to-bcc transformation as first proposed by Bogers and Burgers [34] and later by Olson and Cohen [33], may explain the smaller displacements for atoms at the low potential energy areas at the bcc/fcc interfaces.

4.4 Conclusions

MD simulations were performed using the Mendelev potential [23] to study the mechanisms controlling the growth of the original bcc phase during the fcc-to-bcc transformation in three systems with semi-coherent bcc/fcc interfaces, which are NW, KS and Nagano orientation relationships, respectively. Simulations show that:

- The bcc/fcc interfaces of System NW, System KS and System Nagano propagate into the fcc bulk involving a limited number of atomic layers in a faceted style. The propagation of the bcc/fcc interface following a faceted style is also observed in the MD simulation of the bcc/fcc interface in the NW OR in iron using the Ackland potential [22]. The same transformation mechanism at the interfaces has been observed with the two different potentials.
- Growth of bcc phase starts in the areas of low potential energy at the original bcc/fcc interfaces and develops into the high-energy areas.
- Growth of bcc phase at low potential energy areas follows the faulting mechanism proposed by Olson and Cohen [33] based on the Bogers-Burgers model [34]. A collective motion of atoms is involved and is of a martensitic character.
- The MD simulations indicate that growth of bcc phase in the high potential energy areas at the original fcc/bcc interfaces involves diffusional atomic jumps for a small fraction of the atoms.

4.5 References

- [1] A. L. Roitburd and G. V. Kurdjumov, 'The nature of martensitic transformations', *Mater. Sci. Eng.*, 1979, 39, 141-167.
- [2] M. J. Santofimia, L. Zhao, R. Petrov, C. Kwakernaak, W. G. Sloof and J. Sietsma, 'Microstructural development during the quenching and partitioning process in a newly designed low-carbon steel', *Acta Mater.*, 2011, 59, 6059-6068.
- [3] R. F. Bunshah and R. F. Mehl, 'The rate of propagation of martensite', *Trans. AIME*, 1953, 197, 1251-1258.
- [4] C. Bos, J. Sietsma and B. J. Thijsse, 'Molecular dynamics simulation of interface dynamics during the fcc-bcc transformation of a martensitic nature', *Phys. Rev. B*, 2006, 73, 104117.
- [5] B. J. Wang, E. Sak-Saracino, N. Gunkelmann and H. M. Urbassek, 'Molecular-dynamics study of the α - γ phase transition in Fe-C', *Comput. Mater. Sci.*, 2014, 82, 399-404.
- [6] Z. Yang and R. A. Johnson, 'An EAM simulation of the alpha-gamma iron interface', *Modell. Simul. Mater. Sci. Eng.*, 1993, 1, 707-716.
- [7] T. Nagano and M. Enomoto, 'Calculation of the interfacial energies between α and γ iron and equilibrium particle shape', *Metall. Mater. Trans. A*, 2006, 37, 929-937.
- [8] E. C. Bain and N. Y. Dunkiri, 'The nature of martensite', *Trans. Am. Inst. Min. Metal. Eng.*, 1924, 70, 25-47.
- [9] G. Miyamoto, N. Takayama and T. Furuhashi, 'Accurate measurement of the orientation relationship of lath martensite and bainite by electron backscatter diffraction analysis', *Scripta Mater.*, 2009, 60, 1113-1116.
- [10] Z. Nishiyama, 'Mechanism of transformation from face-centred to body-centred cubic lattice', *Sci. Rep. Tohoku Imp. Univ.*, 1934, 23, 637-664. Cited by M. G. Hall, H. I. Aaronson and K. R. Kinsman, 'The structure of nearly coherent fcc: bcc boundaries in a Cu-Cr alloy', *Surf. Sci.*, 1972, 31, 257-274.
- [11] G. V. Kurdjumov and G. Sachs, 'Über den mechanismus der stahlhärtung', *Z. Phys.*, 1930, 64, 325-343. Cited by M. G. Hall, H. I. Aaronson and K. R. Kinsman, 'The structure of nearly coherent fcc: bcc boundaries in a Cu-Cr alloy', *Surf. Sci.*, 1972, 31, 257-274.
- [12] S. Tateyama, Y. Shibuta and T. Suzuki, 'Orientation relationship in fcc-bcc phase transformation kinetics of iron: a molecular dynamics study', *ISIJ Int.*, 2010, 50, 1211-1216.
- [13] S. Tateyama, Y. Shibuta and T. Suzuki, 'A molecular dynamics study of the fcc-bcc phase transformation kinetics of iron', *Scripta Mater.*, 2008, 59, 971-974.
- [14] B. J. Wang and H. M. Urbassek, 'Atomistic dynamics of the bcc-fcc phase transition in iron: Competition of homo- and heterogeneous phase growth', *Comput. Mater. Sci.*, 2014, 81, 170-177.
- [15] B. J. Wang and H. M. Urbassek, 'Molecular dynamics study of the α - γ phase transition in Fe induced by shear deformation', *Acta Mater.*, 2013, 61, 5979-5987.
- [16] H. Song and J. J. Hoyt, 'An atomistic simulation study of the migration of an austenite-ferrite interface in pure Fe', *Acta Mater.*, 2013, 61, 1189-1196.
- [17] H. Song and J. J. Hoyt, 'A molecular dynamics simulation study of the velocities, mobility and activation energy of an austenite-ferrite interface in pure Fe', *Acta Mater.*, 2012, 60, 4328-4335.

- [18] B. J. Wang and H. M. Urbassek, 'Phase transitions in an Fe system containing a bcc/fcc phase boundary: An atomistic study', *Phys. Rev. B*, 2013, 87, 104108.
- [19] S. Tateyama, Y. Shibuta, T. Kumagai and T. Suzuki 2011, 'A molecular dynamics study of bidirectional phase transformation between bcc and fcc iron', *ISIJ Int.*, 2011, 51, 1710-1716.
- [20] R. A. Johnson and D. J. Oh, 'Analytic embedded atom method model for bcc metals', *J. Mater. Res.*, 1989, 4, 1195-1201.
- [21] R. Meyer and P. Entel, 'Martensite-austenite transition and phonon dispersion curves of $\text{Fe}_{1-x}\text{Ni}_x$ studied by molecular-dynamics simulations', *Phys. Rev. B*, 1998, 57, 5140-5147.
- [22] G. J. Ackland, D. J. Bacon, A. F. Calder and T. Harry, 'Computer simulation of point defect properties in dilute Fe-Cu alloy using a many-body interatomic potential', *Philos. Mag. A*, 1997, 75, 713-732.
- [23] M. I. Mendeleev, S. Han, D. J. Srolovitz, G. J. Ackland, D. Y. Sun and M. Asta, 'Development of new interatomic potentials appropriate for crystalline and liquid iron', *Phil. Mag.*, 2003, 83, 3977-3994.
- [24] M. Müller, P. Erhart and K. Albe, 'Analytic bond-order potential for bcc and fcc iron-comparison with established embedded-atom method potentials', *J. Phys.: Condens. Matter*, 2007, 19, 326220.
- [25] X. S. Yang, S. Sun, X. L. Wu, E. Ma and T. Y. Zhang, 'Dissecting the mechanism of martensitic transformation via atomic scale observations', *Sci. Rep.*, 2014, 4, 6141.
- [26] X. S. Yang, S. Sun and T. Y. Zhang, 'The mechanism of bcc α' nucleation in single hcp ϵ laths in the fcc $\gamma \rightarrow$ hcp $\epsilon \rightarrow$ bcc α' martensitic phase transformation', *Acta Mater.*, 2015, 95, 264-273.
- [27] J. H. Van der Merwe and G. J. Shiflet, 'The role of structural ledges at phase boundaries; 1: Interfaces with rectangular atomic nets', *Acta Mater.*, 1994, 42, 1199-1205.
- [28] S. Plimpton, 'Fast parallel algorithms for short-range molecular dynamics', *J. Comp. Phys.*, 1995, 117, 1-19. <http://lammps.sandia.gov/>. Accessed on September 4th, 2017.
- [29] A. Stukowski, 'Structure identification methods for atomistic simulations of crystalline materials', *Modell. Simul. Mater. Sci. Eng.*, 2012, 20, 045021.
- [30] A. Stukowski, 'Visualization and analysis of atomistic simulation data with OVITO-the open visualization tool', *Modell. Simul. Mater. Sci. Eng.*, 2010, 18, 015012.
- [31] T. Waitz, T. Antretter, F. D. Fischer, N. K. Simha and H. P. Karnthaler, 'Size effects on the martensitic phase transformation of NiTi nanograins', *J. Mech. Phys. Solids*, 2007, 55, 419-444.
- [32] C. H. Lei, L. J. Li, Y. C. Shu and J. Y. Li, 'Austenite-martensite interface in shape memory alloys', *Appl. Phys. Lett.*, 2010, 96, 141910.
- [33] G. B. Olson and M. Cohen, 'A general mechanism of martensitic nucleation- Part II. FCC \rightarrow BCC and other martensitic transformations', *Metall. Trans. A*, 1976, 7, 1905-1914.
- [34] A. J. Bogers and W. G. Burgers, 'Partial dislocations on the $\{110\}$ planes in the bcc lattice and the transition of the fcc into the bcc lattice', *Acta Met.*, 1964, 12, 255-261.

Chapter 5

Homogeneous nucleation of bcc phase in fcc iron by molecular dynamics simulation

Abstract:

The present chapter pioneers in studying the formation process of a stable nucleus during solid-solid phase transformations at the atomic scale by molecular dynamics simulation, for which a new method is proposed to analyse the thermodynamics of the nucleation process. The simulation shows homogeneous nucleation of bcc phase in fcc iron. The high energy barrier for the homogeneous nucleation that is predicted by the classical nucleation theory is avoided by the occurrence of nonclassical nucleation processes, namely the formation of a metastable intermediate phase and the aggregation of subcritical clusters. These processes take place with a significantly lower energy barrier.

* This chapter is based on a scientific paper:

X Ou, J Sietsma and M J Santofimia, Nucleation mechanisms of bcc phase in fcc Fe by molecular dynamics simulation, in manuscript.

5.1 Introduction

Metallic alloys are at the core of existing and emerging technologies, of which iron alloys are the most manufactured due to their versatility [1-3]. The wide properties that can be delivered with iron alloys are a consequence of the multiple microstructures in which these materials can be produced. These microstructures are created via phase transformations during processing, which in the most majority of the cases are controlled by nucleation and growth processes [1,4]. Although growth phenomena are well understood, nucleation processes remain as one of the most complex and unknown phenomena in materials science.

Through development and modification for 90 years, the classical nucleation theory (CNT) has been found able to describe nucleation processes in phase transformations and crystallisation to a certain extent, but its predictive strength is very limited [1-3,5]. According to the CNT, the Gibbs free energy change ΔG during a homogenous nucleation event is given by:

$$\Delta G = -V\Delta g_V + A\gamma \quad (5-1)$$

in which V is the volume of the nucleus, Δg_V is the Gibbs free energy difference between the parent and product phases per unit of volume, A is the area of the interface forming during the nucleation process and γ is the interfacial free energy per unit area of the created interface, as shown in figure 5-1(a) [6]. Equation (5-1) implies that ΔG goes through a maximum, i.e. an energy barrier, when the nucleus develops. Before overcoming the energy barrier, a nucleus may grow or disappear leading to fluctuations of the energy change ΔG . After the energy change ΔG overcomes the energy barrier, the nucleus is stabilised and grows continuously.

In recent years the universal applicability of the CNT has been questioned in the field of nanoscience and nanotechnology, where nonclassical nucleation mechanisms, like “aggregation of nuclei” and “stepwise nucleation” were proposed [3,7-12]. The mechanism “aggregation of nuclei” involves a nucleation process in which two or more subcritical clusters merge to form a nucleus beyond the activation energy, as marked by the blue arrow in figure 5-1(b). Each time two subcritical clusters merge, the free energy of the system decreases because a certain area of interfaces is eliminated. Thus, the nucleus is stabilised by aggregation instead of overcoming the high energy barrier, as indicated in figure 5-1(b) [8,10,11].

As an alternative nonclassical nucleation pathway, “stepwise nucleation” proposes that an intermediate state forms between the parent phase and the product phase, which reduces the interfacial energy. As a consequence, the high energy barrier for nucleation predicted by the CNT is replaced by two lower energy barriers, as shown in figure 5-1(c) [3, 9].

The pathways of “aggregation of nuclei” and “stepwise nucleation” were studied independently in previous works, while they may also take place simultaneously during the nucleation process of a new phase [3,7-11]. In such a case, ΔG for the nucleus follows both pathways in a complementary way. It is therefore assumed that the corresponding schematic picture of ΔG displaying the characteristics of both nonclassical nucleation mechanisms can be illustrated as in figure 5-1(d), which will be discussed in the present chapter. The nonclassical nucleation mechanisms are mainly studied for crystallisation processes in solutions or colloids [7,8], with few studies focusing on solid-solid phase transformations [3]. Further investigations are required to determine whether nonclassical nucleation processes can take place in solid-solid phase transformations.

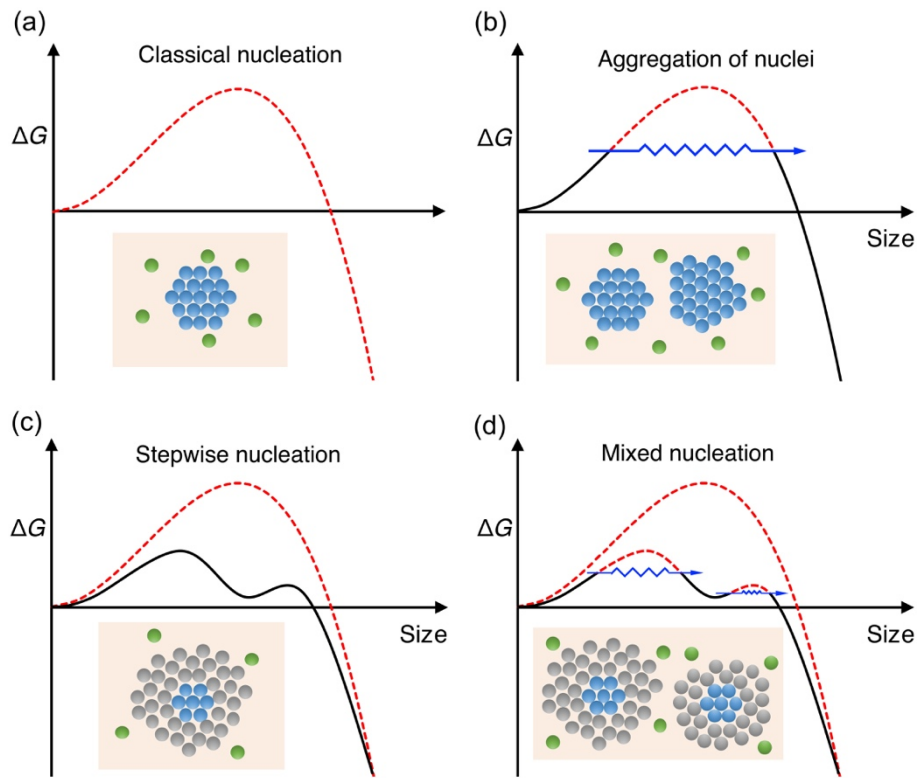


Figure 5-1 Schematic of ΔG with the evolution of nucleation by different pathways. (a) Classical nucleation through atom-by-atom addition [6,12]. (b) Nucleation by aggregation of subcritical clusters [8,10-12]. (c) Stepwise nucleation involving an intermediate state between the parent and product phases [3,9,12]. (d) Hypothetical ΔG for nucleation combining “aggregation of nuclei” and “stepwise nucleation”. Colours of atoms in the inserts in figures (a)-(d) represent phase structures: green-parent phase; grey-intermediate state; blue-product phase. The dashed red curves predicted by the CNT are avoided by nonclassical nucleation pathways in figures (b)-(d).

Regardless of the long history of experimental and theoretical studies, nucleation processes during solid-solid phase transformations are still poorly understood due to the experimental difficulty in observing small nuclei in bulk materials [1-3]. Thus divergent results for essential parameters like the critical nucleus size, were reported by different researchers [1,13]. Such studies [1-3,13] were largely based on the growth of stable nuclei, but not on the nucleation process itself. Molecular dynamics (MD) simulation is a suitable tool to observe the entire nucleation process of a new phase at the atomic scale. In previous studies [14], MD simulations have been applied to study the homogeneous nucleation of

bcc phase inside fcc iron under isothermal conditions. Knowledge of homogeneous nucleation, although often less abundantly occurring than heterogeneous nucleation in real materials, can also strengthen the knowledge and insight into heterogeneous nucleation of a new phase at defects, such as grain boundaries [15]. The heterogeneous nucleation of bcc phase at fcc/fcc grain boundaries will be discussed in the following chapter.

In the present study, homogeneous nucleation during the fcc-to-bcc transformation in iron is studied by MD simulation. The CNT is employed to analyse the energetics of nucleation and initial growth of the bcc nuclei. Significant shortcomings in the fit lead to the conclusion that alternative mechanisms occur during nucleation. Nonclassical nucleation mechanisms are then discussed with regard to their functions in the stabilization of a bcc nucleus during the fcc-to-bcc phase transformation.

5.2 Methods

5.2.1 Simulation methods

In the present work, the embedded-atomic method (EAM) potential from Mendeleev *et al.* [16] is used, which describes the stable ferromagnetic bcc phase. Two cubic simulation systems with fcc single crystals are studied with the x , y and z axes parallel to the $[1\ 0\ 0]_{fcc}$, $[0\ 1\ 0]_{fcc}$ and $[0\ 0\ 1]_{fcc}$ directions, respectively. The system is built with 864,000 atoms in a box of $60 \times 60 \times 60$ fcc unit cells ($219.48 \times 219.48 \times 219.48 \text{ \AA}^3$). The lattice parameter for the fcc crystal is 3.658 \AA . The simulation is performed using a barostat and a thermostat of the Nosé-Hoover type (NPT ensemble) under a constant pressure of 100,000 Pa. The temperature is fixed at 160 K. Periodic boundary conditions are employed in the x , y and z directions. The simulation involves 10,000 steps with the time step of 0.5 fs. Calculations are performed with the open-source LAMMPS code [17]. The adaptive common neighbor analysis (a-CNA) [18] is used to determine atoms as belonging to either the fcc, hcp, bcc phase or remaining unidentified. Atoms that are located at the defects, i.e. boundaries, are unidentified, because there is a significant lattice mismatch. The configurations are displayed using the software OVITO [19].

5.2.2 Thermodynamic analysis

The thermodynamics of the nucleation process during phase transformation is studied in the framework of CNT, as illustrated by Equation (5-1). The CNT is modified as follows for its applicability in MD simulation.

During the study of the nucleation, n_0 atoms within a small volume are manually selected, inside which only one bcc nucleus is included. Thus the homogeneous bcc nucleation is exempted from the

effects of other nucleation processes. At the simulation time t , the potential energy of the selected volume U_t can be presented as sum of the energy of the n_0 atoms:

$$U_t = \sum_{i=1}^{n_f} u_{i,t} + \sum_{j=1}^{n_u} u_{j,t} + \sum_{k=1}^{n_b} u_{k,t} \quad (5-2)$$

$$n_f + n_u + n_b = n_0 \quad (5-3)$$

in which n_f , n_u and n_b are the number of fcc, unidentified and bcc atoms, respectively, in the selected volume with $u_{i,t}$, $u_{j,t}$ and $u_{k,t}$ the corresponding potential energies. Note that hcp atoms are included in n_u . Then the potential energy change ΔU_t of the fixed volume at the simulation time t due to the homogenous nucleation process is defined as:

$$\Delta U_t = \sum_{j=1}^{n_u} u_{j,t} + \sum_{k=1}^{n_b} u_{k,t} - \left(\frac{n_u+n_b}{n_f}\right) \times \sum_{i=1}^{n_f} u_{i,t} \quad (5-4)$$

The third term accounts for the potential energy of the $(n_u + n_b)$ atoms if they would still be in the parent fcc phase. Both the unidentified and the bcc atoms contribute to energy change due to the bcc nucleation inside the fcc phase.

Under the conditions of fixed temperature T (160 K) and pressure P (100,000 Pa), the Gibbs free energy change due to complete fcc-to-bcc transformation $\Delta G_{fcc-bcc}$ consists of three parts [20]:

$$\Delta G_{fcc-bcc} = \Delta U_{fcc-bcc} + P\Delta V_{fcc-bcc} - T\Delta S_{fcc-bcc} \quad (5-5)$$

where $\Delta U_{fcc-bcc}$ is the potential energy difference between the bcc and fcc phase; $\Delta V_{fcc-bcc}$ is the volume change due to the fcc-to-bcc transformation; $\Delta S_{fcc-bcc}$ is the entropy difference between the bcc and fcc phase. The potential energy difference $\Delta U_{fcc-bcc}$ calculated from the Mendelev potential [16] is $10.13 \text{ meV}/\text{\AA}^3$ at 160 K. Compared with the contribution of $\Delta U_{fcc-bcc}$ to the Gibbs free energy change $\Delta G_{fcc-bcc}$, the value of $P\Delta V_{fcc-bcc}$ is $3.79 \times 10^{-5} \text{ meV}/\text{\AA}^3$ at 160 K, which is six orders of magnitude smaller. Caro *et al.* [21] calculated the enthalpies and entropies of bcc and fcc iron using the so-called CALPHAD (Computer Coupling of Phase Diagrams and Thermochemistry) approach [22]. According to their results [21], the entropy difference $\Delta S_{fcc-bcc}$ between the bcc and fcc iron at temperatures below 200 K is as small as about $5 \text{ J}/(\text{K}\cdot\text{mol})$, while the enthalpy difference $\Delta H_{fcc-bcc} = \Delta U_{fcc-bcc} + P\Delta V_{fcc-bcc}$ between the bcc and fcc iron is on the order of $10^4 \text{ J}/\text{mol}$. This indicates that the contribution of the entropy difference $T\Delta S_{fcc-bcc}$ to the Gibbs energy difference $\Delta G_{fcc-bcc}$ is negligible compared with that of the enthalpy difference $\Delta H_{fcc-bcc}$ during the fcc-to-bcc transformation at temperatures below 200 K. Therefore, the potential energy change $\Delta U_{fcc-bcc}$ is used to extract information of the nucleation process and evaluate the applicability of the CNT. Thus the expression for the CNT equivalent to Equation (5-1) can be indicated as:

$$\Delta U = -V\Delta u_V + A\gamma \quad (5-6)$$

where ΔU represents the potential energy change $\Delta U_{fcc-bcc}$, Δu_V is the potential energy difference per unit volume between the parent fcc phase and the product bcc phase, which is $10.13 \text{ meV}/\text{\AA}^3$ calculated from the Mendeleev potential at 160 K [16].

The activation energy for the nucleus and critical nucleus size are derived from the CNT expressed in Equation (5-6) as follows. At the simulation time t , the nucleus includes n_b atoms in the bcc structure. Thus the volume of the nucleus is given by:

$$V = V_a n_b \quad (5-7)$$

in which V_a is the atomic volume of bcc phase, which is $11.6637 \text{ \AA}^3/\text{atom}$ at 160 K from the Mendeleev potential [16]. An effective one-dimensional size d and the interface area A of the nucleus are defined as:

$$d = V^{\frac{1}{3}} \quad (5-8)$$

$$A = f d^2 \quad (5-9)$$

where f is the shape parameter of the nucleus. For a spherical nucleus, parameter f is equal to $(36\pi)^{\frac{1}{3}}$. Then Equation (5-6) can be expressed as:

$$\Delta U = -d^3 \Delta u_V + f d^2 \gamma \quad (5-10)$$

Differentiating Equation (5-10), the following equation is obtained:

$$\frac{d(\Delta U)}{d(d)} = -3d^2 \Delta u_V + 2f d \gamma + d^2 \gamma \frac{d(f)}{d(d)} \quad (5-11)$$

If the parameter f is assumed to be independent of d , $\frac{d(f)}{d(d)} = 0$. The critical nucleus results when $\frac{d(\Delta U)}{d(d)}$ equals to zero. Consequently, the size of the critical bcc nucleus d^* can be calculated as:

$$d^* = \frac{2f\gamma}{3\Delta u_V} \quad (5-12)$$

Thus the number of atoms inside the critical nucleus n^* can be obtained as:

$$n^* = \frac{(d^*)^3}{V_a} = \frac{8f^3 \gamma^3}{27(\Delta u_V)^3 V_a} \quad (5-13)$$

Subsequently, the activation energy ΔU^* can be calculated by substituting d^* into Equation (5-10):

$$\Delta U^* = \frac{4f^3 \gamma^3}{27\Delta u_V^2} \quad (5-14)$$

The temperature of a group of atoms is calculated according to:

$$T = \frac{2E_k}{3k_B N} \quad (5-15)$$

in which T represents the temperature; E_k is the total kinetic energy of the group of atoms; k_B is the Boltzmann constant and N is the number of atoms.

The above describes the thermodynamic analysis when only the atoms that are identified as bcc are considered to be part of the nucleus. However, when the unidentified atoms are also considered to be part of the nucleus, the effective one-dimensional size d can be defined as:

$$d = V^{\frac{1}{3}} = [V_a(n_b + n_u)]^{\frac{1}{3}} \quad (5-16)$$

Correspondingly, the Δu_V in Equation (5-10), which is the potential energy difference per unit volume between the parent fcc phase and the product phase involving both the bcc and unidentified structures, will be determined based on the relation between the energy change and the nucleus size.

5.2.3 Calculation of shape parameter

The shape parameter f of a nucleus, is derived from the volume V' and area A' by the ‘Construct Surface Mesh’ modifier in OVITO [23]. Atoms with the bcc and unidentified structures in the selected volume are involved in the calculation of parameter $f = \frac{A'}{(V')^{2/3}}$.

5.3 Results and discussion

5.3.1 Molecular dynamics simulation of the bcc nucleation

MD simulation shows that homogeneous nucleation of the bcc phase takes place in the fcc iron at 160 K. In figure 5-2 all atoms with the fcc structure have been removed from the simulation box. The largest three bcc nuclei are labeled by the yellow arrows as N1, N2 and N3, respectively. In the present study, the bcc nuclei N1-N3, which provide fundamental information on nucleation mechanisms, are chosen as the representative and are extensively discussed in the following sections.

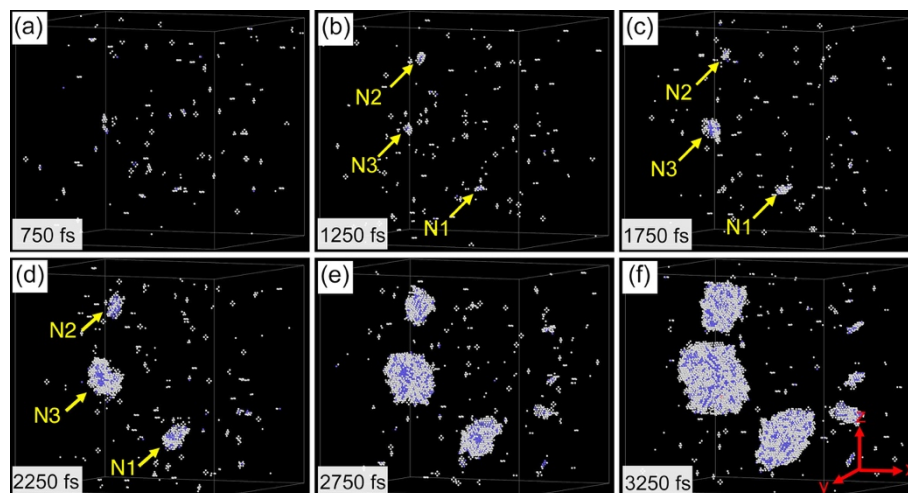


Figure 5-2 Configurations of bcc nucleation at 160 K. Colours of atoms represent phase structures: blue-bcc; white-unidentified. Atoms in the fcc structure are not displayed.

Besides the atoms in the bcc structure, a number of atoms, which are neither in the fcc nor the bcc structure and therefore unidentified by the a-CNA method [18], are present around the nucleus clusters in figure 5-2. One reason for atoms to have an unidentified structure may be that those atoms are located at the bcc/fcc phase interfaces, where the local structure is neither the one or the other. Another reason may be that the atoms with unidentified structure are not in the equilibrium positions either for the bcc or fcc lattices due to the strain and stress resulting from the fcc-to-bcc transformation. In both cases they can be considered to form an intermediate state.

5.3.2 Classical nucleation of bcc phase from fcc bulk

Homogeneous nucleation of N1-N3 is studied according to the CNT interpreted in MD simulations by Equation (5-10). The energy ΔU is plotted as a function of the size d of the individual bcc nucleus forming inside the fcc crystal, as shown in figure 5-3. Regardless of local fluctuations, the energy change of the nucleus initially shows an overall increasing trend and then decreases with the increasing nucleus size. The energy ΔU is fitted as a function of the size d according to Equation (5-10), as shown by the red curves in figures 5-3 (a)-(c), in which ΔU_V is taken equal to the value resulting from the Mendeleev potential [16]. The nucleus size d in figures 5-3 (a)-(c) considers only the atoms that are identified as bcc, those unidentified atoms are not considered as part of the nucleus. It is seen that the CNT reasonably describes the energy change during the stable stage of the nucleation, i.e. the growth period. However, it predicts a rather high activation energy for nucleation, as seen from inserts in figures 5-3 (a)-(c), which is not followed by the nucleus energy. This will be discussed in more detail in the sections 5.3.3 onwards. Fitting to different values of the size d does not result in a better match between the model curves and the thermodynamic data points. In order to make optimal use of the available data, the fits have been performed over the maximum range of d . Before growing to contact each other at around 3250 fs, the bcc nuclei N1, N2 and N3 reach the largest size of around 28.0 Å, 23.8 Å and 38.2 Å, respectively, thus $d = 23.8$ Å is chosen as the cutoff of the fitting dimensions. The fitting parameters (the product $f\gamma$), which is the coefficient of the quadratic term in Equation (5-10), are represented in Table 5-1.

Based on the fitting parameter (the product $f\gamma$), the interface energy γ can be estimated for a nucleus with a specific shape parameter f . From figure 5-4(a), it is seen that the shape parameter f of the bcc nuclei is changing with time during the nucleation stage and varies mainly from 7 to 16. A value of $f > 30$ is obtained for the nucleus when it is too small to apply $f = \frac{A'}{(V')^{2/3}}$ and therefore is not displayed in figure 5-4(a). The nuclei have an ellipsoidal morphology with the average shape parameter $f \approx 12$. The interface energy is therefore approximately 134 to 138 mJ/m² for the three nuclei, as indicated in Table 5-1. It was reported that coherent phase interfaces in metals and alloys have an interface energy less than 200 mJ/m², while semi-coherent interfaces have an energy in the range of 200 to 500 mJ/m² [3,24]. The low interface energy of less than 150 mJ/m² thus indicates evident coherency between the nucleus and fcc phase, which can be seen from the alignment of atoms in the

bcc nucleus and fcc phase on a monolayer of the $(1\bar{1}0)_{fcc}$ plane for N1 to N3, as shown in figure 5-4(b).

Table 5-1 indicate approximately the same energy barrier ΔU^* and critical nucleus size for the three nuclei. The one-dimensional critical size d^* is in the range of 6.61 to 6.84 Å, which corresponds to approximately 25 to 27 atoms in the critical bcc nucleus. Offerman *et al.* [1] used x-ray diffraction instrumentation at synchrotron sources to study the nucleation rate of ferrite grains as a function of temperature during the austenite-to-ferrite transformation in steel based on the CNT and estimated the critical ferrite nucleus to consist of 10 to 100 atoms. This is consistent with the value obtained in the present paper. Besides, the energy barrier ΔU^* in Table 5-1 is ranged between 1.46 and 1.62 eV which is overestimated by the CNT, as shown by the inserts in Fig. 5-3 (a)-(c). Offerman *et al.* [1] also found values for the activation energy for nucleation that are far too low to be consistent with the CNT assuming any conceivable nucleus shape.

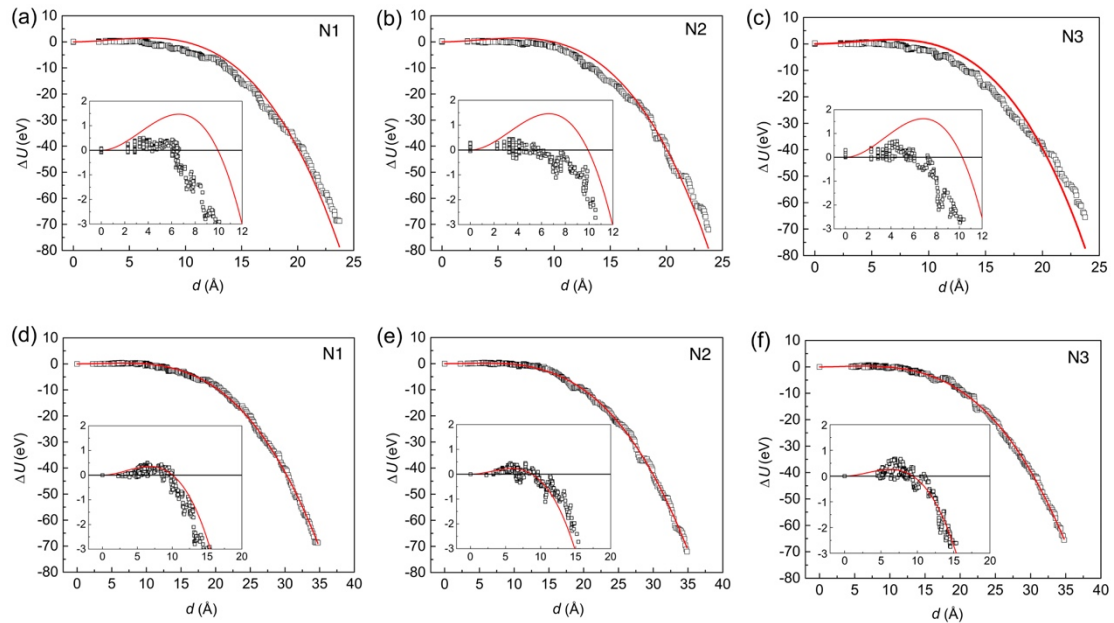


Figure 5-3 Plots of the energy change ΔU as a function of nucleus size d based on CNT: (a), (d) for N1; (b) (e) for N2; (c), (f) for N3. The black open dots represent the thermodynamic MD-data. The nucleus size d in figures (a)-(c) considers only the atoms that are identified as bcc, those unidentified atoms are not considered as part of the nucleus. The MD data in figures (a)-(c) is fitted according Equation (5-10) with fixed $\Delta u_V=10.13 \text{ meV}/\text{\AA}^3$ (red curves). The nucleus size d in figures (d)-(f) considers both the bcc and unidentified atoms as part of the nucleus. The MD data in figures (d)-(f) is fitted according Equation (5-10) automatically without fixing Δu_V (red curves). The inserts in figures (a)-(f) are the enlarged views of the nucleation stage for each individual nucleus.

Table 5-1 The fitting parameter (the product $f\gamma$) to Equation (5-10) for bcc nuclei N1, N2 and N3, when the nucleus size d considers only the atoms identified as bcc to be part of the nucleus. The values of ΔU^* , d^* and n^* are calculated according to Equation (5-14), (5-12) and (5-13), respectively. $n_{0,n}$ and $n_{0,g}$ are the number of atoms in the selected volume for individual nucleus in the nucleation and growth periods. $\gamma_{f=12}$ is the interface energy of individual nucleus with $f = 12$.

Nucleus	$n_{0,n}$	$n_{0,g}$	ΔU_V (meV/Å ³)	$(f\gamma)$ (meV/Å ²)	$\gamma_{f=12}$ (mJ/m ²)	ΔU^* (meV)	d^* (Å)	n^*
N1	1575	11774	(Fixed) 10.13	100.7	134.4	1473	6.63	25
N2	1687	11284	(Fixed) 10.13	100.4	134.0	1460	6.61	25
N3	1638	11148	(Fixed) 10.13	103.9	138.8	1621	6.84	27

As explained, the energy barrier ΔU^* for the homogenous nucleation is overestimated by the CNT, as can be seen from the inserts in figures 5-3 (a)-(c). However, when the unidentified atoms are considered as part of the nucleus, it is seen that the calculated energy barrier ΔU^* from the fitting curves in figures 5-3 (d)-(f) decreases to a value ranged between 0.22 and 0.35 eV, as shown in Table 5-2. This implies that the existence of unidentified atoms surrounding the bcc nuclei is related to the overestimated energy barrier by the CNT. Besides, the corresponding values of the driving force ΔU_V , interface energy γ and critical nucleus size (including both the bcc and unidentified atoms) in Table 2 are also much lower than those in Table 1 when the effective nucleus size d involves only the atoms identified as bcc.

The CNT reasonably describes the growth period of a postcritical nucleus but not its nucleation stage and therefore the calculated activation energy is not relevant for the nucleation process in the MD simulation. The number of atoms in a critical nucleus in Table 1 is somewhat lower than the transition to the growth stage in the MD simulation. The bcc nucleation event where the CNT fails to work will be discussed in the following section.

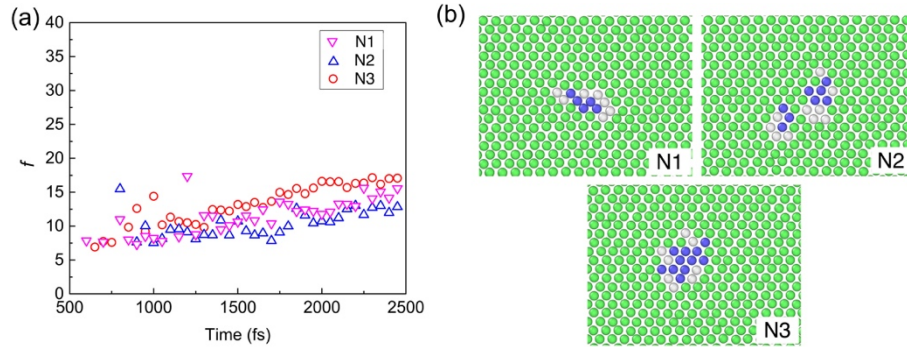


Figure 5-4 (a) Shape parameter f of nuclei N1-N3; (b) Monolayer of the $(1 \bar{1} 0)_{fcc}$ plane indicating the lattice matching between the bcc and fcc phases for N1 (1550 fs), N2 (1800 fs) and N3 (1250 fs), respectively. Colours of atoms represent different phase structures: blue-bcc; green-fcc; white-unidentified.

Table 5-2 The fitting parameters (the product $f\gamma$ and ΔU_V) to Equation (5-10) for bcc nuclei N1, N2 and N3, when the nucleus size d considers both the bcc and unidentified atoms as part of the nucleus. The values of ΔU^* , d^* and n^* are calculated according to Equation (5-14), (5-12) and (5-13), respectively. $n_{0,n}$ and $n_{0,g}$ are the number of atoms in the selected volume for individual nucleus in the nucleation and growth periods. $\gamma_{f=12}$ is the interface energy of individual nucleus with $f = 12$.

Nucleus	$n_{0,n}$	$n_{0,g}$	ΔU_V (meV/Å ³)	$(f\gamma)$ (meV/Å ²)	$\gamma_{f=12}$ (mJ/m ²)	ΔU^* (meV)	d^* (Å)	n^*
N1	1575	11774	(Auto) 2.32	23.3	31	349	6.7	26
N2	1687	11284	(Auto) 2.23	19.5	26	222	5.84	17
N3	1638	11148	(Auto) 2.13	19.9	27	258	6.24	21

5.3.3 Nonclassical nucleation of bcc phase from fcc bulk

As shown by the inserts in figure 5-3, the CNT overestimates the energy barrier to form a stable nucleus. In the view of the CNT, the bcc nucleus grows through the atom-by-atom addition and develops with a distinct shape and definite bcc/fcc interfaces separating product bcc and parent fcc phases. Reality is, however, more complex. The simulation shows that in the nucleation stage atoms in the bcc structure are located in several clusters, with unidentified atoms binding them into a single nucleus, as indicated in figure 5-5. Therefore, the shape is not clearly defined. This behaviour is not captured by the CNT. In fact, with this more complex behaviour, the system chooses a lower-energy route in the nucleation event. This section describes the homogeneous nucleation of bcc phase in the frame of nonclassical nucleation mechanisms.

5.3.3.1 Aggregation of nuclei

During the nucleation of colloidal nanoparticles in solutions [8-10,25], aggregation of nearby prenucleation clusters has been observed to play an important role in the formation of a stable nucleus. Similarly, aggregation of nearby prenucleation clusters is observed in the formation of a stable bcc nucleus in the present MD simulation, as shown in figure 5-5. The interaction of two neighbouring prenucleation clusters enables the survival of both. In this process, the two clusters combine, effectively forming a larger nucleus, which leads to stability. This can take place regardless of whether or not the two clusters have the same crystallographic orientation, as shown in figure 5-6. For N1, one prenucleation cluster has the Nishiyama-Wassermann (NW) orientation relationship (OR) [26] with the fcc phase, while its neighbour has the Kurdjumov-Sachs (KS) OR [27]. Due to their different ORs, a bcc/bcc grain boundary forms inside the obtained aggregate but still the overall interfacial energy is lowered during the aggregation process. For N2, however, the two prenucleation clusters merge into a single crystal after aggregation, because they have the same crystallographic orientation, the KS OR with the fcc phase. For N3, both clusters also have the KS OR with fcc, but in different variants, leading to a bcc/bcc grain boundary inside the aggregate.

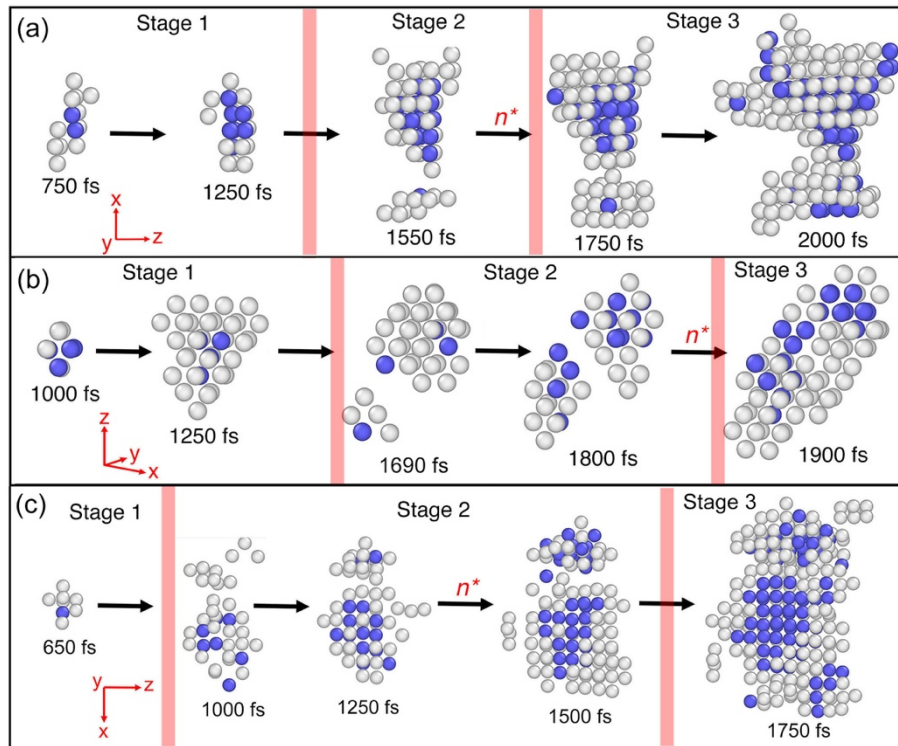


Figure 5-5 Nucleation process by aggregation of neighbouring clusters: (a) N1, (b) N2 and (c) N3. n^* represents the occurrence of the critical nucleus size. Colours of atoms represent different phase structures: blue-bcc; white-unidentified. Atoms in the fcc structure are excluded in figures (a) to (c).

Each bcc nucleus initiates with a single prenucleation cluster. This primary cluster is unstable in size and morphology before reaching the critical size. During the nucleation process, the number of atoms in the nucleus fluctuates until 1750 fs for N1, 1900 fs for N2 and 1550 fs for N3, as shown in figure 5-7. After that, the aggregation of a neighbouring cluster results in a jump of the number of atoms in the nucleus, which surpasses the critical size. The number of atoms in the aggregated crystal increases quickly during the growth period.

There are small neighbouring clusters forming and disappearing around the primary cluster during the nucleation event. In the present study, we focus on the period in which nuclei are stabilised by aggregation of the primary cluster and a neighbouring prenucleation cluster in figures 5-8 (a)-(d). The nucleation process is divided into three stages, as shown in figure 5-5, figure 5-7 and figure 5-8. The schematic picture illustrating Stage 1 to 3 is in figure 5-8(d). Stage 1 represents the period before the formation of the neighbouring prenucleation cluster close to the primary cluster. At Stage 2, the neighbouring prenucleation cluster forms and grows nearby the primary one, which corresponds to the time periods inside the dashed blue lines in figure 5-7. At Stage 3, the primary cluster aggregates with the neighbouring prenucleation cluster to form a larger cluster.

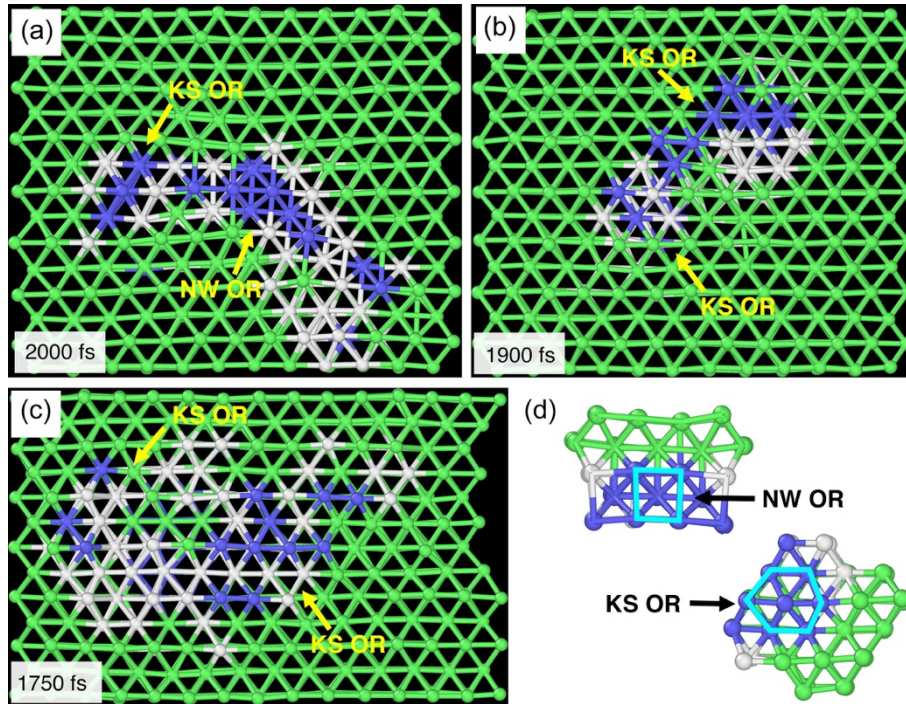


Figure 5-6 The orientation of the aggregated clusters for: (a) N1, (b) N2 and (c) N3. The view direction is parallel to $[1\bar{1}0]_{fcc}$. Bonds are created between atoms within the cutoff distance of 3.2 Å. Illustration of the NW and KS OR are highlighted in light blue in figure (d). Colours of atoms represent different phase structures: blue-bcc; green-fcc; white-unidentified.

After aggregation, the energy of the combined nucleus decreases to a negative value, as shown in figures 5-8 (a)-(c) and figure 5-9. In other words, the formation and aggregation with a neighbouring prenucleation cluster stabilises the primary prenucleation cluster by climbing over an energy barrier that is much lower than predicted by the CNT. The number of atoms in each nucleus starts to grow monotonically after aggregation, i.e. when entering into Stage 3, as seen from figure 5-7. The bcc nuclei are stabilised by effectively increasing in size and reducing the interfacial energy by aggregation, which circumvents the necessity to overcome the high energy barrier for the homogeneous nucleation envisioned by the CNT [7,25]. This explains the lower energy barrier than the one predicted by the CNT for the bcc nuclei in figure 5-3.

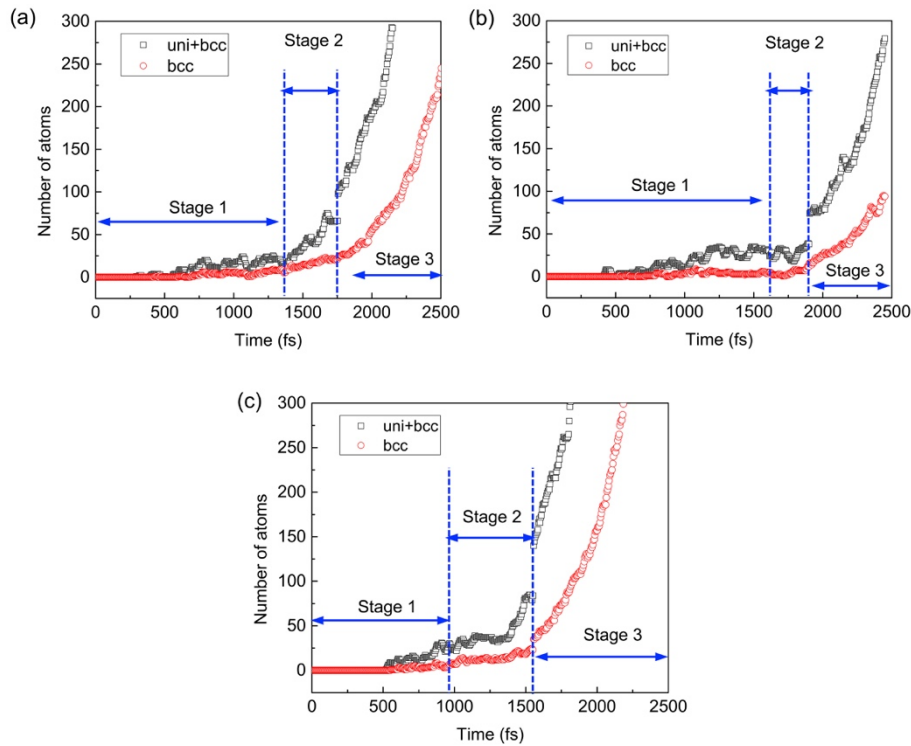


Figure 5-7 Number of atoms in the bcc nuclei: (a) N1, (b) N2 and (c) N3. The area in the dashed blue rectangle represents Stage 2 (1400-1750 fs for N1, 1650-1900 fs for N2 and 950-1550 fs for N3), when a neighbouring nucleus cluster forms and grows nearby the primary cluster. The red circle represents the number of atoms belonging to the bcc structure and the black square represents the sum of both the bcc and unidentified structures. The labels “uni” and “bcc” in figures (a)-(c) represent unidentified and bcc structures.

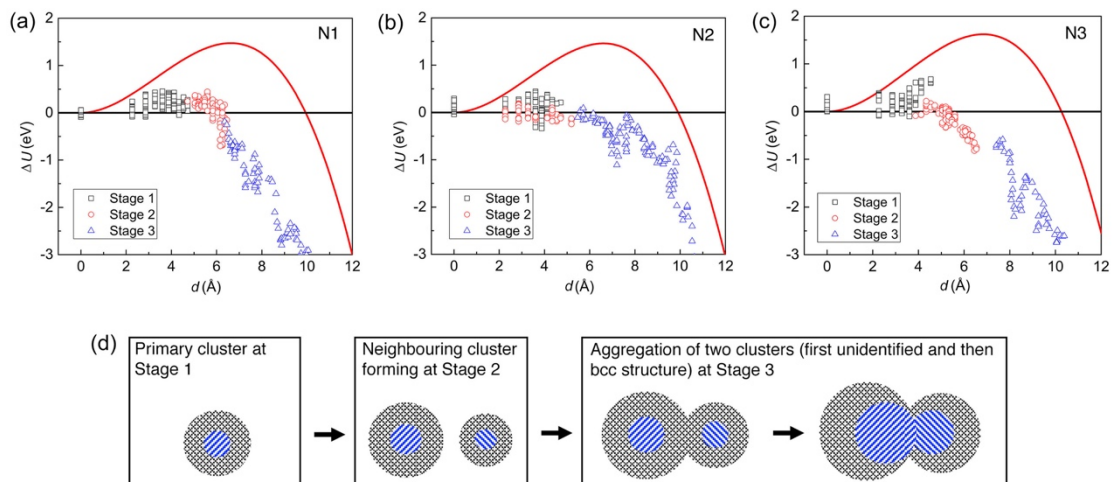


Figure 5-8 The energy ΔU as a function of the nucleus size at different stages for nuclei: (a) N1, (b) N2 and (c) N3. (d) Scheme illustrating the three stages in figures (a)-(c). The energy ΔU involves in both the bcc and unidentified structures, which correspond to the blue and grey regions in figure (d). The energy ΔU at Stage 1 and 2 is only contributed by the primary cluster while that at Stage 3 is contributed by the aggregate.

Besides the eventually stable nuclei, there are a number of bcc nuclei that fail to reach the critical size: they disappear. The number of atoms in such nuclei reaches a maximum of about 20 atoms in the unidentified and bcc structures, which then gradually diminishes if no aggregation with neighbouring

prenucleation clusters takes place. Therefore, it is deduced that the bcc nuclei fail to surpass the critical size through the atom-by-atom addition. The aggregation of neighbouring prenucleation clusters provides the opportunity for the primary nucleus to reach and surpass the critical size and to circumvent the high CNT-predicted energy barrier for homogeneous nucleation.

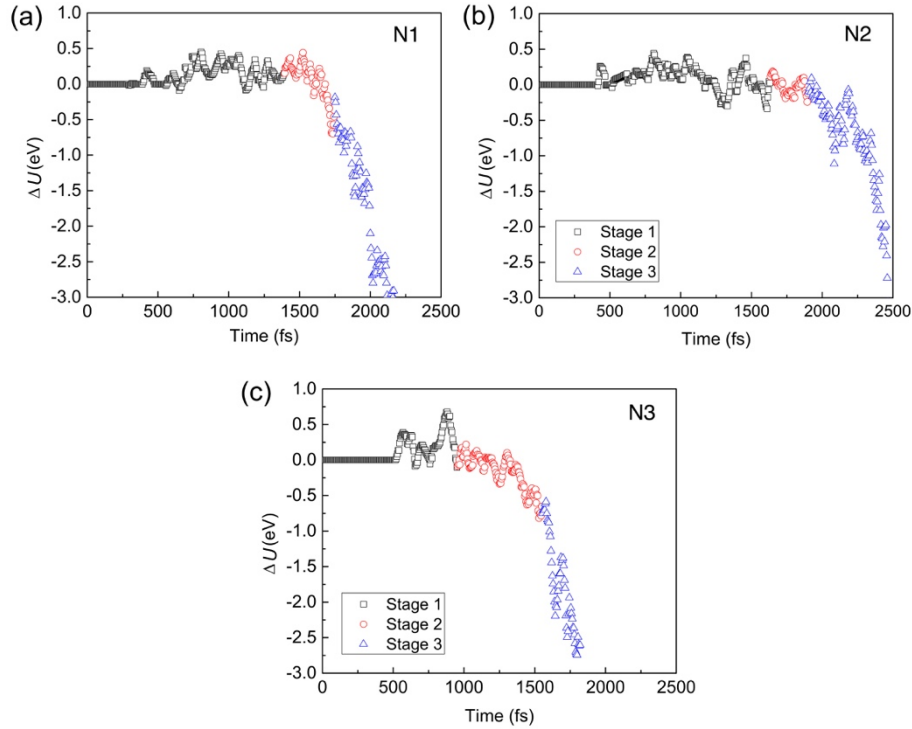


Figure 5-9 The energy change in Stage 1 to 3 as a function of time for the bcc nucleus: (a) N1, (b) N2 and (c) N3. The energy change is contributed by atoms both in the bcc and unidentified structure. The dots with energy change smaller than -3.0 eV are excluded.

5.3.3.2 Stepwise nucleation

The bcc nuclei are composed of a core consisting of atoms in the bcc structure surrounded by a number of unidentified atoms, as shown in figure 5-2, figure 5-5 and figure 5-6. The unidentified atoms not only act as the interfaces dividing the fcc and bcc structures, but also as an intermediate state existing between the clusters, which will be discussed later in this section. Note that the unidentified atoms extend over a distinctly broader range than can be envisioned for an interface. Furthermore, it binds the distinct bcc clusters to form a single nucleus.

The energy change of individual bcc nuclei in figures 5-8 (a)-(c) is contributed to by both the bcc and unidentified atoms. Regardless of local fluctuations, the energy change of the unidentified structure goes through a maximum value first, which is followed by a maximum for the bcc structure for each nucleus, as shown in figures 5-10 (a)-(d) and figures 5-11 (a)-(c). Both maxima are much lower than predicted by the CNT. Furthermore, the energy change of each nucleus is dominated by that of the unidentified atoms. Thus, it is inferred that the nucleation of bcc phase in the fcc bulk essentially follows a stepwise “fcc \rightarrow intermediate \rightarrow bcc” process instead of a single-step “fcc \rightarrow bcc”

transformation. The fcc phase transforms into the metastable intermediate state first, because of the lower barrier for its nucleation than the direct nucleation of the stable bcc phase. By using the single-particle-resolution video microscopy of colloidal films of diameter-tunable microspheres, Peng *et al.* [3] also found a two-step nucleation process with an intermediate liquid forming during solid-solid phase transitions. In our case, the unidentified structure that acts as the shell around the core bcc structure is similar to such an intermediate state, which is disordered from the parent fcc lattice and has a lower symmetry than the product bcc lattice.

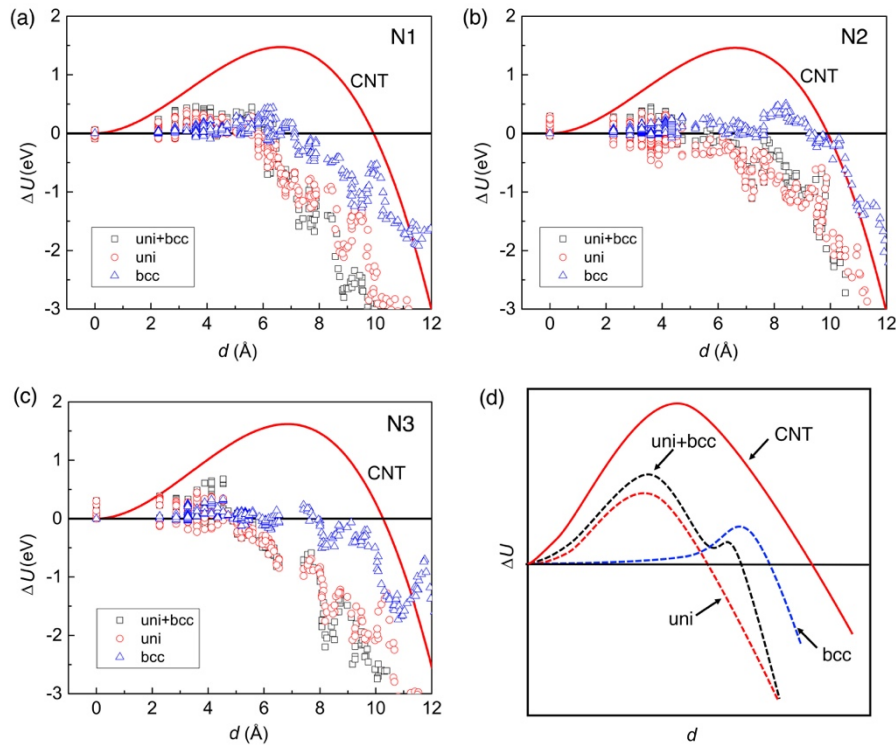


Figure 5-10 Contributions of the bcc (blue triangles) and unidentified (red circles) structures to the energy change of the bcc nuclei (black squares) as a function of the nucleus size: (a) N1, (b) N2 and (c) N3. The solid red curves in figures (a)-(c) show the prediction by the CNT. (d) Schematic picture of the energy ΔU in (a)-(c). The labels “uni” and “bcc” in (a)-(d) represent unidentified and bcc structures.

Peng *et al.* [3] proposed two low energy barriers for the two-step nucleation during the solid-solid phase transitions based on the Ostwald step rule. The first step refers to the barrier for the nucleation of the intermediate state in the parent solid phase and the second for the nucleation of the product solid from the generated intermediate state. This is similar to the nucleation during precipitation sequences in the solid state [12]. Also in the present study the high energy barrier of homogeneous nucleation predicted by the CNT is replaced by two or more lower energy barriers, as indicated in figure 5-9. Because the stepwise nucleation coincides with the aggregation of prenucleation clusters, it makes the overall energy change during the nucleation process more complex. The proposed schematic picture in figure 1(d) displays the energy change of the nucleus when both nonclassical nucleation mechanisms take place simultaneously during the nucleation process of the bcc phase.

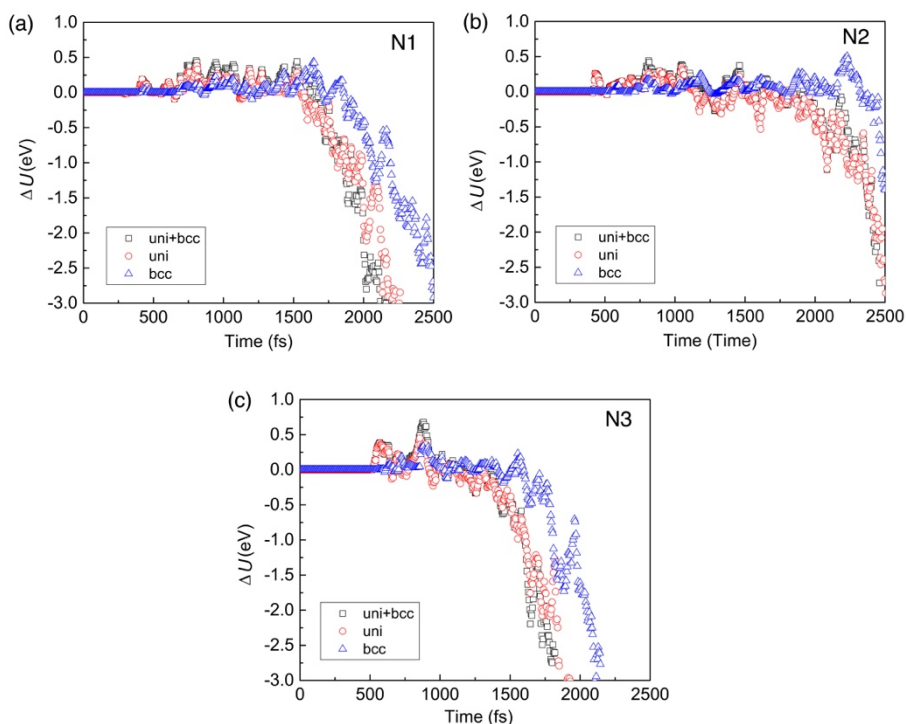


Figure 5-11 Contributions of the bcc and unidentified structures to the energy change of the bcc nucleus as a function of simulation time: (a) N1, (b) N2 and (c) N3. The labels “uni” and “bcc” in (a)-(c) represent unidentified and bcc structures.

5.3.4 Temperature of the bcc nuclei

Additionally, the local temperature fluctuation of the bcc nuclei may contribute to its stabilization. Figures 5-12 (a)-(c) show the temperatures of the bcc/unidentified structures and the corresponding fcc surroundings during the nucleation stage. Regardless of the constant temperature of the simulation cells, the local temperature of the region with bcc nucleation varies during the nucleation and growth stages of the bcc phase. From figures 5-12 (a)-(c), it can be seen that the temperature of the fcc structure almost remains constant. However, the temperature of the bcc/unidentified structures fluctuates around the system temperature during the nucleation period. In the growth period, the temperature of the nuclei increases up to about 200 K, which is 50 K above the system temperature, and fluctuates mildly. The reason may be that the heat induced by the fcc-to-bcc transformation due to nucleation cannot be conducted out of the simulation cell efficiently during the short MD simulation time.

Ford and Clement [28] reported that, physically, a subcritical nucleus which is cooler than average would be more likely to grow past the critical size for liquid droplet nucleation from vapour. They also found that the temperature of a droplet nucleus was bound to fluctuate due to the release of heat upon absorption of further molecules, and the collisions with the surrounding gas molecules. Correspondingly, the temperature fluctuation of the bcc nuclei during the fcc-to-bcc transformation can result from the release of heat upon aggregation of the neighbouring prenucleation clusters. The temperature difference between the nucleus and the parent phase was found by other researchers [29] as well. By molecular dynamics simulation of nucleation in the liquid-vapour system, Wedekind *et al.*

[30] found that the subcritically sized nucleus clusters are colder while postcritically sized clusters are warmer than the bath temperature. The above studies [28-30], either by experiments or by simulations, were based on the nucleation of liquid droplets from the vapour. Nevertheless, similar results are found in the present study about the temperature differences between the bcc nuclei and the parent fcc phase during the solid-solid phase transformations. Thus, the reasons for the temperature fluctuation during nucleation in the liquid-vapour system may apply to the nucleation during the solid-solid phase transformation in the present study, since the fcc-to-bcc transformation is, just like the droplets formation from the vapour, a transformation in which the low-temperature phase becomes stable.

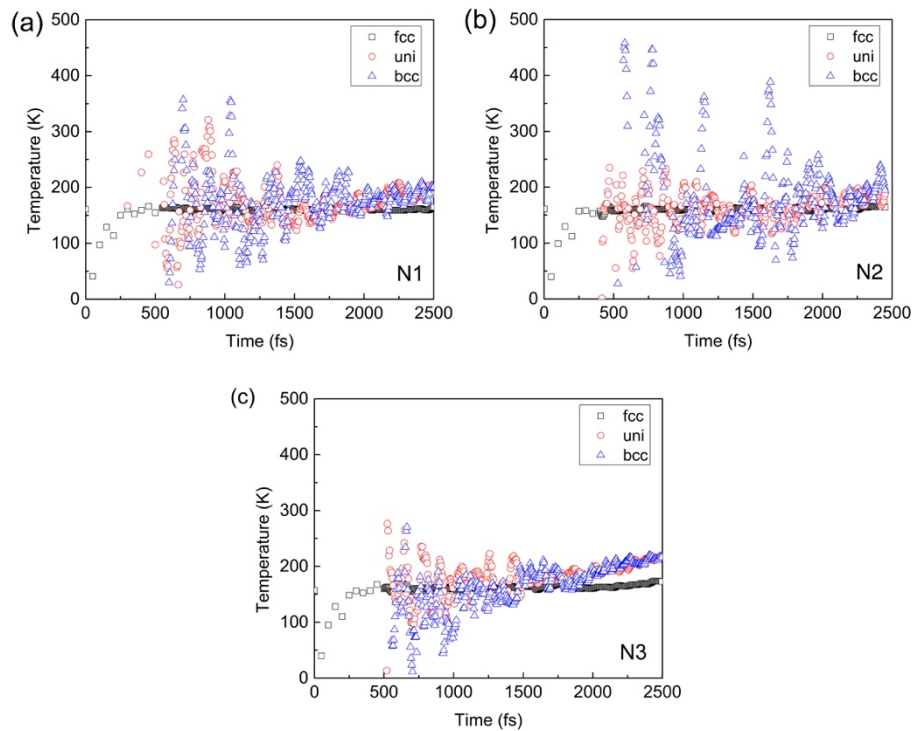


Figure 5-12 Temperature of nuclei: (a) N1, (b) N2 and (c) N3.

5.4 Conclusions

The present study pioneers in analysing the thermodynamics of the homogenous nucleation of bcc phase in fcc iron using MD simulation. Besides estimation from a postcritical bcc grain, this study also analyses the nucleus formation stage directly. The CNT is adapted for its applicability in analysing the nucleation from the atomic scale. The thermodynamic analysis of nucleation is proposed for the bcc nucleation during fcc-to-bcc transformation in iron, but can be generally applicable to nucleation processes during recrystallisation and other solid-solid phase transformations in a variety of materials. This adapted CNT turns out to roughly predict the thermodynamic tendency only during the post-nucleation period of the bcc phase in the parent phase not during the actual nucleation. The CNT predicts an energy barrier for the nucleation of bcc phase in fcc iron that is much higher than found in the present MD simulation. Nonclassical mechanisms, such as aggregation of prenucleation clusters and the formation of metastable intermediate states, help to circumvent the high energy barrier during

the nucleation event. The energy change of a nucleus in the present study conforms well to the hypothetical scheme in figure 5-1(d), when both “aggregation of nuclei” and “stepwise nucleation” take place during the nucleation event. The neighbouring clusters aggregate, also if they have different crystallographic orientations. Regardless of the constant temperature of the systems, the local temperature of the region with bcc nucleation is non-isothermal and fluctuates around the equilibrium temperature of the system.

5.5 References

- [1] S. E. Offerman, N. H. van Dijk, J. Sietsma, S. Grigull, E. M. Lauridsen, L. Margulies, H. F. Poulsen, M. Th. Rekvelde and S. van der Zwaag, 'Grain nucleation and growth during phase transformations', *Science*, 2002, 298, 1003-1005.
- [2] N. H. Van Dijk, S. E. Offerman, J. Sietsma and S. van der Zwaag, 'Barrier-free heterogeneous grain nucleation in polycrystalline materials: The austenite to ferrite phase transformation in steel', *Acta Mater.*, 2007, 55, 4489-4498.
- [3] Y. Peng, F. Wang, Z. Wang, A. M. Alsaye, Z. Zhang, A. G. Yodh and Y. Han, 'Two-step nucleation mechanism in solid-solid phase transitions', *Nat. Mater.*, 2015, 14, 101-108.
- [4] A. Gamboa, B. Farbos, P. Aurel, G. L. Vignoles and J. M. Leyssale, 'Mechanism of strength reduction along the graphenization pathway', *Sci. Adv.*, 2015, 1, e1501009.
- [5] L. Y. Yu, M. R. Niazi, G. O. Ngongang Ndjawa, R. Li, A. R. Kirmani, R. Munir, A. H. Balawi, F. Laquai and A. Amassian, 'Programmable and coherent crystallization of semiconductors', *Sci. Adv.*, 2017, 3, e1602462.
- [6] J. W. Christian, 'The theory of transformations in metals and alloys', first ed., Pergamon, Oxford, 1981.
- [7] J. Lee, J. Yang, S. G. Kwon and T. Hyeon, 'Nonclassical nucleation and growth of inorganic nanoparticles', *Nat. Rev. Mater.*, 2016, 1, 16034.
- [8] J. Park, H. Elmlund, P. Ercius, J. M. Yuk, D. T. Limmer, Q. Chen, K. Kim, S. H. Han, D. A. Weitz, A. Zettl and A. P. Alivisatos, '3D structure of individual nanocrystals in solution by electron microscopy', *Science*, 2015, 349, 290-295.
- [9] S. Y. Chung, Y. M. Kim, J. G. Kim and Y. J. Kim, 'Multiphase transformation and Ostwald's rule of stages during crystallization of a metal phosphate', *Nat. Phys.*, 2009, 5, 68-73.
- [10] H. M. Zheng, R. K. Smith, Y. Jun, C. Kisielowski, U. Dahmen and A. P. Alivisatos, 'Observation of single colloidal platinum nanocrystal growth trajectories', *Science*, 2009, 324, 1309-1312.
- [11] Z. R. Wang, F. Wang, Y. Peng, Z. Y. Zheng and Y. L. Han, 'Imaging the homogeneous nucleation during the melting of superheated colloidal crystals', *Science*, 2012, 338, 87-90.
- [12] J. J. De Yoreo, P. U. P. A. Gilbert, N. A. J. M. Sommerdijk, R. L. Penn, S. Whitlam, D. Joester, H. Z. Zhang, J. D. Rimer, A. Navrotsky, J. F. Banfield, A. F. Wallace, F. M. Michel, F. C. Meldrum, H. Cölfen and P. M. Dove, 'Crystallization by particle attachment in synthetic, biogenic, and geologic environments', *Science*, 2015, 349, aaa6760.
- [13] H. I. Aaronson, W. F. Lange III and G. R. Purdy, 'Discussion to "Grain nucleation and growth during phase transformations" by S.E. Offerman et al.', *Science*, 298, 1003 (November 1, 2002)', *Scripta Mater.*, 2004, 51, 931-935.
- [14] B. J. Wang and H. Urbassek, 'Phase transitions in an Fe system containing a bcc/fcc phase boundary: An atomistic study', *Phys. Rev. B*, 2013, 87, 104108.
- [15] Y. Peng, W. Li, F. Wang, T. Still, A. G. Yodh and Y. L. Han, 'Diffusive and martensitic nucleation kinetics in solid-solid transitions of colloidal crystals', *Nat. Comm.*, 2017, 8, 14978.
- [16] M. I. Mendeleev, S. Han, D. J. Srolovitz, G. J. Ackland, D. Y. Sun and M. Asta, 'Development of

new interatomic potentials appropriate for crystalline and liquid iron', *Phil. Mag.*, 2003, 83, 3977-3994.

[17] S. Plimpton, 'Fast parallel algorithms for short-range molecular dynamics', *J. Comp. Phys.*, 1995, 117, 1-19. <http://lammps.sandia.gov/>. Accessed on September 4th, 2017.

[18] A. Stukowski, 'Structure identification methods for atomistic simulations of crystalline materials', *Modell. Simul. Mater. Sci. Eng.*, 2012, 20, 045021.

[19] A. Stukowski, 'Visualization and analysis of atomistic simulation data with OVITO-the open visualization tool', *Modell. Simul. Mater. Sci. Eng.*, 2010, 18, 015012.

[20] A. S. J. Suiker and B. J. Thijsse, 'Nucleation, kinetics and morphology of displacive phase transformations in iron', *J. Mech. Phys. Solids*, 2013, 61, 2273-2301.

[21] A. Caro, P. E. A. Turchi, M. Caro and E. M. Lopasso, 'Thermodynamics of an empirical potential description of Fe-Cu alloys', *J. Nucl. Mater.* 2005, 336, 233-242.

[22] N. Saunders and A. P. Miodownik, 'CALPHAD (calculation of phase diagrams): a comprehensive guide', first ed., Pergamon, New York, 1998.

[23] A. Stukowski, 'Computational analysis methods in atomistic modeling of crystals', *JOM*, 2014, 66, 399-407.

[24] D. A. Porter, K. E. Easterling and M. Y. Sherif, 'Phase transformations in metals and alloys', third ed., CRC Press, UK, 2008.

[25] J. Baumgartner, A. Dey, P. H. H. Bomans, C. Le Coadou, P. Fratzl, N. A. J. M. Sommerdijk and D. Faivre, 'Nucleation and growth of magnetite from solution', *Nat. Mater.*, 2013, 12, 310-314.

[26] Z. Nishiyama, 'X-ray investigation of the mechanism of the transformation from face-centred to body-centred cubic lattice', *Sci. Rep. Tohoku Imp. Univ.*, 1934, 23, 637-664. Cited by M. G. Hall, H. I. Aaronson and K. R. Kinsman, 'The structure of nearly coherent fcc: bcc boundaries in a Cu-Cr alloy', *Surf. Sci.*, 1972, 31, 257-274.

[27] G. V. Kurdjumov and G. Sachs, 'Über den mechanismus der stahlhärtung', *Z. Phys.*, 1930, 64, 325-343. Cited by M. G. Hall, H. I. Aaronson and K. R. Kinsman, 'The structure of nearly coherent fcc: bcc boundaries in a Cu-Cr alloy', *Surf. Sci.*, 1972, 31, 257-274.

[28] I. J. Ford and C. F. Clement, 'The effects of temperature fluctuations in homogeneous nucleation theory', *J. Phys. A: Math. Gen.*, 1989, 22, 4007-4018.

[29] J. H. ter Horst, D. Bedeaux and S. Kjelstrup, 'The role of temperature in nucleation processes', *J. Chem. Phys.*, 2011, 134, 054703.

[30] J. Wedekind, D. Reguera and R. Strey, 'Influence of thermostats and carrier gas on simulations of nucleation', *J. Chem. Phys.*, 2007, 127, 064501.

Chapter 6

Heterogeneous nucleation of bcc phase at dislocations in fcc/fcc grain boundaries in iron by molecular dynamics simulations

Abstract:

Nucleation during phase transformations plays an important role in the crystal structure, the grain size and the texture of the forming product phase, and thus determines the mechanical properties of the obtained material. In the present study, molecular dynamics simulation is employed to study the heterogeneous nucleation of bcc phase in fcc iron. Two systems are included: one has a coherent twin grain boundary and a semicoherent twin boundary, the other has two low-angle grain boundaries. It is found that the bcc phase nucleates at the dislocations in the low-angle boundaries and semicoherent twin boundary in a pseudo-cylindrical morphology. The energy change as a function of the numerical values of bcc nucleus size conforms to Cahn's model with no energy barrier, and provides interface energies and elastic constants comparable to theoretical calculations and experimental data. Nevertheless, there are aspects that cannot be explained by Cahn's model: (a) the bcc nucleation at dislocations follows a stepwise "fcc→intermediate state→bcc" process rather than a single-step "fcc→bcc" phase transformation; (b) the individual bcc nucleus is an aggregate of discrete subnuclei bound by the intermediate state; (c) the temperature of local regions containing bcc nuclei is higher than the surroundings regardless of the isothermal conditions for the entire system.

* This chapter is based on a scientific paper:

X Ou, J Sietsma and M J Santofimia, Thermodynamics of heterogeneous nucleation of bcc phase at dislocations on fcc/fcc grain boundaries in Fe by molecular dynamics simulations. To be submitted.

6.1 Introduction

A few experimental works [1-7] have been dedicated to investigate the nucleation mechanisms of ferrite phase from the austenite phase in steels based on the classical nucleation theory (CNT) [8]. Also molecular dynamics (MD) simulations was applied successfully in studying nucleation processes during solid-solid phase transformations in various materials from an atomic scale [9-13]. Chapter 3 focused on the thermodynamic analysis of the homogeneous nucleation during the fcc-to-bcc transformation in Fe by MD simulation. The fitting based on the CNT gave a critical nucleus consisting of 95 ± 20 atoms with the one dimensional size about 10 \AA . However, the CNT overestimated the energy barrier for the homogeneous nucleation due to nonclassical nucleation processes such as the aggregation of neighbouring nuclei and the formation of an intermediate state between the fcc and bcc phases.

Compared with the homogeneous nucleation of a new phase forming inside the parent grain, heterogeneous nucleation at defects is more favoured in reality. Clemm and Fisher [14] suggested that the preferable sites for heterogeneous nucleation are the corners where four parent grains meet, followed by junctions where three grains meet and then the grain faces where two grains meet. Grain boundaries in the parent phase are eliminated during the nucleation of the new phase, which releases energy leading to the reduction of the energy barrier for nucleation [15]. Specifically, dislocations at grain boundaries can act as sites for nucleation of a new phase [16]. Cahn [17] proposed a theoretical model to describe the thermodynamic features for such a nucleation process at dislocations. According to Cahn's theory, the nucleus is assumed to be a cylinder lying along the core of the dislocation with circular cross-section perpendicular to the dislocation line, as indicated by the insert in figure 6-1. The free energy change ΔG due to the formation of the nucleus per unit length of l can be divided into three terms:

- (a) the strain-energy term (the distortion energy stored in the dislocations), $A \ln \left(\frac{r}{r_0} \right)$;
- (b) the volume-free energy term (the energy difference between the parent and product phase), $\pi f r^2$;
- (c) the surface free energy term (the energy required for creation of new phase interfaces), $2\pi\gamma r$.

In this term, the planar faces of the cylinder are neglected. The first two terms favour the nucleation while the last one tends to oppose it. Therefore, the free energy change ΔG of the nucleus per unit length of l is expressed as:

$$\Delta G = -A \ln \frac{r}{r_0} - \pi f r^2 + 2\pi\gamma r \quad (6-1)$$

where, for the strain energy term, A is equal to $\frac{\mu b^2}{4\pi(1-\nu)}$ for edge dislocations and $\frac{\mu b^2}{4\pi}$ for screw dislocations; μ is the elastic shear modulus, b is the length of Burgers vector and ν is the Poisson ratio.

Heterogeneous nucleation of bcc phase at dislocations in fcc/fcc grain boundaries in iron by molecular dynamics simulations

r_0 is the dislocation core radius, r is the radius of the nucleus, γ is the interface energy, and f is the volume free energy difference between the parent and product phases. When the parameter $\alpha = 2Af/\pi\gamma^2$ is less than 1, a local maximum in ΔG exists at a value of

$$r_0 = \frac{\gamma}{2f} \left(1 + \sqrt{1 - \frac{2Af}{\pi\gamma^2}} \right) \quad (6-2)$$

This corresponds to Curve A in figure 6-1. No local maximum of ΔG exists when $\alpha > 1$ (Curve B in figure 6-1).

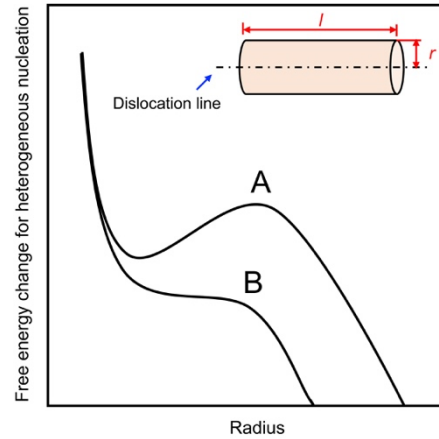


Figure 6-1 Free energy change per unit length of a cylindrical nucleus forming at a dislocation. No local maximum exists with α greater than 1 (Curve B). A similar figure can be found in Reference [17]. The insert shows the nucleus with a cylindrical morphology, r and l represent the radius and the length of the nucleus, $r \ll l$.

As one of the most important construction materials, steel is widely used in various fields of industry, such as the automotive, gas transport and power generation. Its technological importance and fundamental scientific significance induce extensive studies regarding the phase transformations in iron (or steels), such as the martensitic transformation. The present chapter employs Cahn's model in studying the thermodynamics of heterogeneous nucleation of bcc phase at dislocations on fcc/fcc grain boundaries in iron by MD simulations. Nonclassical nucleation mechanisms are also considered. This investigation contributes to the understanding of the heterogeneous nucleation nature during the solid-solid phase transformations in materials.

6.2 Methods

6.2.1 Simulation methods

In the present work, the embedded atomic method (EAM) potential by Mendelev *et al.* [18] is used, which was fitted to a wide range of defect configurations and describes ferromagnetic bcc phase as the stable phase in iron. Two simulation systems with fcc/fcc grain boundaries in pure iron are studied, as shown in figure 6-2. System A in figure 6-2(a) includes two low-angle grain boundaries (LAGB) and involves a rotation of one fcc grain from the other by about 5.7° around the $[0\ 1\ 0]_{fcc}$ direction,

leading to an array of edge dislocations with the Burgers vectors $b_{LAGB} = \frac{1}{2} \langle 101 \rangle_{fcc}$ at the grain boundaries. The lattice parameter for the fcc crystal is 3.658 Å. The simulation cell of System A has a total number of 443,520 atoms with the box size $161.52 \times 146.32 \times 230.21 \text{ \AA}^3$. System B in figure 6-2(b) includes two boundaries between two fcc twinned grains. One of the grain boundaries is a coherent twin grain boundary (CTGB) with its twin boundary parallel to the close-packed $(111)_{fcc}$ twinning plane [19]; the other is a semi-coherent twin grain boundary (STGB) involving 5.7° rotation around the $[1\bar{1}0]_{fcc}$ direction from the $(111)_{fcc}$ twinning plane. A total of 669,456 atoms are included in System B with the box dimensions as $286.75 \times 124.16 \times 230.55 \text{ \AA}^3$. Details of the dislocations, as marked by the dashed yellow rectangle in figures 6-2 (a) and (b), are shown in figures 6-2 (c) and (d), respectively.

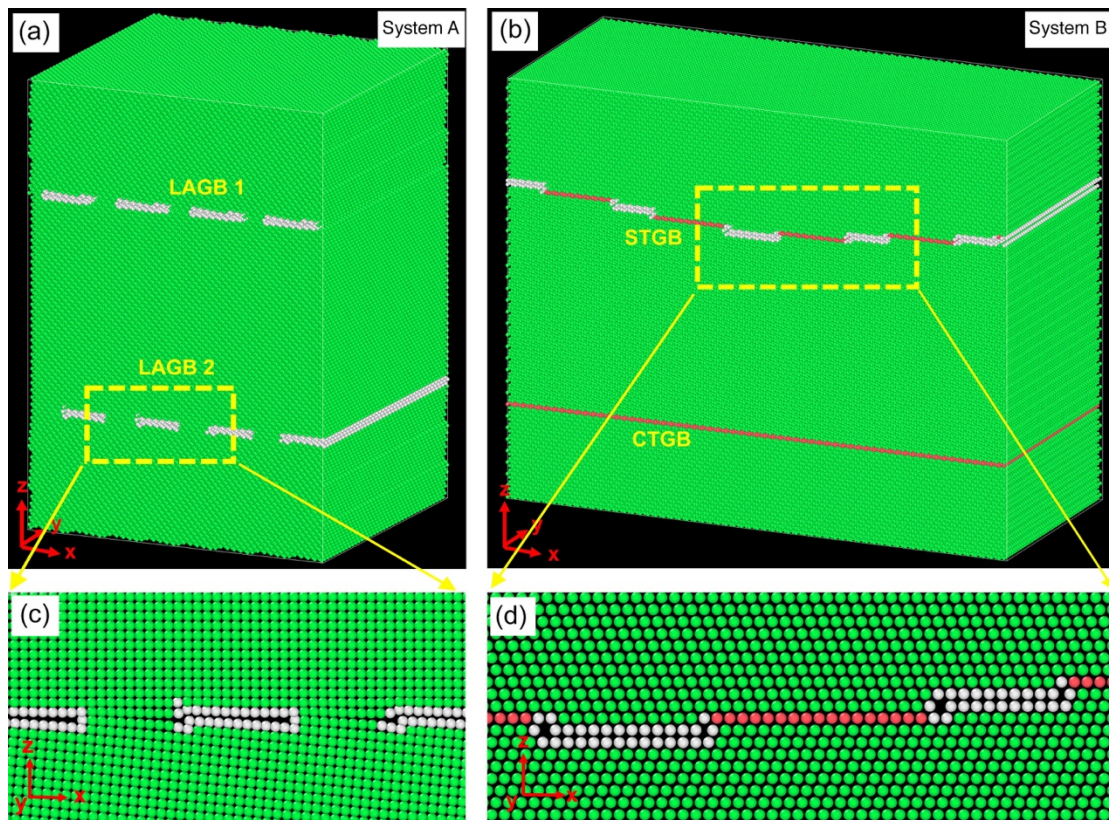


Figure 6-2 (a) Three dimensional configuration for System A, the axis x , y and z are parallel to the $[100]_{fcc}$, $[010]_{fcc}$ and $[001]_{fcc}$ directions of the fcc grain without tilt; (b) Three dimensional configuration for System B, the axis x , y and z are parallel to the $[\bar{1}\bar{1}2]_{fcc}$, $[1\bar{1}0]_{fcc}$ and $[111]_{fcc}$ directions of one twinning fcc grain. The enlarged views of the regions marked by dashed yellow rectangles in figures (a) and (b) are shown in figures (c) and (d), respectively. Colours of atoms represent different phase structures: blue-bcc; green-fcc; red-hcp; white-unidentified.

The configurations in figure 6-2 have been relaxed in the z direction by energy minimization, the dimensions in the x and y directions are fixed so that the structures of grain boundaries are maintained. The configurations are displayed using the software OVITO [20]. The adaptive common neighbor analysis (a-CNA) [21] is the discriminator to determine atoms as belonging to either the fcc, bcc or another phase. The fcc, bcc and hcp structures are coloured in green, blue and red, respectively. The

dislocation extraction algorithm (DXA) [22] is used to analyse dislocation in the simulation cells. Periodic boundary conditions are employed in x , y and z directions in the simulations, which are performed using a barostat and a thermostat of the Nosé-Hoover type (NPT ensemble) at 100 K under a constant pressure of 100,000 Pa. Each simulation involves a calculation of 20,000 steps with the time step of 0.5 fs. The present study focuses on the initial 2000 steps for System A and 3000 steps for System B. This is because the phase transformation after those steps for the two systems involves only the growth of the bcc grains and is thus out of the range of the interest in the present chapter. Simulations are performed with the open-source LAMMPS code [23].

6.2.2 Thermodynamic analysis

In the present MD simulations, the bcc phase nucleates heterogeneously at dislocations in iron. Cahn's model [17] is then employed to study the bcc nucleation at dislocations during the fcc-to-bcc transformation at the atomic scale. According to Equation (6-1), two variants, namely the energy change ΔG per unit length of l and the radius r of a nucleus, will be monitored during the nucleation period. The methods of calculating the energy change and size of a nucleus are illustrated as follows.

Calculation of the energy change and size of a nucleus is limited to a small volume with n_0 atoms in order to eliminate the influences from other nuclei. It is required that the selected volume includes only a single bcc nucleus and no neighbouring bcc nucleus grows into it during the simulation time of interest. At simulation time t , the potential energy of the volume, U_t , can be presented as a sum of the energy of the n_0 atoms:

$$U_t = \sum_{i=1}^{n_f} u_{i,t} + \sum_{j=1}^{n_m} u_{j,t} + \sum_{k=1}^{n_b} u_{k,t} \quad (6-3)$$

$$n_f + n_m + n_b = n_0 \quad (6-4)$$

in which, n_f , n_m and n_b are the number of atoms in the fcc, intermediate (including the unidentified and hcp atoms) and bcc structures, respectively, in the selected volume, with $u_{i,t}$, $u_{j,t}$ and $u_{k,t}$ the corresponding potential energies. Then the potential energy change ΔU_t of the selected volume at the simulation time t due to the nucleation process is defined as:

$$\Delta U_t = \sum_{j=1}^{n_m} u_{j,t} + \sum_{k=1}^{n_b} u_{k,t} - \sum_{i=1}^{n_f} u_{i,t} \times \left(\frac{n_m + n_b}{n_f} \right) \quad (6-5)$$

The third term accounts for the potential energy of the $(n_m + n_b)$ atoms if they would still be in the parent fcc phase. Both the atoms in the intermediate state and the atoms in the bcc structure contribute to the energy change of the nucleus during the nucleation process.

Under the conditions of fixed temperature T (100 K) and pressure P (100,000 Pa), the Gibbs free energy change during the fcc-to-bcc transformation $\Delta G_{fcc-bcc}$ consists of three parts [24]:

$$\Delta G_{fcc-bcc} = \Delta U_{fcc-bcc} + P\Delta V_{fcc-bcc} - T\Delta S_{fcc-bcc} \quad (6-6)$$

where $\Delta U_{fcc-bcc}$ is the potential energy difference between the bcc and fcc phase; $\Delta V_{fcc-bcc}$ is the change of volume due to the fcc-to-bcc transformation; $\Delta S_{fcc-bcc}$ is the entropy difference between the bcc and fcc phase. The potential energy difference $\Delta U_{fcc-bcc}$ calculated from the Mendeleev potential [18] is $10.23 \text{ meV}/\text{\AA}^3$ at 100 K. Compared with the contribution of $\Delta U_{fcc-bcc}$ to the Gibbs free energy change $\Delta G_{fcc-bcc}$, the value of $P\Delta V_{fcc-bcc}$ is five orders of magnitudes smaller, being $3.75 \times 10^{-5} \text{ meV}/\text{\AA}^3$ at 100 K. Moreover, Caro *et al.* [25] calculated the enthalpies and entropies of bcc and fcc iron using the so-called CALPHAD (Computer Coupling of Phase Diagrams and Thermochemistry) approach [26]. According to their results [25], the entropy difference $\Delta S_{fcc-bcc}$ between the bcc and fcc iron at temperatures below 200 K is as small as about $5 \text{ J}/(\text{K}\cdot\text{mol})$, while the enthalpy difference $\Delta H_{fcc-bcc} = \Delta U_{fcc-bcc} + P\Delta V_{fcc-bcc}$ between the bcc and fcc iron is on the order of 10^4 J/mol . This indicates that the contribution of the entropy difference $T\Delta S_{fcc-bcc}$ to the Gibbs energy difference $\Delta G_{fcc-bcc}$ is negligible compared with that of the enthalpy difference $\Delta H_{fcc-bcc}$ during the fcc-to-bcc transformation at temperatures below 200 K. Thus the contribution of the $P\Delta V_{fcc-bcc}$ and $T\Delta S_{fcc-bcc}$ terms to $\Delta G_{fcc-bcc}$ can be neglected and $\Delta G_{fcc-bcc}$ is taken to be equal to $\Delta U_{fcc-bcc}$. These calculations show that it is a good approach to use the potential energy change ΔU per unit length of l to represent the Gibbs free energy change ΔG during the bcc nucleation process. Thus Equation (6-1) can be expressed as:

$$\Delta U = -A \ln \frac{r}{r_0} - \pi \Delta u_V r^2 + 2\pi\gamma r \quad (6-7)$$

in which $\Delta U = \frac{\Delta U_t}{l}$, l represents the length of the nucleus along the dislocation line. In the present study, l is seen to be equal to the length of the box in the y direction l_t for each individual system at the simulation time t . Δu_V is the potential energy difference per unit volume between the parent fcc phase and the product bcc phase, which is $10.23 \text{ meV}/\text{\AA}^3$ at 100 K calculated from the Mendeleev potential [18].

At the simulation time t , the nucleus includes n_b atoms in the bcc structure. Thus the volume of the nucleus is given by:

$$V = V_a n_b \quad (6-8)$$

in which V_a (11.6478 \AA^3 per atom) is the atomic volume of bcc phase at 100 K. Regardless of the morphologies of the nucleus, the effective radius r of the cross-section perpendicular to the dislocation line, as shown by the insert in figure 6-1, can be calculated by:

$$r = \left(\frac{V_a n_b}{l\pi} \right)^{\frac{1}{2}} \quad (6-9)$$

By fitting the energy change ΔU due to nucleation with the nucleus radius r according to Equation (6-7), the values of parameter A , r_0 and the interface energy γ can be obtained from the fitting curve for individual nucleus. The parameter α can be calculated from $\alpha = 2A\Delta u_V/\pi\gamma^2$. This determines whether there is an energy barrier for the nucleation of bcc phase at dislocations.

The temperature of a group of atoms is calculated according to:

$$T = \frac{2E_k}{3k_B N} \quad (6-10)$$

in which T represents the temperature; E_k is the total kinetic energy of the group of atoms; k_B is the Boltzmann constant and N is the number of atoms in the group.

6.3 Results and discussion

6.3.1 Nucleation of bcc phase at dislocations

Figure 6-3 shows the configurations of the bcc nuclei during nucleation at dislocations on the LAGB at different simulation times. It is seen that the edge dislocations, as indicated by the unidentified atoms in figure 6-3(a), appear periodically at the fcc/fcc grain boundaries and act as nucleation sites for the heterogeneous nucleation of the bcc phase. The enlarged views of the regions inside the dashed red rectangle, as shown by the inserts in figure 6-3(a), show the details of the nucleation process. Figure 6-3(b) shows all atoms that are not in the fcc structure. An individual bcc nucleus forms at the core of each dislocation extending along the dislocation line. These nuclei contact each other with the subsequent growth into the fcc parent grains after 500 fs. It is noted that already after 250 fs some of the atoms that initially were in an unidentified structure due to the dislocation (white atoms in figure 6-3(b) at 0 fs) have been relaxed to the fcc structure.

Figure 6-4 shows the configurations of the bcc nucleation at the STGB in System B at different simulation times. The enlarged view of the area marked by the dashed red rectangle is included in the inserts in figure 6-4(a). No phase transformation takes place at the CTGB, which is a stacking fault on the $\{1\ 1\ 1\}_{fcc}$ plane and exhibits an hcp structure at the corresponding grain boundary. The STGB is 5.7° rotated from the $(1\ 1\ 1)_{fcc}$ plane, leading to the alternating appearance of coherent (hcp structure) and incoherent (unidentified structure) regions at the grain boundary. The nucleation of bcc phase initiates from the incoherent part along the dislocation line at the STGB, as seen in figure 6-4(b). The bcc nuclei are therefore separated from each other by the coherent parts. Every single bcc nucleus is exempted from the influence of its neighbouring nucleus during the range of time considered in the present study. The neighbouring bcc nuclei begin to overlap after 1500 fs. The bcc nuclei grow in multiple directions by consuming the two fcc parent grains as well as hcp stacking faults at the STGB grain boundary.

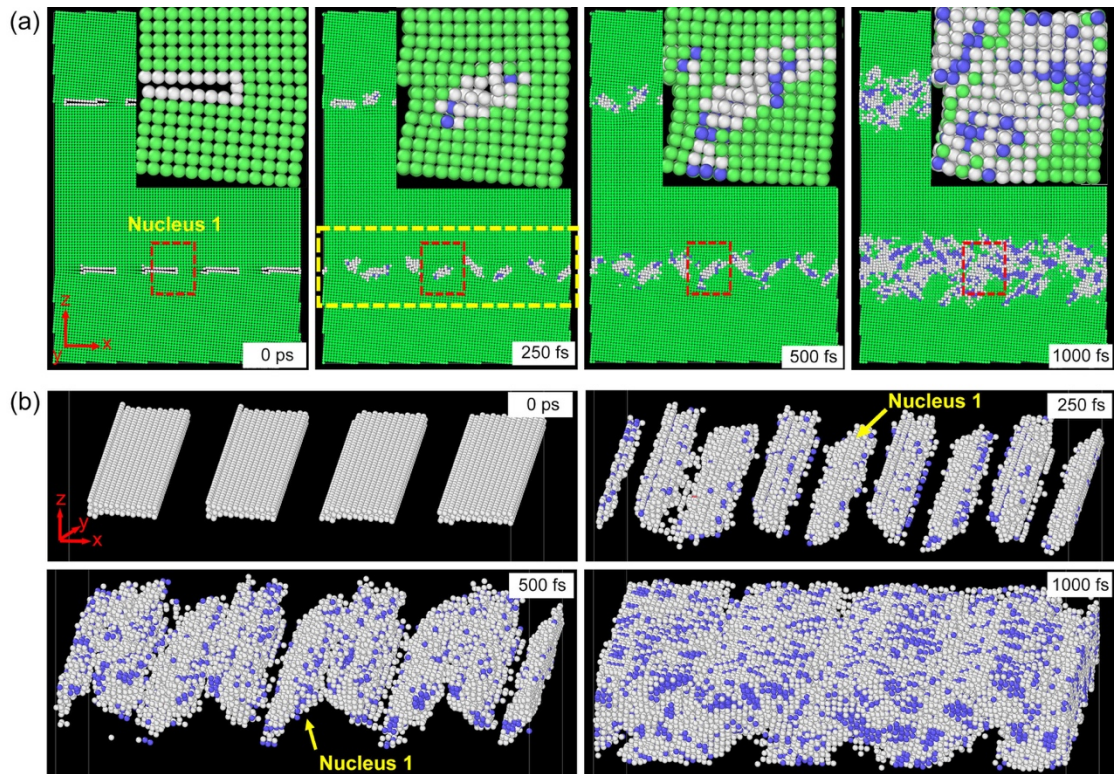


Figure 6-3 (a) Time evolution of the bcc nucleation at the edge dislocations at the LAGB at 0 fs, 250 fs, 500 fs and 1000 fs; (b) Time evolution of the bcc nucleation at the LAGB 2, as marked by the yellow dashed rectangle in figure (a), the fcc phase is excluded. Enlarged views of the regions marked by the dashed red rectangle are inserted in figure (a). Colours of atoms represent different phase structures: blue-bcc; green-fcc; red-hcp; white-unidentified.

Figures 6-5 (a) and (b) show the time evolution of the dislocations at the LAGB and STGB, respectively. From figure 6-5(a), the dislocations present at the LAGB mainly have the Burgers vector $\frac{1}{2} \langle 110 \rangle_{fcc}$, the dislocation lines of which are nearly parallel to the y axis before 200 fs. After that, the parallel dislocation lines are interrupted due to the nucleation of bcc phase at the LAGB. The dislocation lines become discontinuous with the growth of bcc nuclei and disappear after around 600 fs. At the STGB in figure 6-5(b), however, there are mainly Shockley dislocations with the Burgers vector $\frac{1}{6} \langle 112 \rangle_{fcc}$. Rather than straight lines, the dislocation lines at the STGB are curved and intersect with each other at multiple locations. Similar to the behaviour at the LAGB, the dislocations also diminish as the nucleation and growth of bcc phase at the STGB. Nearly no dislocations are detected after 1000 fs.

Heterogeneous nucleation of bcc phase at dislocations in fcc/fcc grain boundaries in iron by molecular dynamics simulations

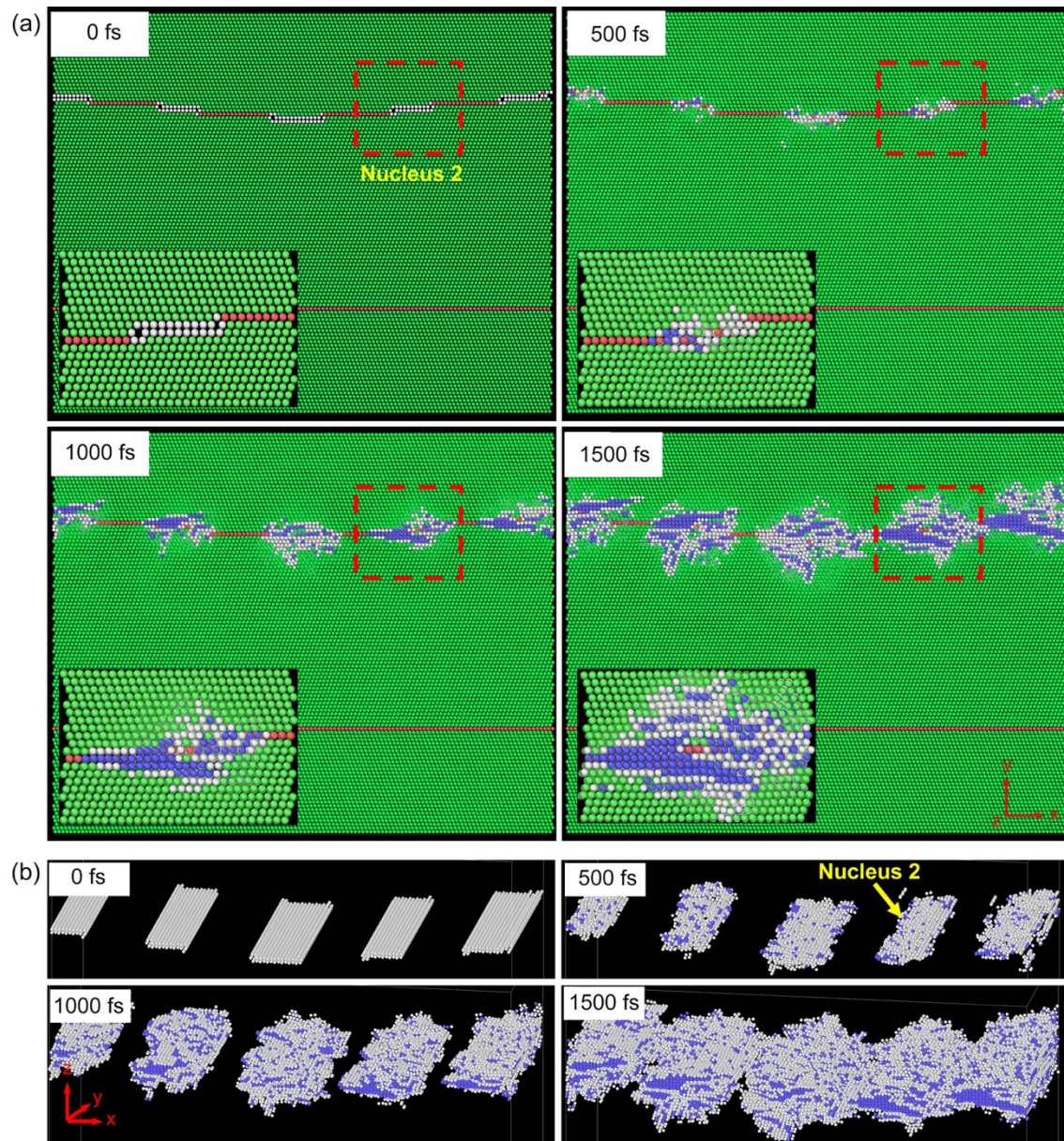


Figure 6-4 (a) Time evolution of the bcc nucleation at the edge dislocations at the STGB at different simulation times; (b) Time evolution of the bcc nucleation at the STGB, the fcc structure is excluded. The inserts in figure (a) are the enlarged views of the corresponding areas marked by the dashed red rectangles. Colours of atoms represent different phase structures: blue-bcc; green-fcc; red-hcp; white-unidentified.

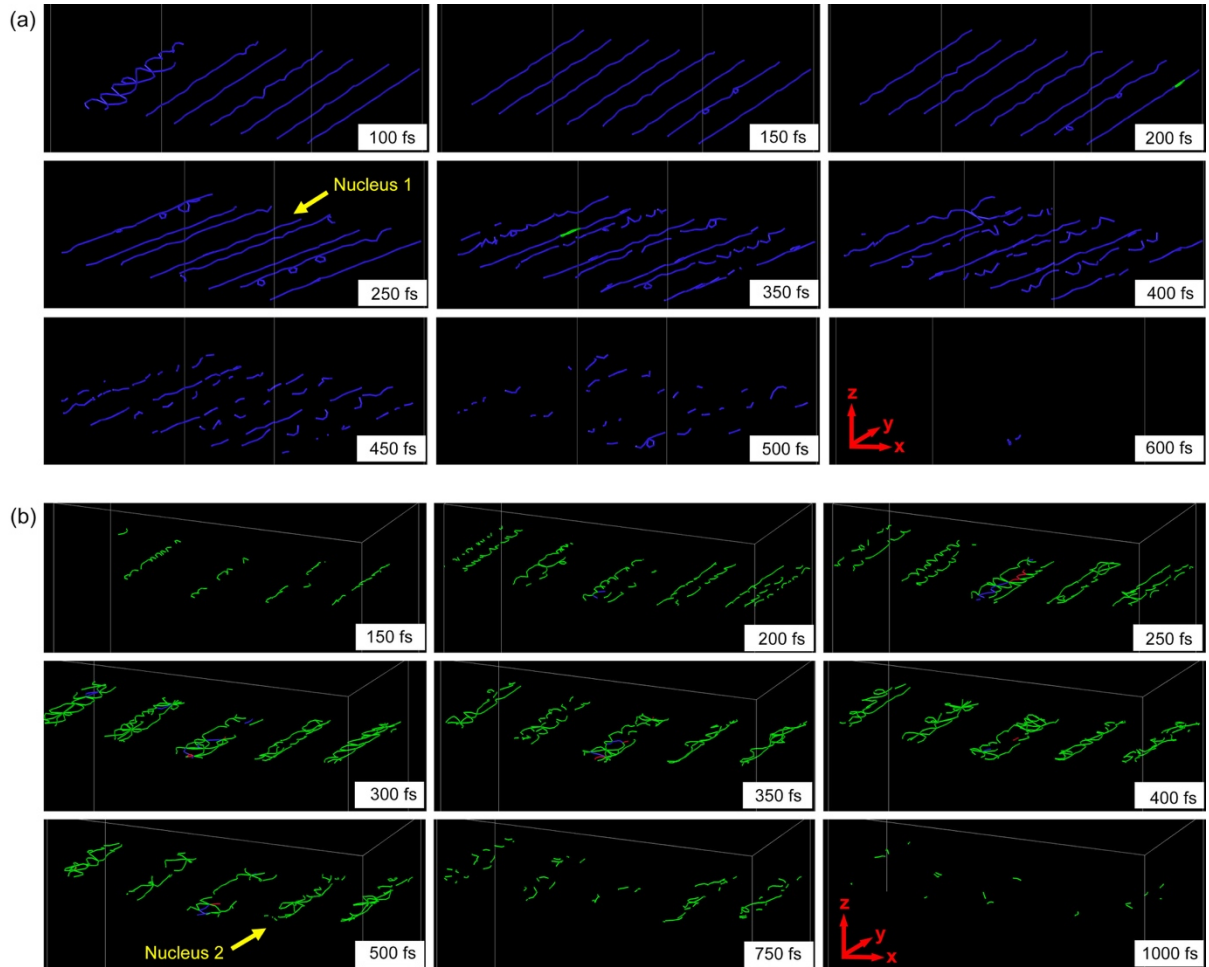


Figure 6-5 Time evolution of the dislocation lines at: (a) LAGB 2, (b) STGB, respectively. Colours of the dislocation lines represent different dislocation types: blue - $\frac{1}{2} \langle 110 \rangle$; green - $\frac{1}{6} \langle 112 \rangle$; red - other.

6.3.2 Applicability of Cahn's nucleation theory

Two bcc nuclei, namely Nucleus 1 and Nucleus 2, are included in the selected volumes marked by the dashed red rectangle in figure 6-3 and figure 6-4, respectively. The number of atoms in the selected volumes is indicated in Table 6-1. Figures 6-6 (a) and (b) show the relationship between the energy change ΔU and the effective radius r of Nucleus 1 and 2, respectively. The red curves are fitted to the thermodynamic data of Nucleus 1 and 2 according to Cahn's model in Equation (6-7), with the values of the fitting parameters listed in Table 6-1. It is seen that the energy change as a function of the radius for both nuclei agrees well with Cahn's model, which corresponds to a shape as described as "B" in figure 6-1. The parameters $\alpha = 2A\Delta u_V/\pi\gamma^2$ for both Nucleus 1 and Nucleus 2 are greater than 1, which means that no activation energy is involved in the bcc nucleation at the edge dislocations on the LAGB or at the dislocation on the STGB. In such cases, the sum of the removed strain energy and the volume energy change due to the formation of the bcc nucleus is larger than the surface energy [17]. Similar results are obtained for a second nucleus, Nucleus 1' on LAGB and Nucleus 2' on STGB, in each system, as indicated by the fitting parameters in Table 6-1.

Heterogeneous nucleation of bcc phase at dislocations in fcc/fcc grain boundaries in iron by molecular dynamics simulations

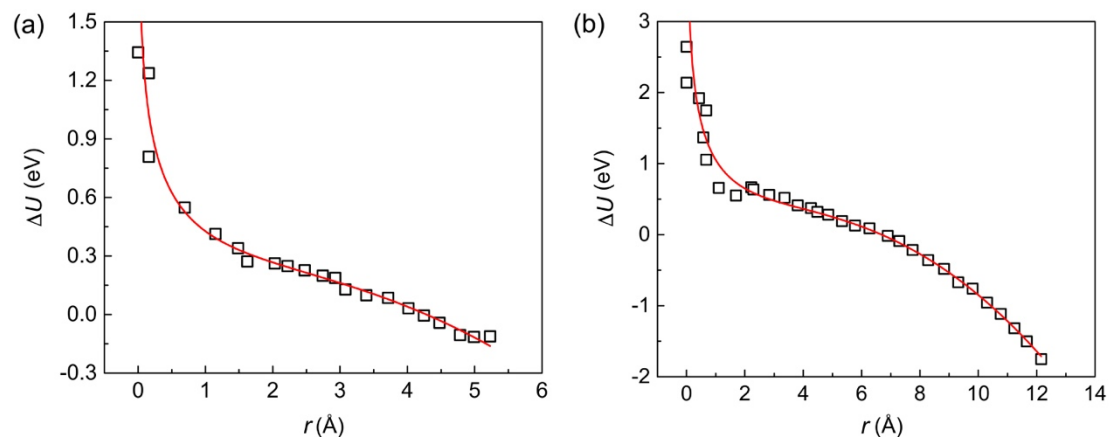


Figure 6-6 The relation between the energy change ΔU per unit length along the core of the dislocation and radius r of the nuclei: (a) Nucleus 1 and (b) Nucleus 2. The black dots are the MD data. The energy change ΔU is contributed by the bcc and unidentified structures. The red curves are fitted according to Equation (6-7).

According to Equation (6-7), the coefficient A is equal to $\frac{\mu b^2}{4\pi(1-\nu)}$ for edge dislocations. The elastic shear modulus μ and Poisson's ratio ν for cubic structures are related to the elastic constants C_{ij} through the following equations [27]:

$$\mu = \frac{C_{11} - C_{12} + 3C_{44}}{5} \quad (6-10)$$

$$\nu = \frac{C_{11} + 4C_{12} - 2C_{44}}{2(2C_{11} + 3C_{12} + C_{44})} \quad (6-11)$$

For the fcc Fe crystal, the elastic constants C_{ij} at different temperatures from either theoretical calculations or experiments [18,28-32] are included in Table 6-2. By substituting the elastic constants into Equation (6-10) and (6-11), the corresponding shear modulus μ , Poisson's ratio ν and thus the coefficient A are calculated and included in Table 6-2. It is seen that the shear modulus μ is between 11.4 GPa and 89.2 GPa with the Poisson's ratio ν between 0.2729 and 0.3920 calculated from the elastic constants in references [18, 28-32]. Therefore, the coefficient A calculated from the corresponding μ and ν ranges between 1×10^{-10} J/m and 7×10^{-10} J/m, which is comparable to the fitted coefficient ($A = 7 \times 10^{-10}$ J/m) for Nucleus 1 in Table 6-1. The fitted coefficient A for Nucleus 2 is larger than that for Nucleus 1 and equals to 16×10^{-10} J/m. This may result from the complex dislocations existing at the STGB, as seen from figure 6-5(b).

Experimental data proposes approximately 800 mJ/m^2 for the bcc/fcc interface energy, which is an average of the values obtained for the existing incoherent, semicoherent and coherent interfaces in materials [33]. Peng *et al.* [4] reported that the interface energy in metals and alloys for incoherent interfaces ranges from 500 to 1000 mJ/m^2 , for the semi-coherent interfaces from 200 to 500 mJ/m^2 and for coherent interfaces below 200 mJ/m^2 . Based on the models by MD simulations in [34], the authors calculate the interface energies to be 530 mJ/m^2 and 686 mJ/m^2 for the semi-coherent bcc/fcc interfaces in the Nishiyama-Wassermann (NW) [35] and Kurdjumov-Sachs (KS) [36] orientation relationship (OR), respectively. Thus, from Table 6-1, the interface energy $\gamma = 567 \text{ mJ/m}^2$ for Nucleus 1 may

indicate a semicoherent interface, while a value as high as 1031 mJ/m² possibly indicates an incoherent bcc/fcc interface for Nucleus 2.

Table 6-1 The fitting parameters Nucleus 1 and Nucleus 2 in figure 6-6 according to Equation (6-7).

Nucleus	n_0	A (10^{-10} J/m)	Δu_V (meV/Å ³)	γ (mJ/m ²)	r_0 (Å)	α
1	7,000	7	10.23	567	1.8	2.1
1'	7,600	8	10.23	663	1.6	2.0
2	26,928	16	10.23	1031	1.9	1.6
2'	28,171	16	10.23	941	3.1	1.9

Besides, the fitting dislocation core radius r_0 is in the range of 1.6 to 3.1 Å, as indicated in Table 6-1. The smallest radius of the dislocation core r_0 can be approximately equal to the length of a Burgers vector [37]. For the lattice parameter $a_{fcc} = 3.658$ Å, the shortest length of Burgers vector $b = \frac{1}{2} \langle 110 \rangle_{fcc}$ is 2.6 Å, which is comparable with the fitting values of r_0 for Nucleus 1 and Nucleus 2 in Table 1.

Table 6-2 The elastic constants, shear modulus and Poisson's ratio for fcc Fe from References [18,28-32]. The G , ν and parameter A are calculated and included. By assuming the lattice parameter $a = 3.658$ Å, the square of the Burgers vector $b^2 = 6.6905$ Å².

Reference	T (K)	C_{11} (GPa)	C_{12} (GPa)	C_{44} (GPa)	μ (GPa)	ν	A (10^{-10} J/m)
[18,28]	0	67	40	10	11.4	0.3920	1
[32]	298	230	135	117	89.2	0.2729	7
[29]	1428	154	122	77	52.6	0.3249	4
[30]	1428	154	143.9	78.4	49.1	0.3501	4
[31]	1428	181	156	83.3	55.0	0.3495	5

6.3.3 Deviations from Cahn's nucleation theory

Regardless of the applicability, simulations have shown phenomena that are not considered in Cahn's model. In the following section, three of these will be explained in detail: (a) the parent fcc phase transforms to the bcc phase following a stepwise nucleation process; (b) discrete subnuclei aggregate to form a single nucleus with the intermediate state as the binding medium; (c) the local regions containing the bcc nuclei are non-isothermal and warmer than their surroundings.

6.3.3.1 Stepwise nucleation

It is seen from figure 6-3 and figure 6-4 that the bcc nuclei are composed of a core bcc structure surrounded by a number of unidentified atoms. As it will be shown in this section, part of the

Heterogeneous nucleation of bcc phase at dislocations in fcc/fcc grain boundaries in iron by molecular dynamics simulations

unidentified atoms represent the dislocations at the grain boundaries and part of them act as the interfaces dividing the fcc and bcc structures. Such interfaces consist of a broad range rather than a monolayer of atoms between the parent fcc and product bcc lattices. The rest unidentified atoms may act as an intermediate separating bcc clusters and bind the discrete bcc clusters to form a single nucleus, similar to the observations in previous chapter 5. Due to the complexity, it is difficult to distinguish the interfacial atoms from those acting as an intermediate state or dislocations. Figures 6-7 (a) and (b) show the time evolution of the number of atoms with different structures for Nucleus 1 and 2. The number of atoms in the bcc structure and intermediate state shows an overall increasing trend with time, which indicates that the fcc phase may transform partly to the bcc phase and partly to the intermediate state. Furthermore, the number of atoms in the unidentified structure amounts more than that in the bcc structure during the nucleation process.

From figures 6-7 (c) and (d), it is seen that the energy ΔU of individual nucleus mainly results from the unidentified atoms with minor effects from the atoms in the bcc structure, especially in the initial nucleation stage. The energy change of the unidentified atoms shows a continuously decreasing trend with time, while that of the bcc structure exhibits an energy barrier during the nucleation process, as seen from the inserts in figures 6-7 (c) and (d). According to the previous study in Chapter 5, the homogeneous nucleation of bcc phase in fcc iron prefers to follow the stepwise “fcc→intermediate→bcc” process rather than the traditionally accepted one-step “fcc→bcc” process, which helps to avoid the high energy barrier for homogeneous nucleation. Similarly, in the present study the fcc phase transforms firstly to an intermediate state (the unidentified atoms), the nucleation of which initiates from the dislocations and follows Cahn’s model. No barriers exist for the nucleation of the intermediate state. However, it should be noted that all unidentified atoms are taken as the intermediate state in the present study due to the difficulty in distinguishing between atoms belonging to dislocations, intermediate state and fcc/bcc interfaces. Then the bcc phase nucleates either from the forming intermediate state or from the fcc phase. An energy barrier exists for the stabilisation of each bcc nucleus, as can be seen from the peak values of the energy change in the inserts in figures 6-7 (c) and (d), respectively. The approximate values for the activation energy are 0.04 eV/Å and 0.13 eV/Å for Nucleus 1 and Nucleus 2, respectively.

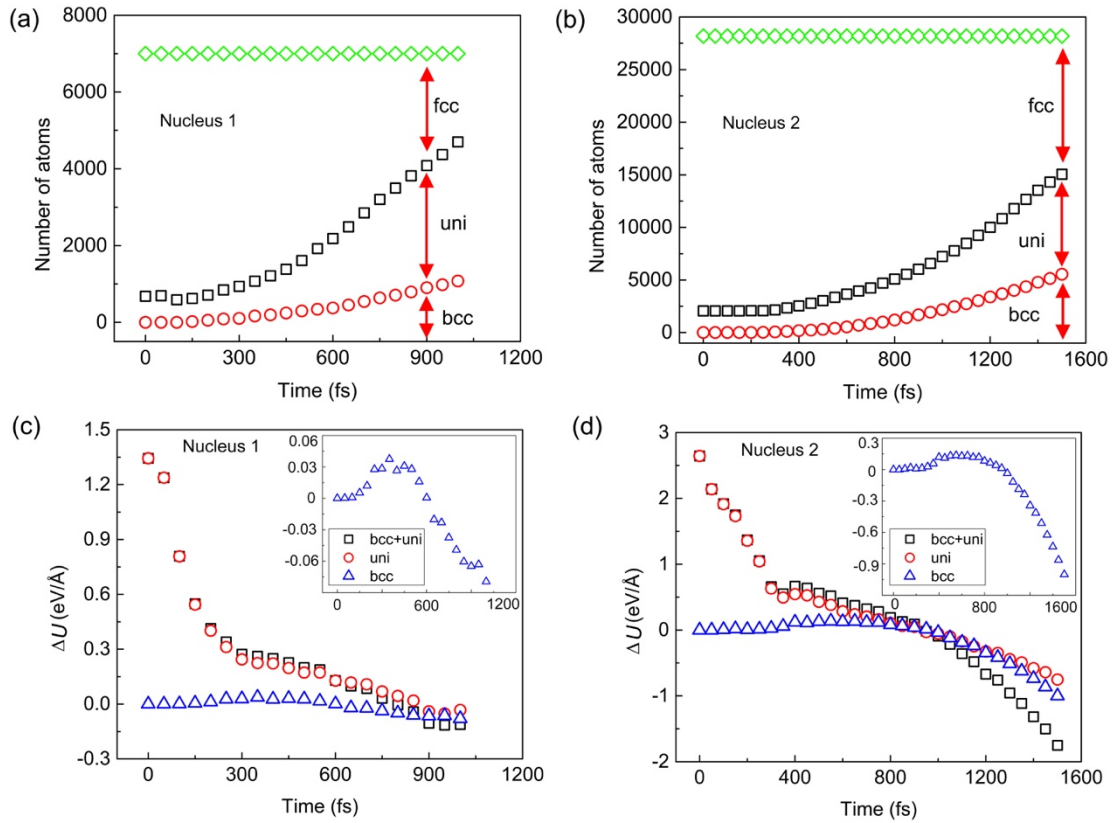


Figure 6-7 (a) (b) Time evolution of the number of atoms with different structures in the selected volume for Nucleus 1 and Nucleus 2, respectively; (c) (d) Contribution of the bcc (triangles) and unidentified atoms (circles) to the energy ΔU (squares) of the bcc Nucleus 1 and Nucleus 2, respectively. The inserts in figures (c) and (d) shows the enlarged view for the energy change of the bcc atoms during nucleation.

6.3.3.2 Aggregation of bcc nuclei

Figure 6-8(a) shows snapshots of the bcc Nucleus 1 along the dislocation line on LAGB at 500 fs. All atoms are included in the small volume analysed for Nucleus 1. The core bcc phase is mainly surrounded by the intermediate state (the unidentified atoms). By removing the intermediate state, as shown in figure 6-8(b), the core bcc phase is found to consist of multiple discrete subnuclei in the bcc structure, which align along the dislocation line. It is the intermediate state that binds the bcc subnuclei as a continuous integral nucleus. From figure 6-8(b), the bcc subnuclei can be divided into two groups with different ORs, with the upper one aligning in one OR and the lower group in another. A slice parallel to the $(\bar{1} 1 0)_{fcc}$ plane, as marked by the dashed yellow rectangle in figures 6-8 (a) and (b), is selected across Nucleus 1. Configurations in figure 6-8(c) present the atomic arrangements on the slice with the view direction perpendicular to the $(\bar{1} 1 0)_{fcc}$ plane at 500 fs and 1000 fs, respectively. The bcc subnuclei locating on the two sides of the dislocation (yellow marks) evolve in two different ORs. The upper group of the subnuclei is in the NW OR while the lower one is in the KS OR with the parent fcc phase, as illustrated by figure 6-8(c) at 1000 fs.

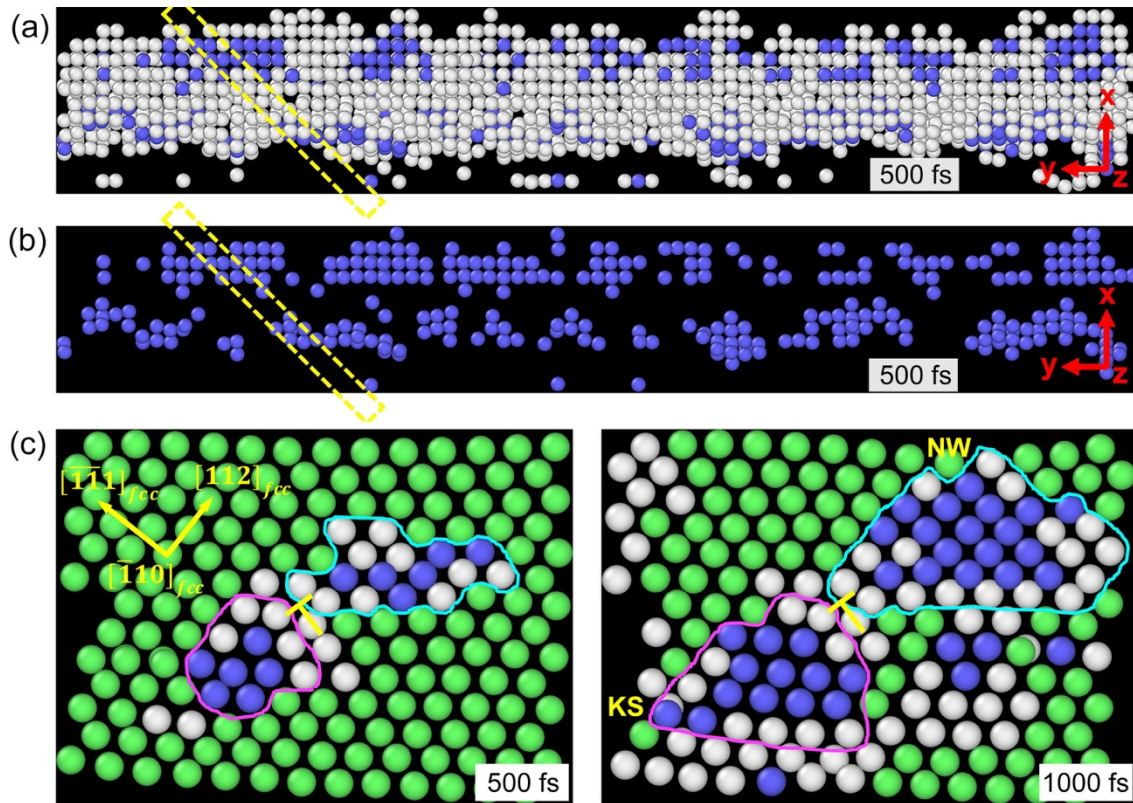


Figure 6-8 (a) Snapshot of the volume containing Nucleus 1 at 500 fs, the fcc atoms are excluded; (b) The same snapshot as in figure (a) but without the unidentified atoms; (c) The slice (2.8 Å in thickness) selected on the $(111)_{fcc}$ plane of Nucleus 1 at 500 fs and 1000 fs, respectively. The position of the slice in figure (c) is marked by the dashed yellow rectangle in figures (a) and (b), the view direction is parallel to $[\bar{1}10]_{fcc}$. Colours of atoms represent different phase structures: blue-bcc; green-fcc; white-unidentified.

Similar results are observed for Nucleus 2 forming at the dislocation on STGB, as indicated in figures 6-9 (a)-(c). The nucleus consists of discrete bcc subnuclei, which are bond by the intermediate structure. Considering the complexity of the dislocations on the rotated twin boundary, those bcc subnuclei forming around the dislocation core have different ORs, as shown by the slice at 1500 fs in figure 6-9(c). A bcc cluster in the KS OR is neighboured by two bcc clusters in the NW OR.

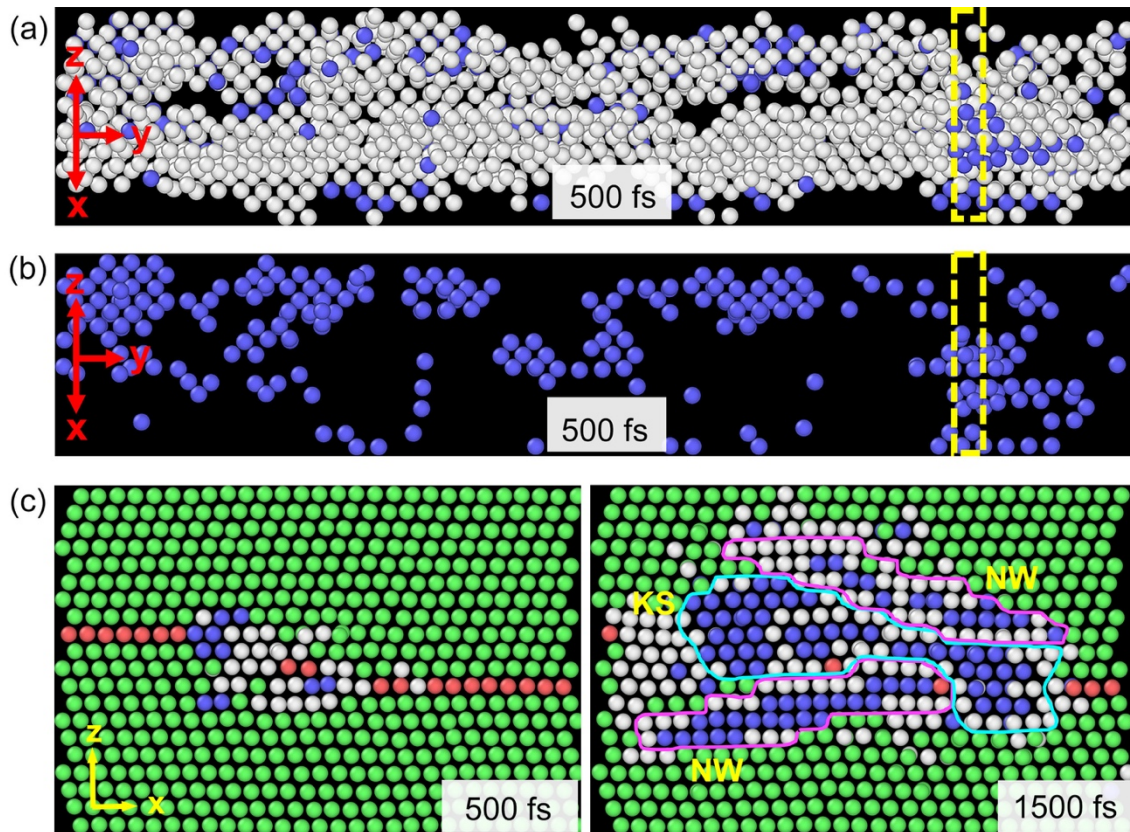


Figure 6-9 (a) Snapshot of the volume containing Nucleus 2 at 500 fs, the fcc atoms are excluded; (b) The same snapshot as in figure (a) but without the unidentified atoms; (c) The slice (2.8 Å in thickness) selected on the $(1 \bar{1} 0)_{fcc}$ plane of Nucleus 2 at 500 fs and 1500 fs, respectively. The position of the slice in figure (c) is marked by the dashed yellow rectangle in figures (a) and (b). Colours of atoms represent different phase structures: blue-bcc; green-fcc; red-hcp; white-unidentified.

6.3.3.3 Temperature of bcc nuclei

Regardless of the isothermal conditions for the systems, the local temperature of the selected volume containing Nucleus 1 and Nucleus 2 increases to values higher than 100 K during the bcc nucleation at the dislocations on the LAGB and STGB, as indicated in figures 6-10 (a) and (b), respectively. The temperature of the bcc phase and the intermediate state first increases up to a value higher than 500 K, which then decreases to around 150 K. It is noted that the surrounding fcc parent phase also has a temperature higher than 100 K during the nucleation stage. The bcc nucleation inside the fcc phase evolves in the stepwise “fcc→intermediate state→bcc” transformations, which is accompanied by a heat release process. The heat induced by the fcc-to-bcc transformation due to nucleation cannot be conducted out of the simulation cell efficiently during the short MD simulation time. The released heat thus increases the temperature of the related atoms. By molecular dynamics simulation of nucleation in the liquid-vapour system, Wedekind *et al.* [38] found that the subcritically sized nucleus clusters are colder while postcritically sized clusters are warmer than the bath temperature. Besides, the experimental results by Ford and Clement [39] indicate that the temperature of a droplet nucleus was bound to fluctuate due to both the release of heat upon absorption of further molecules, and the

Heterogeneous nucleation of bcc phase at dislocations in fcc/fcc grain boundaries in iron by molecular dynamics simulations

collisions with the surrounding gas molecules. Those studies [38,39] were based on the nucleation of liquid droplets from the vapour. Nevertheless, similar results are found in the present studies about the temperature differences between the bcc nuclei and the parent fcc phase during the solid-solid phase transformations. Thus, the reasons for the temperature fluctuation during nucleation in the liquid-vapour system may apply to the nucleation during the solid-solid phase transformation in the present study, since the fcc-to-bcc transformation is, just like the droplets formation from the vapour, a transformation in which the low-temperature phase becomes stable.

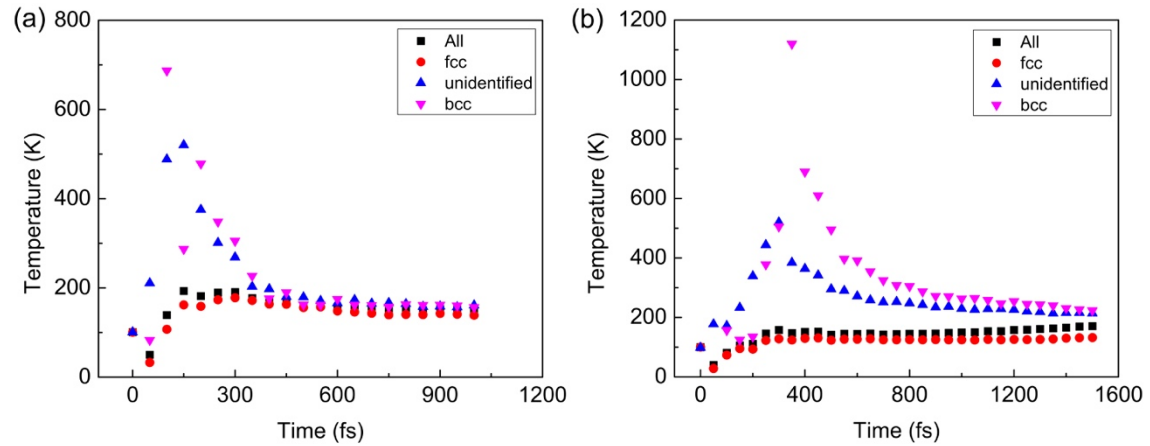


Figure 6-10 (a) Temperature of different structures in the selected volume for Nucleus 1; (b) Temperature of different structures in the selected volume for Nucleus 2.

6.4 Conclusions

The present study pioneers the thermodynamic analysis of heterogeneous nucleation of one phase during solid-solid phase transformation in materials by MD simulations. Two fcc/fcc grain boundaries are studied: one is a low-angle grain boundary with the other, having a semicoherent structure. Heterogeneous nucleation of the bcc phase occurs at the dislocations on the two fcc/fcc grain boundaries. The energy change of the nucleus including both the bcc and unidentified structures as a function of the nucleus size agrees with Cahn's model, where no energy barrier is involved. The estimated elastic constants and interface energies are comparable to the published theoretical values and experimental results.

However, there are aspects observed in the simulations that are not considered by Cahn's model. The fcc phase transforms to the bcc phase preferably following a stepwise "fcc→intermediate state→bcc" rather than a single-step "fcc→bcc" process. The intermediate state initiates from the dislocations without energy barrier. This is followed/accompanied by the nucleation of bcc phase from the intermediate state or from the fcc phase, where an energy barrier for nucleation is involved. The bcc nuclei are aggregates of discrete subnuclei, which are bond to an integral nucleus by the intermediate state. Such neighbouring subnuclei may have different crystallographic orientations. Regardless of isothermal conditions, the local regions containing the bcc nuclei are warmer than the surroundings due to the heat release during the phase transformation.

The proposed method in the analysis of the thermodynamics of nucleation is applied to pure iron in the present work, but it is universal and can be extended to other metals or alloys. The findings in the present study should contribute to a better understanding of nucleation mechanisms during isothermal heat treatments, which further facilitates the control of microstructures and thus enhance the mechanical properties of materials in industry.

6.5 References

- [1] L. Zhang, W. Q. Ren, A. Samanta and Q. Du, 'Recent developments in computational modelling of nucleation in phase transformations', *npj Comput. Mater.*, 2016, 2, 16003.
- [2] S. E. Offerman, N. H. van Dijk, J. Sietsma, S. Grigull, E. M. Lauridsen, L. Margulies, H. F. Poulsen, M. Th. Rekveldt and S. van der Zwaag, 'Grain nucleation and growth during phase transformations', *Science*, 2002, 298, 1003-1005.
- [3] N. H. Van Dijk, S. E. Offerman, J. Sietsma and S. Van der Zwaag, 'Barrier-free heterogeneous grain nucleation in polycrystalline materials: The austenite to ferrite phase transformation in steel', *Acta Mater.*, 2007, 55, 4489-4498.
- [4] Y. Peng, W. Feng, Z. R. Wang, A. M. Alsayed, Z. X. Zhang, A. G. Yodh and Y. L. Han, 'Two-step nucleation mechanism in solid-solid phase transitions', *Nat. Mater.*, 2015, 14, 101-108.
- [5] H. I. Aaronson, W. F. Lange III and G. R. Purdy, 'Discussion to "Grain nucleation and growth during phase transformations" by S.E. Offerman et al.', *Science*, 298, 1003 (November 1, 2002)', *Scripta Mater.*, 2004, 51, 931-935.
- [6] W. F. Lange III, M. E. Enomoto and H. I. Aaronson, 'The kinetics of ferrite nucleation at austenite grain boundaries in Fe-C alloys', *Metall. Trans. A*, 1988, 19, 427-440.
- [7] S. E. Offerman, N. H. van Dijk, J. Sietsma, S. van der Zwaag, E. M. Lauridsen, L. Margulies, S. Grigull and H. F. Poulsen, 'Reply to the discussion by Aaronson et al. to "Grain nucleation and growth during phase transformations" by S.E. Offerman et al.', *Science*, 298, 1003 (November 1, 2002)', *Scripta Mater.*, 2004, 51, 937-941.
- [8] J. W. Christian, 'The theory of transformations in metals and alloys', first ed., Pergamon, Oxford, 1981.
- [9] H. Song and J. J. Hoyt, 'An atomistic simulation study of the migration of an austenite-ferrite interface in pure Fe', *Acta Mater.*, 2013, 61, 1189-1196.
- [10] B. J. Wang and H. M. Urbassek, 'Phase transitions in an Fe system containing a bcc/fcc phase boundary: An atomistic study', *Phys. Rev. B*, 2013, 87, 104108.
- [11] X. S. Yang, S. Sun and T. Y. Zhang, 'The mechanism of bcc α' nucleation in single hcp ϵ laths in the fcc $\gamma \rightarrow$ hcp $\epsilon \rightarrow$ bcc α' martensitic phase transformation', *Acta Mater.*, 2015, 95, 264-273.
- [12] S. Y. Hu, M. I. Baskes, M. Stan and L. Q. Chen, 'Atomistic calculations of interfacial energies, nucleus shape and size of θ' precipitates in Al-Cu alloys', *Acta Mater.*, 2006, 54, 4699-4707.
- [13] H. Song and J. J. Hoyt, 'Barrier-free nucleation at grain-boundary triple junctions during solid-state phase transformations', *Phys. Rev. Lett.*, 2016, 117, 238001.
- [14] P. J. Clemm and J. C. Fisher, 'The influence of grain boundaries on the nucleation of secondary phases', *Acta Metall.*, 1955, 3, 70-71.
- [15] H. Sharma, J. Sietsma and S. E. Offerman, 'Preferential nucleation during polymorphic transformations', *Sci. Rep.*, 2016, 6, 30860.
- [16] C. C. Dollins, 'Nucleation on dislocations', *Acta Metall.*, 1970, 18, 1209-1215.
- [17] J. W. Cahn, 'Nucleation on dislocations', *Acta Metall.*, 1957, 5, 169-172.
- [18] M. I. Mendeleev, S. Han, D.J. Srolovitz, G. J. Ackland, D. Y. Sun and M. Asta, 'Development of

- new interatomic potentials appropriate for crystalline and liquid iron', *Phil. Mag.*, 2003, 83, 3977-3994.
- [19] D. A. Porter and K. E. Easterling, 'Phase transformation in metals and alloys', second ed., Chapman & Hall, London, 1992.
- [20] A. Stukowski, 'Visualization and analysis of atomistic simulation data with OVITO-the open visualization tool', *Modell. Simul. Mater. Sci. Eng.*, 2010, 18, 015012.
- [21] A. Stukowski, 'Structure identification methods for atomistic simulations of crystalline materials', *Modell. Simul. Mater. Sci. Eng.*, 2012, 20, 045021.
- [22] A. Stukowski, V. V. Bulatov and A. Arsenlis, 'Automated identification and indexing of dislocations in crystal interfaces', *Modell. Simul. Mater. Sci. Eng.*, 2012, 20, 085007.
- [23] S. Plimpton, 'Fast parallel algorithms for short-range molecular dynamics', *J. Comp. Phys.*, 1995, 117, 1-19. <http://lammps.sandia.gov/>. Accessed on September 4th, 2017.
- [24] A. S. J. Suiker and B. J. Thijssse, 'Nucleation, kinetics and morphology of displacive phase transformations in iron', *J. Mech. Phys. Solids*, 2013, 61, 2273-2301.
- [25] A. Caro, P. E. A. Turchi, M. Caro and E. M. Lopasso, 'Thermodynamics of an empirical potential description of Fe-Cu alloys', *J. Nucl. Mater.*, 2005, 336, 233-242.
- [26] N. Saunders and A. P. Miodownik, 'CALPHAD (calculation of phase diagrams): a comprehensive guide', first ed., Pergamon, New York, 1998.
- [27] G. Ghosh and G. B. Olson, 'The isotropic shear modulus of multi-component Fe-base solid solutions', *Acta Mater.*, 2002, 50, 2655-2675.
- [28] M. Müller, P. Erhart and K. Albe, 'Analytic bond-order potential for bcc and fcc iron-comparison with established embedded-atom method potentials', *J. Phys.: Condens. Matter.*, 2007, 19, 326220.
- [29] J. Zaretsky and C. Stasis, 'Lattice dynamics of γ -Fe', *Phys. Rev. B*, 1987, 35, 4500-4502.
- [30] F. Gao, R. L. Johnston and J. N. Murrell, 'Empirical many-body potential energy functions for iron', *Phys. Chem.*, 1993, 97, 12073-12082.
- [31] N. Singh, 'Lattice dynamics of γ -iron at 1428 K', *Phys. Stat. Sol. B*, 1989, 156, K33-K36.
- [32] E. A. Brandes and G. B. Brook, *Smithells metals reference handbook*, seventh ed., Butterworth-Heinemann, Oxford, 1992.
- [33] Z. Yang and R. A. Johnson, 'An EAM simulation of the alpha-gamma iron interface', *Model. Simul. Mater. Sci. Eng.*, 1993, 1, 707-716.
- [34] X. Ou, J. Sietsma and M. J. Santofimia, 'Molecular dynamics simulations of the mechanisms controlling the propagation of bcc/fcc semi-coherent interfaces in iron', *Modell. Simul. Mater. Sci. Eng.*, 2016, 24, 055019.
- [35] Z. Nishiyama, 'X-ray investigation of the mechanism of the transformation from face-centred to body-centred cubic lattice', *Sci. Rep. Tohoku Imp. Univ.*, 1934, 23, 637-664. Cited by M. G. Hall, H. I. Aaronson and K. R. Kinsman, 'The structure of nearly coherent fcc: bcc boundaries in a Cu-Cr alloy', *Surf. Sci.*, 1972, 31, 257-274.
- [36] G. V. Kurdjumov and G. Sachs, 'Über den mechanismus der stahlhärtung', *Z. Phys.*, 1930, 64, 325-343. Cited by M. G. Hall, H. I. Aaronson and K. R. Kinsman, 'The structure of nearly coherent fcc: bcc boundaries in a Cu-Cr alloy', *Surf. Sci.*, 1972, 31, 257-274.
- [37] D. Hull and D. J. Bacon, 'Introduction to dislocations', fifth ed., Butterworth-Heinemann, Oxford,

2011.

[38] J. Wedekind, D. Reguera and R. Strey, 'Influence of thermostats and carrier gas on simulations of nucleation', *J. Chem. Phys.*, 2007, 127, 064501.

[39] I. J. Ford and C. F. Clement, 'The effects of temperature fluctuations in homogeneous nucleation theory', *J. Phys. A: Math. Gen.*, 1989, 22, 4007-4018.

Chapter 7

Effects of elastic strain on the nucleation and growth of bcc phase in fcc iron by molecular dynamics simulations

Abstract:

Molecular dynamics simulations are used to study the effects of external strain on nucleation and successive growth of bcc phase in pure fcc iron. Two simulation cells are investigated: one contains a single fcc crystal and the other has semicoherent fcc/fcc twin boundaries with periodic boundary conditions. The results show that a tensile stress promotes the coarsening of the final structure by coalescence of neighbouring bcc platelets with identical orientation.

No phase transformation takes place in the single fcc crystal at 100 K without strain. A strain in the $[1\ 0\ 0]_{fcc}$ direction leads to the fcc-to-bcc transformation both at 50 K and 100 K. In both cases, the bcc phase nucleates mainly in the Nishiyama-Wassermann (NW) and Kurdjumov-Sachs (KS) orientation relationships (ORs) with the parent fcc phase. One plate-like bcc grain in the NW OR is accompanied by two neighbouring grains in the KS OR. One orientation is dominant in each case, with the KS OR dominant at 50 K and the NW OR at 100 K. At 50 K, the number of grains in the NW OR gradually diminishes, which is followed by the merging of their neighbouring bcc grains in the KS OR. This coalescence of the bcc grains leads to a single bcc crystal in the KS OR in the final structure. Inversely, the bcc grains in the NW OR survive and coalesce to form a single bcc crystal at 100 K.

For the cell containing semicoherent fcc/fcc twin boundaries, nucleation and the successive growth of bcc phase occurs at the semicoherent fcc/fcc twin boundary at 100 K without a tensile strain. The forming bcc grains are mainly in the NW and KS ORs with the fcc phase. In this case, the bcc grains display normal grain growth through the migration of grain boundaries. Bcc grains both in the NW and KS ORs remain in the final structure. However, different results are found for simulations under a tensile strain in either the $[\bar{1}\ \bar{1}\ 2]_{fcc}$ or $[1\ \bar{1}\ 0]_{fcc}$ directions. The KS OR dominates in the former case while the NW OR is the main orientation in the latter. Besides, the strain in the $[\bar{1}\ \bar{1}\ 2]_{fcc}$ direction results in the formation of twinning bcc grains in the KS OR in the final structure. A single bcc crystal in the NW OR is obtained for the simulation cell strained in the $[1\ \bar{1}\ 0]_{fcc}$ direction. The coarsening of bcc grains is mainly due to the coalescence of neighbouring bcc grains in the same OR.

7.1 Introduction

In recent years, the effects of external stress and strain on martensitic transformation has become a relevant topic both by experiments and by simulations [1-4]. While internal stress and strain is induced due to microstructural deformation during the martensitic transformation, external stress and strain in turn contributes to the face-centered cubic (fcc) to the body-centered cubic (bcc) phase transformation as well. In steels with transformation induced plasticity (TRIP), for example, austenite transforms into martensite during plastic deformation [1-3]. Previous molecular dynamics (MD) simulations by Sandoval and Urbassek [4] indicated that a tensile axial stress lowered the fcc-to-bcc transformation temperature in a nanowire system. Furthermore, the nucleation of bcc phase also occurred in iron with bcc/fcc interfaces at different temperatures under a shear strain in MD simulations [5]. From the experimental results, both enhanced hardness and ductility are obtained for steels due to the strain induced martensitic transformation [1,3,6,7]. The mechanisms governing the strain-induced martensitic transformation are difficult to be revealed by experiments but possible by MD simulation. The microstructural development of materials under external strain can be tracked at the atomic scale by MD simulation.

It is well known that grain size affects the mechanical properties, especially the hardness and toughness, of materials. Coarsening of ferrite grains may take place through two mechanisms: the normal grain growth by migration of the grain boundaries and/or coalescence of neighbouring bcc grains with identical orientation during phase transformation [8]. It was observed by experiment that adjacent platelets of martensite or bainite tend to coalesce to form much coarser structures in appropriate circumstances in steels [9-13]. Such coarse structures are detrimental to the mechanical properties, especially the strength and toughness, because of the homogeneous crystallography and low resistance to the cleavage crack propagation [9,13].

It was reported that adjacent platelets of martensite or bainite tend to coalesce on condition that they share the same habit plane and variant of the orientation relationship with austenite without intervening phases [9,10,12,13]. The fine adjacent platelets nucleated separately at the austenite grain boundaries but remained all identically oriented during prolonged growth [9,10,13]. It was found that significant orientation gradients exist across the dimensions of the coalesced grains after the merging of the individual fine platelets of martensite [9]. The martensite growth was accompanied by transformation strain, which induced plasticity in austenite and change of the local orientation of austenite. Subsequently forming martensite, which formed from the deformed austenite, thus inherited the crystallographic orientation relations and was slightly rotated relative to the original martensite [9]. However, it was impossible to observe the exact magnitude of the resulting rotation by experiment, due to the fine scale of the structure as well as the absence of austenite [9].

Pak *et al.* [11] found that a tensile stress strangely promoted the formation of coalesced bainite platelets during phase transformation in steels. The proposed reason is that the tensile stress reduced the number

of occurring crystallographic variants, which therefore contributed to the formation of platelets with the same or close orientation. In the present paper, MD simulations are used to study the effects of tensile stress on the nucleation, growth and coarsening of bcc grains forming in iron with and without fcc/fcc grain boundaries at different temperatures. This provides information on the influence of strain or stress on the microstructural evolution during the fcc-to-bcc phase transformation in iron, which thus contributes to a better control of the final structures, especially the refinement of the grains, in steels.

7.2 Simulation methods

An embedded-atom method (EAM) potential for Fe by Mendeleev *et al.* [14] is used in the present work. Two simulation cells are involved in the present study: one is a single fcc crystal and the other includes two semicoherent fcc/fcc twin boundaries. The details of the two simulation cells are as follows.

Simulation cell 1: The dimensions of the former cell are $219.5 \text{ \AA} \times 219.5 \text{ \AA} \times 219.5 \text{ \AA}$ in the x , y and z directions, which contains 864,000 atoms. The x , y and z axes are parallel to the $[1\ 0\ 0]_{fcc}$, $[0\ 1\ 0]_{fcc}$ and $[0\ 0\ 1]_{fcc}$ directions, respectively. The simulation cell is first thermally equilibrated using a barostat and a thermostat of the Nosé-Hoover type at a constant temperature T under vacuum atmosphere (NPT ensemble) for 2.5 ps, which is followed by deformation in the $[0\ 1\ 0]_{fcc}$ direction at a constant strain rate of 0.01/ps under the same NPT ensemble for 10 ps. Two temperatures T are studied, namely 50 K and 100 K.

Simulation cell 2: One of the grain boundaries is a coherent twin boundary with its twin boundary parallel to the close-packed $(1\ 1\ 1)_{fcc}$ twinning plane; the other is a faceted twin boundary involving about 5.7° rotation around the $[1\ \bar{1}\ 0]_{fcc}$ from the $(1\ 1\ 1)_{fcc}$ twinning plane. The dimensions of the simulation cell are $286.7 \text{ \AA} \times 124.2 \text{ \AA} \times 230.2 \text{ \AA}$ in the x , y and z directions, which consists of 669,456 atoms. The fcc lattice parameter is 3.658 \AA obtained at 0 K. The simulation cell is relaxed by the method of energy minimisation by fixing the dimensions of the box in the x and y directions but letting the dimension in z direction expand or contract freely. Then, three independent simulations are performed based on the relaxed simulation cell. The first simulation is done at 100 K under the atmospheric pressure (NPT ensemble) without strain for 10 ps. In the second and third simulations, the system is first thermally equilibrated at 100 K under vacuum atmosphere (NPT ensemble) for 0.25 ps, which is followed by a deformation at strain rate 0.01/ps in the $[\bar{1}\ \bar{1}\ 2]_{fcc}$ and $[1\ \bar{1}\ 0]_{fcc}$ directions, respectively, under the same NPT ensemble, for 10 ps.

All simulations are performed assuming periodic boundaries in all directions and in absence of free surfaces. The MD time step is fixed at 0.0005 ps per step. Calculations are performed with the open-source LAMMPS code [15]. The adaptive common neighbour analysis (a-CNA) method [16] is chosen as the discriminator in the present study to determine local crystallographic configuration. The configurations are displayed using the software OVITO [17]. Colours of atoms represent different

phase structures. The snapshot in figure 7-1(a) represents the initial, relaxed configuration for the simulation cell with fcc/fcc grain boundaries. Two twin boundaries are included: Boundary 1 is a faceted twin boundary and Boundary 2 is a coherent twin boundary. Boundary 2 is stable and has low grain boundary energy [18]. Figures 7-1 (b) and (c) show the enlarged views of the local regions of the two boundaries. The atoms lying on the twinning plane at the coherent Boundary 2 are all identified with an hcp structure, while the lattice mismatch at the faceted Boundary 1 results in dislocations and unidentified atoms.

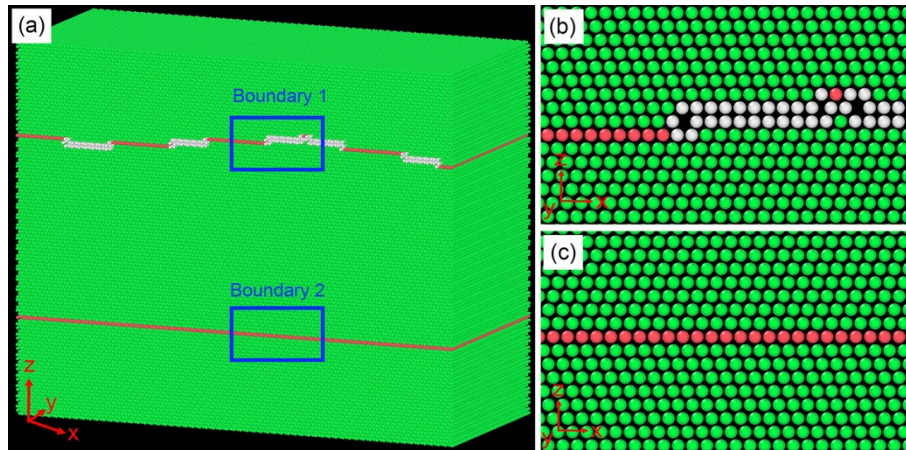


Figure 7-1 (a) The initial, relaxed configuration of the simulation cell including two fcc/fcc grain boundaries; (b) The enlarged region selected by the blue rectangle for Boundary 1 in figure (a); (c) The enlarged region selected by the blue rectangle for Boundary 2 in figure (a). The system consists of 669,456 atoms. For one of the twinned fcc grains between the two fcc/fcc boundaries, the x axis is parallel to its $[\bar{1} \bar{1} 2]_{fcc}$ direction, the y axis is parallel to the $[1 \bar{1} 0]_{fcc}$ direction and z axis is parallel to the $[1 1 1]_{fcc}$ direction. Colours represent different crystallographic structures: blue-bcc; green-fcc; red-hcp; white-unidentified.

7.3 Results and discussion

7.3.1 System with a single fcc crystal in Simulation cell 1

There is no phase transformation in the single fcc crystal at 100 K under vacuum atmosphere up to 50 ps when no external strain is applied, while a tensile strain induces the fcc-to-bcc transformation in the single fcc phase at or below 100 K. Figures 7-2 and 7-3 show the fcc-to-bcc transformation in the single fcc iron which is elastically strained by 10% in the $[1 \bar{1} 0]_{fcc}$ direction at 50 K and 100 K, respectively. Nucleation of bcc phase starts after 3.0 ps (corresponding to a strain of 3%) at 50 K, while the bcc nucleation initiates earlier, after around 2.5 ps (corresponding to a strain of 2.5%), at 100 K. Therefore, the fcc-to-bcc transformation takes place at a lower strain when the isothermal temperature is higher. The parent fcc phase transforms to the bcc phase efficiently with remaining grain boundaries (the unidentified atoms in figures 7-2 and 7-3). This can be seen from a-CNA for both systems at 50 K and 100 K in figures 7-4 (a) and (b), respectively. At 50 K, the percentage of fcc phase decreases to about 15% at 3.5 ps with the fraction of unidentified atoms, acting as the bcc/bcc or fcc/bcc boundaries, increasing up to 55%. At 100 K, 85% of the fcc phase transforms at 3.0 ps, 53% of which have become

Effects of elastic strain on the nucleation and growth of bcc phase in fcc iron by molecular dynamics simulations

unidentified atoms and 32% bcc phase. Therefore, a large quantity of the bcc/bcc and the fcc/bcc boundaries are created during this period. After that, the fractions of the retained fcc structure and the unidentified atoms decrease gradually, accompanied by a steady increase of the fraction of the bcc structure. In this period, the grain boundary density gradually diminishes under the continuous strain, leading to the coarsening of bcc grains, as seen from the regions inside the yellow rectangles in figures 7-2 (b)-(e) and figures 7-3 (b)-(e). At the end of 10 ps, a single bcc crystal is obtained both at 50 K and 100 K, with some remaining defects locally.

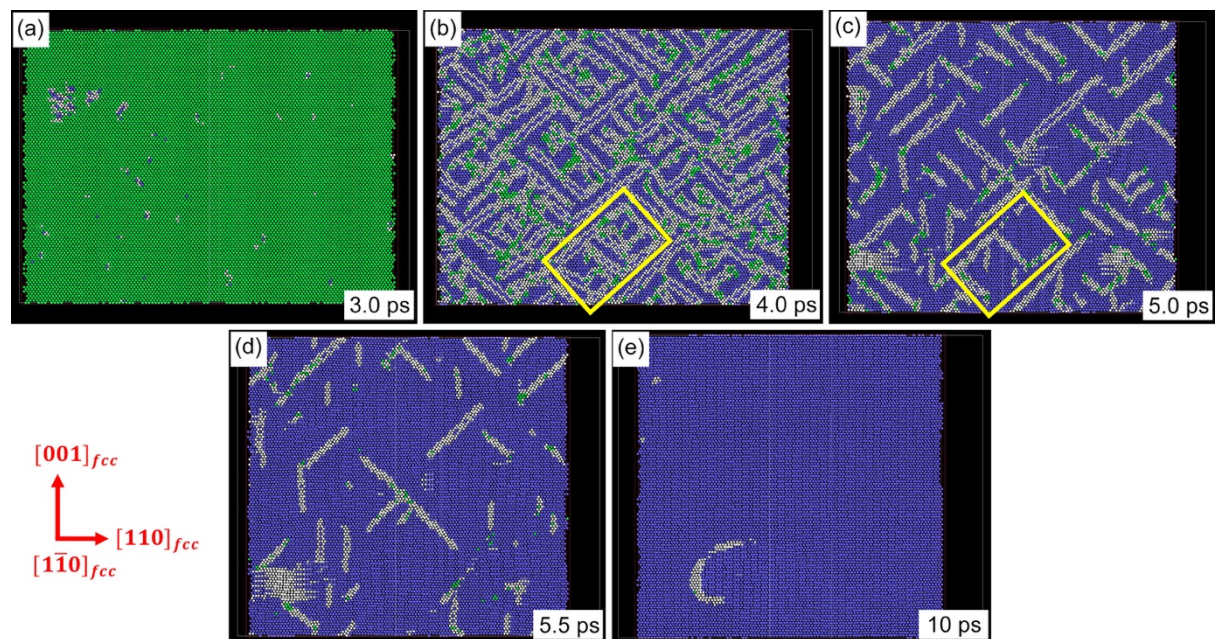


Figure 7-2 Time evolution of the structure in a slice of 3.5 Å in the $[1 \bar{1} 0]_{fcc}$ direction indicating the fcc-to-bcc transformation in fcc iron under strain at 50 K. Colours represent different phase structures: blue-bcc; green-fcc; red-hcp; white-unidentified.

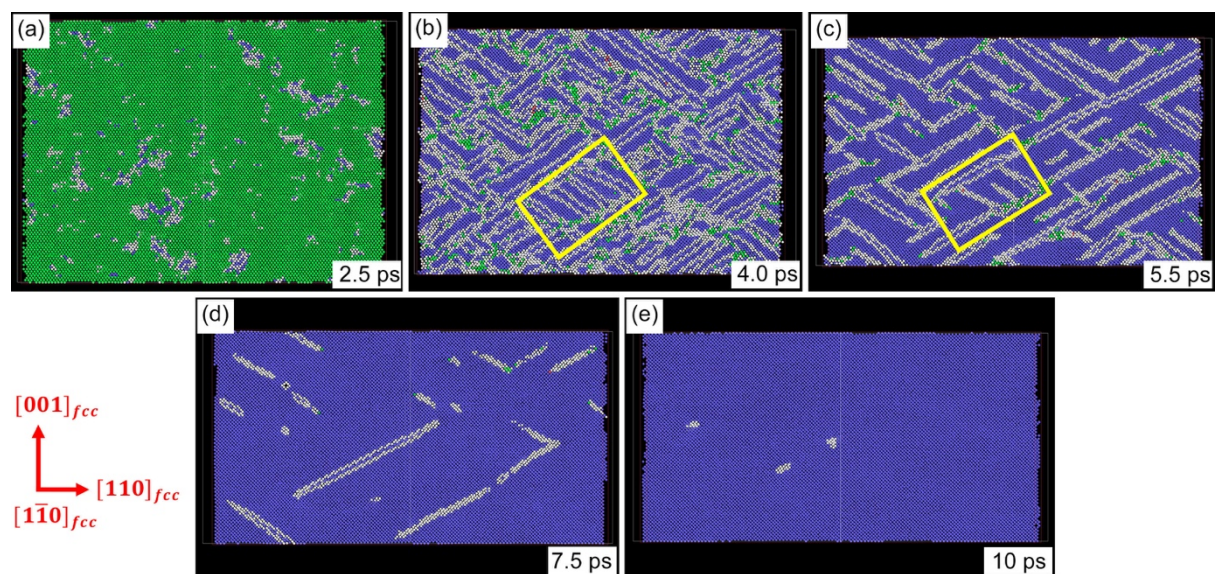


Figure 7-3 Time evolution of the structure in a slice of 3.5 Å in the $[1 \bar{1} 0]_{fcc}$ direction indicating the fcc-to-bcc transformation in fcc iron under strain at 100 K. Colours represent different phase structures: blue-bcc; green-fcc; red-hcp; white-unidentified.

Figures 7-4 (c) and (d) illustrate the change of stresses in x , y and z directions (σ_{xx} , σ_{yy} , and σ_{zz}) with the increasing overall strain in the y direction (ϵ_y) for the simulation cell during the nucleation and growth of bcc phase in fcc iron at 50 K and 100 K, respectively. It is seen that the stress in the y direction (σ_{yy}) of the simulation cell first increases monotonically up to 2.0 GPa with the strain increasing to around 0.03 at 50 K. This period corresponds to a critical strain before which no phase transformation takes place inside the fcc iron.

The onset of transformation is followed by a sudden drop of the stress in the y direction (σ_{yy}) to around -6.0 GPa with a minor strain increase to 0.035, which is due to the internal stress induced by the fcc-to-bcc transformation [1,3,6,7], as indicated by figures 7-4 (a) and (b). After that, the internal stress reduces gradually to zero because of the coarsening of bcc grains with the elimination of the grain boundaries, as indicated by the decreasing fraction of unidentified boundary atoms in figures 7-4 (a) and (b). The stress in the y direction (σ_{yy}) for the simulation cell at 100 K shows a similar trend to that at 50 K.

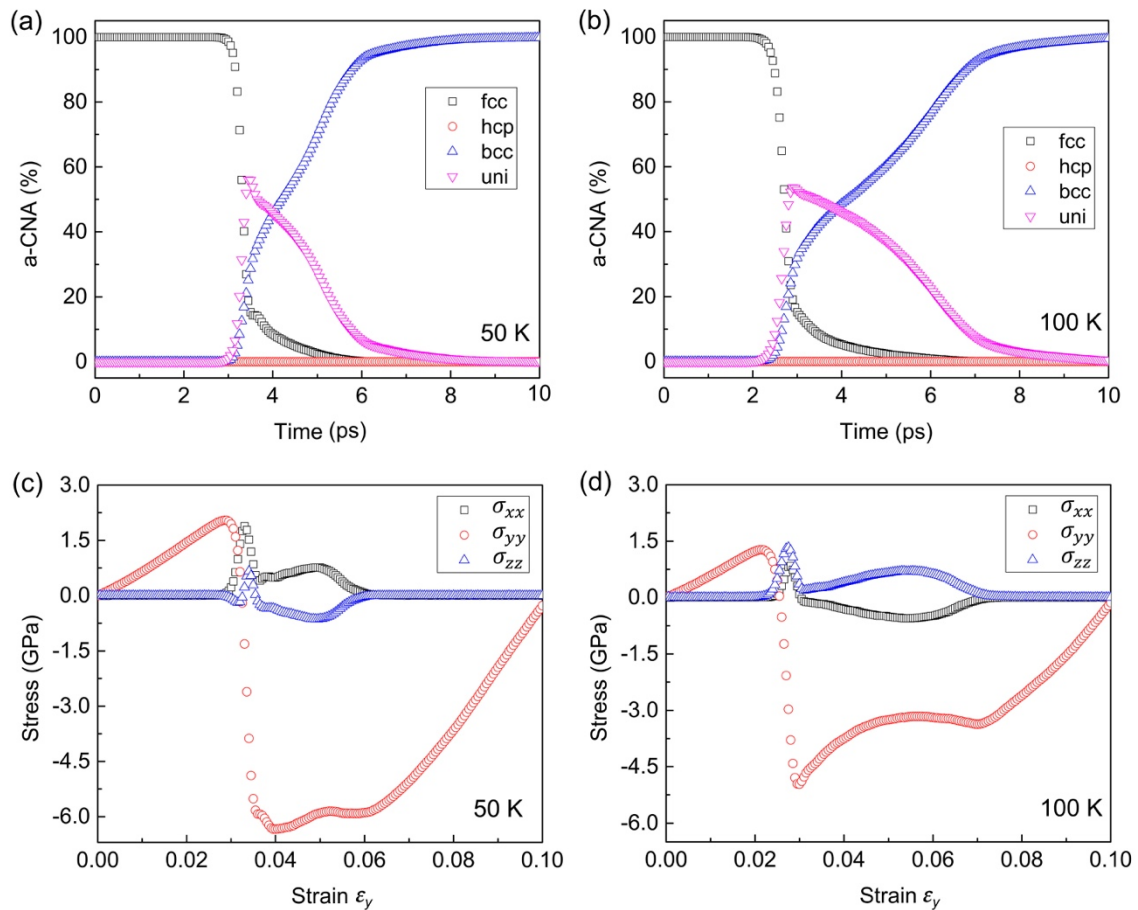


Figure 7-4 (a) Time evolution of the phase fraction for the system at 50 K; (b) Time evolution of the phase fraction for the system at 100 K; (c) The stresses of the system in the x , y and z directions (σ_{xx} , σ_{yy} , and σ_{zz}) as a function of the overall strain ϵ_y (strain rate: 0.01 ps^{-1}) at 50 K; (d) The stresses of the system in the x , y and z directions (σ_{xx} , σ_{yy} , and σ_{zz}) as a function of the overall strain ϵ_y (strain rate: 0.01 ps^{-1}) at 100 K.

Effects of elastic strain on the nucleation and growth of bcc phase in fcc iron by molecular dynamics simulations

Figure 7-5(a) indicates the fraction of bcc phase as a function of the external strain ϵ_y in system at 50 K and 100 K. It is seen that the fcc-to-bcc transformation takes place at a smaller strain at 100 K than at 50 K. Correspondingly, a lower stress (σ_{yy}) is involved for the start of bcc nucleation in fcc iron strained at 100 K, as seen in figure 7-5(b). This may be related to the different magnitude of shear strain of atoms induced by the external strain ϵ_y at different temperatures, as shown by the histogram in figures 7-5 (c) and (d). It is found that the same external strain induces larger shear strain of atoms at 100 K than at 50 K before the start of the bcc nucleation. The peak of the distribution shifts from around 0.018 to 0.020 with the increasing strain at 50 K, while the peak at 100 K increases from 0.025 to 0.030 with the increasing strain at 100 K. It is known that the transformed bcc phase usually has an orientation relationship (OR) with the parent fcc phase, mainly the Nishiyama-Wassermann (NW) [19] and the Kurdjumov-Sachs (KS) [20] ORs, which involve a main shear in the $\langle 1\ 1\ 2 \rangle_{fcc}$ direction of the $\{1\ 1\ 1\}_{fcc}$ plane. Thus the larger shear strain induced by the external strain at 100 K is more favourable to the nucleation of bcc phase and the continual fcc-to-bcc transformation. The fraction of bcc phase transformed from the fcc phase increases quickly to around 50% at $\epsilon_y=0.04$ both at 50 K and 100 K (figure 7-5 (a)). Correspondingly, the stress in the y direction (σ_{yy}) decreases linearly from a positive to a negative value (figure 7-5 (b)). The strain ($\epsilon_y>0.04$) results in the growth and coarsening of bcc grains, which relaxes the stress (σ_{yy}) induced by the fcc-to-bcc transformation.

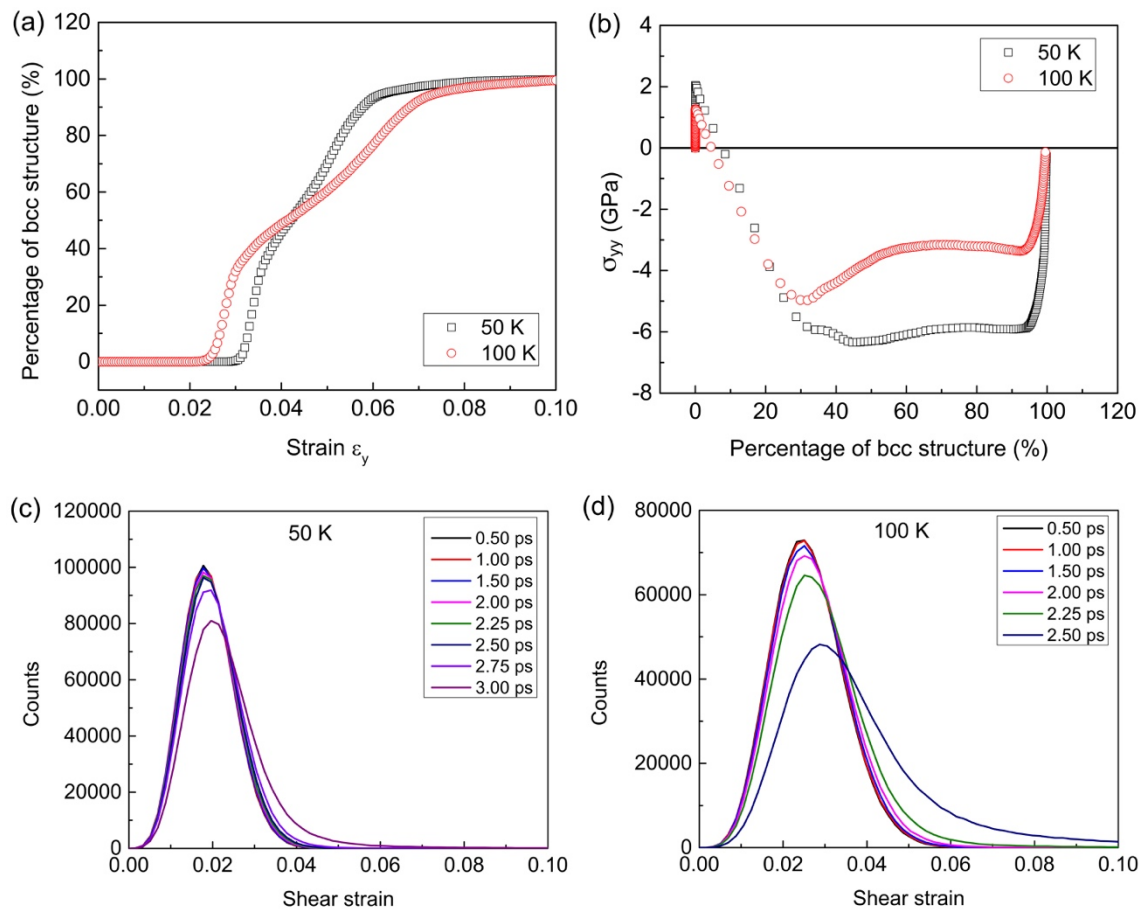


Figure 7-5 The fraction of bcc phase as a function of the external strain ϵ_y at 50 K and 100 K; (b) The stress in the y direction σ_{yy} as a function of the fraction of bcc phase at 50 K and 100 K; (c) Histogram of shear strain of atoms

until 3.00 ps when bcc nucleation takes place in fcc iron at 50 K; (d) Histogram of shear strain of atoms until 2.50 ps when bcc nucleation takes place in fcc iron at 100 K.

Besides, it is found from figures 7-4 (c) and (d) that differences exhibit between the simulation cells at 50 K and 100 K regarding to their stresses in the x and z directions. The stress in the x direction is positive whereas that in the z direction is negative during the grain coarsening period at 50 K, as shown in figure 7-4(c). That is opposite to the stresses in the x and z directions for the simulation cell at 100 K. Correspondingly, the length of the cell in the z direction increases with that in the x direction decreasing at 50 K, as shown in figure 7-6(a). Inversely, the dimension of the cell in the z direction decreases with that in the x direction increasing at 100 K, as seen from figure 7-6(b). Nonetheless, almost the same volume is obtained for the final structure of the simulation cell at 50 K and 100 K, respectively. The differences either in the stresses or the dimensions in the x and z directions may be related to the varied orientations of the forming bcc grains at different temperatures, as illustrated in figures 7-7 and 7-8.

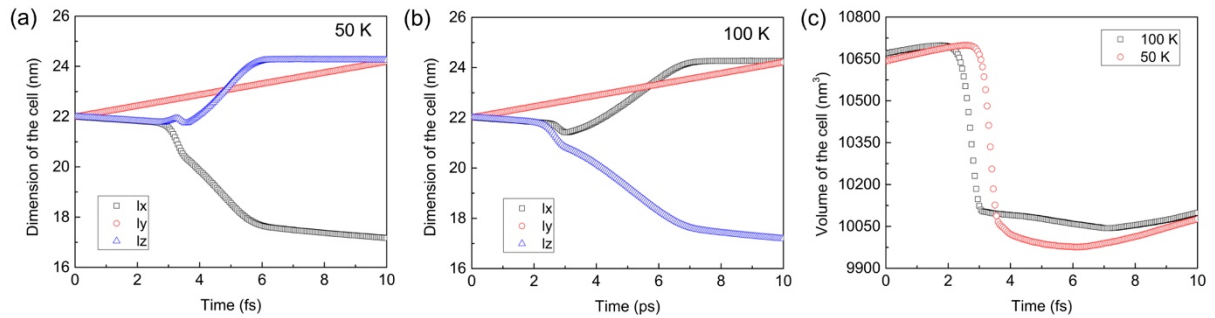


Figure 7-6 (a) Time evolution of the dimensions of the simulation cell at 50 K; (b) Time evolution of the dimensions of the simulation cell at 100 K; (c) Time evolution of the volume of the simulation cells both at 50 K and 100 K. l_x , l_y and l_z represent the length of the simulation cell in the x , y and z directions.

Figures 7-7 (a)-(d) show the enlarged view of the area marked by the yellow rectangle for the simulation cell at 50 K in figure 7-2. The bcc grains are either in the (near-) NW or the (near-) KS OR. It is known that there are 24 variants for the KS OR and 12 variants for the NW OR [21]. Each variant involves in one compression axis and two tensile axes for the martensitic transformation, which is known as the Bain distortion [3]. Han *et al.* [22] proposed the relation between the mechanical interaction energy (U^i) for the i th martensitic variant, the external applied stress (σ_{ij}) and the lattice strain in austenite during the phase transformation:

$$U^i = m_v \sigma_{ij} \cdot \varepsilon_{ij}^i \quad (7-1)$$

where ε_{ij}^i represents the transformation strain tensor for the i th martensitic variant in the specimen coordinate system, m_v is the molar volume of austenite. The mechanical interaction energies vary for different martensitic variants under an external strain or stress. This leads to the selection of a specific martensitic variant, which minimizes the total energy required for the mechanically induced phase transformation of metastable fcc phase [3,22]. Therefore, the number of the possible variants are reduced during the stress-induced phase transformation [11]. In the present studies, the bcc platelets mainly follow four variants of the KS OR at 50 K, as included in Table 7-1, without taking into

Effects of elastic strain on the nucleation and growth of bcc phase in fcc iron by molecular dynamics simulations

account the symmetry of the bcc lattices. Two of the bcc platelets that follow two of the four variants are marked as KS1 and KS2 as an example in figure 7-7(a). The other two variants can also be seen from a view direction of $[1\ 1\ 0]_{fcc}$, the snapshots of which are similar to figure 7-7(a) and thus will not be discussed further here. A minor number of bcc grains in the NW OR exist as thin platelets involving only 3-4 layers of atoms. Such a bcc platelet is neighbored on its broadsides by another two in the KS OR with the same variant. The intermediate bcc platelet in the NW OR gradually diminishes, thus the two neighbouring bcc grains in the KS OR forming from the same variant merge into a coarser grain.

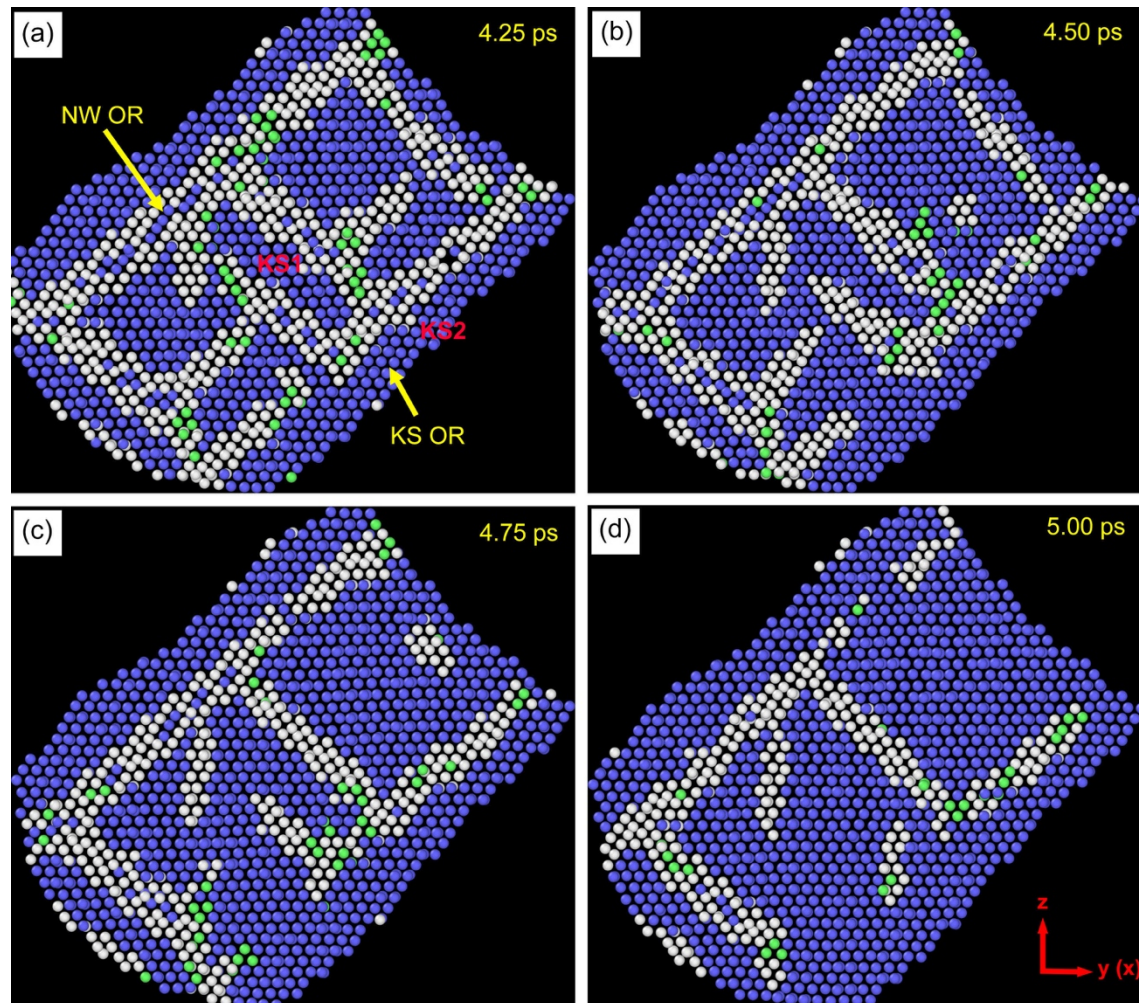


Figure 7-7 Enlarged snapshots of the grain coarsening by coalescence of bcc grains in identical orientation for the simulation cell at 50 K. The view direction is parallel to the $[1\ \bar{1}\ 0]_{fcc}$ direction. The region in figures (a)-(d) corresponds to the area inside the yellow rectangle in figure 7-2. Colours represent different phase structures: blue-bcc; green-fcc; red-hcp; white-unidentified.

At 100 K, however, the NW OR dominates the bcc grains, as shown in figures 7-8 (a)-(d). The bcc grains mainly follow four of the 12 variants NW OR at 100 K, as included in Table 7-1. Two bcc grains that have two of the variants are indicated and labeled as NW1 and NW2 in figure 7-8(a). Similar to the coalescence process at 50 K, two bcc grains in the NW OR merge to form a coarser grain with the elimination of the intermediate bcc platelet in the KS OR. By combining figures 7-4 (c)-(d) and figures 7-6 (c)-(d), the different main orientations of the bcc grains at 50 K and 100 K explain their varied stress-strain behaviours as well as the lengths in the x and z directions.

Table 7-1 The variants of the orientations for the simulation cells at 50 K and 100 K, respectively.

OR	fcc plane	bcc plane	fcc direction	bcc direction
KS1	$(1\ 1\ 1)_{fcc}$	$(0\ 1\ 1)_{bcc}$	$[\bar{1}\ 1\ 0]_{fcc}$	$[1\ 1\ \bar{1}]_{bcc}$ or $[\bar{1}\ 1\ \bar{1}]_{bcc}$
KS2	$(1\ 1\ \bar{1})_{fcc}$	$(0\ 1\ 1)_{bcc}$	$[1\ \bar{1}\ 0]_{fcc}$	$[1\ 1\ \bar{1}]_{bcc}$ or $[\bar{1}\ 1\ \bar{1}]_{bcc}$
KS3	$(\bar{1}\ 1\ 1)_{fcc}$	$(0\ 1\ 1)_{bcc}$	$[\bar{1}\ \bar{1}\ 0]_{fcc}$	$[1\ 1\ \bar{1}]_{bcc}$ or $[\bar{1}\ 1\ \bar{1}]_{bcc}$
KS4	$(1\ \bar{1}\ 1)_{fcc}$	$(0\ 1\ 1)_{bcc}$	$[1\ 1\ 0]_{fcc}$	$[1\ 1\ \bar{1}]_{bcc}$ or $[\bar{1}\ 1\ \bar{1}]_{bcc}$
NW1	$(1\ 1\ 1)_{fcc}$	$(0\ 1\ 1)_{bcc}$	$[\bar{1}\ 1\ 0]_{fcc}$	$[1\ 0\ 0]_{bcc}$
NW2	$(1\ 1\ \bar{1})_{fcc}$	$(0\ 1\ 1)_{bcc}$	$[1\ \bar{1}\ 0]_{fcc}$	$[1\ 0\ 0]_{bcc}$
NW3	$(\bar{1}\ 1\ 1)_{fcc}$	$(0\ 1\ 1)_{bcc}$	$[\bar{1}\ \bar{1}\ 0]_{fcc}$	$[1\ 0\ 0]_{bcc}$
NW4	$(1\ \bar{1}\ 1)_{fcc}$	$(0\ 1\ 1)_{bcc}$	$[1\ 1\ 0]_{fcc}$	$[1\ 0\ 0]_{bcc}$

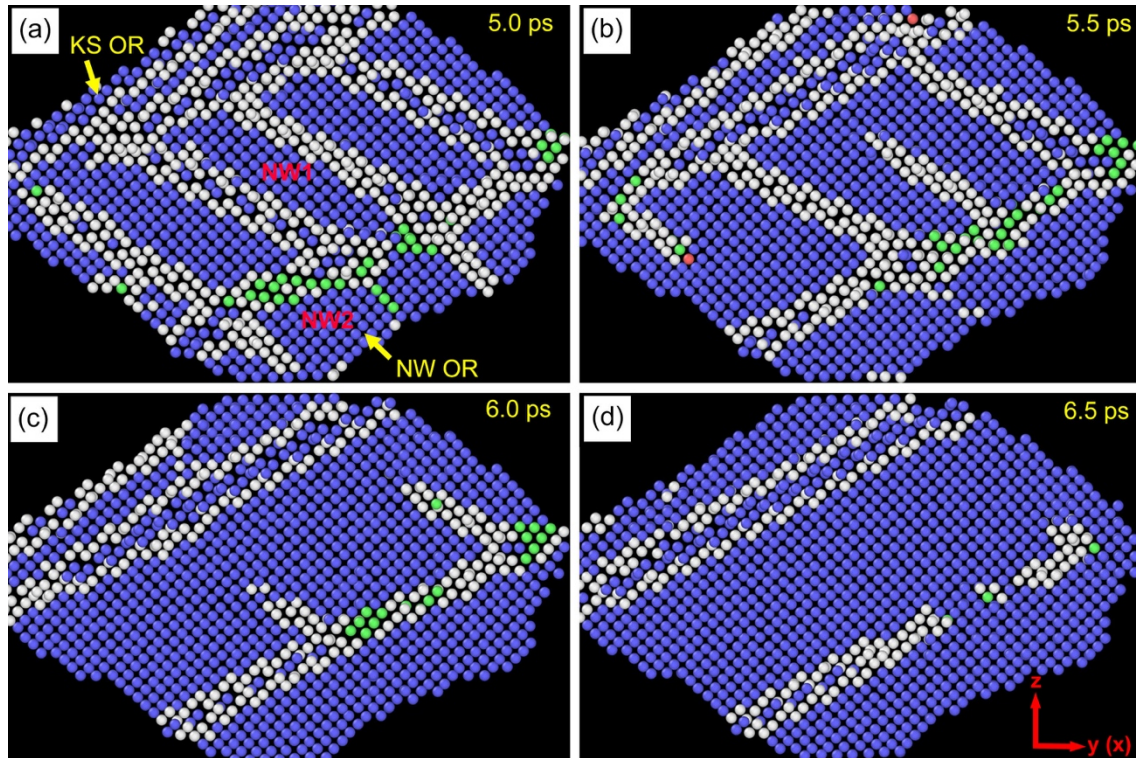


Figure 7-8 Enlarged snapshots of the grain coarsening by coalescence of bcc grains in identical orientation for the simulation cell at 100 K. The view direction is parallel to the $[1\ \bar{1}\ 0]_{fcc}$ direction. The region in figures (a)-(d) corresponds to the area inside the yellow rectangle in figure 7-3. Colours represent different phase structures: blue-bcc; green-fcc; red-hcp; white-unidentified.

The fcc-to-bcc transformation induced by the external strain follows specific variants of crystallographic orientations, which therefore leads to the formation of bcc/bcc grain boundaries preferably at the corresponding habit planes. The bcc grains (or the grain boundaries) tend to form about 45° to the tensile stress direction (the y direction), as can be seen from figures 7-9 (a) and (b).

Similar results were observed in experiments by Pak *et al.* [11] that bainite platelets transformed from the austenitic steel under external stress had a strong tendency to lie approximately 45° to the tensile stress axis. The reason is that the coalesced bcc platelets comply best with the external stress when they forms at 45° to the stress direction. Additionally, the forming bcc grains are mainly in the NW OR with the variants at 50 K, as seen in Table 7-1, leads to the expansion of the simulation cell in the z direction and shrinkage in the x direction, as shown in figure 7-6(a). For the variant KS1 in Table 7-1 ($(1\ 1\ 1)_{fcc} \parallel (0\ 1\ 1)_{bcc}$, $[\bar{1}\ 1\ 0]_{fcc} \parallel [1\ 1\ \bar{1}]_{bcc}$), for example, the original $[1\ 0\ 0]_{fcc}$ corresponds to the $[1\ 0\ 0]_{bcc}$ in the x axis, while the original $[0\ 0\ 1]_{fcc}$ corresponds to the $[1\ 0\ 1]_{bcc}$ in the z axis after phase transformation. Therefore, the dimension of simulation cell shrinks in the x direction but expands in the z direction. The coalescence of bcc grains is accompanied by the reduction of the bcc/bcc grain boundary area, which further extends the dimension in the z direction and reduces the dimension in the x direction. Inversely, for the simulation at 100 K, the dominant NW orientation with variants in Table 7-1 leads to the expansion in the x axis and shrinkage in the z axis. For example, the variant NW1 has the parallel relations $[1\ 0\ 0]_{fcc} \parallel [\bar{3}\ 3\ 1]_{bcc}$ in the x axis and $[0\ 0\ 1]_{fcc} \parallel [0\ 0\ 1]_{bcc}$ in the z axis, which explains the expansion in the x direction and shrinkage in the z direction of the simulation cell. The change of those two dimensions continues until a single bcc grain is obtained by the coalescence process.

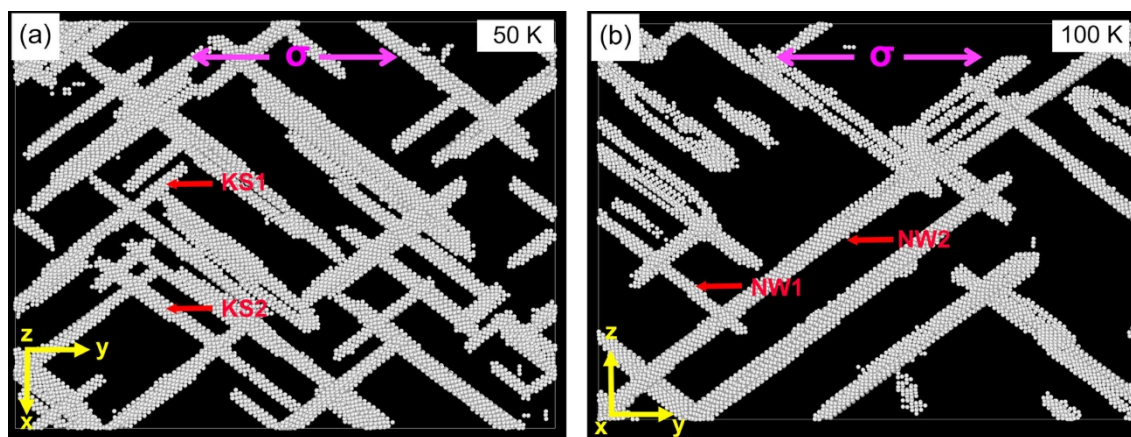


Figure 7-9 (a) Snapshot of the simulation cell at 50 K at 6.5 ps; (b) Snapshot of the simulation cell at 100 K at 9.0 ps. In figures (a) and (b), only the unidentified atoms acting as the grain boundaries are displayed.

7.3.2 System with fcc/fcc grain boundaries

7.3.2.1 The fcc-to-bcc transformation in Simulation cell 2

For the system with fcc/fcc boundaries, the fcc-to-bcc transformation initiates preferably from the semicoherent twin boundary with or without external strain, as seen from figures 7-10 to 7-12. A slice of 6 \AA in thickness perpendicular to the y direction of the simulation cell is selected for a better view of the phase transformation. Figures 7-10 (a)-(f) show the nucleation and growth of bcc phase in iron at 100 K without external strain. It is seen that the fcc-to-bcc transformation takes place initially from the semicoherent fcc/fcc twin boundary, as marked by the yellow dashed rectangles. Then the bcc nuclei grow by consuming both fcc grains and hcp stacking faults at the boundary. However, no phase

transformation occurs at the coherent fcc/fcc twin boundary until it is interrupted by the bcc grains growing from the semicoherent boundary, as indicated in figure 7-10(d). Grain boundaries form between neighbouring bcc grains with a plate-like morphology, because the neighbouring bcc plates have different orientations. One bcc platelet in the NW OR is always neighbored on its broadside by another in the KS OR. A large amount of grain boundaries, indicated by atoms with unidentified structure, remains in the final structure at 10 ps.

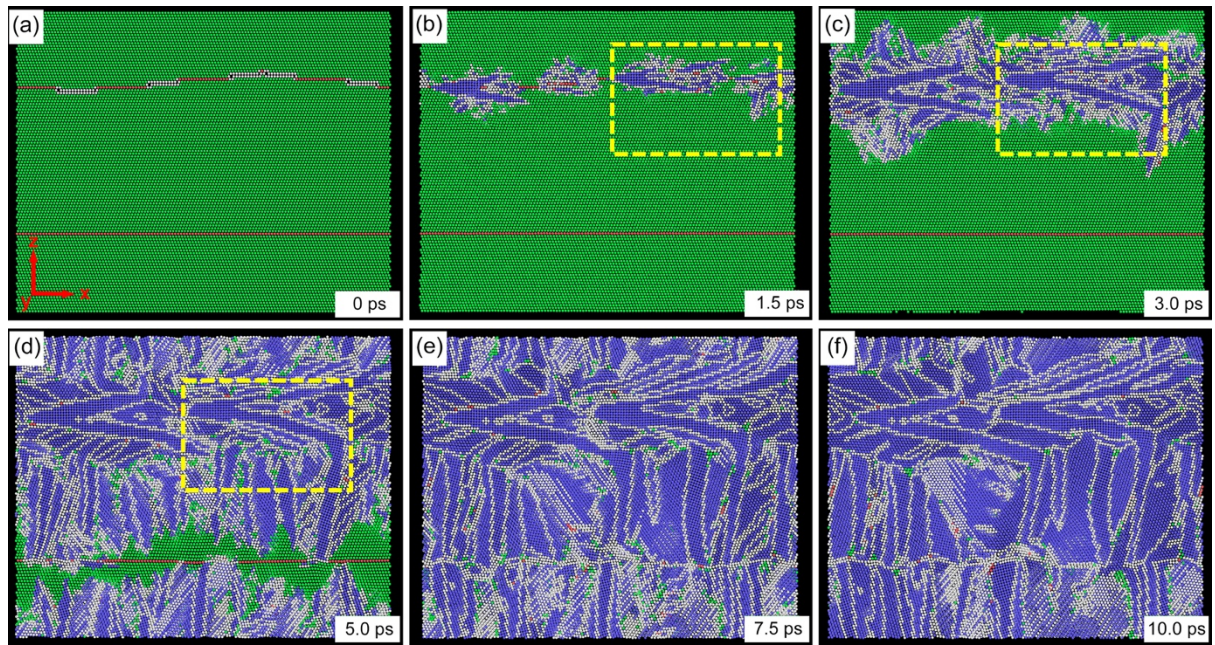


Figure 7-10 Time evolution of the nucleation and growth of bcc phase in fcc iron at 100 K without external strain.

Colours represent different phase structures: blue-bcc; green-fcc; red-hcp; white-unidentified.

Figures 7-11 and 7-12 show the configurations of the simulation cell under an external strain in the x ($\langle 112 \rangle_{fcc}$) and y ($\langle 110 \rangle_{fcc}$) directions, respectively. Besides occurring from the semicoherent fcc/fcc twin boundary, the nucleation of bcc phase also takes place homogeneously inside the fcc bulk (marked by the yellow arrows) as well as heterogeneously at the coherent fcc/fcc twin boundary (marked by the blue arrows). When the external strain is in the $\langle 112 \rangle_{fcc}$ direction, the KS OR dominates the bcc nuclei. However, the NW OR is dominant under the external strain in the $\langle 110 \rangle_{fcc}$ direction. This may be related to the reduced variants for each OR during the stress-induced phase transformation [11]. Grain boundaries exist in the final structure under strain in the $\langle 112 \rangle_{fcc}$ direction, while a single bcc grain with local defects is obtained under strain in the $\langle 110 \rangle_{fcc}$ direction.

Figure 7-13 (a) shows the time evolution of the fraction of different phases in simulation cell without strain. When there is no external strain, the fraction of the fcc structure decreases sharply to about 5% in the initial 5 ps, accompanied by the quick increase of those in the bcc and unidentified structures. During this period, the fcc phase transforms to the bcc phase leading to the formation of phase interfaces and bcc/bcc grain boundaries, which appear as the unidentified atoms. After 5 ps, the bcc phase continues to increase mildly, while simultaneously the amount of unidentified atoms decreases

Effects of elastic strain on the nucleation and growth of bcc phase in fcc iron by molecular dynamics simulations

slowly. The bcc grains grow and coarsen in this period, thus the amount of grain boundaries or the content of unidentified structure decreases. By contrast, the fcc phase transforms to the bcc phase more efficiently under an external strain either in the $\langle 112 \rangle_{fcc}$ or $\langle 110 \rangle_{fcc}$ direction, as seen from figures 7-13 (b) and (c). Above 95% of the fcc phase transforms before 4 ps. However, the content of the unidentified structures decreases to approximately zero when the external strain is in the $\langle 110 \rangle_{fcc}$ direction. This is equivalent to the diminishment of bcc/bcc grain boundaries, which leads to a single bcc grain in the final structure. Strain in the other direction, nonetheless, does not guarantee one single crystal but twinning crystallography in the final structure, which will be discussed in the following section.

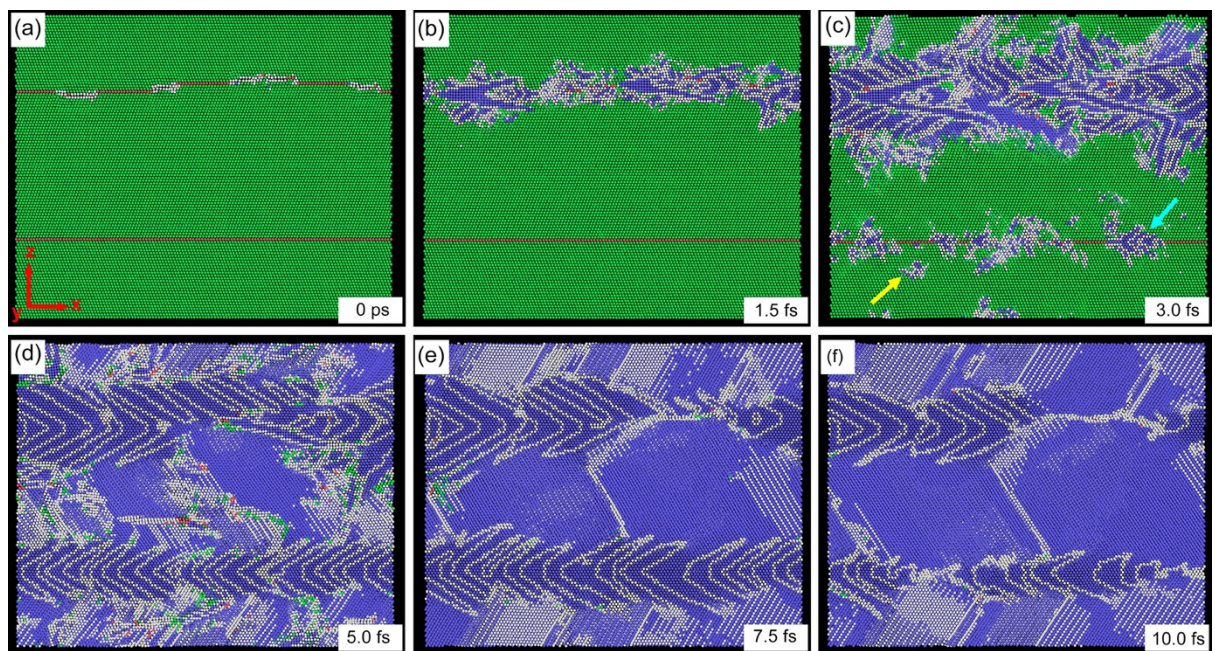


Figure 7-11 Time evolution of the nucleation and growth of bcc phase in fcc iron at 100 K with external strain in the x direction. Colours represent different phase structures: blue-bcc; green-fcc; red-hcp; white-unidentified.

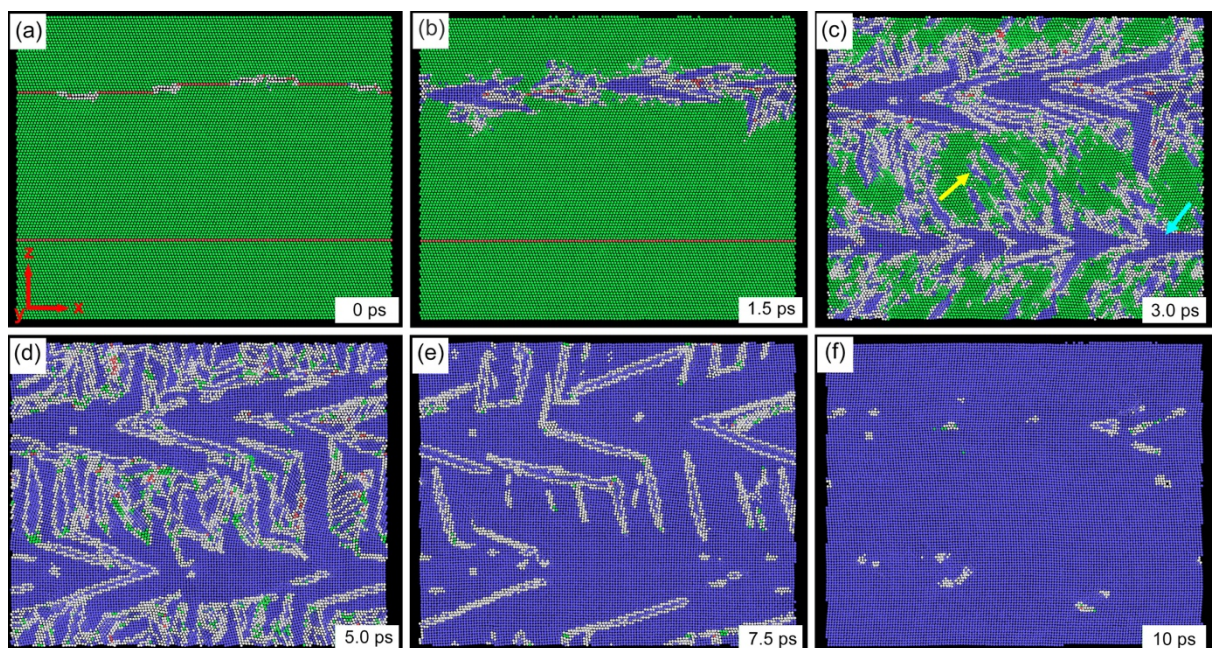


Figure 7-12 Time evolution of the nucleation and growth of bcc phase in fcc iron at 100 K with external strain in the y direction. Colours represent different phase structures: blue-bcc; green-fcc; red-hcp; white-unidentified.

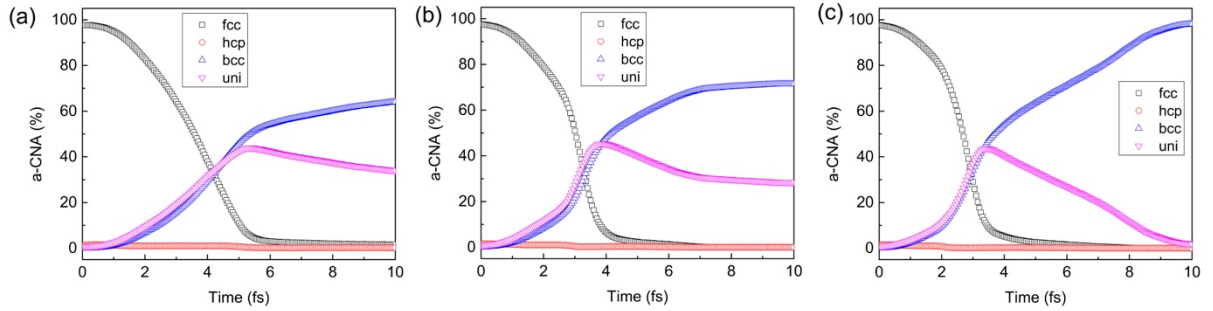


Figure 7-13 The phase fractions of Simulation cell 2: (a) without external strain, (b) with strain in the x direction, (c) with strain in the y direction.

7.3.2.2 Coarsening of bcc grains

For a better view of the grain coarsening process, figure 7-14 shows the enlarged snapshots of the regions inside the yellow dashed rectangles in figure 7-10. The bcc grain, as indicated by Arrow A, nucleates at the incoherent parts at the boundary separated by the coherent part or the stacking faults from each other. The nucleation of bcc phase at the boundaries leads to the generation of bcc/fcc interfaces, which act as sites for the bcc nucleation. The bcc grains pointed by Arrow B and C are two such grains which nucleate at the newly generated bcc/fcc interfaces. Although the two bcc grains labeled by Arrow A and B nucleate independently at different sites, they merge into one coarser bcc grain, as is labeled by Arrow D in figure 7-14(a), upon impingement during their prolonged growth. Both Grain A and Grain B are in the NW OR forming from the same variant $(1\ 1\ 1)_{fcc} || (1\ 1\ 0)_{bcc}$, as indicated by the small pink rectangles in figure 7-14(a). Then the merged Grain D inherits the variant of Grain A and B as indicated by the blue coordinates, with the parallel plane $(1\ 1\ 1)_{fcc} || (1\ 1\ 0)_{bcc}$ and the parallel direction $[\bar{1}\ \bar{1}\ 2]_{fcc} || [\bar{1}\ 1\ 0]_{bcc}$. For Grain C, it follows a different variant, where the corresponding parallel plane and direction are $(1\ 1\ \bar{1})_{fcc} || (1\ 1\ 0)_{bcc}$ and $[1\ 1\ 2]_{fcc} || [\bar{1}\ 1\ 0]_{bcc}$, respectively, as indicated in figure 7-14(b). All bcc grains except Grain C and Grain D are invisible in figure 7-14(b). Although Grain C and D are in the NW OR with different variants, they merge to form a coarser grain upon impingement at 5000 fs. Besides, it is observed that both the Grain C and D grow into the fcc phase in a faceted style with stepped morphology at the bcc/fcc interfaces, as is indicated by the steps at the boundaries of the bcc grains in figure 7-14 (a) and (b). The stepped configuration of the $\{1\ 1\ 1\}_{fcc}$ and $\{1\ 1\ 0\}_{bcc}$ planes was previously observed by Hall *et al.* [23]. It was found that the conjugate habit planes for the NW OR were 10-20° from the $\{1\ 1\ 1\}_{fcc}$ planes for a good fit between the bcc and fcc structures. The corresponding conjugate habit plane between Grain D and the parent fcc phase locates about 15° from the invariant $(1\ 1\ 1)_{fcc}$ plane, as is the same case for Grain C from the $(1\ 1\ \bar{1})_{fcc}$ plane. This leads to an angle of about 100° for the bend in the merged grain in figure 7-14(b), by taking into account of the existing 70° between the $(1\ 1\ 1)_{fcc}$ and $(1\ 1\ \bar{1})_{fcc}$ planes.

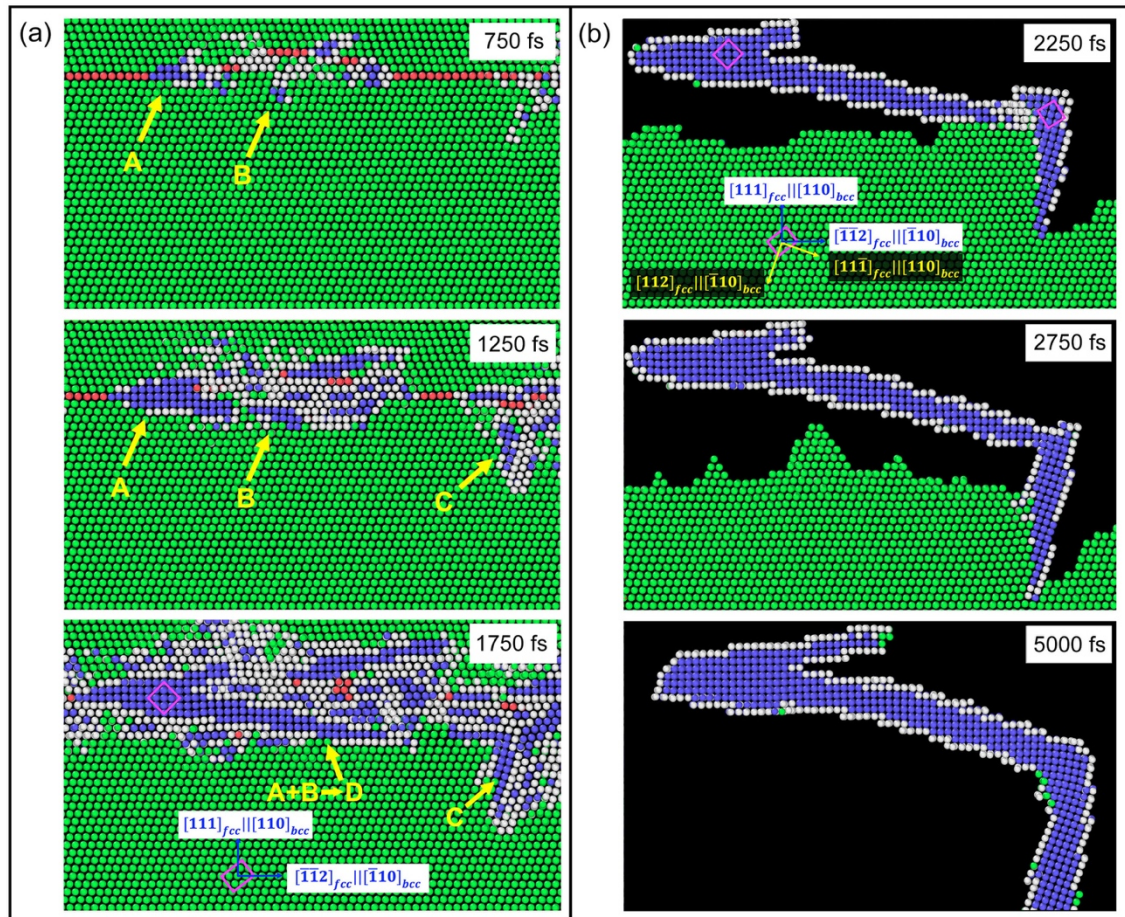


Figure 7-14 Snapshots showing the impingement of bcc grains: (a) in the NW OR forming from the same variant; (b) in the NW OR forming from different variants. The simulation cell is under no external strain. Only the two bcc grains that merge are included in figure (b), while the other bcc grains are excluded for a better view of the merging process.

The deviation angles of the unit cells in Grain D from the ideal NW OR, namely from the parallel direction $[\bar{1}\bar{1}2]_{fcc} || [\bar{1}10]_{bcc}$ and the parallel plane $(111)_{fcc} || (110)_{bcc}$, are calculated, as shown in figures 7-15 (a) and (b), respectively. Because Grain A and Grain B share the identical orientation, small deviation angles of the unit cells from the ideal NW OR are obtained for the merged Grain D. It is seen from figure 7-15(a) that the deviation angles are less than 5° from either the parallel direction or plane for the ideal NW OR. However, the deviation angles of the coarse grain merged from Grain C and D are scattered in the range of 0 to 20° from the NW OR with the parallel plane $(111)_{fcc} || (110)_{bcc}$ and the parallel direction $[\bar{1}\bar{1}2]_{fcc} || [\bar{1}10]_{bcc}$, as indicated in figures 7-15 (c) and (d). This is because Grain C and D have the NW OR but from different variants, and the misorientation between the two variants is 19.5° . Although the orientation gradients as high as 20° remain in the coalesced bcc grain at 5 ps, while no grain boundary exists in the grain, as seen from figure 7-14(b). This indicates that the merging of two adjacent bcc grains involves in only the deformation/distortion of lattices locating at their joint point, but not the rotation of the orientation of a whole bcc grain. This provides a new possibility for the existence of orientation gradients along the laths of martensite, which was observed in experiment by Pak *et al.* [11].

When the simulation cell is under an external strain in the x direction, the coalescence of neighbouring bcc grains takes place, as the regions inside the dashed red rectangles in figures 7-16 (a)-(c). Besides, twinning bcc platelets form in the final structures at 10 ps, as marked by the red lines in figure 7-16(d). In experiments, there were discrepancies with regard to the crystallography of lath martensite in Fe-Alloys. The orientation between neighbouring lath martensite has been reported to be twin-related in [24,25] or non-twin relationship in [26]. Furthermore, a bcc/bcc grain boundary remains where there is originally the semicoherent fcc/fcc twin grain boundary, as pointed by the blue arrow in figure 7-16(d). In the simulation cell under external strain in the y direction (or the $\langle 110 \rangle_{fcc}$ direction), however, one single bcc crystal is obtained in the final structure. The grain coarsening in this system is mainly through coalescence of neighbouring bcc grains, as is marked by the yellow arrows in figure 7-17, in the identical orientation relationship (the NW OR).

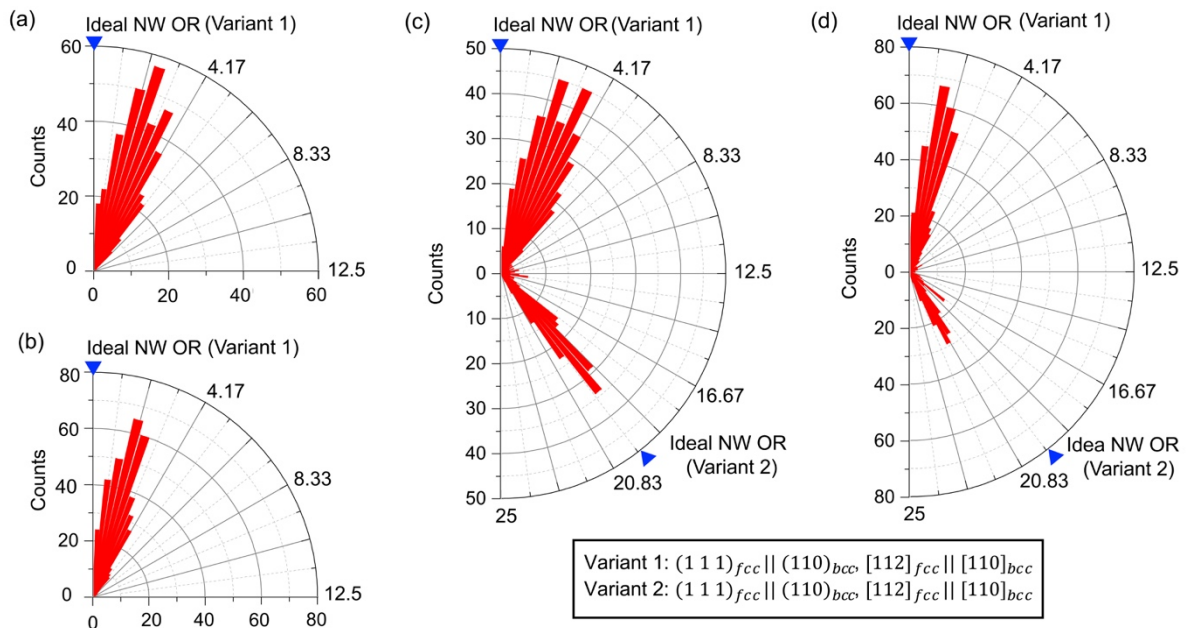


Figure 7-15 Deviation angles of unit cells from: (a) the parallel direction $[\bar{1} \bar{1} 2]_{fcc} || [\bar{1} \bar{1} 0]_{bcc}$; (b) the invariant plane $(1 1 1)_{fcc} || (1 1 0)_{bcc}$ for the merged Grain D in the NW OR at 2250 fs; Deviation angles from: (c) the parallel direction $[\bar{1} \bar{1} 2]_{fcc} || [\bar{1} \bar{1} 0]_{bcc}$; (d) the invariant plane $(1 1 1)_{fcc} || (1 1 0)_{bcc}$ for the coarse grain merged from Grain C and D in the NW OR at 5 ps. The blue triangles in figures (a)-(c) indicate each perfect NW OR variant and a misorientation angle of 19.5° exists between variants 1 and 2.

Different final structures are obtained in the simulation cell with fcc/fcc twin boundaries with or without strain. Besides, strain in different directions also affects the microstructural propagation. Figures 7-18 (a) and (b) show the stress-strain curves in the strained systems under external strain in x and y direction, respectively. The stress in x direction fluctuates when the fcc-to-bcc transformation takes place, which lasts until around 5.0 ps for simulation cell under strain in x direction. For the system under strain in the y direction, the corresponding time lasts until around 4.0 ps. After that, the stress in strained direction increases monotonically in system under strain in x direction, while that decreases to a negative value for system strained in y direction. The different final structures, as shown

Effects of elastic strain on the nucleation and growth of bcc phase in fcc iron by molecular dynamics simulations

by the twinning bcc grains in figure 7-16 and the coalesced single bcc crystal in figure 7-17, explains the different trend of the stress change in the two systems.

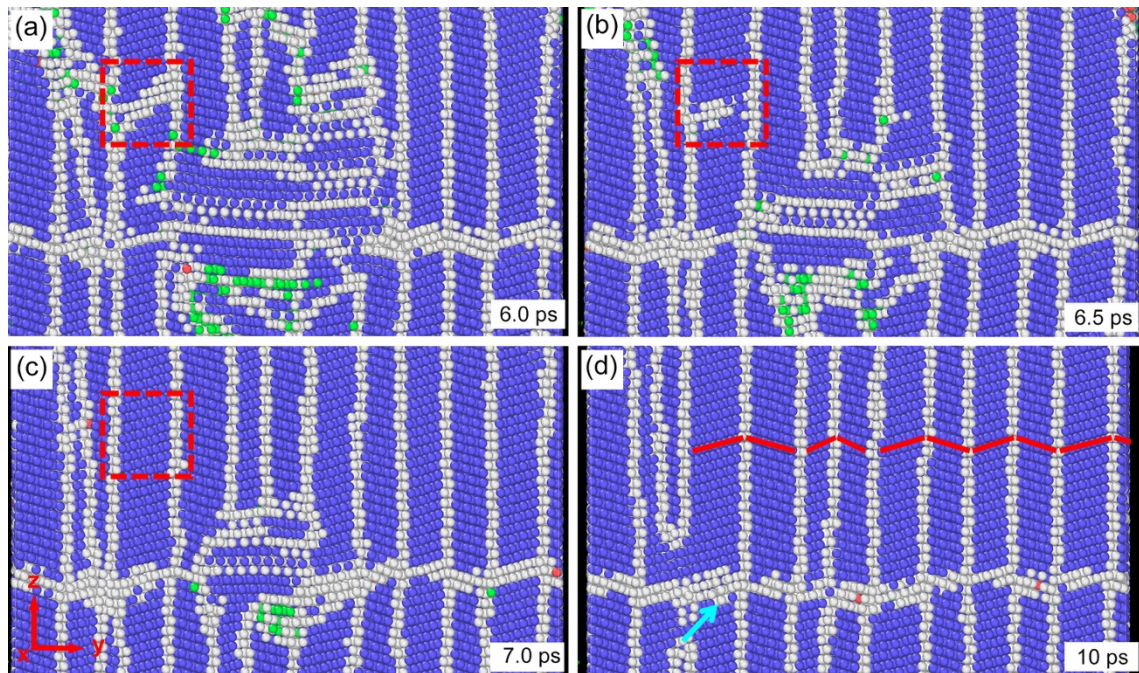


Figure 7-16 Snapshots illustrating the grain coarsening by coalesce of neighbouring bcc grains as well the twinning structures in simulation cell under strain in the x direction.

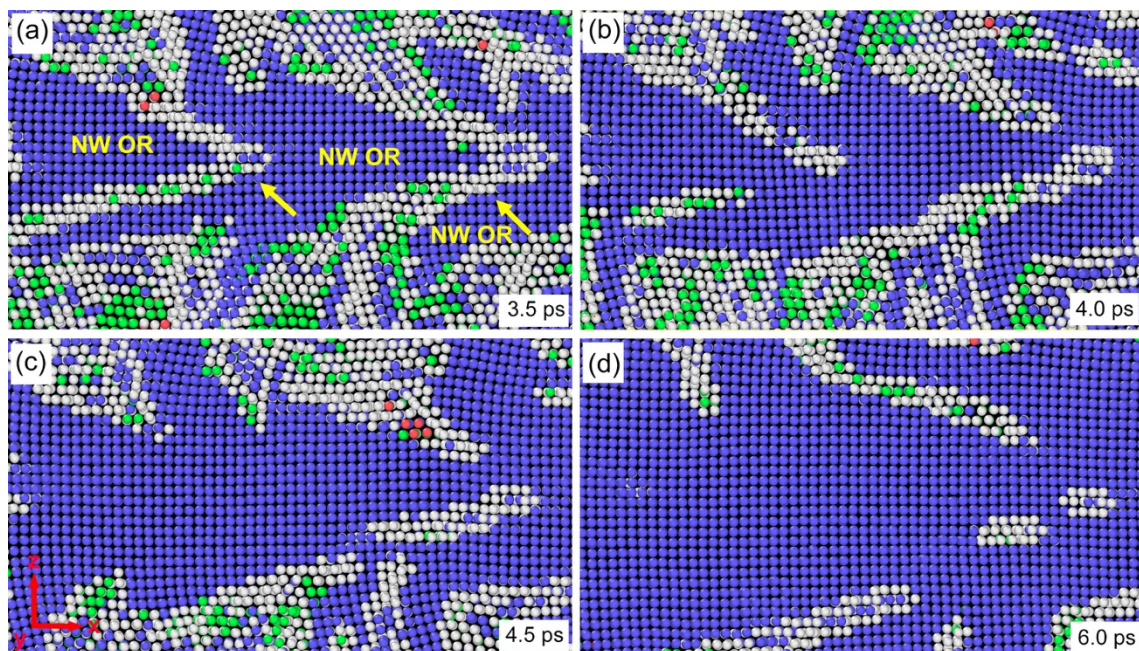


Figure 7-17 Grain coarsening by coalescence of neighbouring bcc grains with the identical orientation in the simulation cell under strain in the y direction.

External strain along the crystallographic direction of $\langle 112 \rangle_{fcc}$ leads to the formation of twinning bcc grains, while the strain along the $\langle 110 \rangle_{fcc}$ results in a single bcc grain in the final structure. The external strain direction has an effect on the selection of preferred orientation variants, as indicated

by Equation (7-1). Thus the underlying mechanisms may be related to the interaction between the external strain and the internal strains induced by the fcc-to-bcc transformation through a specific transformation path, which however needs further studies.

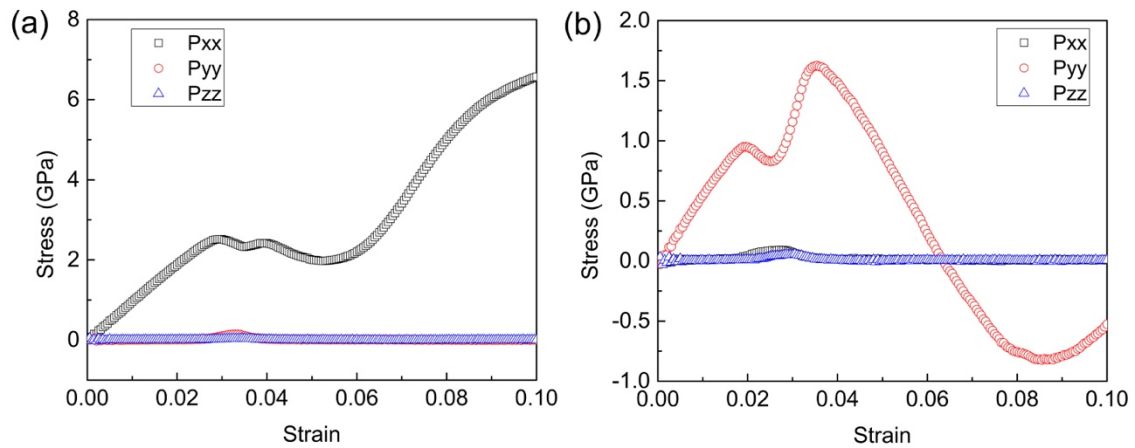


Figure 7-18 The stress-strain curves of Simulation cell 2: (a) with strain in the x direction, (b) with strain in the y direction.

7.4 Conclusions

The present chapter performs a preliminary study of the effects of external strain on the nucleation and growth of bcc phase in fcc iron. The results are summaries as follows:

(1) For the single fcc crystal, the fcc-to-bcc transformation in fcc iron can be induced by an external strain at or below 100 K. The strain-induced bcc grains, which tend to have a plate-like morphology, prefer to form in one dominant orientation with specific variants. The KS OR dominates the bcc platelets at 50 K while the NW OR is the dominant at 100 K. Besides, the external strain contributes to the grain coarsening by coalescence of neighbouring bcc platelets forming from the identical orientation. Those bcc grains tend to lie about 45° to the external strain direction.

(2) For the simulation cell with fcc/fcc grain boundaries, external strain also induces the nucleation of bcc phase from both the semicoherent and coherent fcc/fcc twin boundary. The bcc nuclei forming in the simulation cell with fcc/fcc boundaries are either in the NW or the KS OR without external strain. However, an external strain leads to a dominant crystallographic orientation relation in the simulation cell. A strain in the $\langle 112 \rangle_{fcc}$ direction leads to a dominant KS OR while a strain in the $\langle 110 \rangle_{fcc}$ direction results in a dominant NW OR. Besides, different final structures are obtained for the simulation cells with or without strain. When there is no external strain, the grain coarsening is mainly by impingement of bcc grains with the same OR during the fcc-to-bcc transformation as well as by normal growth resulting from boundary curvature. Small deviations from the ideal crystallographic orientation relation are obtained for the coarse bcc grain when the merging bcc grains are in the identical OR. Otherwise, large deviations exist across the merged bcc grains. An external strain in the

Effects of elastic strain on the nucleation and growth of bcc phase in fcc iron by molecular dynamics simulations

$\langle 112 \rangle_{fcc}$ direction leads to twinning bcc grains in the final structure. The external strain in the $\langle 110 \rangle_{fcc}$ direction, nonetheless, leads to a single bcc crystal.

In summary, the same external strain leads to varied final crystallographic structures at different isothermal temperatures, namely 50 K and 100 K, in the present MD simulations. It was reported in experiments that the tensile strength increases with decreasing temperature during the tensile tests of metastable austenitic steels, because the volume fraction of martensite increases with decreasing deformation temperature [27]. Further studies are needed for the effects of a wider range of temperatures on the fcc-to-bcc transformation in iron by MD simulations. Besides, the strain rate applied in present study is fixed at 0.01 ps^{-1} . According to the experimental investigation [22], different strain rates affect the martensitic transformation in steels, such as the transformation temperature. Therefore, it would be interesting to study the effects of different strain rates on the fcc-to-bcc transformation in iron for future investigations. In the present MD simulations, external strain along the crystallographic direction of $\langle 112 \rangle_{fcc}$ leads to the formation of twinning bcc grains, while the strain along the $\langle 110 \rangle_{fcc}$ results in a single bcc grain in the final structure. Further investigation is needed regarding the underlying mechanisms controlling the formation of bcc grains in specific orientations, as well as the coalescence of bcc grains with identical orientation.

7.5 References

- [1] S. Zaeferrer, J. Ohlert and W. Bleck, 'A study of microstructure, transformation mechanisms and correlation between microstructure and mechanical properties of a low alloyed TRIP steel', *Acta Mater.*, 2004, 52, 2765-2778.
- [2] S. Chatterjee and H. K. D. H. Bhadeshia, 'Transformation induced plasticity assisted steels: Stress or strain affected martensitic transformation?', *Mater. Sci. Technol.*, 2007, 23, 1101-1104.
- [3] T. -H. Ahn, C. -S. Oh, D. H. Kim, K. H. Oh, H. Bei, E. P. George and H. N. Han, 'Investigation of strain-induced martensitic transformation in metastable austenite using nanoindentation', *Scripta Mater.*, 2010, 63, 540-543.
- [4] L. Sandoval and H. M. Urbassek, 'Finite-size effects in Fe-nanowire solid-solid phase transitions: a molecular dynamics approach', *Nano letters*, 2009, 9, 2290-2294.
- [5] B. J. Wang and H. M. Urbassek, 'Molecular dynamics study of the α - γ phase transition in Fe induced by shear deformation', *Acta Mater.*, 2013, 61, 5979-5987.
- [6] G. B. Olson and M. Azrin, 'Transformation behavior of TRIP steels', *Metall. Trans. A*, 1978, 9A, 713-721.
- [7] G. B. Olson and M. Cohen, 'Stress-assisted isothermal martensitic transformation: application to TRIP steels', *Metall. Trans. A*, 1982, 13, 1907-1914.
- [8] E. Cotrina, A. Iza-Mendia, B. López and I. Gutiérrez, 'Study of the ferrite grain coarsening behind the transformation front by electron backscattered diffraction techniques', *Metall. and Mater. Trans. A*, 2004, 35, 93-102.
- [9] H. Pous-Romero and H. K. D. H. Bhadeshia, 'Coalesced martensite in pressure vessel steels', *J. Press. Vessel Technol.*, 2014, 136, 031402.
- [10] J. H. Pak, H. K. D. H. Bhadeshia and L. Karlsson, 'Mechanism of misorientation development within coalesced martensite', *Mater. Sci. Technol.*, 2012, 28, 918-923.
- [11] J. H. Pak, D. W. Suh and H. K. D. H. Bhadeshia, 'Promoting the coalescence of bainite platelets', *Scripta Mater.*, 2012, 66, 951-953.
- [12] J. H. Pak, H. K. D. H. Bhadeshia, L. Karlsson and E. Keehan, 'Coalesced bainite by isothermal transformation of reheated weld metal', *Sci. Technol. Weld. Joi.*, 2008, 13, 593-597.
- [13] H. K. D. H. Bhadeshia, E. Keehan, L. Karlsson and H. -O. Andrés, 'Coalesced bainite', *Trans. Indian Inst. Met.*, 2006, 59, 689-694.
- [14] M. I. Mendelev, S. Han, D. J. Srolovitz, G. J. Ackland, D. Y. Sun and M. Asta, 'Development of new interatomic potentials appropriate for crystalline and liquid iron', *Phil. Mag.*, 2003, 83, 3977-3994.
- [15] S. Plimpton, 'Fast parallel algorithms for short-range molecular dynamics', *J. Comp. Phys.*, 1995, 117, 1-19. <http://lammps.sandia.gov/>. Accessed on September 4th, 2017.
- [16] A. Stukowski, 'Structure identification methods for atomistic simulations of crystalline materials', *Modell. Simul. Mater. Sci. Eng.*, 2012, 20, 045021.
- [17] A. Stukowski, 'Visualization and analysis of atomistic simulation data with OVITO-the open visualization tool', *Modell. Simul. Mater. Sci. Eng.*, 2010, 18, 015012.
- [18] D. A. Porter and K. E. Easterling, 'Phase transformation in metals and alloys', second ed.,

Chapman & Hall, London, 1992.

- [19] Z. Nishiyama, 'X-ray investigation of the mechanism of the transformation from face-centred to body-centred cubic lattice', *Sci. Rep. Tohoku Imp. Univ.*, 1934, 23, 637-664. Cited by M. G. Hall, H. I. Aaronson and K. R. Kinsman, 'The structure of nearly coherent fcc: bcc boundaries in a Cu-Cr alloy', *Surf. Sci.*, 1972, 31, 257-274.
- [20] G. V. Kurdjumov and G. Sachs, 'Über den mechanismus der stahlhärtung', *Z. Phys.*, 1930, 64, 325-343. Cited by M. G. Hall, H. I. Aaronson and K. R. Kinsman, 'The structure of nearly coherent fcc: bcc boundaries in a Cu-Cr alloy', *Surf. Sci.*, 1972, 31, 257-274.
- [21] K. Koumatos and A. Muehlemann, 'A theoretical investigation of orientation relationships and transformation strains in steels', *Acta Cryst.*, 2017, A73, 115-123.
- [22] H. N. Han, C. G. Lee, C. -S. Oh, T. -H. Lee and S. -J. Kim, 'A model for deformation behavior and mechanically induced martensitic transformation of metastable austenitic steel', *Acta Mater.*, 2004, 52, 5203-5214.
- [23] M. G. Hall, H. I. Aaronson and K. R. Kinsma, 'The structure of nearly coherent fcc: bcc boundaries in a Cu-Cr alloy', *Surf. Sci.*, 1972, 31, 257-274.
- [24] T. Inoue, S. Matsuda, Y. Okamura and K. Aoki, 'The fracture of a low carbon tempered martensite', *Trans. JIM*, 1970, 11, 36-43.
- [25] P. M. Kelly, 'The martensite transformation in steels with low stacking fault energy', *Acta Metall.*, 1965, 13, 635-646.
- [26] K. Wakasa, C. M. Wayman, H. Kubo and K. Shimizu, 'The relative orientation between adjacent martensite laths in an Fe-20%Ni-5%Mn alloy', *Scripta Metall.*, 1980, 14, 261-268.
- [27] N. Tsuchida, Y. Morimoto, T. Tonan, Y. Shibata, K. Fukaura and R. Ueji, 'Stress-induced martensitic transformation behaviors at various temperatures and their TRIP Effects in SUS304 metastable austenitic stainless steel', *ISIJ Int.*, 2011, 51, 2011, 124-129.

Chapter 8

Conclusions and outlook

The objective of this project is to understand the nucleation and growth of martensite transformed from the austenite in iron. Molecular dynamics simulation is employed to study the mechanisms controlling the propagation of the semi-coherent and incoherent bcc/fcc interfaces into the fcc bulk in iron. A new universal method is proposed to study the thermodynamics of nucleation during solid-solid phase transformations in metals and alloys from the output data of molecular dynamics simulations. The thermodynamics of the homogeneous nucleation of bcc phase inside the fcc bulk is investigated based on both the classical nucleation theory and nonclassical mechanisms. The thermodynamics of the heterogeneous nucleation of bcc phase at dislocations on fcc/fcc grain boundaries is analysed in the frame of Cahn's theoretical model. Aspects that are not considered by Cahn's model are also discussed. Considering the effects of strain on the microstructures and thus the mechanical properties of materials, the strain-induced fcc-to-bcc transformation is explored. The understanding of the nucleation and growth of bcc phase in fcc iron will contribute to a better control of production processes and thus improved mechanical properties of steels in industry.

8.1 Conclusions

The main contributions of this research are as follows:

1. The mechanisms controlling the growth of the original bcc phase during the fcc-to-bcc transformation are studied in three systems with semi-coherent bcc/fcc interfaces. The bcc/fcc interfaces propagate into the fcc bulk involving a limited number of atomic layers in a faceted style. Growth of bcc phase starts from the areas of low potential energy at the original bcc/fcc interfaces and develops into the high-energy areas. Growth of bcc phase at low potential energy areas follows the faulting mechanism proposed by Olson and Cohen based on the Bogers-Burgers model, which is of a martensitic character. However, the growth of bcc phase in the high potential energy areas at the original fcc/bcc interfaces involves atomic jumps for a small fraction of the atoms.

2. A new universal method is proposed to analyse the thermodynamics of the nucleation during solid-solid phase transformations or the recrystallisation process in materials by molecular dynamics simulation. Rather than estimating the bcc nucleation details based on a growing stable grain, this study analyses the nucleation event directly. This method has been employed to study both the homogeneous and heterogeneous nucleation of bcc phase in fcc iron by molecular dynamics simulations in this thesis.

3. Both the classical nucleation theory and nonclassical mechanisms are employed to determine whether they apply to the homogeneous nucleation during the solid-solid phase transformation. Although the classical nucleation theory is not considering atoms, it turns out to successfully describe the thermodynamic tendency during the postcritical nucleation period of a nucleus during solid-solid phase transformation in systems with discrete atoms. The fitting parameters based on the classical nucleation theory, namely the activation energy, the number of atoms in the critical nucleus and the interfacial energy γ are physically reasonable and comparable to the experimental results. However, the nonclassical processes, such as the aggregation of nuclei and the formation of metastable intermediates, helps to circumvent the high energy barriers for homogeneous nucleation. The fcc phase transforms to the bcc phase preferably following a stepwise “fcc→intermediate state→bcc” rather than a single-step “fcc→bcc” procedure. Two energy barriers are involved, one for the nucleation of the intermediate state from the parent fcc phase and the other for the nucleation of bcc phase from the intermediate state. The bcc nuclei are aggregates of discrete prenucleation bcc clusters, which are bonded as an integral nucleus by the intermediate state. The neighbouring prenucleation clusters may have different orientation relationships with the parent fcc phase. Aggregation of a neighbouring cluster contributes to the stabilisation of a nucleus. Regardless of the constant temperature of the systems, the local temperature of the region with bcc nucleation is non-isothermal and fluctuates around the equilibrium temperature of the system.

4. The thermodynamics of heterogeneous nucleation of bcc phase at dislocations in fcc/fcc grain boundaries in iron is studied by molecular dynamics simulations. The energy change as a function of

the size for the bcc nuclei agrees well with Cahn's model, where no energy barrier is needed. The estimated elastic constants and interface energies are comparable to the published theoretical values and experimental results. However, there are aspects that are not considered by Cahn's model. Similar to the homogeneous nucleation, the fcc phase transforms to the bcc phase preferably following a stepwise "fcc→intermediate state→bcc" rather than a single-step "fcc→bcc" procedure. In this case, the intermediate state initiates from the dislocations without an energy barrier. This is followed by the nucleation of bcc phase from the intermediate state, where an energy barrier is involved. The bcc nuclei are aggregates of discrete prenucleation bcc clusters, which may have different orientation relationships with the parent fcc phase. Regardless of isothermal conditions, the local regions containing the bcc nuclei are warmer than the surroundings due to the heat release during phase transformations.

5. A preliminary study is performed regarding the effects of external strain on the nucleation and growth of bcc phase in fcc iron by molecular dynamics simulation. For the single fcc crystal, the strain-induced bcc grains, which tend to have a plate-like morphology, prefer to form in one dominant orientation with specific variants. Different deformation temperatures affect the crystallographic orientations of the product bcc grains. The Nishiyama-Wassermann orientation relationship dominates at 100 K, while the fcc phase transforms to the bcc phase mainly in the Kurdjumov-Sachs orientation relationship at 50 K. The external strain in a specific direction leads to reduced variants of crystallographic orientations, which contributes to the grain coarsening by coalescence of neighbouring bcc platelets forming from the identical orientation. For the simulation cell with fcc/fcc grain boundaries, the bcc nuclei forming are either in the Nishiyama-Wassermann or the Kurdjumov-Sachs orientation relationship without external strain. The grain coarsening is mainly by impingement of bcc grains with the same crystallographic orientation relation as well as by normal growth resulting from boundary curvature. However, an external strain leads to a dominant crystallographic orientation relation in the simulation cell. A strain in the $\langle 112 \rangle_{fcc}$ direction leads to a dominant Kurdjumov-Sachs orientation relationship while a strain in the $\langle 110 \rangle_{fcc}$ direction results in a dominant Nishiyama-Wassermann orientation relationship. Besides, different final structures are obtained for the simulation cell strained in different directions. An external strain in the $\langle 112 \rangle_{fcc}$ direction leads to twinning bcc grains in the final structure while an external strain in the $\langle 110 \rangle_{fcc}$ direction leads to a single bcc crystal.

8.2 Outlook for future research

Based on the aim of the present thesis, the following recommendations are proposed for the future research:

1. Three semicoherent bcc/fcc interfaces studied in this thesis have parallel $(111)_{fcc} \parallel (110)_{bcc}$ planes. The fcc-to-bcc transformation initiates from the low-energy areas following a faulting

mechanism and develops into the high-energy areas with atomic jumps. In experiments, the habit planes of the bcc/fcc interfaces involve a misorientation angle of 10° to 20° around the $[1\bar{1}0]_{fcc}$ direction. It is expected that those rotated habit planes have different crystallographic stacking patterns between the bcc and fcc structures and therefore different atomic energy distributions. Based on the results in this thesis, the propagation of bcc/fcc interfaces with rotated habit planes about the $[1\bar{1}0]_{fcc}$ direction can be investigated in the future work.

2. The molecular dynamics simulations in this thesis indicate that both the homogeneous and heterogeneous nucleation of bcc phase during the fcc-to-bcc transformation in iron takes place following a stepwise “fcc→intermediate state→bcc” process. The homogeneous nucleation of the intermediate state inside the fcc iron involves an energy barrier, while no energy barrier is needed for the heterogeneous nucleation of the intermediate metastable state at fcc/fcc grain boundaries. For the thermodynamic analysis of bcc nucleation in this thesis, it is assumed that all unidentified atoms belong to the intermediate state due to the difficulty in distinguishing between atoms belonging to dislocations, intermediate state and bcc/fcc interfaces. Thermodynamics regarding the nucleation of the intermediate state in fcc iron can be investigated for future work in case that there is a crystallographic structure discriminator capable of distinguishing the currently “unidentified” atoms.

3. In experiments, the preferable sites for heterogeneous nucleation are the corners where four parent grains meet, followed by junctions where three grains meet and then the grain faces where two grains meet. This thesis studies the heterogeneous nucleation of bcc phase at dislocations in fcc/fcc grain boundaries. Further investigations may adapt the thermodynamic analysis method proposed in this thesis to study the heterogeneous nucleation of bcc phase at the meeting junctions or corners of multiple fcc grains.

4. Molecular dynamics simulations in this thesis indicate that external strain induces the fcc-to-bcc transformation in fcc iron. Varied dominant crystallographic orientations are obtained for the product bcc phase forming in fcc iron at different deformation temperatures, for which the underlying mechanisms need further exploration. In reality, higher deformation temperature leads to smaller volume fraction of martensite and higher tensile strength during the tensile tests of metastable austenitic steels. Besides, strain rate affects martensitic transformation in steels as well. This thesis includes a preliminary study involving one strain rate (0.01 ps^{-1}) and two deformation temperatures (50 K and 100 K). Future work may focus on the effects of different strain rates on the fcc-to-bcc transformation in iron at various deformation temperatures. Furthermore, this thesis indicates that external strains in different directions result in different final structures in iron. External strain along the crystallographic direction of $\langle 112 \rangle_{fcc}$ leads to the formation of twinning bcc grains, while the strain along the $\langle 110 \rangle_{fcc}$ results in a single bcc grain in the final structure. The underlying mechanisms leading to those different final structures in iron remain unclear and need further studies by molecular dynamics simulations.

5. In steels, alloying elements, such as carbon, chromium and manganese, coexist with iron. The contents and distribution of those elements influence the microstructure and thus mechanical properties of steels. The current thesis studies the nucleation and growth of bcc phase in pure iron, which provide information for the future investigations in steels containing alloying elements by molecular dynamics simulation.

6. The knowledge of the nucleation and growth of bcc phase in fcc iron obtained from the molecular dynamics simulations in the present thesis can be applied to understanding the microstructural development during phase transformations, such as martensitic transformation, in steels in the experimental studies. This enables a better control of the microstructure and mechanical properties in the production of steels in industry.

Summary

The aim of this PhD. thesis is to use molecular dynamics (MD) simulations to comprehend the mechanisms governing nucleation and growth of martensite phase in austenitic phases in iron. In view of this objective, the thesis is divided into five parts: Chapter 2 reviews previous investigations of the fcc-to-bcc transformation in iron by MD simulations; Chapter 3 performs a preliminary study of the nucleation and growth of bcc phase into fcc bulk in iron at existing bcc/fcc interfaces in the Nishiyama-Wassermann orientation relationship; Chapter 4 studies the mechanisms governing the growth of bcc phase at bcc/fcc interfaces in iron; Chapter 5 and 6 study the thermodynamics of the homogeneous and heterogeneous nucleation of bcc phase inside the fcc crystals, respectively; Chapter 7 illustrates the effects of external strain on the nucleation and growth of bcc phase in fcc iron with (and without) fcc/fcc grain boundaries. A more detailed description of each chapter are included below.

Chapter 2 reviews the background of the martensitic transformation in steels as well as the development of the researches with regard to the fcc-to-bcc transformation in iron by MD simulations. Factors affecting the simulated fcc-to-bcc transformation in iron are included. The fcc-to-bcc transformation is found to take place in the MD simulations by introducing structural defects, such as fcc/fcc grain boundaries, dislocations, phase interfaces and stacking faults. External conditions, such as temperature, stress/strain and free surfaces, will also affect the evolution of the fcc-to-bcc transformation. Key questions that demand further studies are extracted. The first refers to the way the bcc nucleus initiates and stabilise inside the solid bulk of fcc iron. The thermodynamics of the martensitic nucleation, either homogeneously or heterogeneously, has been rarely studied and needs further study. The second is about the mechanisms of the growth of bcc phase during the fcc-to-bcc transformation. A bcc/fcc interface might be glissile/athermal depending on its crystallographical orientation. A better understanding of the way the bcc phase grows at the bcc/fcc interfaces determines the microstructural homogeneity, for example the grain size, and thus the mechanical properties of the materials.

Chapter 3 studies the fcc-to-bcc transformation in iron with semi-coherent bcc/fcc interfaces in the Nishiyama-Wassermann orientation relationship. The original bcc bulk grows into the fcc bulk in a faceted way. Heterogeneous nucleation of bcc phase takes place at the propagating bcc/fcc interfaces, while homogeneous nucleation of bcc phase occurs inside the fcc bulk. The homogeneous and heterogeneous bcc nuclei impede the further propagation of the bcc/fcc interfaces. Coalescence of neighbouring bcc plates is observed locally. The fcc-to-bcc transformation is of a predominant martensitic nature. Observations in the present chapter, namely growth of bcc phase at the bcc/fcc grains, homogeneous and heterogeneous nucleation of bcc phase as well as the coalescence of neighbouring bcc grain, provides clues for the studies in the following chapters in the present thesis.

Chapter 4 studies the mechanisms controlling the growth of bcc phase into the fcc bulk in iron with bcc/fcc interfaces. Three bcc/fcc interfaces in the Nishiyama-Wassermann, Kurdjumov-Sachs and Nagano orientation relationships propagate into the fcc bulk involving a limited number of atomic layers in a faceted style. Growth of bcc phase starts in the areas of low potential energy at the original bcc/fcc interfaces and develops into the high-energy areas. Growth of bcc phase at low potential energy areas follows the faulting mechanism proposed by Olson and Cohen based on the Bogers-Burgers model. A collective motion of atoms in the low potential energy areas is involved, which is of a martensitic character. However, the high energy areas at the original fcc/bcc interfaces involve diffusional atomic jumps for a small fraction of the atoms.

Chapter 5 proposes a universal method to analyse the thermodynamics of homogeneous nucleation, which applies to a variety of materials during the liquid-solid solidification process or the solid-solid phase transformations. Homogeneous nucleation of bcc phase takes place in single fcc crystal at 160 K. The bcc nuclei are more in elliptical morphologies than spheres. In overall, the energy change of a postcritical nucleus as a function of its size agrees well with the trend predicted by the classical nucleation theory (CNT). The critical nucleus size from the fitting work are comparable to the experimental results. However, the CNT overestimates the energy barriers for homogeneous nucleation of bcc phase. The high energy barrier envisioned by the CNT is circumvented by nonclassical mechanisms, such as the aggregation of nuclei and formation of metastable intermediates. The fcc phase transforms to the bcc phase preferably following a stepwise “fcc→intermediate state→bcc” procedure. The intermediate state nucleates inside the parent fcc phase with an energy barrier. This is followed by another energy barrier for the nucleation of bcc phase inside the intermediate state. Aggregation of a neighbouring subcritical cluster provides the opportunity for the primary nucleus to reach and surpass the critical size and to circumvent the high CNT-predicted energy barrier for homogeneous nucleation. The neighbouring subcritical clusters may have different crystallographic orientations with the primary nucleus. Local temperature of the bcc nuclei fluctuates regardless of the constant temperature of the whole systems.

Chapter 6 investigates the heterogeneous nucleation of bcc phase forming at dislocations on the fcc/fcc grain boundaries. Two simulation systems with different fcc/fcc grain boundaries are studied. One has two low-angle grain boundaries with edge dislocations. The other system consists of one semi-coherent twin grain boundary and one coherent twin grain boundary. Thermodynamics of the bcc nucleation at the dislocation is found to agree with the prediction of Cahn’s model. The estimated elastic constants, and interface energies are comparable to the theoretical calculations and the experimental results. However, there are aspects that are not considered by Cahn’s model. Similar to the homogeneous nucleation of bcc phase in fcc iron, the fcc phase transforms to the bcc phase preferably following nonclassical mechanisms such as the aggregation of nuclei and stepwise “fcc→intermediate state→bcc” nucleation. However, the intermediate state initiates from the dislocations without energy barrier, while the homogeneous nucleation of bcc phase inside the intermediate state involves an energy barrier. The bcc nuclei are aggregates of discrete subcritical bcc clusters, which are bond as an integral by the

intermediate state. Such neighbouring subcritical clusters may have different orientation relationships and are coherent with the parent fcc phase. Regardless of isothermal conditions, the local regions containing the bcc nuclei are warmer than the surroundings due to the heat release during phase transformations.

Chapter 7 studies the effects of external strain on the nucleation and growth of bcc phase in fcc iron. For the single fcc crystal, the fcc-to-bcc transformation in fcc iron can be induced by an external strain or stress at or below 100 K. The strain-induced bcc grains tend to have a plate-like morphology and prefer to form in one dominant orientation with specific variants. The Kurdjumov-Sachs orientation dominates the bcc platelets at 50 K while the Nishiyama-Wassermann orientation is the dominant at 100 K. Besides, the external strain contributes to the grain coarsening by coalescence of neighbouring bcc platelets forming from the identical orientation. Those bcc grains tend to lie about 45° to the external strain direction. For the simulation cell with fcc/fcc grain boundaries, external strain induces the nucleation of bcc phase from both the semicoherent and coherent fcc/fcc twin boundary. The bcc nuclei forming in the simulation cell with fcc/fcc boundaries are either in the Nishiyama-Wassermann or the Kurdjumov-Sachs orientation without external strain. However, an external strain leads to a dominant crystallographical orientation in the simulation cell. A strain in the $\langle 112 \rangle_{fcc}$ direction leads to a dominant Kurdjumov-Sachs orientation while a strain in the $\langle 110 \rangle_{fcc}$ direction results in a dominant Nishiyama-Wassermann relation. Besides, different final structures are obtained for the simulation cells with and without strain. When there is no external strain, the grain coarsening is mainly by impingement of bcc grains with the same crystallographical orientation during the fcc-to-bcc transformation as well as by normal growth resulting from boundary curvature. Small deviations from the ideal crystallographical orientation are obtained for the coarse bcc grain when the merging bcc grains are in the identical orientation forming from the variant. Otherwise, large deviations exist across the merged bcc grains. An external strain in the $\langle 112 \rangle_{fcc}$ direction leads to twinning bcc grains in the final structure. The external strain in the $\langle 110 \rangle_{fcc}$ direction, nonetheless, leads to a single bcc crystal in the final structure.

Finally, Chapter 8 summarises the main conclusions of this study. There are also a number of recommendations for follow-up research.

Samenvatting

Het doel van dit proefschrift is om met behulp van moleculaire dynamica (MD) simulaties de mechanismen te begrijpen achter de kiemvorming en groei van martensiet in austeniet in ijzer. Het proefschrift bestaat uit vier delen: hoofdstuk 2 geeft een overzicht van vorig onderzoek met MD simulaties aan de fcc-naar-bcc transformatie in ijzer; hoofdstuk 3 beschrijft een vooronderzoek naar de kiemvorming en groei van de bcc fase in fcc bulk in ijzer op bestaande bcc / fcc interfaces met de Nishiyama-Wassermann oriëntatierelatie; hoofdstuk 4 onderzoekt de mechanismen die de groei van de bcc fase op bcc / fcc interfaces in ijzer bepalen; hoofdstukken 5 en 6 bestuderen de thermodynamica van respectievelijk de homogene en heterogene kiemvorming van de bcc fase in fcc-kristallen; hoofdstuk 7 illustreert de effecten van extern opgelegde rek op de kiemvorming en groei van de bcc fase in fcc ijzer met (en zonder) fcc / fcc korrelgrenzen. Een meer gedetailleerde beschrijving van elk hoofdstuk is hieronder opgenomen. Hoofdstuk 8 bevat conclusies en aanbevelingen.

Hoofdstuk 2 behandelt de achtergrond van de martensitische transformatie in staal, evenals de ontwikkeling in het onderzoek naar de fcc-naar-bcc-transformatie in ijzer door MD-simulaties. Factoren die de gesimuleerde fcc-naar-bcc transformatie in ijzer beïnvloeden worden ook behandeld. De fcc-naar-bcc-transformatie vindt plaats in de MD-simulaties door structuurdefecten in te voeren, zoals fcc / fcc korrelgrenzen, dislocaties, fase-interfaces en stapelfouten. Externe condities, zoals temperatuur, spanning / rek en vrije oppervlakken, zullen ook de evolutie van de fcc-naar-bcc transformatie beïnvloeden. Belangrijke vragen die verdere studie vereisen worden bepaald. De eerste verwijst naar de manier waarop de bcc-kiem initieert en stabiliseert in het fcc-ijzer. De thermodynamica van de martensitische kiemvorming, hetzij homogeen of heterogeen, is zelden bestudeerd en heeft verdere studie nodig. De tweede gaat over degroeimechanismen van de bcc fase tijdens de fcc-naar-bcc transformatie. Een bcc / fcc interface kan *glissile* / *athermal* zijn, afhankelijk van zijn kristallografische oriëntatie. Een beter begrip van de groei door beweging van bcc / fcc interfaces kan bijdragen aan materialen met betere microstructuren en dus betere mechanische eigenschappen.

Hoofdstuk 3 bestudeert de fcc-naar-bcc transformatie in ijzer met semi-coherente bcc / fcc interfaces met de Nishiyama-Wassermann oriëntatierelatie. Het originele bcc kristal groeit in het fcc kristal op een *faceted* manier. Heterogene kiemvorming van de bcc fase vindt plaats bij de voortschrijdende bcc / fcc interfaces, terwijl homogene kiemvorming van de bcc fase voorkomt binnen het fcc kristal. De homogene en heterogene bcc-kiemen belemmeren de verdere beweging van de bcc / fcc-interfaces. Het aaneengroeien van naburige bcc platen wordt lokaal waargenomen. De fcc-naar-bcc transformatie is voornamelijk van martensitische aard. De waarnemingen in dit hoofdstuk, namelijk groei van de bcc fase bij de bcc / fcc korrelgrenzen, homogene en heterogene kiemvorming van de bcc fase, alsmede het aaneengroeien van naburige bcc korrels, geven aanwijzingen voor de studies in de volgende hoofdstukken in dit proefschrift.

Hoofdstuk 4 bestudeert de mechanismen die de groei bepalen van de bcc-fase in een fcc-kristal in ijzer met bcc / fcc-interfaces. Drie bcc / fcc-interfaces in de Nishiyama-Wassermann-, Kurdjumov-Sachs- en Nagano-oriëntatierelaties groeien in het fcc-kristal dat een beperkt aantal atoomlagen in een gefacetteerde stijl bevat. De groei van de bcc fase begint in een gebied van lage potentiële energie bij de oorspronkelijke bcc / fcc interfaces en ontwikkelt zich naar de gebieden met hogere energie. De groei van de bcc-fase in lage potentiële energiegebieden volgt het '*faulting mechanism*' dat Olson en Cohen voorstellen, gebaseerd op het Bogers-Burgers model. Hierbij is sprake van een collectieve beweging van atomen in de lage potentiële energiegebieden die van martensitisch karakter is. Echter in de hoge energiegebieden bij de oorspronkelijke fcc / bcc interfaces is sprake van diffusionele atoomsprongen voor een klein deel van de atomen.

Hoofdstuk 5 stelt een universele methode voor om de thermodynamica van homogene kiemvorming te analyseren, die van toepassing is op een verscheidenheid aan materialen tijdens het vloeibaar-naar-vast stollingsproces of de vast-naar-vast faseformaties. Homogene kiemvorming van de bcc fase vindt plaats in een fcc één-kristal bij 160 K. De bcc-kiemen zijn meer elliptisch van vorm dan bolvormig. In het algemeen komt de energieverandering van een post-kritische kiem als functie van zijn grootte overeen met de trend die wordt voorspeld door de klassieke kiemvormingstheorie (*Classical Nucleation Theory, CNT*). De kritische kiemgrootte die uit de fit wordt verkregen is vergelijkbaar met de experimentele resultaten. De CNT overschat echter de energiebarrières voor homogene kiemvorming van de bcc-fase. De hoge energiebarrière die door de CNT wordt voorspeld, wordt vermeden door niet-klassieke mechanismen, zoals de aggregatie van kiemen en de vorming van metastabiele tussenfasen. De fcc fase transformeert naar de bcc fase, bij voorkeur na een stapsgewijze "fcc → tussentoestand → bcc" kiemingsprocedure. De tussentoestand ontstaat in de originele fcc fase met een energiebarrière. Dit wordt gevolgd door een andere energiebarrière voor de kiemvorming van de bcc-fase vanuit de tussentoestand. Aggregatie van een naburig sub-kritisch cluster biedt de mogelijkheid voor de primaire kiem om de kritische grootte te bereiken en te overschrijden en de hoge CNT-voorspelde energiebarrière voor homogene kiemvorming te vermijden. De naburige sub-kritische clusters kunnen verschillende kristallografische oriëntatierelaties hebben met de primaire kiem. De lokale temperatuur van de bcc-kiemen fluctueert ondanks de constante temperatuur van het gehele systeem.

Hoofdstuk 6 onderzoekt de heterogene kiemvorming van de bcc-fase die ontstaat op dislocaties op de fcc / fcc korrelgrenzen. Twee simulatiesystemen met verschillende fcc / fcc korrelgrenzen worden bestudeerd. Het ene systeem heeft twee lage hoekkorrelgrenzen met randdislocaties. Het andere systeem bestaat uit een semi-coherente tweeling-korrelgrens en een coherente tweeling-korrelgrens. Thermodynamica van de bcc kiemvorming bij de dislocatie komt overeen met de voorspelling door het model van Cahn. De geschatte elastische constanten en interface-energieën zijn vergelijkbaar met theoretische berekeningen en experimentele resultaten. Er zijn echter aspecten die niet door het model van Cahn worden beschouwd. Vergelijkbaar met de homogene kiemvorming van de bcc-fase in fcc-

ijzer, transformeert de fcc-fase naar de bcc-fase bij voorkeur als gevolg van niet-klassieke mechanismen, zoals de aggregatie van kernen en stapsgewijze "fcc → tussentoestand → bcc" kiemvorming. De tussentoestand initieert echter vanuit de dislocaties zonder energiebarrière, terwijl de homogene kiemvorming van de bcc-fase vanuit de tussentoestand gepaard gaat met een energiebarrière. De bcc-kiemen zijn aggregaten van discrete sub-kritische bcc clusters, die als integraal verbonden zijn aan de tussentoestand. Dergelijke naburige sub-kritische clusters kunnen verschillende oriëntatierelaties hebben en coherent zijn met de originele fcc fase. Ongeacht de isotherme omstandigheden van het systeem zijn de lokale gebieden die de bcc-kernen bevatten, warmer dan de omgeving door de warmteafgifte tijdens fasetransformaties.

Hoofdstuk 7 onderzoekt de effecten van externe rek op de kiemvorming en groei van bcc fase in fcc ijzer. Voor het fcc-eenkristal kan de fcc-naar-bcc-transformatie in fcc-ijzer worden geïnduceerd door een externe rek of spanning op 100 K of lager. De door de rek geïnduceerde bcc-korrels hebben de neiging om een plaatvormige morfologie te hebben en liever één dominante oriëntatie te vormen met specifieke varianten. De Kurdjumov-Sachs oriëntatie domineert de bcc-platen bij 50 K, terwijl de Nishiyama-Wassermann-oriëntatie dominant is op 100 K. Bovendien draagt de externe rek bij tot korrelgroei door het samengaan van naburige bcc-platen met identieke oriëntatie. Die bcc-korrels hebben de neiging om onder een hoek van ongeveer 45° te liggen met de richting van de externe rek. Voor de simulatie met fcc / fcc korrelgrenzen induceert externe rek de kiemvorming van de bcc fase aan zowel de semi-coherente en coherente fcc / fcc tweeling-grens. De bcc-kernen die worden gevormd in de simulatie met fcc / fcc-grenzen, hebben de Nishiyama-Wassermann of de Kurdjumov-Sachs oriëntatie zonder externe rek of spanning. Echter, een externe rek leidt tot een dominante kristallografische oriëntatie. Een rek in de $\langle 112 \rangle_{fcc}$ richting leidt tot een dominante Kurdjumov-Sachs oriëntatie, terwijl een rek in de $\langle 110 \rangle_{fcc}$ richting resulteert in een dominante Nishiyama-Wassermann relatie. Daarnaast worden voor de simulaties met en zonder spanning verschillende eindstructuren verkregen. Wanneer er geen externe rek is, is de korrelvergroting hoofdzakelijk door *impingement* van bcc-korrels met dezelfde kristallografische oriëntatie tijdens de fcc-naar-bcc transformatie, evenals door normale groei als gevolg van de korrelgrens-kromming. Kleine afwijkingen van de ideale kristallografische oriëntatie worden verkregen voor de grove bcc-korrel wanneer de fuserende bcc-korrels in de identieke oriëntatie van de variant zijn; anders zijn er grote afwijkingen in de samengevoegde bcc-korrels. Een externe rek in $\langle 112 \rangle_{fcc}$ richting leidt tot tweeling-bcc korrels in de uiteindelijke structuur. De externe rek in de $\langle 110 \rangle_{fcc}$ richting leidt niettemin tot een bcc-eenkristal in de uiteindelijke structuur.

Tenslotte vat hoofdstuk 8 de belangrijkste conclusies van dit onderzoek samen. Ook worden een aantal aanbevelingen voor vervolgonderzoek gedaan.

Acknowledgements

I would like to express my sincere gratitude to all those who helped me during my PhD. study.

My deepest gratitude goes first and foremost to my supervisors Assoc. Prof. Maria J. Santofimia and Prof. Jilt Sietsma. Maria, thank you very much for your patient guidance, consistent encouragement and support during the past four years. I learned quite a lot from you, both in research and life. I still remember how you led me into the world of my research step-by-step. By explaining to you my comprehension of related literatures weekly, I began to understand what I was going to do during my PhD. study. I was then provided adequate sources and freedom to carry out my studies. When I fell behind the expectation of the project, you have been always the one standing behind me and helping me find the way out. When I had improvements, you were always ready to praise and encourage. I learned a lot in scientific writing and thinking from our regular discussions. Following your wise and scientific supervision, I surprisingly found that I was able to work independently one day. Outside the scientific world, you also act as my “life mentor”. I have been always keeping your words in mind. You told me “Never let others wait for you, but arrive early and get the coffee ready” and “Think carefully before presenting”, etc. You taught me how to defend my research properly and what to prepare for the unexpected occasions. You also encouraged me to have more communication and contact with the colleagues and other researchers. There are quite a lot of such moments that benefits both in my life and research. I will always bear them in mind in the future.

Jilt, thank you very much for your inspiring instruction during the past four years. You always remind me to think critically when doing research. In the progress meetings of the project, I cannot remember how many times I was stuck with the critical questions you raised. The questions are like the fire in the hand of Prometheus, which lights up the lamp of intelligence and leads to absolute new ways of thinking. It has been one of my goals to be able to think critically like you do. I believe that I am already on the way there under your leading. Besides, I admire your patience and carefulness when doing research. I would have given up the thermodynamic analysis of nucleation from the very beginning without your patient instruction. Together with Maria, we discussed this problem time and time again. Each time after the discussion, we had new ideas and progressed either a little bit or a lot. Finally, we managed to reach the furthest point we could do regarding to this problem. Furthermore, I would like to thank you for your careful revisions of my papers. Even a small comma misuse in the papers was found and corrected. However busy, you always managed to send me the revisions even by sacrificing your rest time. I would like to say a lot of thanks to you for your precious time and great efforts in supervision, which broadens my horizons and strengthens my ability of thinking in the past four years.

I would like to extend my thanks to my bachelor and master supervisor, Prof. Min Song. It was your tiny stories about your studying experience abroad during the classes of ‘Heat Treatment of Materials’

that stimulated my dream to pursue a doctor's degree outside China. I was also the six years as a bachelor and then a master student under your supervision, that built me the foundation for my further PhD. studies. Your enthusiasm in research motivates my interest in materials science, and your personality also acts as a good model for me to follow. I would like to say 'Thank you very much for your consistent encouragement and support for all these years'. I would also like to express my thanks to the other supervisor, Prof. Daihong Xiao. You taught me a lot in doing experiments. You have been one of most easy-going supervisors I have ever met. You work very hard, which reminds me to be diligent all the time. Besides, I would like to thank Professor Song Ni. Your encouragements and suggestions help me make the right choices around the corner. Thank you all, I could not walk so far without your efforts.

I would like to thank the colleagues from the computational group. Prof. Barend Thijsse, thank you for guiding me into the gate of molecular dynamics simulation by teaching me the Camellion. That helps me a lot in my PhD. studies. The meetings with you were quite challenging, which nevertheless contributed to improving my simulation skills largely and swiftly. You are a strict but warm-hearted supervisor. You provided me a lot of suggestions and help in my research during the four years. Thank you very much! I would also like to thank Prof. Lucia Nicola, Assoc. Prof. Marcel Sluiter and Assoc. Prof. Amarante Bottger for your precious suggestions and comments in the previous meetings. Dr. Peter Klaver, thank you for teaching me the simulation tool-LAMMPS. You are a very mild and patient person. The skills learned from you benefit my research during the four years. Also, Astrid, thank you for the discussions in all our meetings.

I would like to thank my colleagues in our own group. Assoc. Prof. Erik Offerman, thank you for the useful suggestions about my research in nucleation. I would like to thank Pina and Li for your suggestions in our meetings as well as Richard for helping me with the equipment installation. Bijna, thank you very much for being a good friend and officemate. I admire your independence, courage and high organizing ability. You are a good example for me to learn from. I hope you a happy and fruitful future. Shivraj, thank you for the fruitful discussions in modeling for the past two years. You are very nice and good-tempered. I am very happy to have a colleague like you in our group who is also doing MD simulations. Alfonso, Ashwath, Konstantinos, Jun, Carola, Zaloa, Farideh, Javier, Tungky, Goro, Arthur, Ankit and Viviam, thank you for the enjoyable time with you. We have a lot of good memories together at parties, lunches, dinners and trips. You provided me a lot of useful information and suggestions both in my everyday life and in research. Reina, Jan-Henk, Roumen, and Leo, it is nice to have your greetings and smiles at the corridor in weekdays. Thank you too.

I would also like to thank my mentor Assoc. Prof. Matthijs. The conversations with you always gave me helpful clues both in my study and life. I would also like to thank the committee members for assessing my draft thesis. Your valuable comments help to improve the final thesis. I would like to thank the sectary Olga and Prisca for your assistance in all the paperwork during these years. Thanks are also given to Assoc. Prof. Chad Sinclair for the fruitful discussions on one of my journal papers.

The research leading to these results has received funding from the European Research Council under the European Union' s Seventh Framework Programme FP7/2007 – 2013/ERC grant agreement no. [306292]. Thanks!

Many thanks to my Chinese friends in the Netherlands for the precious friendship. Lu, Jie, Li, Yulan, Shanshan, Liyuan, Ling, Meimei, Wanrou, Shuai, Jia, Jinglang, Chunchun, Dongjuan, Siqu, Jianbin, Xi, Yong, Minxin, Minhe, Haiyang, Bei, Qujiang, Guangmin, Meng, Qian, Lianshi, Willian, Xiaohua, Xiaolin, Zhi, Chenteng, Wei, Yao, Jiefu, Xueyuan, Cheng, Qiyu, Yiming, Yanchen, Yifan, Sihui, April and Philip, thank you for the accompany from you.

I am also grateful to my good friends in China or in other countries. Xiangkai, Qing, Mei, Lujun, Juan and Dongmei, thank you for the frequent chats via online medias. Your care companies me through ups and downs in all these years. I would also like to thank Fei and Lin for your hospitality during my visit to your countries. The sisters and brothers in the research group at CSU, thank you all for holding a comfortable and warm atmosphere wherever we have get-togethers. All the best to you.

Finally, I would like to express my sincerest gratitude to my parents, my elder sister and my brother. Thank you for your endless love, support and dedication for all these years, which gives me strength and courage to go forward with firm steps.

Xiaoqin
Delft, 2017

List of publications

Journal papers

1. **X Ou**. Molecular dynamics simulations of fcc-to-bcc transformation in pure iron - a review. *Materials Science and Technology*, 33(7), 822-835 (2016).
2. **X Ou**, J Sietsma, M J Santofimia. Molecular dynamics simulations of the mechanisms controlling the propagation of bcc/fcc semi-coherent interfaces in iron. *Modelling and Simulation of Materials Science and Engineering*, 24, 055019 (2016).
3. **X Ou**, J Sietsma and M J Santofimia, Thermodynamics of homogeneous nucleation of bcc phase in fcc Fe by molecular dynamics simulations. *To be submitted*.
4. **X Ou**, J Sietsma and M J Santofimia, Thermodynamics of heterogeneous nucleation of bcc phase at the dislocations on different fcc/fcc grain boundaries in Fe by molecular dynamics simulations. *To be submitted*.
5. **X Ou**, J Sietsma and M J Santofimia, Coalescence of ferrite during the fcc-to-bcc transformation in iron by molecular dynamics simulations. *To be submitted*.

Conference paper

1. **X Ou**, J Sietsma, M J Santofimia. Molecular dynamics simulation of the effects of fcc/bcc interfaces on the nucleation and growth of martensite in iron. *Proceedings of the International Conference on Solid-Solid Phase Transformations in Inorganic Materials (PTM)*, Whistler, Canada. 2015, pp 817-823.

Presentations on international conferences

1. **X Ou**, J Sietsma, M J Santofimia. Effects of fcc/fcc grain boundaries on the formation of bcc phase in pure iron by molecular dynamics simulation. *The 8th Multiscale Materials Modeling international conference (MMM 2016)*, France, 2016. (Oral presentation)
2. **X Ou**, J Sietsma, M J Santofimia. Crystallography and thermodynamics of bcc nucleation in fcc-Fe by molecular dynamics simulation. *2016 Europe's Material Science and Engineering (MSE Congress 2016)*, Germany, 2016. (Oral presentation)
3. **X Ou**, J Sietsma, M J Santofimia. A new method to study the thermodynamics of the homogenous nucleation of bcc phase from fcc in pure iron by molecular dynamics simulation. *International Conference on PROCESSING & MANUFACTURING OF ADVANCED MATERIALS Processing, Fabrication, Properties, Applications (THERMEC' 2016)*, Austria, 2016. (Poster presentation)

4. **X Ou**, J Sietsma, M J Santofimia. Molecular dynamics simulation of the effects of the fcc/bcc interfaces on the nucleation and growth of martensite in iron. *2015 international conference on Solid-Solid Phase Transformations in Inorganic Materials (PTM 2015)*, Canada, 2015. (Oral presentation)

About the author

Xiaoqin Ou was born on September 26, 1986 in Chongqing, China. After graduating from Chongqing Dazu Middle School in 2006, Xiaoqin started her bachelor's study at Powder Metallurgy Research Institute (PMRI), Central South University (CSU), China. In 2010, she obtained her B.Sc. degree in Material Chemistry, entitled as the "Excellent Graduate Student". As one of the top 20% graduates, she was exempted from the entrance examination and recommended to continue with her master programme in Materials Science and Engineering. In 2013, she obtained her M.Eng. degree as the top 1% student under the supervision of Prof. Min Song from PMRI, CSU. During the master studies, she published two papers on high-quality international journals and one conference paper as the first author. She also had three journal papers and one authorised patent as a co-author. From July 2013, she began with her doctoral research under the supervision of Assoc. Prof. Maria J Santofimia and Prof. Jilt Sietsma in the department of Materials Science and Engineering at Delft University of Technology, the Netherlands. From 2013 to 2014, she attended the summer school on atomistic simulation techniques in Belgium and the training courses on 'Thermo-Calc Software' in Sweden.

Xiaoqin's main research interests are to understand the mechanisms controlling the nucleation and growth of bcc phase in fcc iron by molecular dynamics simulations.